Semiconductors, Vol. 35, No. 8, 2001, pp. 861–863. Translated from Fizika i Tekhnika Poluprovodnikov, Vol. 35, No. 8, 2001, pp. 897–899.

ATOMIC STRUCTURE AND NONELECTRONIC PROPERTIES OF SEMICONDUCTORS

Growth of Fractal Lithium Clusters in Germanium

S. V. Bulyarskiĭ, V. V. Svetukhin*, O. V. Agafonova, A. G. Grishin, and P. A. Il'in

Ul'yanovsk State University, Ul'yanovsk, 432700 Russia

**e-mail: slava@sv.uven.ru*

Submitted October 12, 2000; accepted for publication January 24, 2001

Abstract—The growth kinetics of lithium clusters in germanium is studied. Ham's theory is generalized to describe the growth of fractal clusters. It is shown that the lithium clusters in germanium are characterized by a fractal geometry with a fractal dimension of 2.4. © *2001 MAIK "Nauka/Interperiodica".*

INTRODUCTION

The small atomic radius of lithium is responsible for the high diffusion mobility of lithium atoms in a germanium lattice; therefore, the decomposition of a supersaturated solid solution occurs at relatively low temperatures [1, 2]. The association of lithium atoms with each other results in the appearance of clusters forming a network with interatomic distances very close to those existing in metallic lithium. However, regardless of the size of a cluster, it differs from metallic lithium since the cluster contains germanium atoms.

Clusterization reduces the concentration of monomers. This process is usually described in terms of the Ham theory of solid-solution decomposition using the Avrami–Ham equation [3, 4]

$$\frac{N(t)-N_E}{N(0)-N_E} = \exp\{-Kt^n\}, \qquad (1)$$

where $N(t)$ is the concentration of monomers; N_E is the equilibrium concentration of monomers; the constant n is determined by the configuration of clusters; and K is a constant dependent on the concentration of nucleation centers, the supersaturation degree of the solution, and the diffusion coefficient of monomers.

This theory was employed to describe the clusterization of lithium [2] on the assumption that clusters are spherical, which corresponds to $n = 3/2$. Another situation was observed in [1], where it was shown that at the initial stage of decomposition $n = 2$, while at the final stage $n = 1$; i.e., the exponent n was found to be time-dependent.

In order to explain the kinetics of decomposition of a lithium solid solution in germanium, a more general model proposed in [5] is used in this study. This model adequately describes other types of decomposition of solid solutions, for instance, of oxygen in silicon.

ANALYSIS OF EXPERIMENTAL DATA ON KINETICS OF GROWTH OF Li CLUSTERS IN Ge

For analysis, we chose the experimental data on decomposition of a solid solution of lithium in germanium reported in [1] and [2]. The circles and triangles in Fig. 1 represent the experimental kinetic curves obtained in both studies. The curves are plotted in the coordinates linearizating Eq. (1). The slope of these kinetic curves, according to Eq. (1), is equal to the exponent n. It should be emphasized that Ham equation is valid at a constant value of the exponent n; however, as can be seen from Fig. 1, the exponent n is time-dependent. Consequently, the Ham theory can only asymptotically describe the initial ($n = 2$) and final ($n = 1$) stages of decomposition of a solid solution and cannot describe the experiment in the entire time interval of the process. The change of n with time can be readily calculated by the numerical differentiation of the experimental data as

$$n(t) = \frac{d}{d(\log t)}\left(\log\left(\ln\frac{N(0)-N_E}{N(t)-N_E}\right)\right). \qquad (2)$$

Figure 2 illustrates the results of calculation of the time dependence $n(t)$ on the basis of the experimental data published in [1, 2].

We now show that the experimental data can be more adequately described by numerically solving the relevant exact differential equation rather than by using a semiempirical Avrami–Ham expression (1). This recently suggested equation [5] corresponds to a model for the growth of precipitates or clusters at the nucleation centers with the concentration N_C and is written as

$$\frac{dN(t)}{dt} = -k_D N_C^{(d-1)/d}(N(t)-N_E) \times \{N(0)+mN_C-N(t)\}^{1/d}. \qquad (3)$$

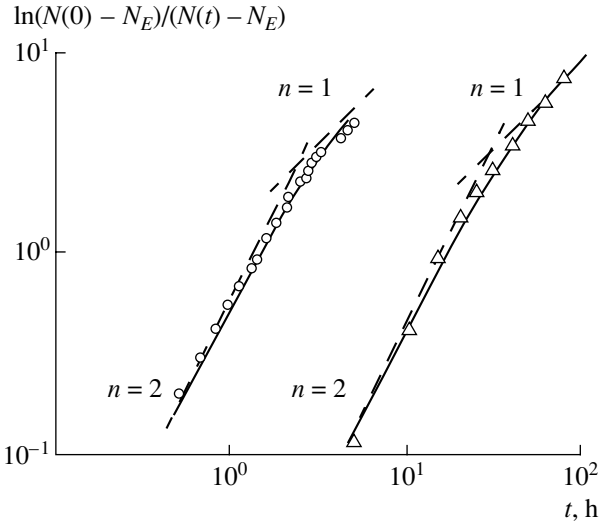

Fig. 1. Kinetics of change in concentration of Li atoms in Ge: data from [1] are shown by triangles (annealing at 33°C), data from [2] are shown by circles (annealing at 59°C). Asymptotes of the initial and final stages of cluster growth with $n = 2$ and $n = 1$ are shown by dashed lines; the numerical solutions of Eq. (3) for $d = 2.4$ are shown by solid lines.

Here, d is the dimension of a cluster (for spherical clusters $d = 3$, for disk-shaped, $d = 2$); m is the number of particles at the nucleation center; and $k_D = 4\pi Db$, where D is the diffusion coefficient of monomers and b is the distance on the order of the interparticle spacing in a cluster.

The asymptotes of Eq. (3) for short and long times yield the expressions from which Ham theory follows. The initial and final stages of decomposition are described respectively by the following expressions:

$$\frac{N(t)-N_E}{N(0)-N_E} = \exp\{-N_C\{(d-1)/d \times [N(0)-N_E]^{1/d}k_D t\}^{d/(d-1)}\}, \quad (4)$$

$$N(t)-N_E = A\exp\{-N_C^{(d-1)/d} \times [N(0)+mN_C-N_C]^{1/d}k_D t\}. \quad (5)$$

Equation (4) is reduced to the Ham equation (1) if $d/(d-1) = n$. Thus, all partial results of Ham theory can be obtained from Eq. (4). For instance, the results for disk-shaped and spherical clusters can be obtained assuming that $d = 2$ and $d = 3$, respectively. The details of calculation of the asymptotic expressions are given elsewhere [5].

It should be remembered that Eqs. (4) and (5) are merely asymptotic. For the description of the entire process of decomposition, it is necessary to use the differential equation (3) in which the shape of a cluster is governed by the parameter d.

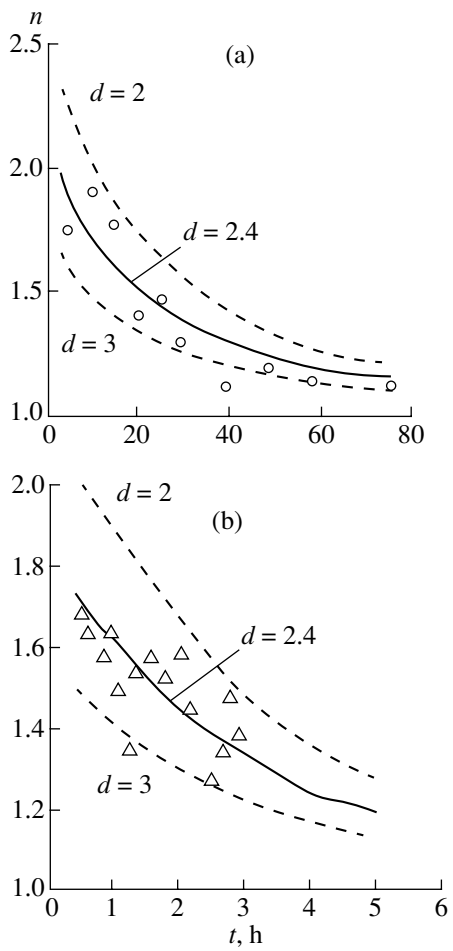

Fig. 2. Changes of the exponent n with the duration of annealing of solid solution of Li in Ge: (a) data (circles) from [1] (annealing at 33°C); and (b) data (triangles) from [2] (annealing at 59°C). The numerical solution to Eq. (3) for various values of d is shown by solid and dashed lines.

When fitting the parameter d, we used the method of least squares. The experimental curves obtained in [1] and [2] can best be described using the same value of $d = 2.4$ (see Fig. 2). This result suggests that the dimensionality of fractal clusters in question is equal to 2.4.

For a detailed study of the shape of lithium clusters in germanium, the clusterization process was simulated using the Monte Carlo method. The precise nature of the nucleation centers of lithium clusters is unknown; however, we may assume that they can be associated with vacancy–lithium or vacancy–oxygen–lithium complexes [1].

The interstitial atoms in a diamond-type lattice can occupy three sites: the tetragonal interstitial site (a T configuration), the hexagonal site (an H configuration), and the "atom-at-bond" configuration (the B configuration). The simulation by the Monte Carlo method was performed for each type of configuration.

The following model was chosen. The space was partitioned into cells. Each cell corresponded to a site where a lithium atom could be located. Thus, the structure of germanium crystal was taken into account. The cells in the Ge lattice were randomly filled with lithium atoms, with the nucleation center of a cluster being located at the center of the space. Each particle (lithium atom) can execute a random walk until it comes in contact with a cluster. The particles are reflected from the space boundary and do not interact with each other.

For a cluster having a fractal geometry, the following relation exists [6] between the sphere radius R drawn from the center of a cluster and the number of particles i inside the sphere: $R \sim i^d$. The slope of the straight line in the representing the $\ln R$ ($\ln i$) dependence yields the fractal dimension. The results obtained by the Monte Carlo method are random and require averaging over several simulations of the process.

The results of simulation for the interstitial atoms in the T and H configurations are shown in Fig. 3. The slope of this curve yields the fractal dimension of clusters obtained by the Monte Carlo method. It is found that, for clusters with atoms having T and H configurations, $d = 2.43 \pm 0.03$. For clusters formed by the atoms in the B configuration, $d = 2.13 \pm 0.03$.

These values are in good agreement with the dimension obtained from the kinetic curves for the decomposition of a supersaturated solid solution of lithium in germanium.

It should be noted that the use of the differential Eq. (3) allows the determination of an average number of particles in a cluster

$$\langle i(t)\rangle = \frac{N(0) - N(t)}{N_C}. \quad (6)$$

For lithium clusters in germanium, this number is equal to about 9×10^5 particles provided the time is long enough. The cluster size distribution function can be obtained in the Gaussian approximation from the Fokker–Planck equation [5]:

$$C(i, t) = \frac{1}{\sqrt{2\pi w^2(t)}} \exp\left[-\frac{(i - \langle i(t)\rangle)^2}{2w^2(t)}\right], \quad (7)$$

where $w(t)$ is the distribution variance defined by the equation

$$\frac{d(w^2)}{dt} = k_D(N(t) + N_E)(\langle i(t)\rangle + m)^a + 2w^2 k_D(N(t) - N_E)a(\langle i(t)\rangle + m)^{a-1}. \quad (8)$$

Thus, the solution of differential Eq. (3) yields not only a more accurate description of the experimental data but also provides more information than the semiempirical Avrami–Ham expression (1).

Our studies showed that the decomposition of a solid solution of lithium in germanium is accompanied by the formation of fractal clusters. The results obtained are quite reasonable since the fractal geometry describes natural objects more adequately than such mathematical idealizations as spheres and disks.

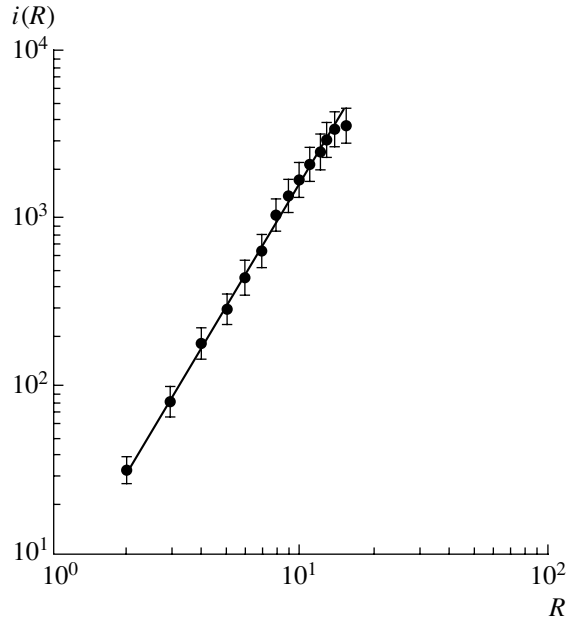

Fig. 3. The number of particles i in a cluster inside a sphere as a function of the radius R of a sphere, where R is expressed in units of Ge lattice constant. The results of simulation by the Monte Carlo method are shown by dots; the approximation by the power law is shown by the line ($d = 2.43 \pm 0.03$).

ACKNOWLEDGMENTS

This study was supported by the Russian Foundation for Basic Research, project nos. 01-00209 and 01-00283.

REFERENCES

1. V. I. Fistul', *Decomposition of Supersaturated Semiconductor Solid Solutions* (Metallurgiya, Moscow, 1977).
2. B. I. Boltaks, *Diffusion and Point Defects in Semiconductors* (Nauka, Leningrad, 1961).
3. F. S. Ham, J. Phys. Chem. Solids **6**, 335 (1958).
4. F. S. Ham, J. Appl. Phys. **30**, 1518 (1959).
5. S. V. Bulyarskiĭ, V. V. Svetukhin, and O. V. Prikhod'ko, Fiz. Tekh. Poluprovodn. (St. Petersburg) **33**, 1281 (1999) [Semiconductors **33**, 1157 (1999)].
6. B. M. Smirnov, *Physics of Fractal Clusters* (Nauka, Moscow, 1991).

Translated by A. Zalesskiĭ

Semiconductors, Vol. 35, No. 8, 2001, pp. 864–869. Translated from Fizika i Tekhnika Poluprovodnikov, Vol. 35, No. 8, 2001, pp. 900–905.

ATOMIC STRUCTURE AND NONELECTRONIC PROPERTIES OF SEMICONDUCTORS

Vibration Modes of Oxygen Dimers in Germanium

V. V. Litvinov*,[1], L. I. Murin, L. Lindström***, V. P. Markevich**, and A. A. Klechko***

** Belarussian State University, Leningradskaya ul. 14, Minsk, 220050 Belarus*

[1] e-mail: litvvv@phys.bsu.unibel.by

*** Institute of Solid-State and Semiconductor Physics, Belarussian Academy of Sciences, ul. Brovki 17, Minsk, 220072 Belarus*

**** Lund University, Division of Solid-State Physics, S-22100 Lund, Sweden*

Submitted November 20, 2000; accepted for publication November 27, 2000

Abstract—Absorption in the infrared region of the spectrum was studied for both the as-grown Ge crystals and the Ge crystals irradiated with fast electrons (with subsequent heat treatment); the crystals were preliminarily enriched with ^{16}O or ^{18}O isotopes. The vibrational absorption bands observed in Ge and peaked at 780, 818, and 857 cm^{-1} are attributed to complexes composed of two atoms (dimers) of ^{16}O, whereas the bands at 741, 776, and 811 cm^{-1} are attributed to complexes of ^{18}O atoms. It is established that electron irradiation of Ge crystals at temperatures near 295 K with subsequent heat treatment at 120–250°C brings about an increase in the intensities of bands peaked at 780 and 818 cm^{-1}. The band peaked at 857 cm^{-1} does not change its intensity under irradiation and, by analogy with Si, is identified with another configuration of oxygen dimers in Ge. The bonding energy of dimers responsible for the bands peaked at 780 and 818 cm^{-1} is estimated at 0.35–0.4 eV.

The formation of oxygen dimers O_{2i} (pairs of interstitial oxygen atoms O_i) represents the initial stage of decomposition of the oxygen solid solution in Si and Ge crystals. Therefore, it is understandably impossible to adequately describe all the processes related to the mass transport and complex formation for oxygen atoms in these crystals without knowing the characteristics of the O_{2i} complexes. This circumstance has motivated an enhanced interest in the determination of the properties of oxygen dimers and in the clarification of their microstructure [1–3].

Oxygen dimers have been detected experimentally in Si using vibration spectroscopy [4]. Three local vibration modes at 1060, 1012, and 1105 cm^{-1} were attributed to O_{2i} in Si. The theoretical simulation of the dimers' structure [5, 6] indicates that the complex is stable in two configurations: Si–O_i–Si–O_i–Si (the staggered configuration) and Si–O_i–Si–Si–O_i–Si (the skewed configuration). The first two of the above bands are in better agreement with the local vibration modes calculated for the first dimer configuration, whereas the high-energy band peaked at 1105 cm^{-1} is attributed to the second configuration [6]. The existence of complexes involving two oxygen atoms in Ge was first noted in studies on the isotopic shift of the band peaked at 780 cm^{-1} in samples irradiated with fast electrons [7]. If the crystals were doped with both ^{16}O and ^{18}O oxygen isotopes, the formation of two new bands peaked at 739 and 757 cm^{-1} was observed (in addition to the band at 780 cm^{-1}). It has been assumed that the positions of all three bands (i.e., those peaked at 780, 739, and 757 cm^{-1}) correspond to the isotopic shift of the local vibration mode of oxygen in the complexes composed of ^{16}O and ^{16}O atoms; ^{18}O and ^{18}O atoms; and ^{16}O and ^{18}O atoms, respectively. Recently, two poorly pronounced bands peaked at 776.5 and 813.7 cm^{-1} have been observed at room temperature in oxygen-enriched Ge crystals rapidly cooled after heat treatment at 900°C; these bands were attributed to oxygen dimers and/or to quenched-in donors of the first type [8]. The objective of this study was the further identification of local vibrational modes related to oxygen dimers in Ge through a comparative analysis of the spectra of as-grown and irradiated crystals doped with ^{16}O or ^{18}O oxygen isotopes.

The crystals to be studied were doped with oxygen during growth in an atmosphere of water vapor (Ge:^{16}O) or by enriching Ge with the ^{18}O isotope (Ge:^{18}O). The concentration of interstitial oxygen O_i was $(0.9–2.6) \times 10^{17}$ cm^{-3} and $(1.5–6.7) \times 10^{17}$ cm^{-3} in the Ge:^{16}O and Ge:^{18}O samples, respectively. The O_i (N_O) concentration was determined from the absorption coefficient at the peaks of the bands at 856 cm^{-1} (for $^{16}O_i$) and 812 cm^{-1} (for $^{18}O_i$) using a calibration factor equal to 1.25×10^{17} cm^{-2} [9]. The samples were irradiated with electrons ($E \approx 4$ MeV) with an integrated flux density of 6×10^{16} cm^{-2} at about 295 K. The heat treatment of the samples was performed in a furnace in a nitrogen atmosphere. The absorption spectra were measured using a Bruker-113v Fourier spectrometer at 10 and 300 K with a spectral resolution of 0.5 and 1.0 cm^{-1}, respectively.

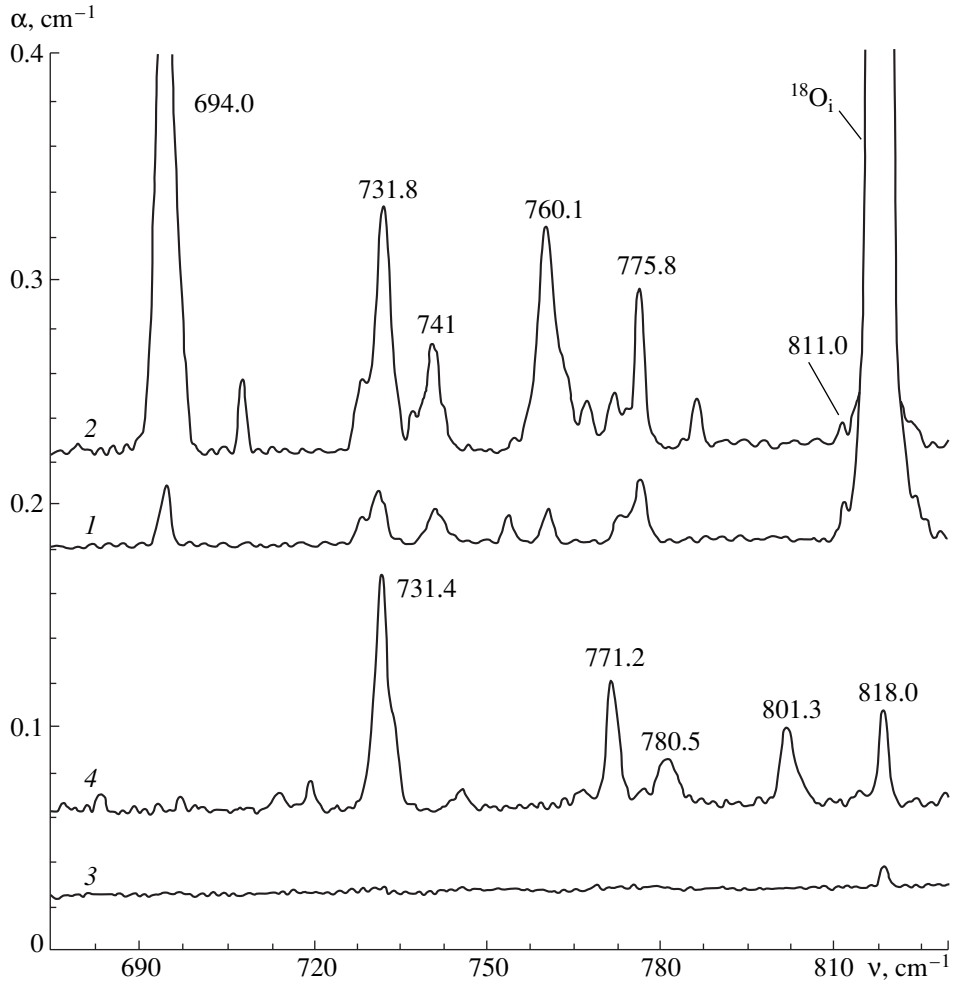

Fig. 1. Absorption spectra (measured at 10 K) of (*1*, *2*) Ge:^{18}O and (*3*, *4*) Ge:^{16}O crystals (*1*, *3*) in the initial state and (*2*, *4*) after irradiation with electrons with subsequent heat treatment for 30 min at 160°C. The concentration of interstitial oxygen was N_O = (*1*) 6.7×10^{17}, (*2*) 3.1×10^{17}, and (*3*, *4*) 9.6×10^{16} cm^{-3}.

In Fig. 1, we show the low-temperature absorption spectra of Ge:^{18}O and Ge:^{16}O crystals in the initial state and also after irradiation with fast electrons and subsequent annealing for 30 min at 160°C. Spectra *1* and *2* correspond to the Ge:^{18}O samples with different $^{18}O_i$ concentrations (6.7×10^{17} and 3.1×10^{17} cm^{-3}), which far exceed the $^{16}O_i$ concentration (9.6×10^{16} cm^{-3}) in Ge:^{16}O (spectra *3*, *4*). Spectra *2* and *4* of the irradiated samples include a number of bands in the range of 680–820 cm^{-1}; these bands were first reported by Whan [7] and are characterized by an isotopic shift in reference to oxygen ($^{16}O \longrightarrow {}^{18}O$). The squared ratio of frequencies at the peaks of the bands $[\nu(^{16}O)/\nu(^{18}O)]^2$ corresponds to the ratio for the antisymmetric stretching vibration of O_i [$(862/818)^2 = 1.11$]. It is of interest that the majority of the bands formed as a result of the heat treatment of irradiated crystals are also observed in unirradiated Ge:^{18}O samples with increased oxygen concentration after they were spontaneously cooled from the melting temperature at which the crystals were enriched with the $^{18}O_i$ isotope (spectrum *1*). Irradiation and subsequent heat treatment of the crystals at 120–250°C resulted only in a manyfold increase in the intensity of bands observed in the initial crystals with an increased O_i concentration (higher than 3×10^{17} cm^{-3}). The band peaked at 811 cm^{-1} is the only exception; its intensity is not appreciably affected by the irradiation and subsequent heat treatment of Ge:^{18}O (spectra *1*, *2*). The poorly pronounced band peaked at 818.0 cm^{-1} and related to antisymmetric stretching vibration (ν_3) of the $^{18}O_i$ residual isotope [10] is only observed in unirradiated Ge:^{16}O samples with a reduced oxygen concentration (spectrum *3*).

Isotopic shift and the dependence of the intensity of bands peaked at 694, 732, 741, 760, 772, and 776 cm^{-1} in Ge:^{18}O and the bands peaked at 731, 771, 780, 801, 814, and 818 cm^{-1} in Ge:^{16}O on the O_i concentration are

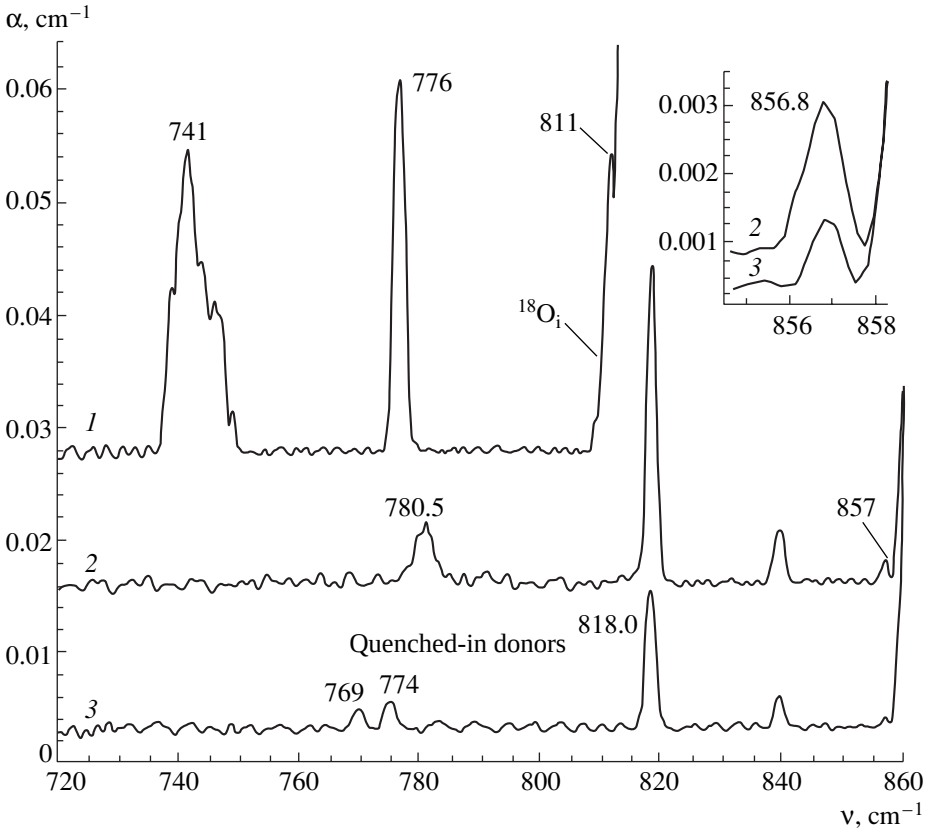

Fig. 2. Absorption spectra (measured at 10 K) of (*1*) Ge:^{18}O and (*2*, *3*) Ge:^{16}O crystals after heat treatment (*1*, *2*) for 20 min at 500°C and (*3*) for 15 h at 300°C. The concentration of interstitial oxygen was N_O = (*1*) 6.3×10^{17} and (*2*, *3*) 2.6×10^{17} cm^{-3}. The portions of the spectra *2* and *3* for $\nu \approx 857$ cm^{-1} are shown in the inset.

indicative of their relation to oxygen-containing complexes. The latter may be represented by O_{2i} dimers and O_{3i} trimers of oxygen and also by oxygen associations with native defects in the Ge lattice. Assignment of the above bands to oxygen-containing quenched-in donors is ruled out owing to inconsistency between the spectral positions of these bands and those of the vibration modes for the aforementioned donor centers [11].

The behavior of the bands in the range from 741 to 776 cm^{-1} (as illustrated in Fig. 2) for heat-treated initial Ge:^{18}O crystals and the bands at 780 and 818 cm^{-1} for Ge:^{16}O after heat treatment is consistent with reliably determined properties of oxygen dimers in Si: high thermal stability (up to the melting temperature) [12] and direct involvement in the formation of quenched-in donors at comparatively low (300–450°C) temperatures [13]. In fact, a short (20 min) heat treatment of the Ge:^{18}O samples at 500°C (with subsequent rapid cooling to room temperature) results in the quenching of the bands peaked at 694, 732, 760, and 772 cm^{-1} with a simultaneous increase in the intensity of the bands peaked at 741 and 776 cm^{-1}. It is noteworthy that, after heat treatment at 500°C, the narrow band peaked at 811 cm^{-1} is still observed in the spectrum, in addition to the bands at 741 and 776 cm^{-1}; however, the measurements of the intensity for the band at 811 cm^{-1} is hampered by the fact that the wing of intense $^{18}O_i$ absorption is superimposed on this band.

It also follows from a comparison of spectra *1* in Figs. 1 and 2 that heat treatment (at 500°C) of the Ge:^{18}O samples with enhanced oxygen concentration brings about an asymmetry of the band peaked at 741 cm^{-1}. This asymmetry is a result of the superposition of the band at 741 cm^{-1} and a broader and less pronounced band peaked at 743–744 cm^{-1}. We relate the origin of the latter band to the formation of higher order quenched-in donors whose vibration modes are responsible for a broad absorption band peaked in the region of 742–745 cm^{-1} [11]. A similar situation also arises in Si. The absorption of Si:^{16}O crystals in the vicinity of 1012 cm^{-1} is caused by two types of oxygen complexes: the oxygen dimers, which exist in the as-grown crystals and are transformed into quenched-in donors in the initial stage of heat treatment at 350–450°C, and the

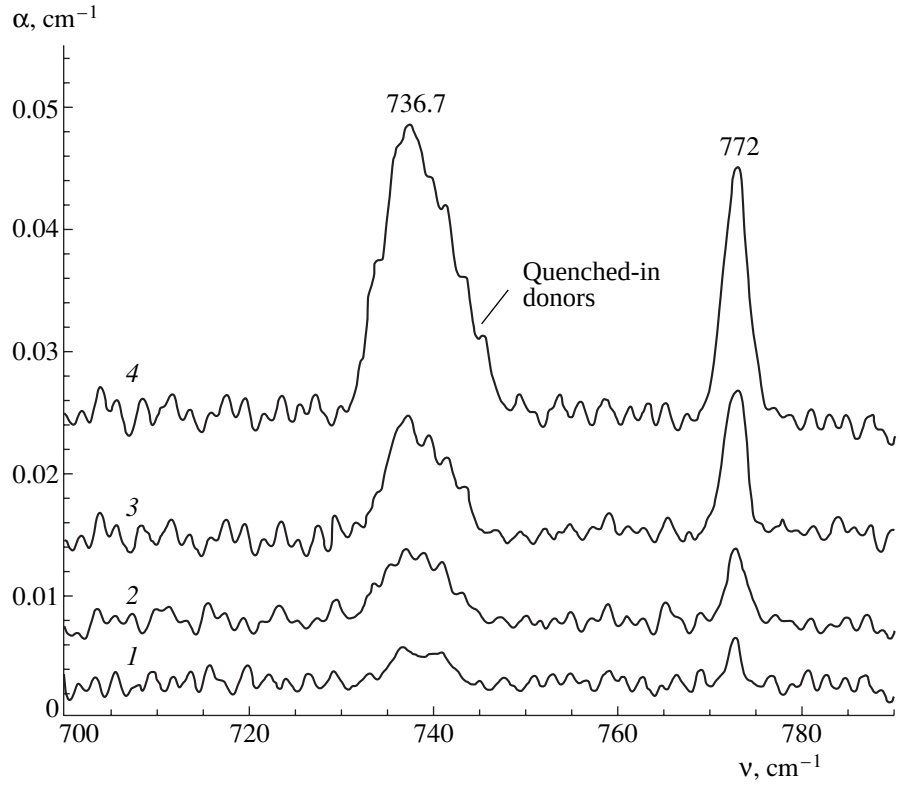

Fig. 3. Absorption spectra of Ge:^{18}O crystals that had different concentrations of O_i and were subjected to heat treatment for 20 min at 500°C. The concentrations of interstitial oxygen was N_O = (*1*) 1.9×10^{17}, (*2*) 3.2×10^{17}, (*3*) 4.4×10^{17}, and (*4*) 6.3×10^{17} cm^{-3}. The spectra were measured at 300 K.

higher order quenched-in donors, which are formed during extended annealing of the samples [12, 13].

Spectrum *2* in Fig. 2 indicates that the bands peaked at 780, 818, and 857 cm^{-1} are distinct in the absorption of the Ge:^{16}O samples that have an oxygen concentration of 2.6×10^{17} cm^{-3} and were subjected to heat treatment for 30 min at 500°C; these bands are isotopic analogues to the bands peaked at 741, 776, and 811 cm^{-1} in Ge:^{18}O. Subsequent heat treatment of the same samples for 15 h at 300°C gives rise to quenched-in donors (QiDs) of the first types (QiD1s and QiD2s with bands at 769 and 774 cm^{-1} [11]). This process is accompanied with the almost complete quenching of the band at 780 cm^{-1} and the band at 818 cm^{-1}; the latter is superimposed on the ν_3 vibrational mode of the residual $^{18}O_i$ isotope (spectrum *3* in Fig. 2). As is shown in the inset in Fig. 2, the intensity of the band at 857 cm^{-1} also decreases as a result of heat treatment of Ge:^{16}O at 300°C. However, this decrease proceeds with a lower rate compared to that for the bands at 780 and 818 cm^{-1}. This indicates that the bands at 780 and 818 cm^{-1}, on the one hand, and the band at 857 cm^{-1}, on the other, are related to oxygen-containing complexes of different origin.

The relation of the bands at 780 and 818 cm^{-1} in Ge:^{16}O and also of the bands at 741 and 776 cm^{-1} in Ge:^{18}O to oxygen dimers ensues from the results of analyzing the spectra measured at room temperature for the samples with various concentrations of $^{18}O_i$ (Fig. 3). Prior to measurement, the samples were subjected to concurrent heat treatment at 500°C and were subsequently cooled by rapid immersion in ethylene glycol. It can be seen that, when the temperature at measurement is changed from 10 K to room temperature, the bands are shifted by about 4 cm^{-1} to lower energies, which is typical of all the oxygen-containing complexes observed in Ge. It is notable that a similar increase in the temperature of the samples when measuring the spectra results in an insignificant (0.5–1.5 cm^{-1}) shift of O_{2i}-related vibrational modes at 1012 and 1060 cm^{-1} in Si to higher frequencies [14]. The absorption band peaked at 737 cm^{-1} (Fig. 3) features a "wing" at higher energies and is representative of the situation illustrated by low-temperature spectrum *1* in Fig. 2 at 741 cm^{-1}. Simulation of the spectrum in the vicinity of 737 cm^{-1} demonstrates a satisfactory agreement with the experimental data if the band at 736.7 cm^{-1} is superimposed on the broad band in the region of 738–745 cm^{-1}. However, it is difficult to

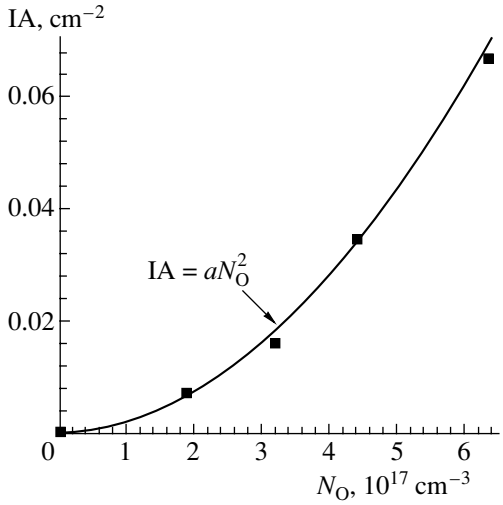

Fig. 4. Integrated areal intensity (IA) of the band peaked at 772 cm^{-1} as a function of $^{18}O_i$ concentration according to the data shown in Fig. 3. The solid line represents the approximation of experimental points by a quadratic dependence.

obtain an accurate quantitative estimate of the area under the band at 736.7 cm^{-1} because the spectrum of background absorption caused by the vibration modes of quenched-in donors of higher order varies owing to differences in oxygen concentration.

The band peaked at 772 cm^{-1} (at 776 cm^{-1} at 10 K) is adequately described by a Gaussian contour with the half-width on the order of 3 cm^{-1}, and its integrated intensity depends quadratically on the $^{18}O_i$ concentration in the samples under investigation (Fig. 4). This dependence is characteristic of the bands related to the O dimers in Si and is consistent with the expression for the dimer concentration (N_2) if the equilibrium is attained in the reaction $O_i + O_i \rightleftharpoons O_{2i}$ and if O_{2i} is not trapped by other centers [4, 15]; i.e.,

$$N_2 = \frac{N_O^2 g_2}{N_{sO} g_1} \exp\left(\frac{E_{b2}}{kT}\right), \quad (1)$$

Spectral positions (ν) and half-widths (Δ) for local vibration modes of oxygen dimers in Si [19] and Ge

	Si ν/Δ, cm^{-1}		Ge ν/Δ, cm^{-1}	
	10 K	293 K	10 K	293 K
$^{16}O_{2i}$	1012.4/3	1013.0/6	780.5/3	776.5/3.5
	1059.7/6	1061.8/7	818.0/2	813.7/3
	1105/1.2		856.8/1.2	
$^{18}O_{2i}$	969.3	969.7	740.7/3.5	736.7/4
	1011.9	1012.7	776.0/2.3	772.3/3
	1057		811/1.4	

where N_{sO} stands for the density of states for O_i in the lattice (for Ge, $N_{sO} = 8.8 \times 10^{22}$ cm^{-3}); g_1 and g_2 are the constants corresponding to the number of possible sites of O_i and O_{2i} in the unit cell of the semiconductor (for Si and Ge, we have $g_1 = 4$ and $g_2 = 12$); and E_{b2} stands for the bonding energy of a dimer.

Experimental values of integrated areal intensity (IA) of the band peaked at 772 cm^{-1} are approximated in Fig. 4 (the solid line) by a quadratic dependence IA = aN_O^2, where $a = 1.7 \times 10^{-37}$ cm^4. On the other hand, IA = kN_2, and the ratio N_2/N_O^2 in formula (1) is defined by the ratio of the coefficients a/k. Assuming that the dipole moment and the oscillator mass for O_i are equal to those for O_{2i}, we may consider the quantity k equal to the coefficient of proportionality of integrated intensity of the band peaked at 812 cm^{-1} with the $^{18}O_i$ concentration. By analyzing the integrated intensity and the absorption coefficient at the peak of the band for $^{18}O_i$ in the samples we studied, the value of k was found to be equal to 3×10^{-17} cm.

The calculation based on the above relations and formula (1) yields the value of the bonding energy equal to $E_{b2} = 0.34$ eV. Taking into account the above assumptions and uncertainties of determining the value of the calibration factor for O_i (1.25×10^{17} cm^{-2} [9] and 5×10^{16} cm^{-2} [16]), we estimate the bonding energy of O_{2i} complexes at 0.35–0.4 eV. The value obtained is 0.05–0.1 eV higher than the bonding energy of O_{2i} in Si [4]. This relation is consistent with the higher concentration of quenched-in donors in Ge than in Si for a comparable concentration of O_i in the samples (see [17]) and also with theoretical inference [18] that the O_{2i} complexes are more stable in Ge than in Si.

A comparison of local vibrational modes for oxygen dimers in Si and Ge (see table) demonstrates the consistency between their number and similarities between the isotopic shift and spectral positions of O_{2i} bands in reference to the band ν_3 for O_i in Ge and Si. In fact, the ratios of the frequencies 780/1012, 818/1060, and 857/1105 for $^{16}O_{2i}$ and 741/969, 776/1011.9, and 811/1057 for $^{18}O_{2i}$ are equal to 0.77 ± 0.01 and coincide with the ratio between the frequencies of the modes ν_3 856/1107 for $^{16}O_i$ and 812/1058 for $^{18}O_i$ in Ge and Si, respectively. The opposite temperature shift and inverse relation between the corresponding half-widths are characteristic special features of the bands peaked at 780 and 818 cm^{-1} (741 and 776 cm^{-1}) for O_{2i} in Ge:^{16}O (Ge:^{18}O) in comparison to their analogues at 1012 and 1060 cm^{-1} (969 and 1011.8 cm^{-1}) in Si:^{16}O (Si:^{18}O). A special feature of the bands peaked at 857 cm^{-1} in Ge:^{16}O and at 811 cm^{-1} in Ge:^{18}O is their insensitivity to electron irradiation and to the subsequent heat treatment of the crystals at temperatures of 120–250°C. The latter is also characteristic of the band peaked at

1105 cm^{-1} for oxygen dimers in Si [19]. The effect observed in Ge:^{16}O (Ge:^{18}O) and related to irradiation-induced enhancement of the bands at 780 and 818 cm^{-1} (741 and 776 cm^{-1}), on the one hand, and the absence of such an effect for the band at 857 cm^{-1} (812 cm^{-1}), on the other hand, support the results of the theoretical simulation [5, 6] concerning the existence of two different configurations of oxygen dimers in Si and Ge.

ACKNOWLEDGMENTS

This study was supported in part by Belarussian Republic Foundation for Basic Research and by the INTAS–Belarus, grant no. 97-0824.

REFERENCES

1. U. Gosele, K.-Y. Ahn, B. P. R. Marioton, *et al.*, Appl. Phys. A **A48**, 219 (1989).
2. S. A. McQuaid, M. J. Binns, C. Z. Londos, *et al.*, J. Appl. Phys. **77**, 1427 (1995).
3. R. C. Newman, J. Phys.: Condens. Matter **12**, R335 (2000).
4. L. I. Murin, T. Hallberg, V. P. Markevich, and J. L. Lindström, Phys. Rev. Lett. **80**, 93 (1998).
5. S. Oberg, C. P. Ewels, R. Jones, *et al.*, Phys. Rev. Lett. **81**, 2930 (1998).
6. M. Pesola, J. von Boehm, and R. M. Nieminen, Phys. Rev. Lett. **82**, 4022 (1999).
7. R. E. Whan, Phys. Rev. **140**, A690 (1965).
8. P. Clauws and P. Vanmeerbeek, Physica B (Amsterdam) **273–274**, 557 (1999).
9. E. J. Millett, L. S. Wood, and G. Bew, Br. J. Appl. Phys. **16**, 159 (1965).
10. E. Artacho, F. Yndurain, B. Pajot, *et al.*, Phys. Rev. B **56**, 3820 (1997).
11. V. P. Markevich, L. I. Murin, V. V. Litvinov, *et al.*, Physica B (Amsterdam) **273–274**, 570 (1999).
12. T. Hallberg and J. L. Lindström, J. Appl. Phys. **79**, 7570 (1996).
13. J. L. Lindström and T. Hallberg, J. Appl. Phys. **77**, 2684 (1995).
14. T. Hallberg, J. L. Lindström, L. I. Murin, and V. P. Markevich, Mater. Sci. Forum **258–263**, 361 (1997).
15. L. I. Murin and V. P. Markevich, in *Proceedings of the 7th International Conference "Shallow-Level Centers in Semiconductors"* (World Sci., Singapore, 1997), p. 339.
16. W. Kaiser and C. D. Thurmond, J. Appl. Phys. **32**, 115 (1961).
17. C. S. Fuller, J. Phys. Chem. Solids **19**, 18 (1961).
18. D. J. Chadi, Phys. Rev. Lett. **77**, 861 (1996).
19. J. L. Lindström, T. Hallberg, D. Aberg, *et al.*, Mater. Sci. Forum **258–263**, 367 (1997).

Translated by A. Spitsyn

Semiconductors, Vol. 35, No. 8, 2001, pp. 870–872. Translated from Fizika i Tekhnika Poluprovodnikov, Vol. 35, No. 8, 2001, pp. 906–908.

ELECTRONIC AND OPTICAL PROPERTIES OF SEMICONDUCTORS

Effect of Deviations from Stoichiometry on Electrical Conductivity and Photoconductivity of $CuInSe_2$ Crystals

M. A. Abdullaev*, Dz. Kh. Magomedova*, R. M. Gadzhieva*, E. I. Terukov, Yu. A. Nikolaev**, Yu. V. Rud'**, and P. P. Khokhlachev***

** Amirkhanov Institute of Physics, Dagestan Science Center, Russian Academy of Sciences, Makhachkala, 367003 Russia*

*** Ioffe Physicotechnical Institute, Russian Academy of Sciences, Politekhnicheskaya ul. 26, St. Petersburg, 194021 Russia*

Submitted December 6, 2000; accepted for publication December 7, 2000

Abstract—The results of studying the photoelectric properties of bulk $CuInSe_2$ crystals grown at various deviations from the stoichiometry are reported. The crystals were grown by the Bridgman method. The concentration and mobility of charge carriers were measured. The dependence of the properties of $CuInSe_2$ crystals with *n*- and *p*-type conductivities on the deviation of composition from the stoichiometry is discussed. © *2001 MAIK "Nauka/Interperiodica".*

The $CuInSe_2$-based ternary semiconductor compounds and solid solutions are very promising materials for highly efficient thin-film solar cells [1–3]. The efficiency of photovoltaic converters based on $CuIn_xGa_{1-x}Se_2$ compound has been brought to 18% [3]. The improvement of properties of the components of such devices provides possibilities for a further increase in their efficiency.

The increase in efficiency requires homogeneous and perfect $CuInSe_2$ films with a composition close to stoichiometry to be obtained. However, the existence of a highly volatile component in the composition of such semiconductors remains the main source of a high concentration of intrinsic lattice defects [2–5]. In *p*-$CuInSe_2$ crystals, the impurity levels of cation vacancies and interstitial atoms of the chalcogenide are dominant, whereas in compounds with the electronic type of conductivity the chalcogenide vacancies are of primary importance. Table 1 summarizes the data [1, 3, 4] on the main energy levels and formation energy of corresponding lattice defects.

It can be seen that there is a large difference in magnitudes of the formation energy among the following defects: Cu atoms at the In sites (Cu_{In}), vacancies in the In sublattice (V_{In}), and vacancies in Cu sublattice (V_{Cu}). Taking into account this variation, it may be assumed that the Cu_{In} antisite point defects must prevail over V_{Cu} and V_{In} vacancies. In most studies, a shallow-level acceptor determining the properties of *p*-type samples is identified with a Cu_{In} defect [1]. In *n*-$CuInSe_2$ crystals, a donor level usually occurs with the activation energy E_D ranging from 0.01 to 0.018 eV. It should also be mentioned that after the crystallization of $CuInSe_2$ and cooling to room temperature, the crystal always contains Cu_{In} and In_{Cu} antisite defects. This may be the consequence of a sphalerite–chalcopyrite phase transition [1]. The photosensitivity of $CuInSe_2$ crystals can be improved by reducing the concentration of antisite lattice defects by impurity doping [6, 7]. However, the effect of deviation from stoichiometry on electrical properties of $CuInSe_2$ has not been adequately studied [1, 2]. In this paper, we report the first results of studying the electrical and photoelectric properties of $CuInSe_2$ crystals with controlled variation of Cu to In ($Cu/In \le 1$).

The phases were synthesized by alloying a proper amount of extra-pure starting elements in evacuated quartz cells (~10^{-3} Pa) heated to a temperature about 1200°C under the vibration mixing. The $CuInSe_2$ and

Table 1. Lattice defects in $CuInSe_2$ crystals

Type of defect	Type of conductivity	Enthalpy of formation, eV	Activation energy, eV
Cu_{In}	*p*	1.3	$E_v + 0.05$
V_{In}	*p*	2.8	$E_v + 0.22$
Se_i	*p*	22.4	
V_{Cu}	*p*	2.6	$E_v + 0.7$
In_{Cu}	*n*	1.4	$E_c - 0.01$
In_i	*n*	9.1	
V_{Se}	*n*	2.4	$E_c - 0.22$
Cu_i	*n*	4.4	$E_c - 0.6$

Note: Data taken from [1, 3, 4].

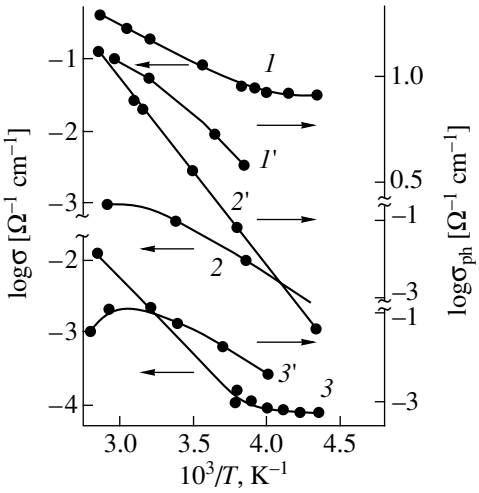

Fig. 1. Temperature dependences of (*1*–*3*) electrical conductivity σ and (*1*'–*3*') photoconductivity σ_{ph} of $Cu_{2-x}In_xSe_2$ crystals with In content x = (*1*, *1*') 1.0, (*2*, *2*') 1.05, and (*3*, *3*') 1.10.

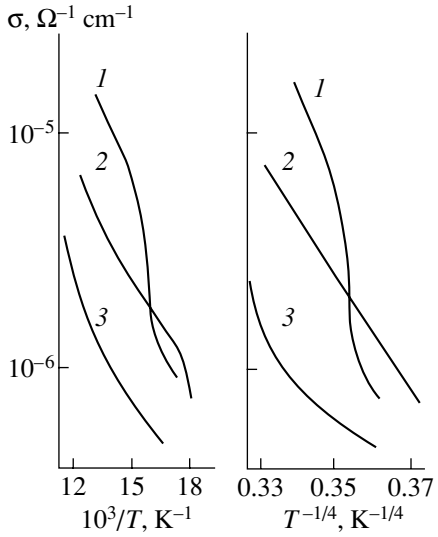

Fig. 2. Temperature dependences of electrical conductivity of $Cu_{2-x}In_xSe_2$ crystals (the numbers at curves correspond to the same values of x as in Fig. 1).

$Cu_{2-x}In_xSe_2$ crystals were grown by the vertical Bridgman method. After crystallization, the ingots were slowly cooled to 500°C and annealed at ~350°C for about 50 h [8–10]. The X-ray phase analysis showed that the crystals in the range $x \le 1.0$–1.2 had a chalcopyrite structure with the unit-cell parameters typical of $CuInSe_2$ [10]. The microphase analysis showed a high homogeneity of the ingots, which indicated that the initial composition was preserved.

The samples cut from the ingots were lapped and had average dimensions of $\sim 0.6 \times 0.1 \times 0.2$ cm. The surface of samples after polishing with a diamond abrasive was chemically treated in a solution of $K_2Cr_2O_7$(4 g) + H_2O(20 ml) + HNO_3(10 ml). The electrical conductivity (σ), thermoelectric power (α), photoconductivity (σ_{ph}), and their temperature dependences were measured by the two- or four-probe method. Pure In was used for electrical contacts. According to the measurements of thermoelectric power, the samples with $x \approx 1$ had a hole conductivity which changed to electron conductivity at $x \gtrsim 1.15$.

From the typical electrical characteristics of the grown crystals with various x given in Table 2, it follows that the degree of compensation $K = N_D/N_A$ increases, and the Hall mobility of charge carriers decreases with increasing x. The increase of x causes a change in the sign of the thermoelectric power ($p \longrightarrow n$).

The temperature dependences of electrical conductivity σ and photoconductivity σ_{ph} for the typical $Cu_{2-x}In_xSe_2$ samples are shown in Fig. 1. Here, it follows that the magnitudes of σ and σ_{ph} decrease with increasing x. This may be caused by the increase in the concentration of antisite defects, which compensate the acceptors. In crystals with $x = 1.05$, the amount of electrically active In appeared to be insufficient to overcome the effect of increasing σ and σ_{ph}, which can be explained by the difference in passivation mechanisms for acceptor and donor impurities. One might expect that the interstitial In suppresses the acceptor behavior of Cu vacancies and interacts with electrically inactive In atoms. This process is probably accompanied by the rearrangement of In atoms to the sites of electrically active trivalent ions. Measurements show that, in the samples with $x \simeq 1$ (Table 2), the rearrangement does not occur because the transition of In atoms into electrically active state requires a higher energy level. We may conclude that the interstitial In atoms in $CuInSe_2$

Table 2. Electrical properties of $Cu_{2-x}In_xSe_2$ crystals at T = 300 K

The sample no.	Indium content, x	Type of conductivity	Concentration of (p) holes and (n) electrons, cm^{-3}	Degree of compensation K	Mobility μ_H, $cm^2\ V^{-1}\ s^{-1}$	Thermoelectric power α, μV K^{-1}
1	1.0	p	4×10^{17}	0.88	28	320
2	1.05	p	7×10^{16}	0.91	6.8	360
3	1.1	n	2×10^{15}	0.98	17.1	−48

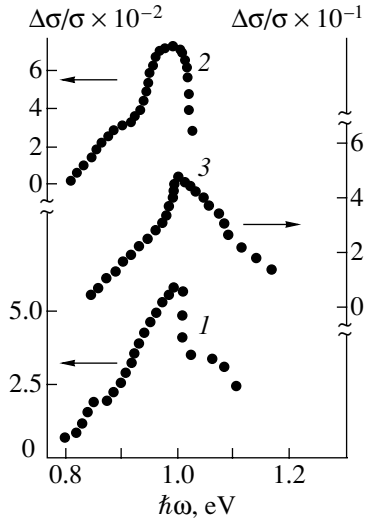

Fig. 3. Spectral variations of the steady-state photoconductivity of $Cu_{2-x}In_xSe_2$ crystals (the numbers at curves correspond to the same values of x as in Fig. 1).

crystals behave like donors with levels localized in band gap with the energy range of 0.45–0.61 eV.

The low-temperature behavior of electrical conductivity of $Cu_{2-x}In_xSe_2$ crystals for various x is illustrated in Fig. 2. This shows that the samples exhibit the Mott transition, as evidenced by the straight lines in a plot $\ln\sigma$ versus $T^{-1/4}$. The slope of the straight lines allows as to estimate the density of states near the Fermi level at $\sim 5 \times 10^{19}$ cm^{-3} eV. The radius of electron localization near E_F ($E_c - E_F = 0.6$ eV) is taken as 56 nm. The occurrence of the conductivity with a constant activation energy (ε_3) is possible below the temperatures $T = k^{-1}\varepsilon_3(\ln k^{-1})^{-1}$, where $\varepsilon_3 = 0.61\varepsilon_D(1 - 0.29K^{1/4})$, $\varepsilon_D = e^2/Kr_D$, $r_D = 0.62N^{-1/3}$ [11], and N is the mean distance between the atoms of the main impurity. The estimations yield $K = 0.98$ for sample 2, which explains the relatively high temperatures at which the Mott transition is observed. Sample 3 shows nonlinear current–voltage characteristics at $T \lesssim 77$ K in weak electric fields E. Assuming that the activation nature of the electric current in a nonuniform field depends on the degree of disorder in the material, $I \propto \exp[(-\varepsilon_A - \alpha E^{1/2})/kT]$; the characteristic length of nonohmic behavior is estimated at ~2 μm, which is larger than the hopping range for the Mott conductivity $R = 3.8\alpha T_0^{1/4}/T^{1/4} \approx 600$ Å.

The spectral dependences of photoconductivity in typical $Cu_{2-x}In_xSe_2$ crystals at 300 K are shown in Fig. 3. As follows from Fig. 3, for $x = 1$, the peak of photoconductivity at the shortest (among the crystals studied) wavelength $\hbar\omega_m \cong 0.98$ eV is located near the edge of the fundamental absorption of $CuInSe_2$ [1] and, therefore, can be attributed to quasi-interband transitions. Estimation of E_g from the position of a long-wavelength edge of the intrinsic photoconductivity in spectra is hampered because of strongly pronounced extrinsic bands in the crystals. The decrease in x reduces the contribution of impurity bands. In a sample with $x = 1.05$, the peak in the photoconductivity spectra shifts to longer wavelengths (to 1.1 μm), although the lifetime of charge carriers, determined from the kinetics of photoconductivity decay, remains almost constant. A further increase in the In content causes a shift of the peak back towards the short-wavelength region of the spectrum due to the changes in type and concentration of dominant lattice defects.

Thus, it may be concluded that the changes in the ratios of In and Cu atomic content in a starting charge provide for the effective control of the electrical properties in $CuInSe_2$ crystals; convert their conductivity $p \longrightarrow n$; and make it possible to control the profile of photoactive absorption, which is of importance for the development of physical grounds for the technology of semiconductor solar cells based on $CuInSe_2$ chalcogenides.

REFERENCES

1. *Copper-Indium Diselenide for Photovoltaic Applications*, Ed. by T. J. Coutts, L. L. Kazmerskii, and S. Wagner (Pergamon, New York, 1986).
2. H. W. Schok, Appl. Surf. Sci. **92**, 606 (1996).
3. L. Stolt, J. Hodstrom, J. Kesslitz, *et al.*, Appl. Phys. Lett. **62**, 597 (1993).
4. S. B. Zhang, W. Su-Huai, A. Zungez, and H. Y. Katayami-Yoshida, Phys. Rev. B **57**, 9642 (1998).
5. M. A. Abdullaev, R. M. Gadzhieva, Dzh. Kh. Magomedova, and P. P. Khokhlachev, Neorg. Mater. **33**, 411 (1997).
6. Sh. Nishiwaki, N. Kohaza, T. Negami, and T. Wada, Jpn. J. Appl. Phys., Part 2 **37**, L71 (1998).
7. R. P. Swarma and J. C. Garg, Indian J. Pure Appl. Phys. **28**, 183 (1990).
8. M. A. Abdullaev, Dzh. Kh. Amirkhanova, and R. M. Gadzhieva, Neorg. Mater. **29**, 785 (1993).
9. M. A. Abdullaev, J. Kh. Magomedova, R. M. Gadjieva, and P. P. Khokhlatchev, in *Proceedings of the XIV International Conference on Thermoelectrics, St. Petersburg, 1995*, p. 198.
10. *Physicochemical Properties of Semiconductor Materials* (Nauka, Moscow, 1975).
11. N. F. Mott and E. A. Davis, *Electronic Processes in Non-Crystalline Materials* (Clarendon, Oxford, 1979; Mir, Moscow, 1982).

Translated by A. Zalesskiĭ

Semiconductors, Vol. 35, No. 8, 2001, pp. 873–876. Translated from Fizika i Tekhnika Poluprovodnikov, Vol. 35, No. 8, 2001, pp. 909–912.

ELECTRONIC AND OPTICAL PROPERTIES OF SEMICONDUCTORS

The Onset of Double Limiting Cycle in the Impurity-Assisted Electric Breakdown of a Compensated Semiconductor with a Shorted Hall Voltage

K. M. Jandieri* and Z. S. Kachlishvili

Faculty of Physics, Tbilisi State University, 380028 Tbilisi, Georgia

** e-mail: faculty@tsu.ge*

Received November 24, 2000; accepted for publication November 25, 2000

Abstract—Nonlinear autooscillations arising in the case of the impurity-assisted breakdown in a compensated semiconductor placed in a classically strong magnetic field with a shorted Hall voltage have been studied by means of computer simulation. A double limiting cycle appears in the phase portrait of the system in a certain range of load resistances (connected in series with the sample) and external DC voltages. This effect makes it possible, in principle, to construct a high-frequency generator operating in different amplitude modes under the same external conditions. © *2001 MAIK "Nauka/Interperiodica".*

The low-temperature electric breakdown in a compensated semiconductor is a favorable condition for the onset of an oscillating instability. This issue has been intensively studied both experimentally (see, e.g., [1]) and theoretically [2]. It has been found that the magnetic field plays an important role among external parameters strongly affecting the nonlinear dynamics of the semiconductor conductivity. In this connection, two modes can naturally be distinguished: those of fixed current direction (Hall current $J_Y = 0$) and those of a fixed field direction (Hall field $E_Y = 0$). In the first case, the Hall-field relaxation plays an important role along with the dielectric relaxation of the applied field [3, 4]. Regular and stochastic autooscillations in the fixed-current mode were obtained in these studies with the use of this concept. The ground and excited states of a hydrogen-like impurity were taken into account in [3], whereas in [4] the excited state was disregarded, which made it possible to establish a simple and intuitive analytical criterion for the onset of undamped autooscillations. The results obtained in [3] and [4] are qualitatively similar.

In this study, we analyze nonlinear autooscillations in a homogeneous semiconductor in the fixed-field direction mode by means of computer simulation.

Let us consider a compensated semiconductor (*n*-type to be specific) connected in series with a load resistance R and a dc power supply with voltage $\mathscr{E}$. A magnetic field **H** is applied to the semiconductor perpendicularly to the electric field **E**. The study was carried out in terms of the mathematical model that included the following differential equations [5]:

$$\frac{dn}{dt} = (J_{op} + A_T)(N_d - N_a - n) + A_I(N_d - N_a - n)n - B_T(N_a + n)n, \quad (1)$$

$$\frac{dE}{dt} = \frac{4\pi L}{\varepsilon SR}\left[\zeta - E - \frac{eSR}{L}\mu nE\right], \quad (2)$$

$$\frac{d\theta}{dt} = -\frac{\theta - \theta_0(E)}{\tau_d}, \quad (3)$$

where n, N_d, and N_a are, respectively, the densities of free electrons, donors, and compensating acceptors; J_{op} and A_T are, respectively, the rates of optical and thermal carrier generation from donor states; A_I and B_T are, respectively, the coefficients of impact ionization and thermal recombination; L, S, and ε are the sample length along the current lines, cross section of the sample, and its dielectric constant; $\zeta \equiv \mathscr{E}/L$; μ is the free electron mobility; $\theta \equiv T_e/T$ is the electronic temperature normalized to the lattice temperature T and $\theta_0(E)$ is its steady-state value determined from the energy balance equation for a given E; and τ_d is the delay time proportional to the energy relaxation time [6].

Equation (1) describes the kinetic processes taking place in the hydrogen-like donor state. Equation (2) describes the dielectric relaxation of the electric field in the semiconductor. Equation (3) characterizes the retardation of the electronic temperature relative to changes in the electric field. The retardation is due to the inertia of the electronic gas heating. Such an equation was first used in [7] for describing the retardation of the impact

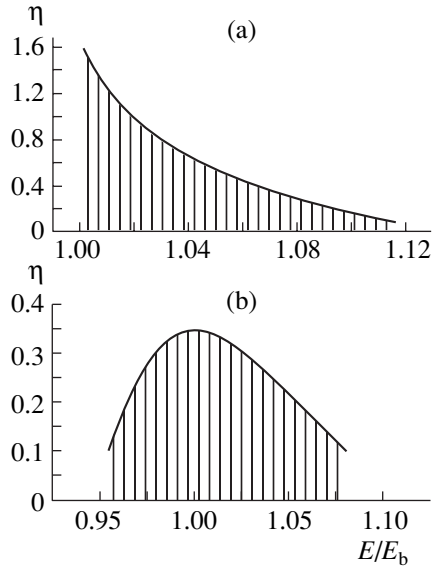

Fig. 1. Bifurcation diagrams for *n*-Ge on the (E/E_b, η) plane. System parameters: $T = 4.2$ K, degree of compensation $c = 0.95$, $N_d = 5 \times 10^{16}$ cm^{-3}, optical generation rate J_{op}: (a) 10^3 and (b) 10^8 s^{-1}.

ionization coefficient. This equation was generalized in [8] to describe the relaxation of the average energy of the electronic gas.

Thus, the problem is considered with the use of the electronic temperature method. Therefore, all kinetic coefficients are considered to be functions of θ. Let us use for the $A_I(\theta)$ and $B_T(\theta)$ functions the expressions derived in [9, 10] in terms of the Dravin ionization cross section and the corrected Lax's cascade capture theory. The carrier mobility has the form [11, 12]

$$\mu = \frac{e}{m^*}\left\langle \frac{\tau}{1+\omega_c^2\tau^2}\right\rangle, \quad (4)$$

where m^* is the free carrier effective mass, τ is the momentum relaxation time, $\omega_c = eH/m^*c_0$ is the cyclotron frequency, and c_0 is the speed of light in free space. In a classically strong magnetic field ($\omega_c^2\tau^2 \gg 1$), expression (4) takes a simpler form:

$$\mu = \frac{e}{m^*\omega_c^2}\left\langle \frac{1}{\tau}\right\rangle. \quad (5)$$

It is noteworthy that we obtained in [5] (on the basis of the above-described model) the necessary and sufficient condition for the onset of undamped autooscillations. This condition was transformed, on physical grounds and after some algebra, to a rather simple analytic criterion. It means that the onset of oscillation instability is favored by a high donor concentration, a high degree of compensation, and a classically strong magnetic field. The strong magnetic field, leading to a dramatic change in how the mobility depends on the electron temperature, is among the most important factors favoring the onset of oscillation instability in a semiconductor. For example, in the case of scattering on impurity ions, we have $\mu \propto \theta^{3/2}$ instead of $\mu \propto \theta^{-3/2}$, in accordance with Eq. (5). As a result, the saturation of the drift velocity becomes possible, which is extremely important for the onset of autooscillations [7]. Within our mathematical model, the magnetic field effect is in fact manifested only in the above change in the type of the $\mu(\theta)$ dependence. Certainly, the coefficients A_I and B_T also depend on magnetic field because of the $\theta(H)$ dependence, but it is not this dependence that is responsible for the change in the system's behavior.

For the computer simulation, the parameters of the system were chosen on the basis of the analytical criterion derived in our previous work.

For convenience, the following dimensionless variables are introduced:

$$X \equiv (n-n^*)/n^*, \quad Y \equiv (E-E^*)/E^*,$$
$$Z \equiv (\theta-\theta^*)/\theta^*.$$

In what follows, the asterisk indicates equilibrium values of the indicated physical quantities. We used in calculations the following approximate expressions:

$$A_I(\theta) = C_1\theta^{C_2}\exp(-C_3\theta), \quad B_T(\theta) = \frac{C_4}{\theta^{3/2}},$$

$$\mu_I(\theta) = C_5\theta^{C_6}, \quad \theta_0(E) = C_7E^{C_8},$$

where

$$C_1 = 7.2\times10^{-10}\ \text{cm}^3/\text{s}, \quad C_2 = 2.86,$$
$$C_3 = 0.05, \quad C_4 = 2.12\times10^{-5}\ \text{cm}^3/\text{s},$$
$$C_5 = 9.45\times10^{5}\ \text{cm}^3/\text{s}, \quad C_6 = -1.013,$$
$$C_7 = 11.86, \quad C_8 = 0.87$$

describe the real dependences [9, 10] in the vicinity of the breakdown point, where the onset of nonlinear oscillations is anticipated.

Bifurcation diagrams on the plane (E/E_b, η), where E_b is the breakdown electric field and $\eta \equiv E/(\zeta - E)$, are presented in Fig. 1. They are plotted for *n*-Ge under the following conditions: $T = 4.2$ K, degree of compensation $c = 0.95$, $N_d = 5\times10^{16}$ cm^{-3}. The hatched regions in the diagrams correspond to equilibrium points of the saddle focus type (unstable points of other kinds are nonexistent in the problem in question); i.e., they are related to undamped autooscillations in the system. Comparing Figs. 1a and 1b shows that the hatched region spreads toward the electric breakdown fields with an increasing illumination intensity.

The current density oscillations were analyzed in the above range of parameters with the use of computer simulation by applying the numerical Runge–Kutta

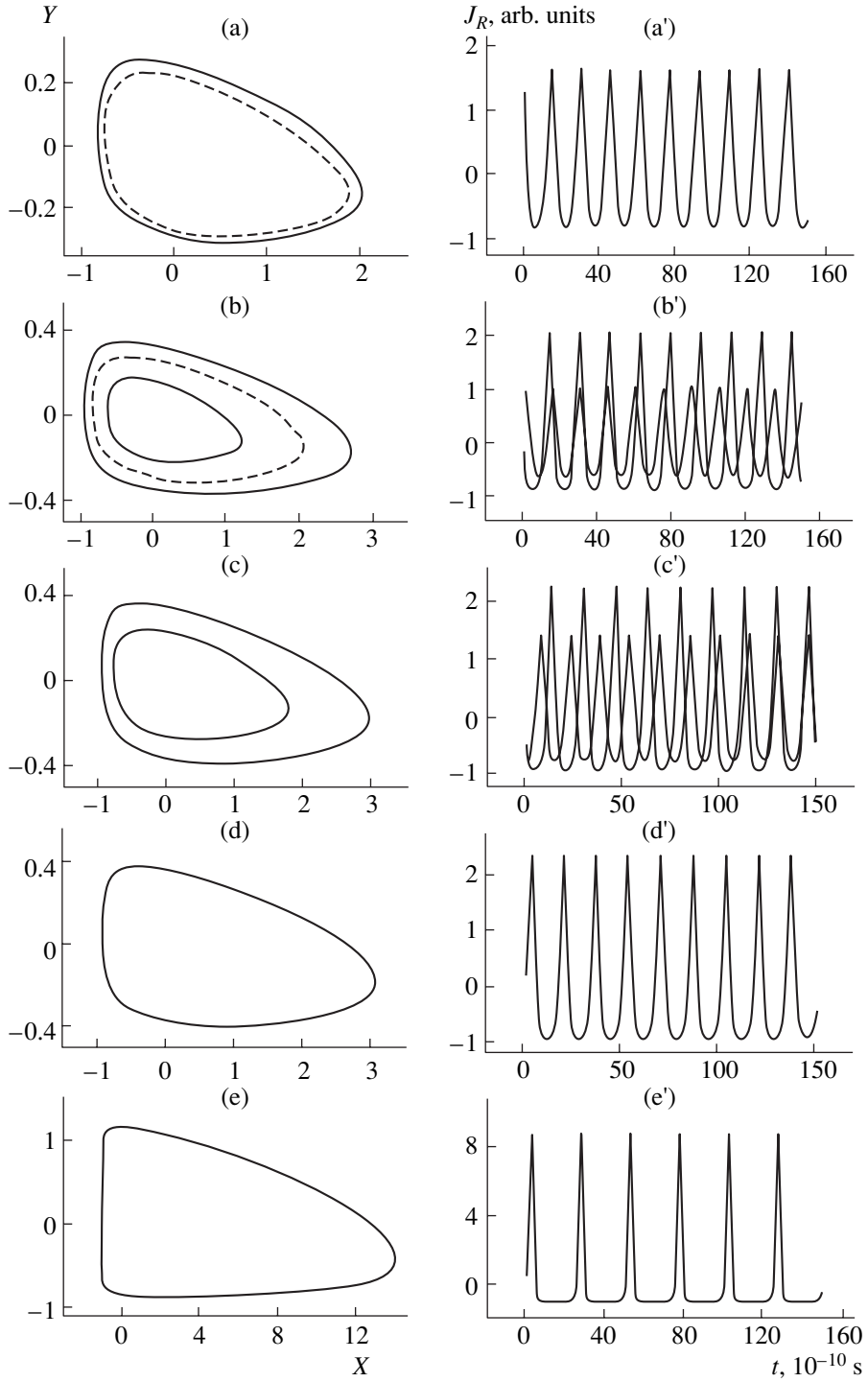

Fig. 2. Phase portraits (a–e) on the (X, Y) plane and the related $J_R(t)$ functions (a'–e') for nonbifurcation parameters identical to those in Fig. 1 and for the following values of the bifurcation parameter η (a, a') 1.2, (b, b') 1.1, (c, c') 1.06, (d, d') 1.05, and (e, e') 0.03.

method. It was found that the oscillation amplitude increases appreciably (about 8- to 10-fold) and the frequency decreases somewhat (approximately twice) with decreasing η at fixed electric field strength in the semiconductor. At the same time, the oscillation amplitude slightly decreases and the frequency slightly increases with increasing electric field at a fixed η. By definition, η is the ratio of voltages applied to the sample and to the load resistance. Therefore, the abovementioned change in the bifurcation parameters can easily be achieved physically by changing the load resistance or the source voltage.

In addition, a double limiting cycle appears in a certain range of η values [12]; i.e., oscillations with different amplitudes may arise at fixed system parameters, depending on the initial conditions. To illustrate the aforesaid, we present in Fig. 2 the phase portraits on the (X, Y) plane, where $\mathbf{E} \parallel X$, $\mathbf{E} \times \mathbf{H} \parallel Y$, as well as the time dependence of the normalized current density $J_R \equiv (J - J^*)/J^*$ for fixed $E/E_b = 1.018$ and varied η. Phase portraits for other planes, not providing any essentially new information, are not presented for the sake of brevity. It can be seen that one stable (solid line) and one unstable (dashed line) limiting cycle emerges at η close to the bifurcation value (Fig. 2a). With a decreasing η ($\eta \approx 1.1$), the first bifurcation occurs—a second limiting cycle of relatively small size with almost the same oscillation frequency as in the case of the large stable cycle (Fig. 2b). With η subsequently decreasing, at $\eta \approx 1.06$ there occurs a second bifurcation—the unstable limiting cycle merges with the large stable one (Fig. 2c). Even after that, the slightest decrease in η leads to the disappearance of the smaller stable limiting cycle with the large limiting cycle remaining as the only stable closed phase path in the phase portrait (Fig. 2d). Then the behavior of the system with decreasing η does not undergo any significant change, with only the oscillations becoming increasingly anharmonic (Fig. 2e'). Obviously, the situation shown in Fig. 2c is unstable and cannot be achieved experimentally. It merely illustrates the way in which the transition between the double- and single-cycle stable states occurs.

The obtained results indicate that such a high-frequency semiconductor generator can in principle be constructed, which can work in the following three distinct modes depending on the electric circuit parameters (load resistance, source voltage).

In the first mode, there are no stationary oscillations at all or only oscillations with fixed amplitude appear, depending on whether the initial point in the phase portrait in Fig. 2a lies inside or outside the unstable limiting cycle. Switching on and off the generator can be achieved by applying an external pulse of, respectively, positive or negative polarity.

In the second mode, there appear oscillations with small (if the corresponding initial point lies inside the unstable limiting cycle (Fig. 2b)) or rather large amplitude (otherwise). Switching between these two states can be achieved by applying external pulses of positive or negative polarity.

In the third regime, fixed-amplitude stationary oscillations appear in the system irrespective of the initial conditions.

To conclude, it should be noted that, compared with Eqs. (1) and (2), Eq. (3) is characterized by an essentially smaller time scale. Presumably, this is why no chaotic autooscillations appear in our theoretical interpretation of the problem; i.e., the system is stable with respect to random, uncontrolled processes.

REFERENCES

1. R. P. Huebener, J. Peinke, and J. Parisi, Appl. Phys. A **A48**, 107 (1989).
2. E. Schöll, Appl. Phys. A **A48**, 95 (1989).
3. G. Hupper and E. Schöll, Phys. Rev. Lett. **66** (18), 2372 (1991).
4. Z. S. Kachlishvili and K. M. Jandieri, Pis'ma Zh. Éksp. Teor. Fiz. **67** (5), 340 (1998) [JETP Lett. **67**, 358 (1998)].
5. K. M. Jandieri and Z. S. Kachlishvili, Pis'ma Zh. Tekh. Fiz. **23** (16), 62 (1997) [Tech. Phys. Lett. **23**, 643 (1997)].
6. Z. S. Kachlishvili and K. M. Jandieri, Bull. Georgian Acad. Sci. **154**, 208 (1996).
7. V. V. Vladimirov and V. N. Gorshkov, Fiz. Tekh. Poluprovodn. (Leningrad) **14**, 417 (1980) [Sov. Phys. Semicond. **14**, 247 (1980)].
8. E. Schöll, Solid-State Electron. **31**, 539 (1988).
9. Z. S. Kachlishvili, Phys. Status Solidi B **48**, 65 (1971).
10. Z. S. Kachlishvili, V. G. Dzhakeli, and T. A. Gegechkori, Soobshch. Akad. Nauk Gruz. SSR **3**, 565 (1981).
11. V. L. Bonch-Bruevich and S. G. Kalashnikov, *The Physics of Semiconductors* (Nauka, Moscow, 1990).
12. A. A. Andronov, A. A. Vitt, and S. E. Khaikin, *Theory of Oscillators* (Fizmatgiz, Moscow, 1959; Pergamon, Oxford, 1966).

Translated by S. Ktitorov

Semiconductors, Vol. 35, No. 8, 2001, pp. 877–879. Translated from Fizika i Tekhnika Poluprovodnikov, Vol. 35, No. 8, 2001, pp. 913–916.

ELECTRONIC AND OPTICAL PROPERTIES OF SEMICONDUCTORS

Preparation and Properties of Isotopically Pure Polycrystalline Silicon

O. N. Godisov*, A. K. Kaliteevskiĭ*, V. I. Korolev, B. Ya. Ber***, V. Yu. Davydov***, M. A. Kaliteevskiĭ***, and P. S. Kop'ev*****

** Electromechanical Plant, St. Petersburg, 198096 Russia*

*** Khlopin Radium Institute, St. Petersburg, 194021 Russia*

**** Ioffe Physicotechnical Institute, Russian Academy of Sciences, Politekhnicheskaya ul. 26, St. Petersburg, 194021 Russia*

Submitted December 28, 2000; accepted for publication January 10, 2001

Abstract—A method for extracting silicon isotopes was developed. Polycrystalline ^{28}Si, ^{29}Si, and ^{30}Si samples isotopically enriched to 99.95, 99.5, and 99.9%, respectively, were prepared. Energies of optical phonons in the isotopically pure samples show the expected dependence on the average atomic mass. © *2001 MAIK "Nauka/Interperiodica".*

Silicon is the most widely used material in present-day solid-state electronics. More than 90% of semiconductor devices are Si-based. Natural silicon is a mixture of three stable isotopes with atomic masses of 28 (92.21%), 29 (4.70%), and 30 (3.09%). The development of electronics calls for further miniaturization of the elements in integrated circuits (ICs) and for an increase of their clock rate, as well as for an improvement of the characteristics of power semiconductor devices, which is hampered by a series of fundamental and technical problems, e.g., heat removal from ICs and the fabrication of heavily doped substrates with uniform dopant distribution.

One possible approach to the problem of heat removal from ICs is the use of isotopically pure Si. The effect of isotopic composition on the thermal conductivity of Ge was first observed in the late 1950s [1]. Further investigations revealed that the low-temperature thermal conductivity of ^{70}Ge isotopically enriched to 99.99% exceeded that of natural Ge by one order of magnitude [2]. Thermal conductivity of diamond was raised by 50% by enriching it to 99.93% in ^{12}C [3, 4]. A considerable increase in the thermal conductivity of Si due to enrichment in ^{28}Si to 99.85% has been reported recently [5, 6].

Uniform doping cannot be obtained for Czochralski-grown Si. An alternative to doping during growth is neutron-transmutation doping. With this method, dopant atoms are produced as a result of nuclear transmutation of lattice atoms when corresponding isotopes capture slow neurons in a nuclear reactor [7–10]. Doping of Si is performed by the transmutation of ^{30}Si according to the reaction

$$^{30}\mathrm{Si} + n^0 \longrightarrow {}^{31}\mathrm{Si} \longrightarrow {}^{31}\mathrm{P} + e^-.$$

The unstable isotope ^{31}Si with a half-life of 2.6 h is transmutated into to the stable isotope ^{31}P, which is a donor impurity in Si. The use of isotopically enriched ^{30}Si for neutron-transmutation doping should allow heavily doped Si with uniform impurity distribution to be obtained.

Spitzer *et al.* [11] demonstrated specific features of crystal-lattice dynamics in low-dimensional ^{70}Ge/^{74}Ge isotopic superlattices. Preparation of Si-isotopic heterostructures should allow a closer examination of phonon properties in Si.

The use of isotopically pure Si should make it possible to improve the characteristics of synchrotron-radiation monochromators [12] and elementary-particle detectors [13–17]. Isotopically pure Si can also be used for the fabrication of mass standards and refinement of the Avogadro constant [18].

Although isotopically pure Si attracts considerable interest, investigations of this material are hampered, because highly isotopically enriched and chemically pure Si is difficult to produce in sufficiently large amounts.

This study is devoted to the development of a method for the industrial production of isotopically pure Si. This method involves separating the chemical compounds of Si isotopes followed by chemical conversion to high-purity Si.

The Si isotopes were separated by centrifugation [19]. This method is based on the separation of gas molecules with different molecular masses in a high centrifugal-force field produced in a rotor of a gas centrifuge (centrifugal acceleration $>5 \times 10^6$ m/s^2). The gas centrifuge has one inlet and two outlets for gas fractions enriched with light and heavy components. SiF_6 is used in the centrifugal separation of Si isotopes. This work-

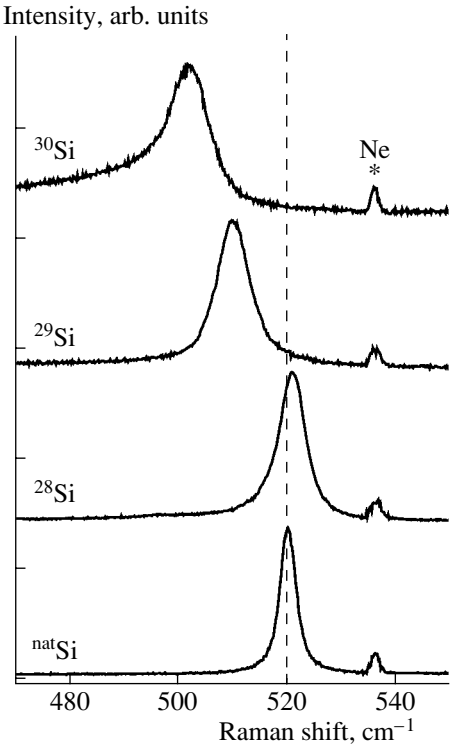

Fig. 1. Room-temperature Raman spectra of ^{28}Si, ^{29}Si, and ^{30}Si samples and single-crystal natural ^{nat}Si. The spectra are shifted along the vertical axis for clarity of presentation. Spectral feature labeled Ne is caused by radiation of an Ne Heusler lamp used for the calibration of the monochromator.

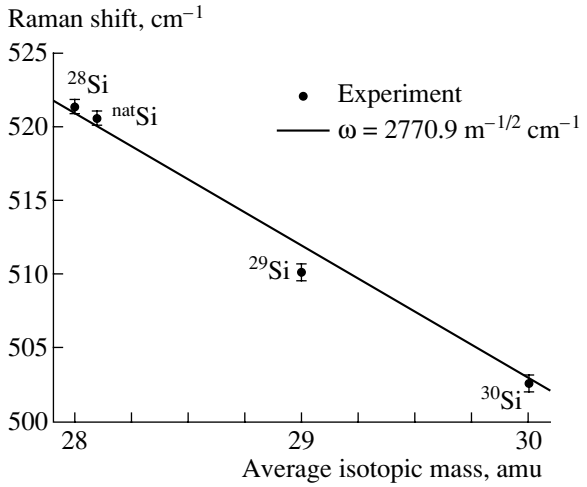

Fig. 2. Phonon frequency as a function of average atomic mass of the ^{28}Si, ^{29}Si, and ^{30}Si samples and natural ^{nat}Si (points). Solid line represents the $\omega(\mathbf{k}) \propto \overline{M}^{-1/2}$ dependence.

ing gas is chosen because fluorine has only one isotope (^{19}F) and SiF_4 exhibits a sufficiently high saturated-vapor pressure at room temperature [20]. Since a single gas centrifuge provides a moderate relative change in Si-isotope concentration, a great number of centrifuges connected in series is required for a significant enrichment of the gas in any isotope.

Intermediate enrichment stages are needed to extract ^{29}Si and ^{30}Si [21], because the concentrations of these isotopes in natural Si are low. At the first stage, $^{28}SiF_4$ is produced with an extraction ratio of about 80%. Simultaneously, the working gas is purified thoroughly from impurities differing from $^{28}SiF_4$ in molecular mass. At the following stages, high enrichment in ^{29}Si and ^{30}Si is achieved by sampling alternately light and heavy fractions. An analysis of isotopic composition, performed with an MC7303M quadrupole mass spectrometer, revealed the following isotopic concentrations: 99.95% ^{28}Si, 99.5% ^{29}Si, and 99.9% ^{30}Si.

Then, SiF_4 was converted to silane according to the nucleophilic-substitution reaction

$$NaAlH_4 + SiF_4 \longrightarrow SiH_4 + NaAlF_4.$$

The silane obtained was purified and converted to elemental Si by pyrolysis

$$SiH_4 \longrightarrow Si + 2H_2.$$

Finally, we obtained Si in the form of irregularly shaped granules 0.3–0.5 mm in size. Chemical and isotopic compositions of the samples were analyzed with an ISP MS VG Plasma Quard quadrupole mass spectrometer with inductively confined plasma. The analysis confirmed the isotopic purity of the samples and showed that a total impurity concentration is no higher than 10^{-3} at. %.

Raman spectra were measured with a computerized spectral setup based on a DFS-24 double grating monochromator. The spectral slit width was 1 cm^{-1}. All spectra were recorded in backscattering geometry at room temperature using an argon laser (488 nm) as a source. The pump-radiation power was 30 mW at a spot 50 μm in size. To minimize the possible heating of the sample, we cooled it in an argon flow. No effects related to heating by the pump radiation were detected.

According to selection rules, only one triply degenerate F_{2g}-symmetry vibration is allowed in the first-order Raman spectrum ($\mathbf{k} = 0$) of crystalline Si. The frequency of this vibration in natural Si is close to 521 cm^{-1} [22]. It is well known that the average atomic mass in the crystal or its sublattices has an influence on phonon frequencies. In the harmonic approximation, the dependence of the phonon frequency on the atomic mass for elemental semiconductors is given by the expression $\omega(\mathbf{k}) \propto \overline{M}^{-1/2}$ for all wave vectors.

Figure 1 shows the Raman spectra of ^{28}Si, ^{29}Si, and ^{30}Si samples. The spectrum of natural Si is shown for comparison. It can be seen that the positions of the phonon lines of ^{29}Si and ^{30}Si are shifted to lower energies, and the line of ^{28}Si is shifted to higher energies rel-

ative to the line of natural Si. This behavior is consistent with the $\omega(\mathbf{k}) \propto \overline{M}^{-1/2}$ dependence as well as with the fact that natural Si is a mixture of three stable isotopes with atomic masses of 28, 29, and 30.

Figure 2 shows the phonon frequency as a function of the average atomic mass of the samples studied. The solid line represents the $\omega(\mathbf{k}) \propto \overline{M}^{-1/2}$ dependence. It can be seen that phonon energies in isotopically pure samples exhibit the expected dependence on the average atomic mass.

The pyrolytic-Si samples are not perfect single crystals. This should manifest itself in the broadening of the phonon lines. Indeed, the Raman line of natural single-crystal Si is narrow and symmetric (Fig. 1), whereas the phonon lines of the ^{28}Si and ^{29}Si samples are noticeably broadened; in addition, the line of ^{30}Si has an asymmetric shoulder on the low-frequency side. It is well known that the presence of defects in the crystal lattice leads to the violation of selection rules for phonons with the wave vector $\mathbf{k} = 0$ in the first-order Raman spectrum, which should eventually result in the broadening of Raman lines. We ascribe the additional broadening of the phonon lines of the Si isotopes to lattice disordering. It can be shown that Raman lines of disordered samples should also have a low-energy shoulder, which is described by a spectral function calculated within the coherent-potential approximation [23].

Thus, we prepared samples of isotopically pure Si, which exhibit the expected frequency positions of the Raman lines. The method devised (after insignificant modification of available capacity) will allow the preparation of kilograms of ^{29}Si and ^{30}Si and hundreds of kilograms of ^{28}Si.

ACKNOWLEDGMENTS

We are grateful to A.N. Ionov, K.L. Muratikov, V.M. Ustinov, and H.J. Pohl for their valuable participation in discussions and to I.N. Goncharuk and A.N. Smirnov for performing the Raman measurements.

REFERENCES

1. T. Gebale and G. W. Hull, Phys. Rev. **110**, 773 (1958).
2. M. Asen-Palmer, K. Bartkowski, E. Gmelin, *et al.*, Phys. Rev. B **56** (15), 9431 (1997).
3. T. R. Anthony, W. F. Banholzer, J. F. Fleisher, *et al.*, Phys. Rev. B **42** (2), 1104 (1990).
4. L. H. Wei, P. K. Kuo, R. L. Thomas, *et al.*, Phys. Rev. Lett. **70** (24), 3764 (1993).
5. W. S. Capinski, H. J. Maris, E. Bauser, *et al.*, Appl. Phys. Lett. **71** (15), 2109 (1997).
6. T. Ruf, R. W. Henn, M. Asen-Palmer, *et al.*, Solid State Commun. **115** (5), 243 (2000).
7. K. Heydorn and N. Hegaard, Chemom. Intell. Lab. Syst. **23** (1), 191 (1994).
8. M. L. Kozhukh, Nucl. Instrum. Methods Phys. Res. A **329** (3), 453 (1993).
9. M. G. Gornov, O. M. Grebennikova, Y. B. Gurov, *et al.*, Instrum. Exp. Tech. **33** (3), 554 (1990).
10. A. N. Erykalov, E. I. Ignatenko, M. L. Kozhukh, *et al.*, At. Énerg. **65** (1), 558 (1988).
11. J. Spitzer, T. Ruf, M. Cardona, *et al.*, Phys. Rev. Lett. **72** (10), 1565 (1994).
12. A. I. Chumakov, R. Ruffer, O. Leupold, *et al.*, Appl. Phys. Lett. **77** (1), 31 (2000).
13. C. S. Rogers and A. T. Macrander, Nucl. Instrum. Methods Phys. Res. A **335** (3), 561 (1993).
14. A. Dimauro, A. Ljubicic, E. Nappi, *et al.*, Nucl. Instrum. Methods Phys. Res. A **343** (1), 323 (1994).
15. B. C. MacEvoy, A. Santocchia, and G. Hall, Physica B (Amsterdam) **274**, 1045 (1999).
16. G. Gasse, P. P. Allport, and M. Hanlon, IEEE Trans. Nucl. Sci. **47** (3), 527 (2000).
17. P. Kuijer, Nucl. Instrum. Methods Phys. Res. A **447** (1–2), 251 (2000).
18. Yu. V. Tarbeev, A. K. Kaliteevskiĭ, V. I. Sergeev, *et al.*, Metrologiya **31** (3), 269 (1994).
19. E. I. Abakumov, V. A. Bazhenov, Yu. V. Verbin, *et al.*, At. Énerg. **67** (4), 255 (1989).
20. V. I. Sergeev, A. K. Kaliteevsky, O. N. Godisov, and R. D. Smirnov, in *Proceedings of the 5th International Symposium on the Synthesis and Applications of Isotopes and Isotopically Labeled Compounds*, Ed. by J. Allen and R. Voges (Wiley, London, 1995).
21. A. K. Kaliteevsky, O. N. Godisov, and V. V. Kuraev, in *Proceedings of the 6th International Symposium on the Synthesis and Applicatoins of Isotopes and Isotopically Labeled Compounds*, Ed. by J. R. Heys and D. G. Melillo (Wiley, London, 1998), p. 683.
22. E. Anastassakis, A. Pinczuk, E. Burstein, *et al.*, Solid State Commun. **8**, 133 (1970).
23. H. D. Fuchs, C. H. Grein, R. I. Devien, *et al.*, Phys. Rev. B **44**, 8633 (1991).

Translated by N. Izyumskaya

Semiconductors, Vol. 35, No. 8, 2001, pp. 880–882. Translated from Fizika i Tekhnika Poluprovodnikov, Vol. 35, No. 8, 2001, pp. 917–919.

ELECTRONIC AND OPTICAL PROPERTIES OF SEMICONDUCTORS

Electrical Properties of $Cd_xHg_{1-x}Te$/CdZnTe Heterostructures

A. G. Belov, A. I. Belogorokhov*, and V. M. Lakeenkov

Giredmet State Scientific Center, 109017 Moscow, Russia

** e-mail: belog@mig.phys.msu.su*

Submitted November 15, 2000; accepted for publication January 18, 2001

Abstract—Specific features of the electrical properties of *p*-type $Cd_xHg_{1-x}Te$/CdZnTe heterostructures have been studied at liquid-nitrogen temperatures. The adopted theoretical model satisfactorily describes the obtained experimental data. Errors in determining the concentration and mobility of heavy holes—arising when contributions to the electrical parameters from electrons and light holes are disregarded—are evaluated. © *2001 MAIK "Nauka/Interperiodica"*.

1. INTRODUCTION

The recent development of epitaxial techniques for obtaining narrow-gap solid solutions has promoted the $Cd_xHg_{1-x}Te$/CdZnTe heterostructures as the most promising materials for the fabrication of infrared detectors. The constituent materials have also been studied rather intensively, but some of their properties obviously have not been investigated in sufficient detail. For example, it is unclear exactly how the influence of substrate should be accounted for in analyzing results of electrical measurements. Moreover, the problem of how such important parameters as the concentration and mobility of free carriers should be determined correctly (taking into account all the relevant factors) is far from being solved. Without aspiring to consider the problem exhaustively, we make an attempt to analyze some specific electrical properties of the materials in question and the influence exerted by a number of factors on the accuracy of determining the concentration and mobility of free carriers in *p*-type samples at liquid-nitrogen temperatures.

$Cd_xHg_{1-x}Te$ epitaxial layers of *p*-type, grown by liquid-phase epitaxy on CdTe and $Cd_{1-y}Zn_yTe$ ($0.03 \le y \le 0.06$) substrates of *n*- and *p*-types, were used.

2. CALCULATIONS AND ESTIMATES

The basic difference of epitaxial heterostructures from single-crystal samples consists, as regards electrical measurements, in the presence of massive substrates whose thickness (500–1000 μm) markedly exceeds that of the layer itself (20–40 μm). In other words, the substrate may shunt the epitaxial layer; consequently, its influence should be taken into account in analyzing the results of electrical measurements. In the general case, the following relations are valid for a system comprising a substrate of thickness d_s and an epitaxial layer of thickness d_{ep} ($d = d_s + d_{ep}$) [1]:

$$\frac{d}{\rho} = \frac{d_{ep}}{\rho_{ep}} + \frac{d_s}{\rho_s}, \tag{1}$$

$$\frac{Rd}{\rho^2} = \frac{R_s d_s}{\rho_s^2} + \frac{R_{ep} d_{ep}}{\rho_{ep}^2}. \tag{2}$$

Here, ρ, ρ_s, and ρ_{ep} are the resistivities of, respectively, the whole heterostructure, substrate, and layer; R, R_s, and R_{ep} are the Hall coefficients for the whole heterostructure, substrate, and layer; and e is the electron charge.

Let us choose, for making an estimate, the following values of the parameters appearing in formulas (1) and (2) (T = 77 K): ρ_{ep} = 1.0 Ω cm; d_{ep} = 20 μm; R_{ep} = 600 cm^3/C; ($1/Re = 1.05 \times 10^{16}$ cm^{-3}); ρ_s = 50 Ω cm; d_s = 1000 μm; $R_s = 10^4$ cm^3/C; ($1/Re = 6.25 \times 10^{14}$ cm^{-3}). Then, we obtain

$$\frac{d_{ep}}{\rho_{ep}}\Big/\frac{d_s}{\rho_s} = 1; \quad \frac{R_{ep} d_{ep}}{\rho_{ep}^2}\Big/\frac{R_s d_s}{\rho_s^2} = 3.$$

It can be seen that the contribution from the substrate to the resistivity is equal to the contribution from the layer, and the Hall coefficient is approximately one-third; i.e., disregarding the contribution of the substrate may lead to a substantial error in determining ρ_{ep} and R_{ep}.

At the same time, the analysis of a vast body of experimental data obtained on a great number of samples (several hundred) failed to reveal any significant differences between the dependences of the Hall coefficient on magnetic induction $R(B)$ for epitaxial heterostructures and similar dependences for single-crystal samples with close electrical parameters. No substrate effect is "felt," which seems strange at first glance.

A special investigation concerned with the substrate contribution to the electrical parameters of a hetero-

structure demonstrated that a potential barrier exists between the layer and the substrate, electrically insulating the epitaxial layer and the substrate [2]. In other words, the influence of the substrate can be ignored in analyzing galvanomagnetic data for $Cd_xHg_{1-x}Te$/CdZnTe heterostructures and all considerations related to the magnetic inductance dependences of the Hall coefficient $R(B)$ for single-crystal samples are applicable to epitaxial layers. Mention should only be made of some fundamental aspects.

In analyzing the electrical properties of $Cd_xHg_{1-x}Te$ solid solutions at $T = 77$ K, it should be kept in mind that free carriers of three kinds are present in a sample: electrons, light holes, and heavy holes (with concentrations n, p_l, and p_h, respectively). At fixed x and T, the relative values of these parameters are determined solely by the reduced Fermi energy ε_F/kT [3]. In this case, the following relations are valid for the magnetic field dependence of the Hall coefficient $R(B)$ and for the electrical resistivity ρ [4]:

$$R = \frac{1}{e}\frac{A}{E^2 + A^2B^2}, \tag{3}$$

$$A = \frac{p_l\mu_l^2}{1+\mu_l^2B^2} + \frac{p_h\mu_h^2}{1+\mu_h^2B^2} - \frac{n\mu_e^2}{1+\mu_e^2B^2},$$

$$E = \frac{p_l\mu_l}{1+\mu_l^2B^2} + \frac{p_h\mu_h}{1+\mu_h^2B^2} + \frac{n\mu_e}{1+\mu_e^2B^2},$$

$$\frac{1}{\rho} = e(p_l\mu_l + p_h\mu_h + n\mu_e). \tag{4}$$

For the samples studied, the second term in the denominator of formula (3) can be neglected, compared with the first term, at $B \le 1.4$ T. If we take as an estimate the mobility values $\mu_e = 10^5$ cm^2/(V s), $\mu_l = 10^4$ cm^2/(V s), and $\mu_h = 500$ cm^2/(V s) ($\mu_l/\mu_h = 30$ [5]), then we obtain that, with B varying from 0.1 to 1.4 T, the multiplier $(1 + \mu_eB^2)$ changes approximately 100-fold and $(1 + \mu_l^2B^2)$ changes 5.5-fold, whereas $(1 + \mu_h^2B^2)$ remains virtually unchanged. This means that electrons contribute to $R(B)$ only in weak magnetic fields ($B \approx 0.1$ T), and the contribution of light holes, although decreasing with increasing B, is comparable with the contribution of heavy holes for the strongest field $B = 1.4$ T. Hence, it follows that, when defining the hole concentration as $1/Re$, we in fact obtain some effective value coinciding with p_h only within an order of magnitude (the same refers to the "mobility" defined as $\mu = R/\rho$).

In the example under consideration, $\rho = 0.87\ \Omega$ cm (formula (4)) and the contribution from light holes does not exceed 3%, meaning $1/\rho \approx ep_h\mu_h$ with good precision. Thus, using the relations

$$p_h = \frac{1}{Re}, \tag{5}$$

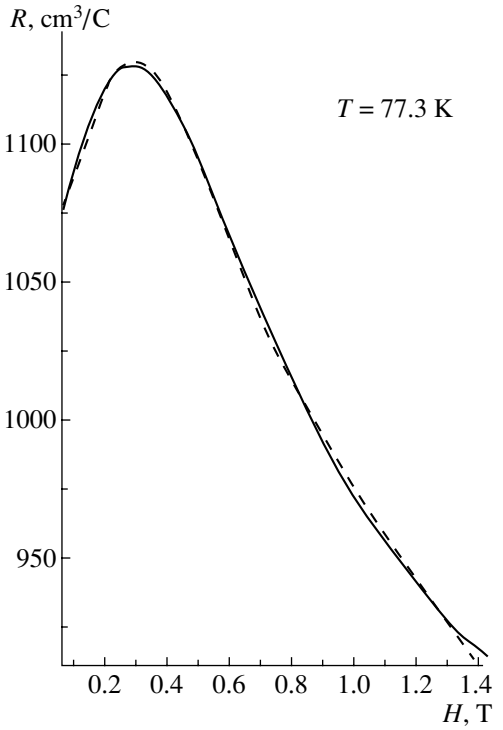

Experimental (solid line) and calculated (dashed line) dependences of the Hall coefficient on magnetic induction, $R(B)$, for a $Cd_{0.215}Hg_{0.785}Te$ sample at $T = 77$ K.

$$\mu_h = \frac{R}{\rho} \tag{6}$$

instead of formulas (3) and (4), we introduce an error that cannot be accurately estimated, since the μ_l and μ_h values are not found from the experiment.

If the theoretical dependence $R(B)$ is fitted to an experimental curve with the use of expression (3), four independent parameters can be determined: one of the concentrations, e.g., p_h (n and p_l are uniquely related to this concentration [3]) and three mobilities (μ_e, μ_l, and μ_h which are to be used as independent variables in fitting). Only two quantities are found experimentally: $R(B)$ and ρ (at $B = 0$). We have two equations (3) and (4) and four unknowns: p_h, μ_e, μ_l, and μ_h. Such a problem cannot be solved uniquely. The uncertainty in the choice of μ_e, μ_l, and μ_h reduces all advantages of fitting to zero, so that the accuracy cannot be improved.

3. EXPERIMENTAL RESULTS

$Cd_xHg_{1-x}Te$ epitaxial layers were obtained by liquid-phase epitaxy in a sealed quartz ampule from a tellurium-based growth solution. To lower the concentration of holes, the epitaxial heterostructures were annealed in saturated mercury vapor. The thicknesses of the epilayers (found by direct visual measurements on cross-sections under a microscope) varied within 20–40 μm; those of substrates, within 500–1000 μm.

Parameters of $Cd_{0.215}Hg_{0.785}Te$ epitaxial layer (d_{ep} = 20 μm) at T = 77 K

Parameter	Experimental data	Results of calculation
Resistivity ρ, Ω cm	2.05	1.72
Carrier concentrations, cm^{-3}:		
electrons, n	–	8.0×10^{10}
light holes, p_l	–	1.5×10^{13}
heavy holes, p_h	6.9×10^{15}	7.0×10^{15}
	($1/Re$; B = 1.4 T)	
Free carrier mobility, $cm^2/(V\,s)$:		
electrons, μ_e	–	3.1×10^4
light holes, μ_l	–	1.8×10^4
heavy holes, μ_h	440	480
	(R/ρ; B = 1.4 T)	
μ_l/μ_h	–	38

The samples were fabricated in the form of a circle 20 mm in diameter. Electrical measurements were done by the van der Pauw method at room temperature and at liquid-nitrogen temperatures at magnetic fields ranging from 0.1 to 1.4 T. Contacts were soldered with indium to a freshly etched surface of the epitaxial layer.

An $R(B)$ dependence at T = 77 K, typical of the samples studied, is shown in the figure together with an $R(B)$ curve calculated using the standard fitting method by the least squares procedure relying upon relations (3) and (4). It can be seen that the employed fitting procedure yields a satisfactory agreement between the theoretical and experimental dependences. The peak in the $R(B)$ curve is due to the influence of electrons; if the electronic terms in formula (3) are disregarded, this peak cannot be reproduced. It can also be seen from the figure that at strong fields (B > 1.0 T) the $R(B)$ curve has nonzero slope; if the curve were horizontal, this would mean that the condition $R = 1/p_h e$ is fulfilled exactly in this range of magnetic fields.

The concentrations and mobilities of free carriers, obtained by fitting for the same sample, are listed in the table. These data can only be used as reference; as already mentioned, the employed fitting procedure gives no way of clearly determining the parameters listed above. Nevertheless, as seen in the table, the experimental value $1/Re = 6.9 \times 10^{15}$ cm^{-3} obtained for the sample under study is close to the calculated concentration of heavy holes $p_h = 7.0 \times 10^{15}$ cm^{-3}, and the value R/ρ = 440 $cm^2/(V\,s)$ correlates well with the calculated mobility of heavy holes μ_h = 480 $cm^2/(V\,s)$. For other samples studied, the values of the mentioned parameters, obtained by fitting, differed from the corresponding experimental values by no more than 20%. In other words, the use of approximate formulas (5) and (6) for evaluating the concentration and mobility of heavy holes in the samples studied, instead of expressions (3) and (4), is well justified, introducing an error not exceeding 20%.

4. CONCLUSION

Thus, the investigation performed established the following:

(1) The contribution of the substrate to the electrical parameters of the $Cd_xHg_{1-x}Te$/CdZnTe heterostructure can be disregarded because of the presence of a potential barrier insulating the epitaxial layer from the substrate.

(2) In analyzing the results of galvanomagnetic measurements on *p*-type epitaxial layers, account should be taken of the presence of three kinds of free carriers: electrons and light and heavy holes.

(3) Use of the approximate relations (5) and (6) for calculating the concentration and mobility of heavy holes (with the contribution from electrons and light holes neglected) at B = 1.4 T and T = 77 K introduces an error not exceeding 20%.

ACKNOWLEDGMENTS

This study was supported by the Russian Foundation for Basic Research (project no. 00-02-17104).

REFERENCES

1. L. F. Lou and W. H. Frye, J. Appl. Phys. **56**, 2253 (1984).
2. A. I. Elizarov, V. V. Bogoboyashchiĭ, and A. G. Belov, Fiz. Tekh. Poluprovodn. (Leningrad) **24**, 923 (1990) [Sov. Phys. Semicond. **24**, 580 (1990)].
3. A. I. Belogorokhov, A. G. Belov, E. A. Vinogradov, and E. P. Rashevskaya, Preprint No. 156, FIAN SSSR (Lebedev Institute of Physics, USSR Academy of Sciences, Moscow, 1988).
4. P. S. Kireev, *The Physics of Semiconductors* (Vysshaya Shkola, Moscow, 1975).
5. G. A. Shneider, Phys. Status Solidi A **31**, K53 (1975).

Translated by M. Tagirdzhanov

Semiconductors, Vol. 35, No. 8, 2001, pp. 883–889. Translated from Fizika i Tekhnika Poluprovodnikov, Vol. 35, No. 8, 2001, pp. 920–926.

ELECTRONIC AND OPTICAL PROPERTIES OF SEMICONDUCTORS

Native and Impurity Defects in ZnSe:In Single Crystals Prepared by Free Growth

Yu. F. Vaksman*, Yu. A. Nitsuk*, Yu. N. Purtov*, and P. V. Shapkin**

** Mechnikov National University, Odessa, 65026 Ukraine*

*** Lebedev Physical Institute, Russian Academy of Sciences, Leninskiĭ pr. 53, Moscow, 117924 Russia*

Submitted December 26, 2000; accepted for publication January 22, 2001

Abstract—The optical absorption and photoluminescence spectra and the Hall effect were studied in ZnSe:In single crystals. The presence of electrically active In_{Zn}^{+} donor centers responsible for the impurity absorption and electrical conduction of crystals is established. It is shown that the conduction compensation in the ZnSe:In crystals is effected by cationic vacancies. The In_{Zn}^{+} donors and cationic vacancies form associative defects responsible for long-wavelength ZnSe:In luminescence. A high crystal conductivity (~5 Ω^{-1} cm^{-1}) is achieved as a result of ZnSe:In annealing in the zinc melt, which results in the extraction of cationic vacancies. The electron mobility in high-conductivity crystals is limited by scattering at the LO phonons and macrodefects formed due to the reduction of In solubility in crystals by their annealing in zinc. © *2001 MAIK "Nauka/Interperiodica".*

1. INTRODUCTION

Zinc selenide single crystals are promising materials for the fabrication of light-emitting diodes and lasers operating in the blue spectral region [1]. Thus, the problem of producing perfect single crystals with a low density of dislocations is topical. In addition, high-conductivity crystals are important in the fabrication of injection light-emitting diodes and lasers.

Recently, a method for growing II–VI bulk single crystals from the vapor phase has been developed, in which crystal contact with the walls of the growth chamber is eliminated [2–4]. In particular, ZnSe single crystals with a diameter of up to 50 mm both undoped and doped during growth were obtained [5, 6]. The dislocation density in these crystals is lower than 10^4 cm^{-2}. The possibility of lowering the resistivity of ZnSe:In crystals by annealing in the zinc melt was shown.

Here, for the first time the results of a complex study of optical absorption spectra, photoluminescence, and the Hall effect in ZnSe:In crystals obtained by free growth are reported. The aim of this study was to clarify the composition of native and impurity defects formed in ZnSe:In crystals during growth and subsequent annealing in the zinc melt.

2. EXPERIMENTAL

Zinc selenide single crystals were obtained by free growth at a seed in the cell placed in a furnace with a vertical gradient. Vapor-phase doping of crystals was performed during growth. In_2Se_3 was used as a doping material. The source temperature was 1450–1520 K. The growth temperature was 15–30 K lower than the source temperature. Adjustment of the temperature profiles and the design of the growth eliminated the possibility of crystal contact with the chamber walls. After growth, the crystals were cooled at a rate no higher than 30 K/h. The optimum growth rate, which ensures the structural perfection of the crystals, did not exceed 30–50 μm/h. A more detailed description of the growth method of the ZnSe crystals is given elsewhere [5, 6]. The In concentration in the samples was determined by the atomic-emission method and varied from 10^{16} up to 10^{18} cm^{-3}.

The annealing of ZnSe:In crystals in the zinc melt was carried out in preliminarily evacuated silica cells at a temperature of 1170–1220 K for 50–100 h. To eliminate the In extraction from the crystals, a certain amount of In was added to the Zn melt.

The optical absorption spectra and luminescence were measured using the KSVU-24 and KSVU-6 spectral setups. The absorption spectra were analyzed in the coordinates D^2–E, where $D = \ln(I_i/I_p)$ is the optical density, I_i and I_p are the intensities of radiation transmitted and incident at the crystal, and E is the photon energy. The long-wavelength luminescence spectra are presented with allowance made for the spectral sensitivity of the measuring setup. The excitation of the edge luminescence was performed by the radiation of an ILGI-503 pulsed nitrogen laser, and the long-wavelength luminescence was excited by an LGN-403K helium–cadmium laser.

The samples for Hall effect measurements were cut in the shape of parallelepipeds and were $10 \times 1.5 \times 1$ mm in size. The In electric contacts were formed by thermally treating the crystals in a vacuum chamber at a

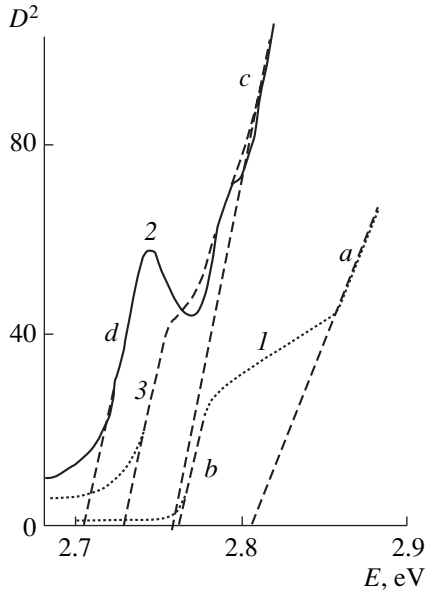

Fig. 1. Optical absorption spectra of (*1*) ZnSe, (*2*) ZnSe:In, and (*3*) ZnSe:(In + Zn) single crystals.

temperature of 600–650 K. The nonrectifying behavior of contacts was checked by measuring the current–voltage (*I–V*) characteristic. The magnetic field induction was 0.8 T, which satisfied the condition for a weak field. The resistivity of crystals (ρ) was determined from the *I–V* characteristic taking into account the sample configuration.

3. OPTICAL PROPERTIES OF CRYSTALS

The spectra of the optical absorption of ZnSe, ZnSe:In, and ZnSe:(In + Zn) crystals were studied.

The absorption spectrum of undoped crystals contains two linear sections (*a* and *b*) at 77 K (Fig. 1, curve *1*). By a linear extrapolation of these regions to the intersection with the abscissa (dashed line), the energies of optical transitions E_a = 2.802 eV and E_b = 2.763 eV were determined. According to the previous data [7, 8], these energies for the optical transitions are characteristic of processes occurring with participation of free excitons. The region *a* is associated with the absorption of light by free excitons, and the region *b*, with absorption by excitons involved in an inelastic exciton–exciton interaction.

The absorption spectrum of ZnSe:In crystals at 77 K (Fig. 1, curve *2*) points to the appearance of several absorption mechanisms. For the In concentration [In] = 3×10^{17} cm^{-3}, two linear regions (*c* and *d*) are distinguishable in this spectra and are characterized by the energies of optical transitions E_c = 2.758 eV and E_d = 2.706 eV, respectively. The presence of an In impurity suggests the possibility of absorption by excitons localized at the defects. At the same time, the value of E_c is indicative of the fact that an exciton can be localized at centers with a relatively large activation energy (~200 meV). Therefore, the most probable exciton localization centers are the neutral vacancies of Zn—$V_{Zn}^{\times}$. According to [9], the activation energy of $V_{Zn}^{\times}$ is 190 meV, and the binding energy of excitons at such centers is E_{ex} = 19 meV. Doping crystals with In should supposedly decrease the semiconductor band gap E_g, the magnitude of which can be estimated from the relation [10]

$$\Delta E_g = -2 \times 10^5 \left(\frac{3}{\pi}\right)^{1/3} \frac{e N_D^{1/3}}{4\pi\varepsilon}, \qquad (1)$$

where e is the elementary charge, N_D is the impurity concentration in cm^{-3}, $\varepsilon = \varepsilon_0 \varepsilon_s$, ε_s = 8.66 is the dielectric constant of ZnSe, and ε_0 is the dielectric constant of free space. For the In impurity concentration N_D = [In] = 3×10^{17} cm^{-3}, we have $\Delta E_g \approx 22$ meV. Thus, the difference $E_a - E_c$ = 44 meV may be represented as $E_a - E_c \approx E_{ex} + \Delta E_g$. Consequently, the *c*-region of the absorption spectrum of a ZnSe:In crystal is accounted for by the absorption of light by excitons localized at the neutral Zn vacancies. Cationic vacancies are formed in ZnSe:In crystals due to the self-compensation effect. The presence of the Zn vacancies is also confirmed by the high compensation degree of the ZnSe:In crystal conductivity.

The crystals doped by In feature a band of impurity absorption (Fig. 1, curve *2*), which is located in the region of low energies. This is confirmed by the dependence of the spectral position of this band on the In concentration in crystals. In particular, with the increase in the In concentration from 3×10^{17} up to 3×10^{18} cm^{-3}, the intersection point of the linear segment of this band with the abscissa shifts from 2.705 up to 2.670 eV. This shift in its magnitude corresponds to the change of the band gap ΔE_g determined according to (1). The spectral position of the impurity band peak E_m = 2.743 eV (for [In] = 3×10^{17} cm^{-3}) allows us to determine the optical activation energy for the absorption center $E_D^0 = E_g - \Delta E_g - E_m$ = 25 meV (the band gap E_g = 2.812 eV [9]). This value corresponds to the optical activation energy of the hydrogen-like In center In_{Zn}^{+} [9].

The absorption spectrum of the ZnSe:In crystals annealed in the Zn melt (ZnSe:(In + Zn)) is indicative of a decrease in the optically active In impurity concentration (Fig. 1, curve *3*). This can be deduced from the shift of the linear *d*-region to higher energies by the value of ΔE_g. By knowing the magnitude of this shift, we find that the In donor concentration in ZnSe:(In + Zn) crystals is reduced by 2–3 times. It is characteristic that the *c*-region of the absorption spectrum of ZnSe:(In + Zn) cannot be linearized. This is indicative of the absence of a noticeable absorption by excitons localized at the neutral vacancies. Actually, in the course of the annealing of the ZnSe:In crystals in the Zn melt, the

vacancies are filled with cations. This is confirmed by the Hall effect measurements in the ZnSe:In and ZnSe:(In + Zn) crystals.

4. LUMINESCENCE OF THE CRYSTALS

Studies of the edge luminescence spectra were carried out at a temperature of 77 K.

Two emission lines were found in the excitonic side of the spectrum at 2.808 and 2.797 eV. These lines are specific for undoped and lightly doped crystals ([In] < 10^{16} cm^{-3}). According to [7, 11], they are caused by free electron radiative transitions from states with $n = 2$ and 1, respectively. These processes take place under high levels of excitation. The appearance of excitonic absorption lines and luminescence are indicative of the low concentration of native defects in undoped ZnSe crystals.

In the luminescence excitonic spectra of more heavily doped crystals, a line of bound excitons is found. In particular, for [In] > 4×10^{16} cm^{-3}, it is located at 2.771 eV. This line has been observed previously [11] under similar excitation conditions and is related to excitons localized at neutral Zn vacancies. The difference in the spectral positions of the absorption line (2.758 eV for [In] = 3×10^{17} cm^{-3}) and emission line (2.771 eV for [In] = 4×10^{16} cm^{-3}) of excitons localized at the Zn neutral vacancies is caused by the dependence of E_g on the In concentration in crystals.

In all the crystals under study doped with In, the lines of donor–acceptor pair edge emission were observed. In crystals with [In] = 3×10^{17} cm^{-3}, these lines are located at 2.689, 2.657, and 2.623 eV. The line with a peak at 2.689 eV is caused by radiative transitions occurring within the donor–acceptor pairs [5]. Obviously, the donor–acceptor pairs contain In^{+}_{Zn} donor centers. The ions of residual Li or Na ions can act as acceptors. The emission lines at 2.657 and 2.623 eV are the LO replicas of the 2.689 eV line.

The long-wavelength luminescence spectra $I(\lambda)$ feature broad bands located in the wavelength range λ = 480–700 nm. In the luminescence spectra of ZnSe with a low In concentration ([In] = 4×10^{16} cm^{-3}), a broad band peaked at the wavelength λ = 490 nm (Fig. 2) is observed. A series of emission lines related to the donor–acceptor pairs and peaked at 2.689, 2.657, and 2.623 eV (461, 466, and 472 nm) is observed against the background of this band. Previously, it was established [12] that a broad emission line of undoped crystals at the wavelength of 490 nm is related to isolated oxygen centers (O_{Se}). The energy of the thermal activation of emission centers is equal to 0.13 eV. This is consistent with data in [10]. Thus, the presence of the long-wavelength band at 490 nm is indicative of oxygen residual impurities in the crystals. In crystals with [In] > 10^{17} cm^{-3}, luminescence was not observed.

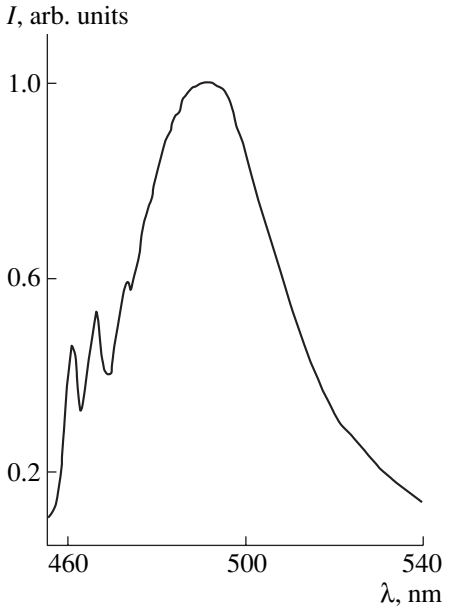

Fig. 2. Photoluminescence spectra of ZnSe:In single crystal with [In] = 4×10^{16} cm^{-3}.

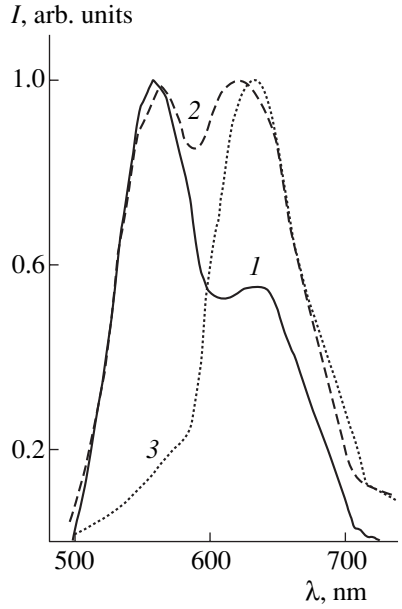

Fig. 3. Photoluminescence spectra of ZnSe:In single crystal with [In] > 10^{17} cm^{-3} under the relative intensity of the exciting light of (*1*) 100, (*2*) 50, and (*3*) 20%.

The long-wavelength luminescence spectra of crystals with a moderate In concentration ([In] ≈ 10^{17} cm^{-3}) feature two bands with peaks at 560 and 625 nm. In this case, in the crystals with [In] = 3×10^{17} cm^{-3}, a yellow-green emission is dominant. With the In concentration increasing up to 3×10^{18} cm^{-3}, a fraction of the red-orange emission increases in the luminescence spectrum.

The long-wavelength luminescence spectrum of ZnSe:In depends on the crystal temperature and on the intensity of the exciting light. The increase of the crystal temperature from 77 up to 300 K results in the increase in the red-orange emission fraction. Such a temperature dependence of the emission spectral features is indicative of the mechanism of the current energy transport between the emission centers, which is characteristic of the recombination luminescence.

Upon decreasing the excitation light intensity from 100 to 20%, the band peaked at 625 nm becomes dominant in the luminescence spectrum $I(\lambda)$ (Fig. 3). The shape of the luminescence spectra of ZnSe:In shown in Fig. 3 testify that they have a complex origin similar to that considered in [13] for the emission spectra of ZnSe:Al.

In order to determine the level energy position of the centers responsible for yellow-green and red-orange emission, the temperature dependences of the emission intensity $I(T)$ in the regions of λ = 560 and 625 nm were studied. The energy activation of thermal quenching was determined from the slope of the linear segment of the plot $I(T)$ represented in coordinates $\ln(I)$–$1/T$. The thermal quenching of luminescence in the region of λ = 560 nm is represented by a curve with two linear segments. In the range of low temperatures, a weak thermal quenching with activation energies ~0.018 eV was observed. The activation energy determined in the high-temperature range is ~0.17 eV. The process of thermal quenching of the red luminescence is also characterized by two activation energies (0.018 and 0.55 eV). The temperature dependences of the luminescence intensity with two linear regions of quenching are explained in the context of the radiative recombination model; this recombination occurs at the donor–acceptor pairs. In this case, the energy of the quantum emitted is determined by equation

$$h\nu = E_g - E_D - E_A + \frac{e^2}{\varepsilon R}, \qquad (2)$$

where E_D and E_A are the activation energies of the donor and acceptor and R is the distance between the donor and acceptor. The activation energy determined in the low-temperature region is equal to the activation energy of the In hydrogen-like donors. The activation energy determined in the high-temperature region according to Eq. (2) is equal to the difference $E_A - e^2/(\varepsilon R)$.

The yellow–green emission of ZnSe:In has been recently attributed [14] to the neutral associative centers $(V_{Zn}In_{Zn})^{\times}$ incorporating the single-charged Zn vacancies. The orange–red emission has been previously related to the associative centers $(V_{Zn}In_{Zn})^{-}$, which incorporate the Zn vacancies in the charge state –2 [13]. Thus, studies of the long-wavelength luminescence suggest that the charged Zn vacancies are present in the crystals in the composition of associative centers $(V_{Zn}In_{Zn})^{\times}$ and $(V_{Zn}In_{Zn})^{-}$.

We should note that a red-emission band is dominant in the luminescence spectra of the high-conductivity ZnSe:In crystals annealed in the Zn melt. This is explained by the fact that less energy is required to fill the single-charged cationic vacancy with the Zn atom in comparison with the corresponding value for a double-charged vacancy.

5. HALL EFFECT STUDIES

The Hall effect was studied for ZnSe:In and ZnSe:(In + Zn) crystals.

The electrical characteristics of the crystals under study are given in the table. As can be seen, the In concentration increases from 2.8×10^{17} up to 2.8×10^{18} cm^{-3} in the ZnSe:In crystals results in a slight increase in its resistivity. This is caused by the decrease in the electron concentration (n) and mobility (μ). The results obtained indicate that, in the course of ZnSe:In crystal growth, a formation of both the In_{Zn}^{+} donor center and Zn vacancies (acceptor centers) occurs; the latter compensate the conductivity. This is confirmed by the high degree of compensation of ZnSe:In crystals ($K \approx 1 - n/[\mathrm{In}] \approx 0.99$).

In ZnSe:In crystals annealed in Zn, the In concentration remains constant. The resistivity of such crystals is as low as 0.2–10 Ω cm (see table). This is caused mainly by an increase in the free electron concentration. The increase of electron concentration in ZnSe:(In + Zn) crystals is a result of cationic vacancy extraction from the crystals in the course of their annealing in the Zn melt. The efficiency of this extraction is caused by the high value of the Zn vacancy diffusivity in ZnSe (its magnitude is estimated at ~10^{-6} cm^2/s at 1120 K [9]). In addition, the extraction of the Zn vacancy lowers the degree of compensation in

Electrical characteristics of the crystals studied

Parameter	Crystals ZnSe:In			Crystals ZnSe:(In + Zn)		
[In], cm^{-3}	4.2×10^{16}	2.8×10^{17}	2.8×10^{18}	4.2×10^{16}	2.8×10^{17}	2.8×10^{18}
ρ, Ω cm	6.0×10^{8}	9.2×10^{3}	1.3×10^{4}	10.0	0.28	0.20
n, cm^{-3}	–	4.9×10^{12}	4.5×10^{12}	1.2×10^{15}	8.1×10^{16}	8.4×10^{16}
μ, cm^2 V^{-1} s^{-1}	–	140	110	500	280	380

ZnSe:(In + Zn) crystals. In particular, $K \approx 0.70$ in the crystals containing 10^{17} cm^{-3} of In.

The temperature dependence of the Hall voltage was studied for low-conductivity ZnSe:(In + Zn) crystals ($\rho = 0.28\ \Omega$ cm). The values of the Hall voltage were used to calculate the temperature dependences of electron concentration and Hall mobility. For the ZnSe:(In + Zn) crystals with a partially compensated electron conductivity, the condition of electroneutrality has the form

$$n + n_D = N_D - N_A, \tag{3}$$

where n and n_D are the electron concentration in the conduction band and at the donors, respectively; and N_D and N_A are the donor and acceptor concentrations, respectively. When deriving Eq. (3), we take into account that, in the temperature range under consideration, the Fermi level is above the acceptor levels; i.e., all the acceptor states are occupied by electrons. According to [15], the solution of the electroneutrality equation for the nondegenerate semiconductor can be written as

$$\frac{n(n + N_A)}{N_D - N_A - n} = \frac{1}{g} N_c \exp\left(-\frac{E_D}{kT}\right), \tag{4}$$

where g is the degeneracy factor equal to 2, and N_c is the effective density of states in the conduction band. In Eq. (4), the quantities N_A, N_D, and E_D are unknown. System of equations (4) was solved for three values of variables T and n, which were selected from the temperature dependence $n(T)$. The equation system was solved in the Mathcad environment using the standard function Find. The calculation yields the following values for the quantities sought: $N_D = 2.8 \times 10^{17}$ cm^{-3}, $N_A = 1.5 \times 10^{17}$ cm^{-3}, and $E_D = 8$ meV for crystals containing 3×10^{17} cm^{-3} of In. The decrease in the donor activation energy E_D to 8 meV is caused by the narrowing of the semiconductor band gap and is quantitatively confirmed by Eq. (1). The compensation degree ($K = N_A/N_D$) of these crystals turns out to be substantially lower ($K = 0.54$), than prior to the annealing in Zn. Taking into account the calculated values of N_A, N_D, and E_D, we calculated the temperature dependence $n(T)$; i.e.,

$$n(T) = \frac{2(N_D - N_A)}{A},$$
$$A = 1 + \left[\left(1 + \frac{2N_A f(T)}{N_c}\right) + \frac{8(N_D - N_A) f(T)}{N_c}\right]^{1/2} + \frac{2N_A f(T)}{N_c}, \tag{5}$$

where $f(T) = \exp(-E_D/kT)$. As can be seen from Fig. 4, the calculated dependence $n(T)$ adequately describes the experimental one.

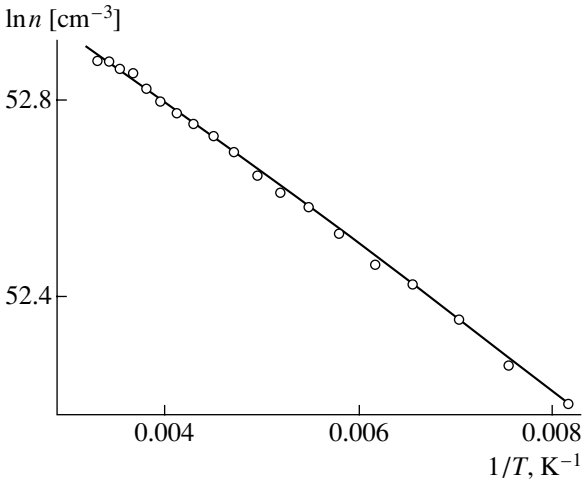

Fig. 4. Temperature dependence of the electron concentration calculated from Eq. (5) (solid line); experimental data are represented by circles.

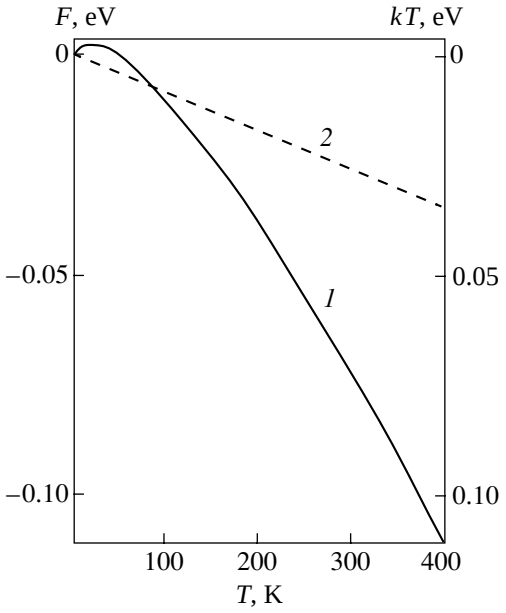

Fig. 5. Temperature dependences of the Fermi level position (*1*) in ZnSe:(In + Zn) and (*2*) of the magnitude of kT.

In view of the relation $n/N_c = \exp[(F - E_c)/kT]$, where F is a Fermi level energy with respect to the conduction band bottom ($E_c = 0$), we obtain

$$F(T) = kT \ln\left\{\frac{2(N_D - N_A)/N_c}{B}\right\},$$
$$B = 1 + \left[\left(1 + \frac{2N_A}{N_c f(T)}\right)^2 + \frac{8(N_D - N_A)}{N_c f(T)}\right]^{1/2} + \frac{2N_A}{N_c f(T)}. \tag{6}$$

The temperature dependence of the Fermi level calculated according to formula (6) for crystals with [In] =

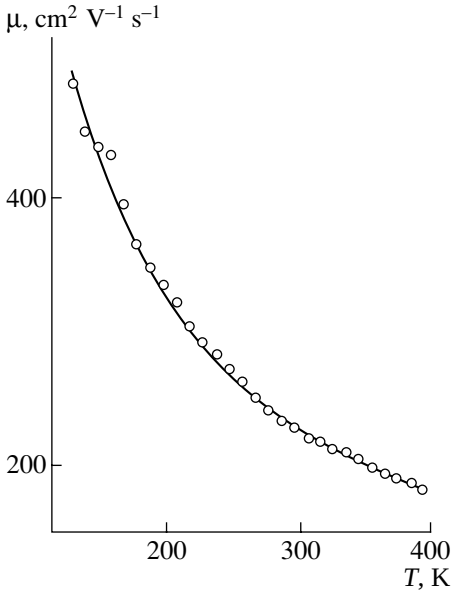

Fig. 6. Temperature dependence of the electron mobility in ZnSe:(In + Zn) calculated from Eqs. (7), (9), and (10) (solid line) and experimental data of μ_H (circles).

3×10^{17} cm^{-3} is shown in Fig. 5. The Fermi level intersects the donor levels at 90 K. At temperatures lower than 70 K, we have $|F - E_c| < kT$ (Fig. 5, the intersection point of curves *1* and *2*), which indicates that the semiconductor is degenerate. The close proximity of the Fermi level (6 meV) and the donor level (8 meV) at 77 K confirms the possibility of optical transitions of electrons from the valence band to the levels of the ionized donors In^+_{Zn}.

6. ELECTRON MOBILITY IN THE LOW-RESISTIVITY CRYSTALS

In order to clarify the scattering mechanisms, which control the electron mobility in the ZnSe:(In + Zn) crystals, we used the data on the Hall voltage in the temperature range of 120–400 K. The temperature dependence of the Hall mobility $\mu_H(T)$ in the temperature range under study has no extremum (Fig. 6). To analyze $\mu_H(T)$, the mechanisms of scattering by optical phonons and by ionized and neutral impurities were considered. However, the calculated value of the electron mobility turned out to be several times higher than the values of μ_H. We also took into account the fact that after annealing in the Zn melt the crystals with [In] > 10^{17} cm^{-3} acquired a gray color. By examining these crystals in an electron microscope, a formation of macrodefects with a size of ~1–10 μm was established. Obviously, in the course of the crystal annealing in the Zn melt at 1170 K, a decrease of the In solubility occurred in the crystals. As a result, some point In defects form macrodefects (clusters). A decrease in the concentration of In optically active In^+_{Zn} centers was noted above during the consideration of absorption spectra of ZnSe:(In + Zn) crystals (Fig. 1).

It should be taken into account that the relative accuracy in the determination of μ_H is ~30%. In view of this circumstance, we may suggest that there is a tendency for μ_H to decrease in ZnSe:(In + Zn) crystals with an increase in the In concentration (see table). This result may also be attributed to the formation of In macrodefects.

Calculations show that the experimental dependence $\mu_H(T)$ is satisfactorily accounted for by the mechanisms of electron scattering at longitudinal optical phonons (LO phonons) and at macrodefects formed by the In impurity. In this case, the mobility was calculated according to the additive law

$$\mu^{-1} = \mu_{LO}^{-1} + \mu_s^{-1}, \quad (7)$$

where μ_{LO} and μ_s are the electron mobilities limited by scattering at LO phonons and macrodefects, respectively. The absence of a noticeable effect of scattering at the impurity ions on the electron mobility in the temperature range under study allows us to take the Hall factor equal to unity and, consequently, to compare the Hall (μ_H) and drift (μ) mobilities of electrons.

The electron mobility limited by the scattering at optical phonons is described [9] by the relation

$$\mu_{LO} = \frac{4e}{3\sqrt{\pi}\alpha\omega_0 m_n^* \sqrt{\chi_0}}\left(\frac{m_n^*}{m_p}\right)^{3/2} G(\chi_0)(e^{\chi_0} - 1), \quad (8)$$

where α is the electron–phonon coupling constant; ω_0 is the frequency of the LO phonon; m_n^* is the electron effective mass; m_p is the polaron mass; $\chi_0 = \hbar\omega_0/kT$; and $(m_n^*/m_p)^{3/2}G(\chi_0)$ is the function calculated in [9] for ZnSe, which varies from 1.1 up to 1.3 in the temperature range under study. Taking into account the numerical values of these quantities for ZnSe crystals, we rewrite relation (8) as

$$\mu_{LO} = 12.9\sqrt{T}[\exp(364/T) - 1]. \quad (9)$$

The mobility μ_{LO} in formula (9) is expressed in cm^2 V^{-1} s^{-1}.

The charge-carrier mobility limited by the scattering at In macrodefects was calculated from the relation [14]

$$\mu_s = e[NS(2\pi m_n^* kT)^{3/2}]^{-1}, \quad (10)$$

where *N* and *S* are the concentration and the effective scattering cross section by macrodefects. The magnitude of the product *NS*, at which the function $\mu(T)$ was calculated using formulas (7), (9), and (10) and the dependence $\mu_H(T)$ obtained experimentally coincide (Fig. 6), was 1.1×10^8 cm^{-1}.

The analysis of the effect of various electron scattering mechanisms indicates the following: the temperature dependence $\mu_H(T)$ is governed by the interaction of electrons and LO phonons. At the same time, the consideration of electron scattering at the In macrodefects allows us to explain the relatively low value of electron mobility in the crystals under study. It is worthwhile to note for comparison that the electron mobility in ZnSe:In and ZnSe:(In + Zn) crystals at 300 K is 500 and 210 $cm^{-2} V^{-1} s^{-1}$, respectively.

7. CONCLUSIONS

The studies of optical, luminescent, and electrical properties of ZnSe:In crystals obtained by free growth allow us to make the following conclusions:

(i) The presence of the absorption and luminescence excitonic lines in the spectra of pure and lightly doped ([In] < 10^{16} cm^{-3}) crystals is indicative of their structural perfection and their low content of native and impurity defects. Edge emission caused by recombination at the donor–acceptor pairs as well as long-wavelength luminescence in the region of λ = 490 nm are indicative of the presence of residual Li (Na) and O impurities in crystals.

(ii) The doping of crystals with In results in the formation of donor centers In_{Zn}^{+}. These centers manifest themselves in the impurity absorption of ZnSe:In (*d*-region), act as electrically active donors, and are incorporated in associative defects responsible for the long-wavelength photoluminescence.

(iii) During the growth of ZnSe:In crystals, native defects (cationic vacancies) are formed. The existence of Zn neutral vacancies is deduced from the exciton luminescence spectrum (emission line at 2.771 eV). The Zn charged vacancies are incorporated into the associative centers $(V_{Zn}In_{Zn})^{\times}$ and $(V_{Zn}In_{Zn})^{-}$ responsible for the conductivity compensation and the long-wavelength photoluminescence.

(iv) The presence of In impurity with a concentration above 10^{17} cm^{-3} results in a noticeable narrowing of the semiconductor band gap and in the corresponding decrease in the donor activation energy. For an In concentration of 2.8×10^{17} cm^{-3}, the value of ΔE_g is 22 meV, and the activation energy of In donor centers decreases from 22 up to 8 meV.

(v) The annealing of ZnSe:In crystals in the Zn melt results in a decrease in the cationic vacancy concentration, which causes conductivity decompensation of the ZnSe:(In + Zn) crystals and an increase in their electrical conductivity. At temperatures lower than 70 K, ZnSe:(In + Zn) crystals with an In concentration above 10^{17} cm^{-3} become degenerate.

(vi) The electron mobility in the high-conductivity ZnSe:In:Zn crystals is limited by the electron scattering at LO phonons and at In macrodefects. Macrodefects are formed as a result of the In solubility decrease in ZnSe:In crystals in the course of their annealing in the Zn melt.

REFERENCES

1. A. N. Georgobiani and M. B. Kotlyarevskiĭ, Izv. Akad. Nauk SSSR, Ser. Fiz. **49**, 1916 (1985).
2. E. V. Markov and A. A. Davydov, Izv. Akad. Nauk SSSR, Neorg. Mater. **7** (4), 575 (1971).
3. E. V. Markov and A. A. Davydov, Izv. Akad. Nauk SSSR, Neorg. Mater. **2** (10), 1755 (1975).
4. Yu. V. Korostelin, V. I. Kozlovsky, A. S. Nasibov, and P. V. Shapkin, J. Cryst. Growth **159**, 181 (1996).
5. Yu. V. Korostelin, V. I. Kozlovsky, A. S. Nasibov, and P. V. Shapkin, J. Cryst. Growth **161**, 51 (1996).
6. Yu. V. Korostelin, V. I. Kozlovsky, A. S. Nasibov, and P. V. Shapkin, J. Cryst. Growth **197**, 449 (1999).
7. J. C. Bouley, P. Blanconnier, and A. Herman, J. Appl. Phys. **46** (8), 3549 (1975).
8. R. Baltramiejunas, J. Vaitkus, and V. Niunka, Litov. Fiz. Sb. **21** (8), 809 (1979).
9. D. D. Nedeoglo and A. V. Simashkevich, *Electrical and Luminescent Properties of Zinc Selenide* (Shtiintsa, Kishinev, 1980).
10. Yu. I. Ukhanov, *Optical Properties of Semiconductors* (Nauka, Moscow, 1977).
11. G. N. Ivanova, D. D. Nedeoglo, A. V. Simashkevich, and K. D. Sushkevich, Fiz. Tekh. Poluprovodn. (Leningrad) **14** (1), 31 (1980) [Sov. Phys. Semicond. **14**, 17 (1980)].
12. Yu. F. Vaksman, Fiz. Tekh. Poluprovodn. (St. Petersburg) **29** (2), 346 (1995) [Semiconductors **29**, 175 (1995)].
13. V. V. Serdyuk, N. N. Korneva, and Yu. F. Vaksman, Phys. Status Solidi A **91**, 173 (1985).
14. Yu. F. Vaksman and A. N. Krasnov, *Photoelectronics* (Odessk. Univ., Odessa, 1997), No. 6, p. 8.
15. V. L. Bonch-Bruevich and S. G. Kalashnikov, *The Physics of Semiconductors* (Nauka, Moscow, 1977).

Translated by T. Galkina

Semiconductors, Vol. 35, No. 8, 2001, pp. 890–894. Translated from Fizika i Tekhnika Poluprovodnikov, Vol. 35, No. 8, 2001, pp. 927–931.

ELECTRONIC AND OPTICAL PROPERTIES OF SEMICONDUCTORS

Origin of an Absorption Band Peaked at 5560 cm^{-1} and Related to Divacancies in $Si_{1-x}Ge_x$

Yu. V. Pomozov[1], M. G. Sosnin[1], L. I. Khirunenko[1,*], N. V. Abrosimov[2,3], and W. Schröder[3]

[1] *Institute of Physics, National Academy of Sciences of Ukraine, Kiev, 03028 Ukraine*

* *e-mail: lukh@iop.kiev.ua*

[2] *Institute of Solid-State Physics, Russian Academy of Sciences, Chernogolovka, Moscow oblast, 142432 Russia*

[3] *Institute of Crystal Growth, D-12489 Berlin, Germany*

Submitted January 17, 2001; accepted for publication January 24, 2001

Abstract—It is found that two types of centers are formed in $Si_{1-x}Ge_x$ single crystals as a result of irradiation with fast electrons: divacancies (V_2) characteristic of silicon and the V_2^* centers; the latter are complexes of divacancies V_2 with germanium atoms (V_2Ge). It is shown that an absorption band peaked at about 5560 cm^{-1} is a superposition of two absorption bands that correspond to the above centers. The V_2 divacancies diffuse during isochronous heat treatment and interact with germanium atoms, thus giving rise to additional V_2^* centers. The latter have a higher thermal stability than the V_2 centers do, and their annealing temperature increases with increasing content of germanium. © *2001 MAIK "Nauka/Interperiodica".*

One of the most important radiation defects in silicon grown both by the floating-zone method and by the Czochralski method is the divacancy V_2. The latter may be formed either as a primary defect during irradiation or as a secondary defect, as a result of the interaction of vacancies during their thermally activated migration. The properties of divacancies in silicon are adequately understood. It has been established using electron spin resonance, infrared (IR) absorption, photoconductivity, and deep-level transient spectroscopy (DLTS) that a divacancy may have four charge states in silicon: $V_2^=$, V_2^-, V_2^0, and V_2^+ [1–7]. Three IR absorption bands peaked at about 2500, 2760, and 5560 cm^{-1} are related to divacancies and correspond to the charge states of V_2^-, V_2^+, and V_2^0, respectively. The intensity of the band at about 5560 cm^{-1} is typically used to estimate the concentration of divacancies introduced by irradiation [8]. As for the $Si_{1-x}Ge_x$ solid solutions, there are only a few publications concerned with the properties of divacancies in these solid solutions. Thus, IR spectroscopy has been used to study the V_2^0 divacancies on the basis of the absorption band peaked at about 5560 cm^{-1} in polycrystalline $Si_{1-x}Ge_x$ ($0 \le x \le 1$) samples irradiated with neutrons or protons [9]. It was found that, as the germanium content increases, the above absorption band shifts to lower frequencies; this shift is believed [9] to correlate with changes in the lattice constant as the solid-solution composition varies. An enhancement of the thermal stability of divacancies in the crystals enriched with silicon and a reduction of thermal stability in the crystals enriched with germanium were also observed [9]. Recently, thin $Si_{1-x}Ge_x$ layers have been studied [10, 11]. It was found that the thermal stability of divacancies is not affected by changes in the $Si_{1-x}Ge_x$ composition; however, a decrease in the enthalpy of activation for the V_2^+ divacancy level in reference to the valence-band top with increasing germanium content was observed.

In single-crystal $Si_{1-x}Ge_x$ samples, the properties of divacancies have been mainly studied for a germanium content lower than 1 at. %. In this paper, we report new data on the origin of the divacancy-related absorption band in the vicinity of 5560 cm^{-1} in the single-crystal $Si_{1-x}Ge_x$ samples with a germanium content as high as 15 at. %.

The B-doped p-$Si_{1-x}Ge_x$ single crystals were grown by the Czochralski method at the Institute of Crystal Growth (Berlin) [12, 13]. The oxygen and carbon concentrations were determined from the intensities of the IR absorption bands at wavelengths of 9 and 16 μm and were found to be (7–9) × 10^{17} and (2–3) × 10^{16} cm^{-3}, respectively. The germanium content in the samples was determined using a JCXA-733 microprobe X-ray analyzer and varied from 0.8 to 15 at. %. In order to clarify the special features of the effect of germanium on the properties of divacancies, we studied the reference silicon crystals that did not contain germanium and whose parameters were close to those of the $Si_{1-x}Ge_x$ solid solutions.

The samples were irradiated with 4-MeV electrons at temperatures of $T_{irr} \approx 300$ and 90 K. The irradiated

samples were then heat-treated isochronously (for 20 min) in the temperature range of T_{ann} = 100–400°C. We studied the processes of the formation and annealing of V_2^0 divacancies (on the absorption band at 5560 cm^{-1}) and their dependence on the germanium content in $Si_{1-x}Ge_x$.

The absorption spectra obtained for the samples irradiated with a dose of 5×10^{17} cm^{-2} at a temperature of $T_{irr} \approx 300$ K are shown in Fig. 1. As can be seen, a gradual shift of the V_2^0-related absorption band to lower frequencies is observed with increasing germanium content in the samples. The dependence of the magnitude of the shift for this band (a variation in the energy position ΔE) on the germanium content in the samples is shown in Fig. 2. A similar dependence of variation in the band gap E_g (ΔE_g) [14] is also plotted for comparison. It can be seen that the curve describing the absorption-band shift does not coincide with that describing the variation in E_g in contrast to what has been reported recently [9]. For the germanium content $N_{Ge} \lesssim 1.7$ at. %, the magnitude of the shift of the V_2^0-related band is close to the variation in E_g; however, for a higher germanium content, the shift of the V_2^0-related band greatly exceeds the variation in E_g. Estimations of the divacancy concentrations from the intensity of the absorption band near 5560 cm^{-1} show that the divacancy-introduction efficiency is affected only slightly by germanium in the range of germanium concentrations under consideration, whereas a decrease in the *A*-center introduction efficiency has been observed previously in these crystals [15].

Interesting features in the behavior of the absorption band corresponding to V_2^0 were observed in the samples subjected to isochronous heat treatment. In Fig. 3, we show experimental data for the samples with a germanium content of 3.5 at. %. In the range of annealing temperatures of T_{ann} = 150–240°C, the high-frequency wing of the absorption band changes, the peak of the band shifts gradually to lower frequencies, and a certain increase in the band intensity is observed (Fig. 3, curve *3* for V_2^*). All these changes occur within the initial absorption band. Such changes are characteristic of the entire range of germanium concentrations in the samples we studied and occur at the same heat-treatment temperatures, irrespective of germanium content. In the reference silicon samples, high proportions of divacancies are annealed out (Fig. 4, curve *1*) in the heat-treatment temperature range of T_{ann} = 150–240°C, which is accompanied by the formation of additional vacancy–oxygen centers (the *A* centers). Heat treatment in this temperature range does not induce any changes in the absorption region corresponding to the *A* centers for all the $Si_{1-x}Ge_x$ samples we studied.

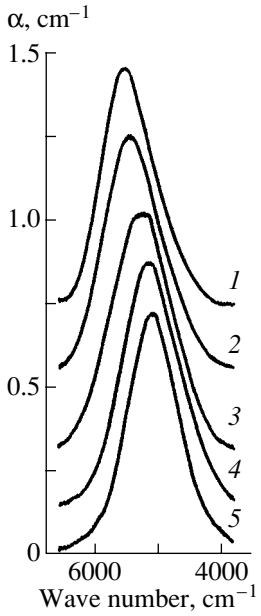

Fig. 1. Absorption spectra in the vicinity of 5560 cm^{-1} for $Si_{1-x}Ge_x$ samples irradiated with fast electrons with a dose 5×10^{17} cm^{-2}. Germanium content in the samples was N_{Ge} = (*1*) 0, (*2*) 3.5, (*3*) 8.5, (*4*) 11.5, and (*5*) 15 at. %.

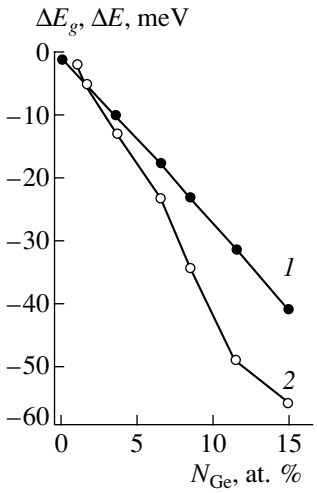

Fig. 2. Dependences of variation in (*1*) E_g [14] and (*2*) the shift of the V_2^0 absorption band in relation to the germanium content in $Si_{1-x}Ge_x$.

For higher heat-treatment temperatures, the intensity of the V_2^* band formed as a result of heat treatment at T_{ann} = 150–240°C remains at first unchanged and then decreases gradually as a whole, with the position of the band being preserved. The results of heat treatment, i.e., the behavior of the V_2^*-related band (the intensity at the peak), are illustrated in Fig. 4 for all the samples studied. As can be seen from Fig. 4, the tem-

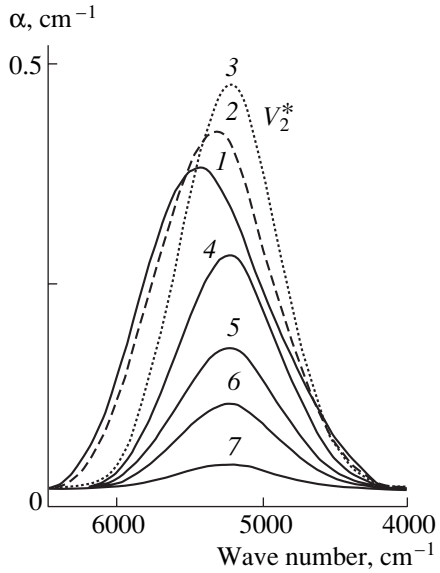

Fig. 3. The absorption band peaked at about 5560 cm^{-1} (*1*) before heat treatment and (*2–7*) the behavior of this band in the $Si_{0.965}Ge_{0.035}$ samples heat-treated at T_{ann} = (*2*) 180, (*3*) 240, (*4*) 310, (*5*) 320, (*6*) 330, and (*7*) 335°C.

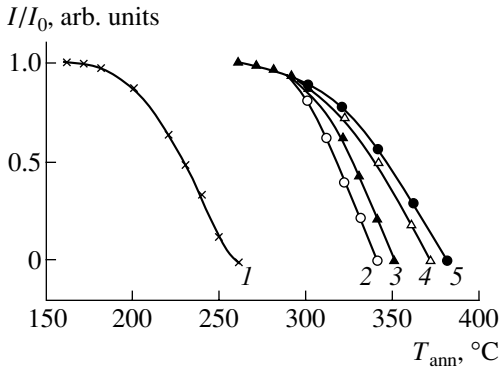

Fig. 4. Relative variation in the intensity (I/I_0) of the absorption bands (*1*) V_2^0 in Si and (*2–5*) V_2^* in $Si_{1-x}Ge_x$ subjected to heat treatment. The germanium content was N_{Ge} = (*2*) 3.5, (*3*) 6.5, (*4*) 8.5, and (*5*) 11.5 at. %.

perature at which the V_2^0-related band disappears is higher than that of the divacancies (the band at 5560 cm^{-1} in silicon) and increases with increasing germanium content in our samples. This is inconsistent with the results obtained by DLTS when studying the thin $Si_{1-x}Ge_x$ layers [10, 11]. It was shown that the thermal stability of divacancies is unaffected by variations in the samples' composition [10, 11].

It is known that divacancies in silicon are annealed out as a result of their diffusion over the lattice and eventual capture by a trap (a sink); furthermore, divacancies can diffuse across large distances over the silicon lattice without dissociation [1]. The activation energy for the diffusion of divacancies is ~1.25 eV, whereas that for divacancy dissociation is higher than 1.6 eV. Divacancies V_2 interact actively with *I* impurities to form $V_2 + I$ complexes (the complexes V_2O, V_2O_2, HV_2, SnV_2, Sn_2V_2, and so on are thus effectively formed) [16–20].

We observed the following specificities in the behavior of the absorption band at about 5560 cm^{-1} in the $Si_{1-x}Ge_x$ samples subjected to heat treatment in the temperature range of T_{ann} = 150–240°C: variation of the band's high-frequency wing, a shift of the peak, increased intensity, and the absence of the *A*-center "negative annealing" stage. These observations suggest that V_2 divacancies interact with impurities (traps) during thermally activated diffusion of V_2 in $Si_{1-x}Ge_x$ crystals at the above temperatures; as a result, V_2 divacancies are transformed into other V_2^* complexes. Taking into account that the concentration of germanium in the samples under consideration far exceeds that of all possible sinks in these samples and that it is the presence of Ge which mainly differentiates the $Si_{1-x}Ge_x$ samples from the reference Si samples, we may reasonably assume that diffusing divacancies interact with Ge atoms in the course of heat treatment and form V_2Ge centers; as a result, the V_2^* band emerges.

In order to verify the above assumption concerning the complicated origin of the absorption band peaked at about 5560 cm^{-1} in $Si_{1-x}Ge_x$, we studied the samples irradiated at $T_{irr} \lesssim 90$ K. As is well known, the Ge*V* centers are intensively formed at these irradiation temperatures; almost all the vacancies are trapped by germanium atoms, which affects the efficiency of the introduction of the secondary radiation defects [21, 22]. In Fig. 5, we show the absorption spectra measured at T = 4.2 K for a Si sample and a $Si_{1-x}Ge_x$ sample with a germanium content of 3.5 at. %; the samples were irradiated with electrons at $T_{irr} \lesssim 90$ K with a dose of 6×10^{17} cm^{-2}. As can be seen, the band at ~835 cm^{-1} corresponding to the *A* centers is not observed in the absorption spectrum of $Si_{0.965}Ge_{0.035}$ immediately after irradiation. However, any appreciable effect of germanium on the absorption band peaked at about 5560 cm^{-1} and related to divacancies is not observed; as a result, the divacancy concentration determined from the intensity of this band is not affected by germanium. This is unusual because the efficiency of formation of the secondary V_2 centers due to the vacancy–vacancy interaction is bound to be lower than that of the *A* centers in the material grown by the Czochralski method for the energies and doses of fast electrons used. On the other hand, the introduction efficiency for Ge*V* centers is known to be far in excess of those for the secondary *A* and V_2 centers [6, 21] (taking into account the high germanium concentration); consequently, the effect of germanium on divacancy formation should be observed.

In order to gain deeper insight into the effect of germanium content on divacancy formation in $Si_{1-x}Ge_x$, we also studied the V_2^+ divacancy charge state; the latter is represented by the absorption band in the vicinity of 2760 cm^{-1} and by its phonon replica observed on the high-frequency side of this band. As can be seen from Fig. 5, the absorption band at ~2760 cm^{-1} in $Si_{0.965}Ge_{0.035}$ is shifted by ~20 cm^{-1} to lower frequencies compared to that in Si (as opposed to the shift of ~100 cm^{-1} for the band peaked at about 5560 cm^{-1}), and the intensity of this band is lower than in Si. A comparison of the areas under the V_2^+ bands indicates that the concentration of divacancies is lower in $Si_{0.965}Ge_{0.035}$ than in Si, which, as was mentioned above, should be observed under the conditions of low-temperature irradiation. Isochronous heat treatment of the samples indicates that the centers represented by the V_2^+ absorption band in $Si_{0.965}Ge_{0.035}$ anneal out similarly to divacancies in Si and that this band disappears in the temperature range of T_{ann} = 180–260°C, which is consistent with the results reported elsewhere [10, 11]. All the aforementioned factors strengthen our assumption that the origin of the band peaked at about 5560 cm^{-1} is intricate.

As can be seen from Fig. 3 and as the results of decomposition of the absorption bands peaked in the vicinity of 5560 cm^{-1} into components demonstrate, the band observed in the spectrum of all the samples studied immediately after irradiation of $Si_{1-x}Ge_x$ is a superposition of two bands; one of these corresponds to the V_2 divacancies, whereas the other corresponds to the V_2^0 centers detected, with the contribution of V_2^* to the absorption band increasing as the germanium content increases. Thus, the V_2^* centers are formed even in the course of irradiation. Since germanium atoms are effective sinks for vacancies, the vacancies directed towards germanium atoms form associations with them, i.e., V_2Ge complexes.

Thus, V_2^* complexes may be formed as a result of two reactions; one of these proceeds during irradiation and is represented as

$$Ge + V + V \longrightarrow V_2Ge, \quad (1)$$

whereas the second reaction is thermally activated and is described by

$$V_2 + Ge \longrightarrow V_2Ge. \quad (2)$$

Taking into account the complicated structure of the divacancy-related absorption band peaked at about 5560 cm^{-1}, we may evidently explain the change in the position of this band observed in $Si_{1-x}Ge_x$ with reference to Si by the simultaneous effect of two factors: (i) a shift related to variation in the band gap as the composition changes and (ii) a contribution of the absorption band that corresponds to V_2^*. As the germanium content increases, the contribution of V_2^* to the absorption band increases, which is apparently responsible for a deviation of the germanium-content dependence of the band shift from the corresponding dependence for E_g.

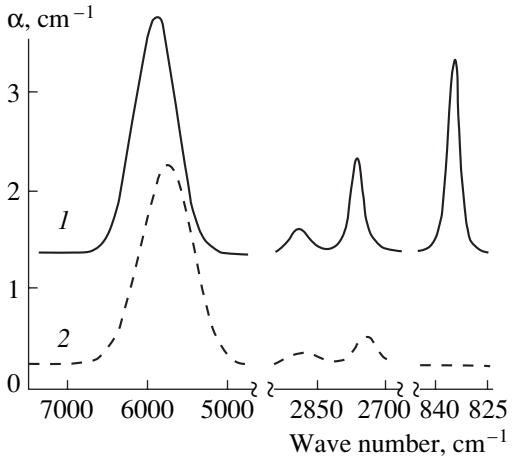

Fig. 5. Absorption spectra of (*1*) Si and (*2*) $Si_{0.965}Ge_{0.035}$ crystals irradiated at $T_{irr} \le 90$ K with fast electrons with a dose of 6×10^{17} cm^{-2}.

Thus, the experimental data obtained here suggest that V_2 divacancies characteristic of silicon are formed in $Si_{1-x}Ge_x$ single crystals during irradiation in addition to complexes of V_2 with germanium atoms (V_2Ge) and that the absorption band peaked in the vicinity of 5560 cm^{-1} is a superposition of two absorption bands that correspond to absorption by these two centers. We found that germanium did not affect the build-up of divacancies (as estimated from the absorption band peaked in the vicinity of 5560 cm^{-1}); this may be attributed to the fact that we experimentally measured the total concentration of divacancies and the detected V_2^* centers. Thus, the absorption intensity at the peak of the band at about 5560 cm^{-1} in the $Si_{1-x}Ge_x$ solid solutions cannot be used to estimate the concentration of divacancies introduced by irradiation.

It should be emphasized that all the aforementioned special features of absorption spectra manifest themselves in the range of high germanium concentrations. This means that it is probably necessary to distinguish between the regions of low and high concentrations of germanium in silicon when studying the processes of defect formation in $Si_{1-x}Ge_x$. The effect of germanium on the formation of secondary radiation defects in silicon in the region of low germanium concentrations (<1 at. %), in which case a germanium atom may be considered as a conventional isovalent impurity, is predominantly governed by the elastic-stress fields intro-

duced by germanium atoms in silicon. It is this factor that evidently accounts for the previously observed reduction of introduction efficiency for all secondary radiation defects [22] in germanium-doped silicon, which is similar to what has been found for the tin impurity in silicon [23, 24]. In the region of high germanium concentrations, the energy-band structure and the probabilities of interaction of defects and the cross sections of the defect production change; it is this circumstance that governs the processes of defect formation.

REFERENCES

1. G. D. Watkins and J. W. Corbett, Phys. Rev. **138**, A543 (1965).
2. J. W. Corbett and G. D. Watkins, Phys. Rev. **138**, A555 (1965).
3. R. C. Young and J. C. Corelli, Phys. Rev. B **5**, 1455 (1972).
4. L. J. Cheng, J. C. Corelli, J. W. Corbett, and G. D. Watkins, Phys. Rev. **152**, 761 (1966).
5. B. G. Svensson and M. Willander, J. Appl. Phys. **62**, 2758 (1987).
6. L. S. Smirnov, *Problems in Radiation Technology of Semiconductors* (Nauka, Novosibirsk, 1980), p. 20.
7. V. V. Emtsev and T. V. Mashovets, *Impurities and Point Defects in Semiconductors* (Radio i Svyaz', Moscow, 1981), p. 42.
8. L. J. Cheng and J. Lori, Phys. Rev. **171**, 856 (1968).
9. H. J. Stein, J. Appl. Phys. **45**, 1954 (1974).
10. E. V. Monakhov, A. N. Larsen, and P. Kringhf, J. Appl. Phys. **81**, 1180 (1997).
11. A. N. Larsen, Solid State Phenom. **69–70**, 43 (1999).
12. N. V. Abrosimov, S. N. Rossolenko, V. Alex, *et al.*, J. Cryst. Growth **166**, 657 (1996).
13. N. V. Abrosimov, S. N. Rossolenko, W. Thieme, *et al.*, J. Cryst. Growth **174**, 182 (1997).
14. E. R. Johnson and S. M. Christian, Phys. Rev. **95**, 560 (1954).
15. Yu. V. Pomozov, M. G. Sosnin, L. I. Khirunenko, *et al.*, Fiz. Tekh. Poluprovodn. (St. Petersburg) **34**, 1030 (2000) [Semiconductors **34**, 994 (2000)].
16. Y. H. Lee, J. C. Corelli, and J. W. Corbett, Phys. Lett. A **60**, 55 (1977).
17. J. L. Lindström and B. G. Svensson, Mater. Res. Soc. Symp. Proc. **59**, 45 (1986).
18. G. Davies, E. C. Lightowlers, R. C. Newman, and A. S. Oates, Semicond. Sci. Technol. **2**, 524 (1987).
19. P. Stallinga, P. Johannesen, S. Herstrom, *et al.*, Phys. Rev. B **58**, 3842 (1998).
20. M. Fanciulli and J. R. Byberg, Phys. Rev. B **61**, 2657 (2000).
21. A. Brelot and J. Charlemagne, in *Proceedings of the International Conference on Radiation Effects in Semiconductors, London, 1971*, p. 161.
22. L. I. Khirunenko, V. I. Shakhovtsov, V. K. Shinkarenko, *et al.*, Fiz. Tekh. Poluprovodn. (Leningrad) **21**, 562 (1987) [Sov. Phys. Semicond. **21**, 345 (1987)].
23. M. G. Sosnin, V. I. Shakhovtsov, and V. L. Shindich, Fiz. Tekh. Poluprovodn. (Leningrad) **15**, 786 (1981) [Sov. Phys. Semicond. **15**, 448 (1981)].
24. B. G. Svensson, J. Svensson, J. L. Lindström, *et al.*, Appl. Phys. Lett. **51**, 2257 (1987).

Translated by A. Spitsyn

Semiconductors, Vol. 35, No. 8, 2001, pp. 895–899. Translated from Fizika i Tekhnika Poluprovodnikov, Vol. 35, No. 8, 2001, pp. 932–936.

ELECTRONIC AND OPTICAL PROPERTIES OF SEMICONDUCTORS

Photoluminescence Kinetics in GaAs under the Influence of Surface Acoustic Waves

K. S. Zhuravlev*, A. M. Gilinskiĭ, A. V. Tsarev, and A. E. Nikolaenko

Institute of Semiconductor Physics, Siberian Division, Russian Academy of Sciences, pr. Akademika Lavrent'eva 13, Novosibirsk, 630090 Russia

** e-mail: zhur@thermo.isp.nsc.ru*

Submitted January 17, 2001; accepted for publication January 30, 2001

Abstract—The kinetics of the low-temperature photoluminescence (PL) of GaAs under the influence of the electric field of a surface acoustic wave (SAW) is investigated experimentally. When a SAW pulse (delayed by 20–30 μs with respect to the laser pulse) with a field strength of up to ~50 V/cm is applied, the rate of the conduction band-to-acceptor transitions increases considerably (by a factor of up to 10–20), while the rate of the donor–acceptor pair transitions does not vary significantly nor is the excitonic PL enhanced. The data obtained provide evidence of shallow-level donor ionization by the SAW electric field and corroborate the recombination model proposed previously, which explains the slow nonexponential decay of the free-electron PL in pure GaAs by the effect of multiply repeated capture of free conduction-band electrons by shallow-level donors. © *2001 MAIK "Nauka/Interperiodica".*

INTRODUCTION

It is currently believed that the mechanisms and the kinetics of radiative recombination in gallium arsenide and related III–V compounds are well investigated. From the data reported in the literature, the relaxation of nonequlibrium charge carriers (generated by a band-to-band excitation optical pulse) at liquid-helium temperature can be described in the following terms. Initially, at a time scale of several nanoseconds, the near-band edge photoluminescence (PL) kinetics in GaAs is governed by the formation and radiative decay of excitons [1, 2]. Subsequently, the impurity-related transitions start to be dominant. Since the cross section of the free-hole capture by shallow-level acceptors is larger than that of the free-electron capture by shallow-level donors [1], emission related to the valence band-to-donor transitions should decay much faster than the emission related to the conduction band-to-acceptor transitions. Furthermore, it is to be expected that, at low excitation levels, the decay of emission originating from transitions of both types follows an exponential law, and, thus, the band-to-impurity transitions vanish from the PL spectra within several microseconds or several tens of microseconds after the excitation is switched off [1, 3]. Consequently, it may be concluded that, at the end of this time interval, only the lines originating from the donor–acceptor pair (DAP) recombination, which decay rather slowly [4], remain in the spectrum. Commonly, experimental data on the kinetics of impurity PL in GaAs can be interpreted in the context of the scheme outlined. For example, in the detailed study of the exciton and impurity PL reported in [1], it was assumed that the decay curves of the band-to-acceptor transitions, recorded in the delay range from 0 to 2 μs, can be approximated by exponential dependences, which makes it possible to compare the experimentally determined transition rates with the calculated ones.

However, we have found recently that this pattern of excitation relaxation disregards important mechanisms that govern low-temperature recombination kinetics of free electrons in GaAs. It was shown experimentally that the decay of the band-to-acceptor PL in undoped or lightly doped GaAs lasts up to delay times as long as 1–2 ms and follows the dependence close to a power law ($I_{PL}(t) \propto 1/t^{\alpha}$, where $\alpha < 1$), which is radically different from the expected exponential decay [5–9]. The observation of long-lived transient PL of shallow acceptors makes it necessary to modify the above concept of dominant recombination processes in GaAs at low temperatures and cannot be interpreted in the concept of free-to-bound, bound-to-bound (donor–acceptor), and excitonic recombination mechanisms treated independently. To explain this effect, we considered a model similar to that proposed previously [9] to treat the luminescence kinetics of crystal phosphors [10, 11]. It has been demonstrated that slow decay of the free-carrier luminescence described by a time dependence close to a power law can take place in the material that contains centers of the charge-carrier trapping, provided the rates of the carrier recombination and carrier capture and escape from the traps satisfy certain relationships [10, 11]. According to this model, the long-lived PL appears when the probability of carrier capture by a trap far exceeds both the probability of its thermal escape and the probability of its transfer to a recombination center, and when the occupancy of the traps at the initial moment of the transient is close to 100%. In

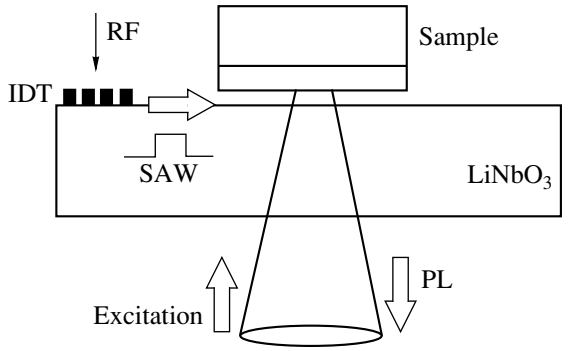

Fig. 1. Schematic representation of the setup used for the application of surface acoustic waves to the sample. IDT stands for the interdigital transducer; RF, for the radio-frequency ac voltage applied to the transducer; SAW, for the surface acoustic wave; and PL, for the photoluminescence radiation.

this case, the carriers experience a large number of capture and escape events prior to recombination, and the PL decay extends over a much longer period of time than a single residence of a carrier on a trap. According to the model, the duration of the band-to-acceptor PL decay falls in the millisecond range if the time of electron thermal escape from the traps is from several to several hundred milliseconds. Since the times of electron thermal escape from deep-level centers in GaAs at liquid-helium temperatures are on the order of several hours to several months [12], it was assumed that shallow-level donors act as traps in the case under study.

To test the proposed model experimentally and to clarify the role of shallow donors in the appearance of long-lived PL, we study this effect under the conditions such that the relationship between the rates of electron capture and escape from the traps can be varied. We carried out for the first time an investigation of the near-band edge PL kinetics under an applied ionizing electric field created using a surface acoustic wave (SAW). The SAWs provide a convenient means for the ionization of excitons and shallow-level donors in GaAs [13, 14].

EXPERIMENTAL

The samples for the PL kinetics studies were grown by molecular-beam epitaxy on semi-insulating GaAs(100) substrates. Surface acoustic waves were applied to the sample using the scheme outlined in Fig. 1. An interdigital transducer (IDT) was deposited on a lithium niobate crystal. The sample was placed near the surface of this crystal at a distance much less than the SAW wavelength; thus, the sample properties are affected by the electric field of SAWs propagating in $LiNbO_3$ [15]. Both the excitation radiation and the PL to be detected pass through the bulk of the $LiNbO_3$ crystal, which is transparent in the wavelength range of interest. In this arrangement, the energy fed into the IDT is efficiently converted into SAW energy. In comparison to the case where the IDT is deposited on the sample itself [16], the efficiency increases almost by a factor of 100, which results in a considerable reduction of the heat generation in the IDT related to the Joule losses. The transducer was composed of 15 electrode pairs; the peak of its frequency-response curve was at 70 MHz, which corresponded to the SAW wavelength of ~40 μm. The time of the SAW propagation from the IDT to the photoexcited region was equal to 3 μs. The strength of the SAW electric field in the sample was calculated from the known amplitude of the normal displacement in the SAW; the latter was determined from the measured intensity of laser beam diffraction (in reflection configuration) on the SAW propagating over the surface of the $LiNbO_3$ crystal. The electric-field strength in the sample varied from 0 to 400 V/cm. The kinetics of the band-to-acceptor, donor-to-acceptor, and excitonic PL under the influence of the SAW was recorded. The measurements were carried out in liquid-helium vapor at a temperature of 4.5–5 K. The PL was excited by the second harmonic of a pulsed LTI-701 Nd:YAG laser (excitation wavelength, 532 nm; the half-amplitude pulse duration, 120–150 ns; and pulse repetition rate, 5 kHz). The diameter of the laser spot at the sample surface was 300 μm. The recombination radiation was dispersed by a grating double monochromator and detected by a cooled photomultiplier operating in the time-resolved photon counting mode. The rectangular SAW pulses of 2–10 μs duration were applied with a delay of 10–50 μs with respect to the exciting laser pulse.

RESULTS AND DISCUSSION

In Figs. 2 and 3, we show the decay curves for near-band edge PL lines and, in Fig. 4, the time-resolved spectra of the acceptor-related PL for a *p*-GaAs sample (with no intentional doping) subjected to SAWs. The density of shallow acceptors in the epilayer determined from the Hall effect data is $N_A = 3 \times 10^{14}$ cm^{-3}, with the degree of compensation being ~1/3. The layer thickness equals 5 μm.

The decay curves for the (conduction band)-to-acceptor PL under the effect of a SAW are plotted in Fig. 2. When the SAW pulse is not applied, slow non-exponential decay of the PL is observed (see the lowest curve). Application of the SAW pulse results in a gradual increase in the (*e*, A) transition rate during the pulse, provided the SAW electric field exceeds 10 V/cm. At higher fields, the increase in the PL intensity is more rapid. After the end of the SAW pulse, slow PL decay (on the time scale of tens of microseconds) is observed. If the electric field strength exceeds 50 V/cm, the decay starts during the pulse itself.

In contrast to the band-to-acceptor PL kinetics, the decay curves of the DAP recombination radiation do not change significantly upon application of SAWs with the field strength of up to 30 V/cm (see Fig. 3).

When the field strength is raised above this value, a gradual decrease in the intensity of the DAP transitions in the tails of the decay curves after the SAW pulse is observed.

The decay curve of the excitonic PL under an applied SAW of the largest amplitude is plotted in Fig. 2. One can see that, at a field strength of up to 400 V/cm, no enhancement of excitonic PL is observed.

The observed rise of the band-to-acceptor PL intensity under the application of the SAW pulse is indicative of an increase in the electron density in the conduction band due to the partial ionization of the electron traps. Trap ionization is caused by an increase in the probability of electron escape under the influence of the SAW electric field. After the SAW is switched off, the initial value of the escape probability is restored, and the conditions for slow decay are established again. This behavior of the band-to-acceptor PL decay curves agrees with the proposed model of the recombination mechanism. The decay of the band-to-acceptor PL during the SAW pulse observed at electric field strengths exceeding 50 V/cm may be related to the intensification of electron transport out of the photoexcitation spot caused by the moving potential lattice created by the traveling SAW [17].

Next, we consider the behavior of the DAP PL decay curves under the application of the SAW and demonstrate that it is also in agreement with the proposed model. According to the model, slow decay is observed when almost all of the traps are occupied by electrons, and the free-electron density at the instant of the SAW pulse application is much lower than the trap density (~0.1% of the latter). Let us now assume that shallow donors act as traps. Then the SAW-induced ionization of a small fraction (on the order of 1%) of donors will result in a severalfold increase in the rate of the band-to-acceptor transitions. Meanwhile, the rate of the DAP transitions will not decrease significantly, since the number of electrons captured by donors changes only slightly. It is exactly such behavior that can be seen in Fig. 3.

Since the excitonic PL intensity does not grow under the influence of the SAW, it may be inferred that the shallow acceptors ($E_A \approx 30$ meV) are not ionized. This indicates that the carrier binding energy at the traps responsible for the slow decay of band-to-acceptor PL is much less than that at shallow acceptors; this is also in agreement with the assumption that shallow donors ($E_D \approx 6$ meV) play the role of these traps. Thus, we conclude that the slow decay of the PL is due to the multiply repeated capture of the conduction-band electrons by shallow donors.

It should be noted that the changes in the PL decay curves brought about by the application of SAWs may be related to heat generation in the IDT leading to an increase in the sample temperature. An additional study was carried out to determine the range of SAW intensities at which IDT heating does not result in the modification of the PL decay curves. To this end, the PL kinetics was recorded for the frequency of the voltage applied to the IDT near the minimum of the transducer frequency response. Under these conditions, the SAW electric field strength is greatly reduced, while the heat

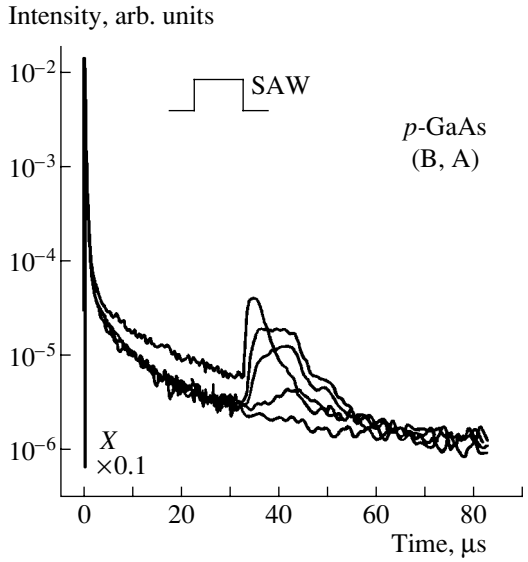

Fig. 2. Decay curves for the band-to-acceptor transition intensity during the application of SAW pulses of different amplitudes. The 10-μs SAW pulse (shown in the figure) is delayed by 33 μs with respect to the laser pulse. The curves correspond to the SAW electric field strength of 0, 10, 20, 30, and 100 V/cm (from bottom to top). For comparison, the excitonic PL decay kinetics under application of the SAW with the field strength of 400 V/cm is also shown (curve *X*).

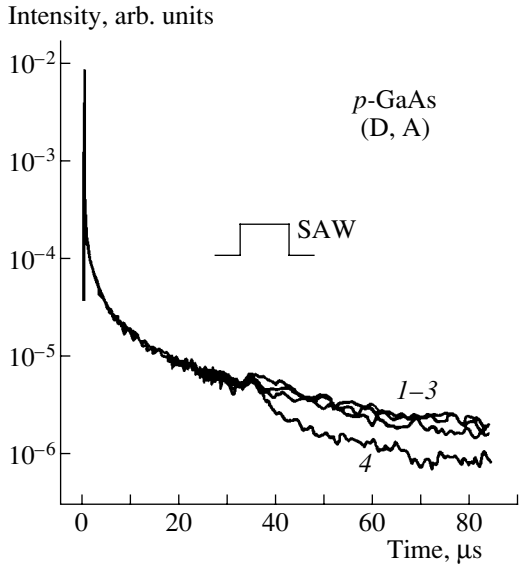

Fig. 3. Decay curves for the donor-to-acceptor transition intensity under application of SAW pulses. The SAW electric field strength is equal to (*1*) 0, (*2*) 10, (*3*) 30, and (*4*) 100 V/cm.

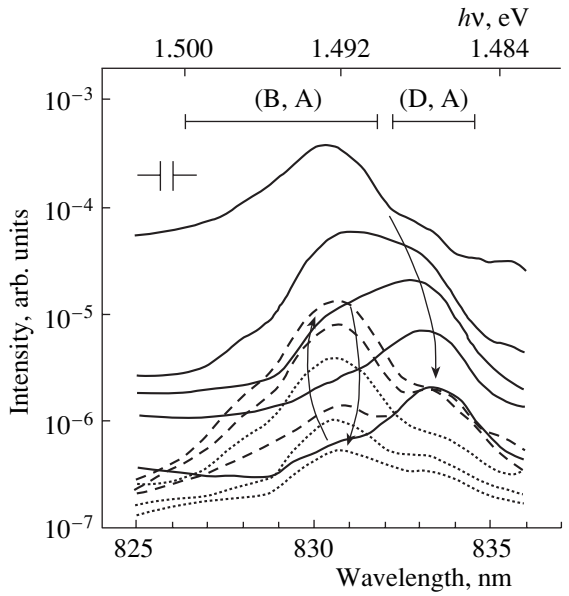

Fig. 4. Spectra of the shallow-acceptor transient PL at different delays with respect to the exciting laser pulse. A 10-μs SAW pulse is applied 23 μs after the laser pulse; the SAW field strength equals 50 V/cm. The solid lines show the spectra recorded before the application of the SAW pulse delayed by 0.4, 0.8, 1.5, 5, and 21 μs (from top to bottom); the dashed lines show the spectra recorded during the SAW pulse delayed by 24, 26, and 28 μs (from bottom to top); and the dotted lines show the spectra recorded after the end of the SAW pulse delayed by 35, 45, and 60 μs (from top to bottom). The arrows indicate the direction of increasing delay time in each group of curves.

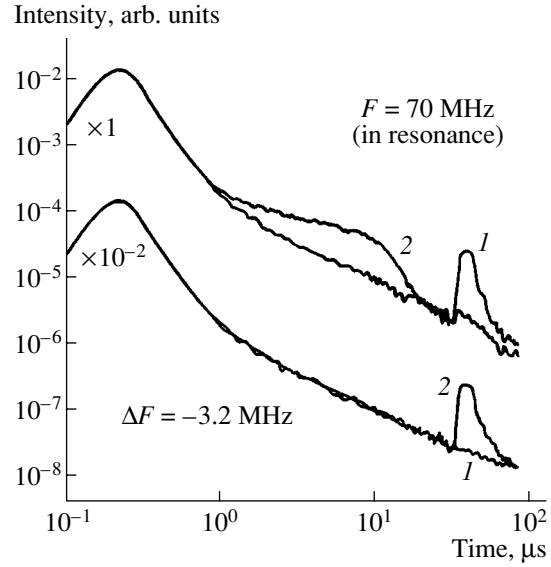

Fig. 5. Effect of the IDT driving-voltage frequency on the decay curves for the band-to-acceptor recombination radiation. For the upper curves, the frequency corresponds to the maximum and, for the lower curves, to the minimum of the transducer frequency response. The voltage amplitude equals (*1*) 20 and (*2*) 200 mV; for the resonance case, this corresponds to the SAW electric field strength of 40 and 400 V/cm, respectively.

generation in the IDT remains virtually unchanged. Figure 5 displays the kinetics of the band-to-acceptor recombination radiation recorded upon application of resonance (upper curves) and nonresonance (lower curves) excitation voltage to the IDT. The voltage amplitude U equals (*1*) 20 and (*2*) 200 mV; for the resonance case, this corresponds to the SAW electric field of 40 and 400 V/cm, respectively. One can see that, for U = 20 mV, the effect of donor ionization vanishes when the IDT excitation frequency is shifted to the minimum of the transducer frequency response, in which case the shape of the PL decay curve is not affected by the SAW application. Thus, it may be concluded that IDT heating does not affect the PL kinetics for field strengths below 40 V/cm. When the resonance voltage applied to the IDT is raised to 200 mV (which corresponds to the SAW field strength of 400 V/cm), an increase in the PL intensity occurs in the delay range from 1 to 20 μs (i.e., before the SAW pulse); the increase is followed by a bend, after which the decay becomes faster. Previously, we observed similar behavior of the decay curves at elevated sample temperatures [6]. In the present case, however, we observe the long-lived PL at longer delays, which should be absent at high lattice temperatures. If the IDT excitation frequency is shifted to the minimum of the frequency response characteristic, the inflection point in the decay curve disappears; only the feature related to the donor ionization after the application of the SAW pulse remains, with the feature amplitude corresponding to the SAW electric field of ~40 V/cm. Since the long-lived PL does not exist at increased lattice temperatures, it may be suggested that the inflection point that appears at the beginning of the decay curve for the SAW electric field exceeding 400 V/cm is related to the short-term increase of the lattice temperature caused by the electron gas heating, rather than by heat generation at the IDT during the SAW pulse. Electron heating is caused by the interaction of the dense carrier gas created by the laser pulse with an acoustic wave that remains for a long time in the resonator formed by the IDT and the edge of the $LiNbO_3$ crystal.

CONCLUSION

Thus, in this study, the influence of the electric field of a surface acoustic wave on the kinetics of the edge PL in GaAs was examined for the first time. It was found that the application of SAW pulses inducing the electric field with a strength exceeding 10 V/cm leads to an increase in the (conduction band)-to-acceptor PL intensity, while the decay kinetics of the donor-to-acceptor transitions is not affected up to a field strength of 50 V/cm. The enhancement of the excitonic PL under the influence of the SAW is not observed up to the maximum fields used (400 V/cm). Such behavior of the edge PL kinetics is indicative of the shallow-level donor ionization under the effect of the SAW electric field. The results obtained corroborate the proposed

model of the recombination mechanism in pure GaAs, which explains the appearance of the long-lived shallow-level acceptor PL by the effect of multiply repeated capture of the free electrons by shallow-level donors. It is shown that the field ionization of donors governs the shape of the PL decay curves up to a SAW field strength of ~100 V/cm; at higher fields, the effect of electron-gas heating becomes important.

ACKNOWLEDGMENTS

We are grateful to A.I. Toropov (Institute of Semiconductor Physics) for supplying the epitaxial GaAs samples and to I.L. Drichko (Ioffe Physicotechnical Institute, St. Petersburg) for familiarizing us with the details of the technique used in [15].

The study was supported by the Russian Foundation for Basic Research, project no. 98-17896.

REFERENCES

1. D. Bimberg, H. Munzel, A. Steckenborn, and J. Christen, Phys. Rev. B **31**, 7788 (1985).
2. Ya. Yu. Aaviksoo, I. Ya. Reĭmand, V. V. Rossin, and V. V. Travnikov, Pis'ma Zh. Éksp. Teor. Fiz. **53** (7), 377 (1991) [JETP Lett. **53**, 395 (1991)].
3. D. Z. Garbuzov, V. B. Khalfin, M. K. Trukan, *et al.*, Fiz. Tekh. Poluprovodn. (Leningrad) **12**, 1368 (1978) [Sov. Phys. Semicond. **12**, 809 (1978)].
4. R. Dingle, Phys. Rev. **184**, 788 (1969).
5. A. M. Gilinsky and K. S. Zhuravlev, Appl. Phys. Lett. **68**, 373 (1996).
6. K. S. Zhuravlev and A. M. Gilinskiĭ, Pis'ma Zh. Éksp. Teor. Fiz. **65** (1), 81 (1997) [JETP Lett. **65**, 86 (1997)].
7. A. M. Gilinskiĭ, K. S. Zhuravlev, T. S. Shamirzaev, *et al.*, in *Proceedings of the 3rd Russia Conference on Physics of Semiconductors, Moscow, 1997*, p. 207.
8. A. M. Gilinsky and K. S. Zhuravlev, in *Collected Abstracts of the International Conference on Luminescence and Optical Spectroscopy of Condensed Matter, Osaka, Japan, 1999*, p. 172.
9. A. M. Gilinskiĭ and K. S. Zhuravlev, in *Proceedings of the 4th Russia Conference on the Physics of Semiconductors, Novosibirsk, 1999*, p. 102.
10. É. I. Adirovich, *Some Problems in the Theory of Luminescence of Crystals* (Gostekhteorizdat, Moscow, 1956).
11. V. V. Antonov-Romanovskiĭ, *Kinetics of Photoluminescence of Phosphor Crystals* (Nauka, Moscow, 1966).
12. G. M. Martin, A. Mittonneau, and A. Mircea, Electron. Lett. **13**, 191 (1977).
13. K. S. Zhuravlev, D. V. Petrov, Yu. B. Bolkhovityanov, and N. S. Rudaja, Appl. Phys. Lett. **70**, 3389 (1997).
14. C. Rocke, A. O. Govorov, A. Wixforth, *et al.*, Phys. Rev. B **57**, 6850 (1998).
15. Yu. M. Gal'perin, I. L. Drichko, A. M. D'yakonov, *et al.*, in *Proceedings of the 4th Russia Conference on the Physics of Semiconductors, Novosibirsk, 1999*, p. 109.
16. A. Wixforth, J. Scriba, M. Wassermeier, *et al.*, Phys. Rev. B **40**, 7874 (1989).
17. C. Rocke, S. Zimmermann, A. Wixforth, *et al.*, Phys. Rev. Lett. **78**, 4099 (1997).

Translated by M. Skorikov

Semiconductors, Vol. 35, No. 8, 2001, pp. 900–903. Translated from Fizika i Tekhnika Poluprovodnikov, Vol. 35, No. 8, 2001, pp. 937–940.

ELECTRONIC AND OPTICAL PROPERTIES OF SEMICONDUCTORS

Optical Band Gap of $Cd_{1-x}Mn_xTe$ and $Zn_{1-x}Mn_xTe$ Semiconductors

P. V. Zhukovskiĭ*, Ya. Partyka*, P. Vengerek*, Yu. V. Sidorenko, Yu. A. Shostak**, and A. Rodzik***

** Lublin Technological University, Lublin, Poland*

*** Belarussian State University, Leningradskaya ul. 14, Minsk, 220050 Belarus*

Submitted January 22, 2001; accepted for publication January 30, 2001

Abstract—The dependence of the optical band gap for $Zn_{1-x}Mn_xTe$ and $Cd_{1-x}Mn_xTe$ semiconductor compounds was investigated by the methods of cathodoluminescence and optical reflection. It was found that, for $Zn_{1-x}Mn_xTe$ compounds in the region $x \lesssim 0.2$, the band gap is additionally broadened by a magnitude of about 0.08 eV, which is related to the high density of interstitial-type defects in single crystals. For $x \gtrsim 0.3$, the probability of the existence of these defects decreases substantially, which is related to the distortion of tetrahedra of the crystal lattice of $Zn_{1-x}Mn_xTe$ by Mn atoms, which are incorporated into each tetrahedron. © *2001 MAIK "Nauka/Interperiodica".*

INTRODUCTION

Certain ternary II–VI compounds with transition metals are wide-gap semimagnetic semiconductors with similar properties [1, 2]. In contrast with $Cd_{1-x}Mn_xTe$, nonlinear variations of the band gap ΔE_g and parameters of electron spin resonance spectra were found in the region of low Mn contents for $Zn_{1-x}Mn_xTe$ materials [3, 4].

The purpose of this study was to clarify the distinctions between the properties of $Cd_{1-x}Mn_xTe$ and $Zn_{1-x}Mn_xTe$ semiconductors, which were found in the region of low Mn contents. With this object in view, the results of measurements of the optical band gap are reported in this paper. These results were obtained by measuring the cathodoluminescence spectra (at temperatures of 77 and 300 K) and optical reflectance spectra (at 300 K).

EXPERIMENTAL RESULTS AND DISCUSSION

The cathodoluminescence spectra obtained for cleaved surfaces of the $Zn_{1-x}Mn_xTe$ crystals are shown in Fig. 1. The electron energy was 10 keV, the beam current was 5 μA, and the surface area exposed to the beam was about 0.2 mm^2. The residual pressure in a vacuum chamber was about 10^{-7} Pa. The signal was detected by a grating monochromator and was measured by a selective voltmeter.

As can be seen from Fig. 1a, the E_0 peak related to the band-to-band transitions is dominant in the cathodoluminescence spectra for the $Zn_{0.995}Mn_{0.005}Te$ sample (curve *1*) at liquid-nitrogen temperatures. Two peaks (E_{M1} and E_{M2}), which can be attributed to intracenter transitions $^4T_1(^4G) \longrightarrow {}^6A_1(^6S)$ and $^4T_2(^4G) \longrightarrow {}^6A_1(^6S)$ [5], are also observed.

For Mn contents $x \geq 0.1$, the transition $^4T_1(^4G) \longrightarrow {}^6A_1(^6S)$ starts to be dominant in the spectra measured at $T = 77$ K. At higher Mn contents, transitions most probably proceed between the impurity bands of Mn atoms, as evidenced by the broadening of the E_{M1} line. The most significant result of investigations of cathodolu-

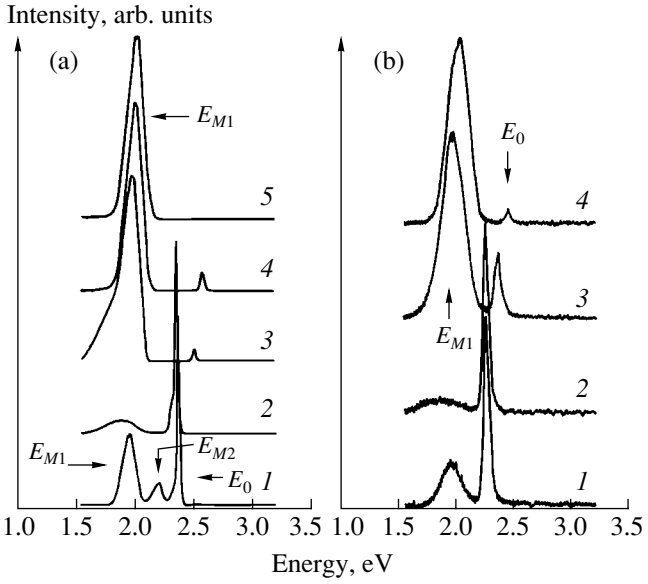

Fig. 1. Cathodoluminescence spectra of the $Zn_{1-x}Mn_xTe$ compounds at temperatures of T = (a) 77 and (b) 300 K. The spectra correspond to the samples with the Mn content x = (*1*) 0.005, (*2*) 0.085, (*3*) 0.283, (*4*) 0.39, and (*5*) 0.532.

1063-7826/01/3508-0900$21.00 © 2001 MAIK "Nauka/Interperiodica"

minescence for $Zn_{1-x}Mn_xTe$ is the fact that the E_0 line related to the band-to-band transitions starts to shift noticeably only at $x > 0.085$.

In order to clarify the effect of Mn atoms on the optical band gap in detail, the optical reflectance spectra were investigated in the energy range 0.8–6 eV. The experiments were carried out in a setup with a two-beam optical scheme. The signals were detected using a photoresistor and selective voltmeter combined with a personal computer.

The optical reflectance spectra for the $Cd_{1-x}Mn_xTe$ and $Zn_{1-x}Mn_xTe$ compounds with various Mn contents are shown in Fig. 2. The peaks observed in the spectra are denoted as E_0, E_1, $E_1 + \Delta_1$, E_2, A, B_1, and B_2. These peaks correspond to electron transitions between the symmetry points of the first Brillouin zone. The transition between Γ_6^v and Γ_8^c points corresponds to the electron transition from the valence band to the conduction band. The energy position of the E_0 peak related to this transition is equal to the band gap accurate to 10 meV [6]. The measurement error in our determination of the position of the E_0 peak was no larger than ±0.02 eV. For this reason, we may assume that the measured energy position of the E_0 peak corresponds to the band gap ΔE_g of the compound.

Figure 3 represents the band-gap dependences on the atomic fraction of Mn for the $Cd_{1-x}Mn_xTe$ and $Zn_{1-x}Mn_xTe$ compounds. These spectra were derived from optical reflectance spectra. An increase in the band gap for the $Cd_{1-x}Mn_xTe$ and $Zn_{1-x}Mn_xTe$ compounds, which is caused by an increase in the Mn content, should be linear.

As can be seen from Fig. 3a, the band gap for the $Cd_{1-x}Mn_xTe$ compounds increases linearly with x. A straight line shown in Fig. 3a was obtained from fitting the experimental results by the method of least squares.

For the $Zn_{1-x}Mn_xTe$ compounds (Fig. 3b), significant distinctions in the dependence of band gap on x are observed for low ($x \lesssim 0.20$) and high ($x \gtrsim 0.30$) Mn contents. More specifically, it is impossible to approximate the results obtained for $0 \le x \le 0.60$ by a straight line. For the region of $x \gtrsim 0.30$, the experimental points fit nicely to the straight line. Extrapolation of this line to $x = 0$ yields the extrapolated band gap for ZnTe $\Delta E_g = 2.18$ eV. This value is smaller than the measured band gap for ZnTe $\Delta E_g = 2.27$ eV. The experimental points for the Mn content range of $0 \le x \lesssim 0.20$ also fall above the straight line plotted using the data for $x \gtrsim 0.30$. The straight line with approximately the same slope but plotted by ~0.08 eV above the former can be drawn through these points. The shift of linear dependences of the band gap for low and high concentration regions significantly exceeds the measurement error. The experimental results obtained seem to indicate that there is an additional mechanism which broadens the

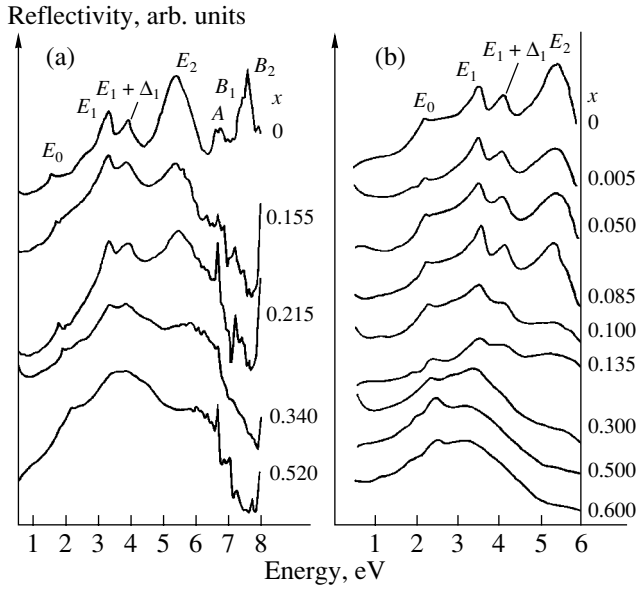

Fig. 2. Optical reflectance spectra (T = 300 K) for compounds: (a) $Cd_{1-x}Mn_xTe$ and (b) $Zn_{1-x}Mn_xTe$. The atomic fraction of Mn is specified by numbers at the curves.

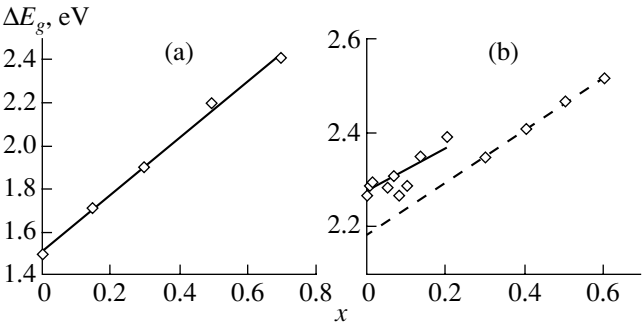

Fig. 3. Band gap dependences on the Mn content (x) obtained from optical reflectance spectra (T = 300 K): (a) for $Cd_{1-x}Mn_xTe$ and (b) for $Zn_{1-x}Mn_xTe$.

band gap by approximately 0.08 eV and manifests itself for the $Zn_{1-x}Mn_xTe$ compounds in the region of $x \lesssim 0.20$. For $x \gtrsim 0.30$, this mechanism ceases to operate. Let us analyze this possibility to interpret the experimental results.

The band gap of ZnTe crystals grown in different laboratories have been studied by measuring the optical reflectance spectra [6, 7]. However, the results reported differ vastly, specifically, 2.35 eV [6] and 2.26 eV [7]. Distinctions as large as these cannot be attributed to the measurement error, since the error in determining the peak position in the reflectance spectra is no larger than ±0.02 eV. In this connection, the cause of distinctions should be related exclusively to the quality of the samples grown in various laboratories. It is our opinion that the distinctions in the band gap values can be caused by

a high concentration of background impurities and structural defects in the samples [6, 7].

It is possible that this hypothesis is confirmed by fluctuations of ΔE_g values, which were obtained by us in the region of $x \lesssim 0.20$, whose magnitude significantly exceeds the measurement error (Fig. 3b). These variations of the ΔE_g value can be related to fluctuations of the defect concentrations in the samples with various Mn contents. For $x \gtrsim 0.30$, the possibility of the existence of defects or impurities which narrow the band gap of the $Zn_{1-x}Mn_xTe$ compounds could be the alternative to this hypothesis. However, cathodoluminescence measurements, from which it follows that the ΔE_g value varies more rapidly at high contents x (Fig. 1), as well as the band gap fluctuations for the region of $x \lesssim 0.20$, are inconsistent with this interpretation of the $\Delta E_g(x)$ dependence.

The existence of a high defect concentration in II–VI semiconductor compounds with transition metals was found from temperature measurements of the dielectric constant [8–10]. It follows from the data shown in Fig. 3b that, for $x \lesssim 0.20$, the experimental band gap exceeds the value obtained by extrapolation to $x = 0$ of the values measured for $x \gtrsim 0.30$. These two regions are separated by a value of $x = 0.25$. Assuming the random distribution of Mn atoms over the Zn sublattice sites at $x = 0.25$, we deduce that one Mn atom resides in each tetrahedron of this sublattice. It follows from the $\Delta E_g(x)$ dependences that the incorporation of one Mn atom into each tetrahedron of the Zn sublattice leads to a significant decrease in the effect of defects on the band gap of the $Zn_{1-x}Mn_xTe$ compounds. The fact that defects cease to affect the ΔE_g magnitude at $x \gtrsim 0.25$ does not mean that their concentration corresponds to 0.25. The upper bound of the defect concentration is probably much lower than 0.25. Its magnitude may be estimated as follows. Let us assume that the defects affect the band gap in the same manner as do the transition metal atoms. As it follows from Fig. 3b, the band gap (in eV) depends on the Mn content for $x \gtrsim 0.30$ as

$$\Delta E_g(x) = \Delta E_g(0) + (0.60 \pm 0.04)x \text{ [eV]}.$$

It follows from this dependence that, in order to increase the band gap by 0.08 eV (as takes place for $x \lesssim 0.20$), it is sufficient to incorporate Mn atoms at the content of $x \approx 0.13$. It should be noted that, for various II–VI compounds, Mn atoms can both increase and decrease the lattice constant. This is related to the sign of the difference in ionic radii between Mn and substituting ion. For example, for the $Cd_{1-x}Mn_xTe$ compound, the lattice constant decreases with an increase in x since the radius of Mn is smaller than that of Cd by ~0.05 Å [1]. On the other hand, the radius of Mn is larger than that of Zn by 0.09 Å [1]. In connection with this, an increase in the Mn content leads to an increase in the lattice constant of the $Zn_{1-x}Mn_xTe$ compound. However, in both cases, the incorporation of Mn leads to an increase in the band gap.

This means that the defects, which additionally broaden the band gap by ~0.08 eV for the region of $x \lesssim 0.20$, can both decrease and increase the lattice constant. Except for impurity atoms, the vacancy- and interstitial-type point defects can vary the lattice constant. Vacancies and their complexes, as a rule, should decrease the lattice constant, whereas the interstitial atoms should increase it. The difference in radii between vacancies (interstitials) and Zn atoms should be significantly larger as compared to Mn and Zn atoms. For II–VI compounds with transition metals, the variation in the band gap, to a first approximation, should be proportional to the product of impurity (defect) radii by their concentration. For this reason, the defect concentration, which additionally broadens the band gap for the region $x \lesssim 0.20$, should by significantly lower than $x \approx 0.13$.

In addition, it is necessary to clarify the fact that the effect of defects on the band gap of the $Zn_{1-x}Mn_xTe$ compounds significantly decreases with an increase in the Mn content to $x \approx 0.25$. Since the atomic radius for Mn is larger compared to that for Zn, the incorporation of a single Mn atom into the tetrahedron leads to its distortion. As a result, the potential energy of the crystal increases and the band gap broadens. The incorporation of interstitial-type defects in distorted tetrahedra, which leads to their further distortion, is less favorable according to its energy. On the contrary, the incorporation of vacancies in tetrahedra (in the Te sublattice) decreases the distortions. In connection with this, it should be expected that for the region of $x \lesssim 0.20$, where the defects and Mn atoms independently affect the ΔE_g magnitude, the defects additionally broaden the band gap.

For $x \gtrsim 0.25$, the presence of interstitial defects in tetrahedra, which are already distorted by Mn atoms, becomes unfavorable by its energy. On the other hand, there are no clear obstacles for the presence of vacancies in them.

Our measurements of $\Delta E_g(x)$ for the $Zn_{1-x}Mn_xTe$ compounds demonstrate that the band gap increases in the region of $x \lesssim 0.20$. This may mean that the interstitial-type defects, which additionally broaden the band gap, occur in this region of x. The number of tetrahedra undistorted, in which the interstitial-type defects can exist, decreases as x increases, and the tetrahedra of this type are completely absent in the $Zn_{1-x}Mn_xTe$ lattice at $x \gtrsim 0.25$. This means that the additional mechanism of broadening the band gap, which is related to the presence of interstitial-type defects in the $Zn_{1-x}Mn_xTe$ lattice, ceases to operate.

CONCLUSION

Based on the analysis of the cathodoluminescence and optical reflectance spectra for the $Zn_{1-x}Mn_xTe$

samples with various Mn contents ($0 \le x \le 0.60$) and their comparison with the reflectance spectra for $Cd_{1-x}Mn_xTe$ samples ($0 \le x \lesssim 0.70$), anomalies were found in the optical band gap dependence $\Delta E_g(x)$ for $Zn_{1-x}Mn_xTe$ with $x \lesssim 0.20$. These anomalies are caused by the presence of Mn atoms and interstitial-type defects in crystals. For $x \gtrsim 0.30$, the probability of the existence of defects in the $Zn_{1-x}Mn_xTe$ samples decreases sharply, which is related to the distortion of tetrahedra by Mn atoms having a larger atomic radius compared to Zn. As a result, the anomaly found for the $\Delta E_g(x)$ dependence disappears.

REFERENCES

1. *Semiconductors and Semimetals*, Ed. by J. Fundyna and J. Kossut (Academic, New York, 1988; Mir, Moscow, 1992), Vol. 25.
2. *Physics of II–VI Compounds*, Ed. by A. M. Georgobiani and M. K. Sheĭnkman (Nauka, Moscow, 1986).
3. A. Twardowski, P. Swiderski, M. von Ortenberg, and R. Pauthenet, Solid State Commun. **56**, 479 (1985).
4. P. W. Zukowski, J. Partyka, P. Wegierek, *et al.*, in *Proceedings of the IV Scientific and Technical Conference "Quality of Electrical Energy and Electrical Products," Poland, 1988*, p. 249.
5. A. Holda, A. Rodzik, A. A. Meknikov, and P. W. Żukowski, Acta Phys. Pol. A **88**, 739 (1995).
6. V. V. Sobolev, *Bands and Excitons in II–VI Compounds* (Shtiintsa, Kishinev, 1980).
7. A. Ebina, M. Yamamoto, and T. Tokahashi, Phys. Rev. B **6**, 3786 (1972).
8. P. W. Zukowski, A. Rodzik, and Yu. A. Shostak, Fiz. Tekh. Poluprovodn. (St. Petersburg) **31**, 714 (1997) [Semiconductors **31**, 610 (1997)].
9. P. W. Zukowski, J. Partyka, P. Wegierek, *et al.*, Fiz. Tekh. Poluprovodn. (St. Petersburg) **33**, 270 (1999) [Semiconductors **33**, 276 (1999)].
10. P. W. Zukowski, J. Partyka, P. Wegierek, *et al.*, Fiz. Tekh. Poluprovodn. (St. Petersburg) **34**, 1174 (2000) [Semiconductors **34**, 1124 (2000)].

Translated by N. Korovin

Semiconductors, Vol. 35, No. 8, 2001, pp. 904–911. Translated from Fizika i Tekhnika Poluprovodnikov, Vol. 35, No. 8, 2001, pp. 941–947.

ELECTRONIC AND OPTICAL PROPERTIES OF SEMICONDUCTORS

The Role of Lead in Growing $Ga_{1-X}In_XAs_YSb_{1-Y}$ Solid Solutions by Liquid-Phase Epitaxy

T. I. Voronina, T. S. Lagunova, E. V. Kunitsyna, Ya. A. Parkhomenko, D. A. Vasyukov, and Yu. P. Yakovlev

Ioffe Physicotechnical Institute, Russian Academy of Sciences, Politekhnicheskaya ul. 26, St. Petersburg, 194021 Russia

Submitted December 27, 2000; accepted for publication February 15, 2001

Abstract—The electrical properties of $Ga_{1-X}In_XAs_YSb_{1-Y}$ (X = 0.14–0.27) solid solutions grown from a Pb-containing solution–melt were investigated for the first time. Three acceptor levels were found to exist, specifically, a shallow level with the activation energy $E_{A1} \approx 0.008$–0.015 eV, and two deep levels $E_{A2} \approx 0.024$–0.033 eV and $E_{A3} \approx 0.07$ eV. It is demonstrated that the use of Pb makes it possible to obtain undoped solid solutions with a low concentration of defects and impurities and with high carrier mobility. © *2001 MAIK "Nauka/Interperiodica"*.

INTRODUCTION

It has been reported previously [1] that Pb can be used as a neutral solvent for growing GaSb epilayers by liquid-phase epitaxy (LPE). It has been demonstrated that the use of Pb makes it possible to decrease the liquidus temperature of the system; vary the ratio between atomic fractions of Sb and Ga in the solution–melt; and decrease the concentration of native structural defects, which are characteristic of GaSb, by two orders of magnitude. As the reduced Sb concentration X^*_{Sb} increased in the liquid phase, the hole density in GaSb decreased and reached a minimum in the range X^*_{Sb} = 0.76–0.8. Here, $X^*_{Sb} = X_{Sb}/(X_{Sb} + X_{Ga})$, where X_i is the atomic fraction of the component in the liquid phase. With a further increase in the value of X^*_{Sb} in the liquid phase, new defects, whose nature is not yet clear, appeared in the epilayers. The majority-carrier mobility was highest at X^*_{Sb} = 0.6 and decreased sharply at X^*_{Sb} = 0.76–0.8. Thus, the use of Pb in growing the GaSb epilayers permitted a material with a charge-carrier density as low as $p^{(77)} = N_A - N_D = 10^{13}$ cm^{-3} at 77 K and a high degree of compensation to be obtained. This material has found wide technological application as an insulating layer.

It has been demonstrated [2, 3] that the main properties of the $Ga_{1-X}In_XAs_YSb_{1-Y}$ solid solutions ($X \le 0.22$, $Y \le 0.18$) lattice-matched to GaSb, which were obtained without using Pb, are similar to GaSb properties in many respects. Undoped layers of solid solutions, as well as GaSb epilayers, were always of *p*-type conduction. Hole density was governed by shallow-level background impurities, which were present in the starting components, and by the double-charged acceptor complex $V_{Ga}Ga_{Sb}$. The activation energy for impurity levels is E_{A1} = 0.008–0.014 eV, and those for levels of the acceptor complex were E_{A2} = 0.035 eV and E_{A3} = 0.07 eV. The shallow-level acceptor density N_{A2} decreased with an increase in X for the solid solution.

By analogy with GaSb obtained from the Pb solution–melt, it is of interest to investigate the role of Pb in growing GaSb-based quaternary $Ga_{1-X}In_XAs_YSb_{1-Y}$ solid solutions from the point of view of decreasing the structure's defect concentration and carrier density in the epilayers.

This study continues previous investigations into obtaining $Ga_{1-X}In_XAs_YSb_{1-Y}$ solid solutions from Pb-containing solution–melt [4, 5]. It is devoted to the investigation of the electrical properties of these solid solutions, the kinetics of variation in the carrier density, carrier mobility, and structure defect concentration with respect to growth conditions, as well as to the possibility of obtaining the narrow-gap solid solutions ($E_g \approx 0.4$ eV) with a high carrier mobility and low concentration of structural defects.

2. PREPARATION OF EXPERIMENTAL SAMPLES

Epilayers of the $Ga_{1-X}In_XAs_YSb_{1-Y}$ solid solutions were grown by LPE, the Pb-containing solution–melt having a cooling rate of 0.6 K/min. The *n*- and *p*-GaSb(100) single-crystal wafers were used as substrates. Binary compounds GaSb, InAs, as well as In

(pure to 99.999 wt %), Sb (99.999 wt %), and Pb (99.9999 wt %) were chosen as the charge components. The procedure of obtaining the epilayers was as follows. According to the thermodynamic method suggested previously [6], mole fractions of components in coexisting liquid and solid (lattice-matched to GaSb) phases were calculated for the Ga–In–As–Sb–Pb heterogeneous system. Calculations were carried out for fixed values of temperature (T) and supercooling (ΔT). Initially, the buffer p-GaSb layer with a low carrier density and high resistivity ($p = 6 \times 10^{14}$ cm^{-3} at $T = 77$ K, $\rho \gtrsim 400$ Ω cm) was grown on the n-GaSb substrate from the Pb-containing solution–melt. The buffer layer thickness was 4–5 μm. After that, based on theoretical calculation, the epilayer of the $Ga_{1-X}In_XAs_YSb_{1-Y}$ solid solution was grown on the p-GaSb buffer layer from the Pb-containing solution–melt at $T = 560$°C and supercooling $\Delta T = (3–8)$°C. The mismatch of lattice parameters for the epilayer and substrate $\Delta a/a$ was measured by double-crystal X-ray diffractometry using a TPC-1 diffractometer. The chemical composition of the solid solutions obtained was determined by qualitative X-ray spectral analysis using a JXA-5 CAMEBAX X-ray microprobe analyzer.

As a result of experiments carried out at $T = (560 \pm 3)$°C, $\Delta T = (3–8)$°C, and various Pb contents in the liquid phase, the epilayers of $Ga_{1-X}In_XAs_YSb_{1-Y}$ solid solutions ($X = 0.14–0.27$, $Y = 0.12–0.22$) lattice-matched to the GaSb(100) substrate were obtained. The growth rate, which was calculated as the ratio between the layer thickness to the growth time, was 0.3–1.0 μm/min. These values are larger than the growth rate of epilayers with the same composition, which were obtained at 560°C from the In-containing solution–melt without using Pb. According to the X-ray spectral analysis data, there was no solid-phase Pb in the samples, although the Pb content in the liquid phase was about 0.039–0.236 atomic fractions.

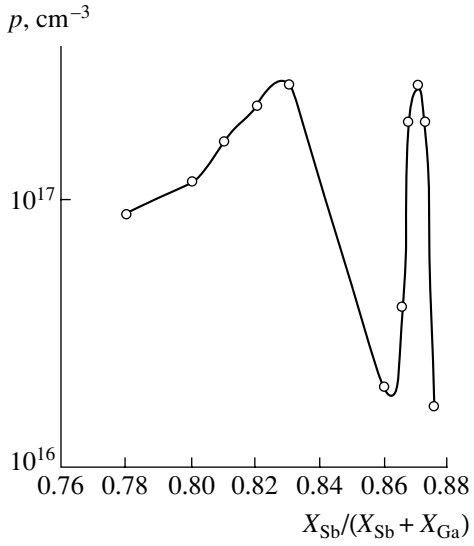

Fig. 1. Hole density p at $T = 77$ K as a function of the reduced Sb concentration $X^*_{Sb} = X_{Sb}/(X_{Sb} + X_{Ga})$.

The solid phase composition as well as the values of the band gap E_g of the $Ga_{1-X}In_XAs_YSb_{1-Y}$ solid solutions were calculated using the semiempirical formula [7] (see Table 1). As can be seen from Table 1, the experimental dependence of the In content in the solid phase on the Pb content in the liquid phase has a clearly defined maximum. Specifically, with an increase in the Pb content to 0.11 atomic fractions, the In content in the solid solution increases to $X = 0.27$. However, with a further increase in the Pb content in the liquid phase, the In content in the solid phase decreases. Such behavior of the dependence confirms the results of theoretical calculations [4, 5], which demonstrate that concentrations of solid-phase components in this system also pass through an extremum, although at other X and Y

Table 1. Dependence of the composition and band gap of the $Ga_{1-X}In_XAs_YSb_{1-Y}$ solid solutions on the Pb content in the liquid phase

Pb content in the liquid phase, atomic fractions	Composition of the $Ga_{1-X}In_XAs_YSb_{1-Y}$, atomic fractions				Band gap E_g, eV	
	calculation		experiment		$T = 300$ K	$T = 77$ K
	X	Y	X	Y		
0.2360	0.0947	0.0800	0.148	0.129	0.51	0.61
0.1951	0.1155	0.0977	0.168	0.138	0.49	0.58
0.1534	0.1417	0.1200	0.205	0.192	0.45	0.54
0.1506	0.1437	0.1217	0.210	0.160	0.44	0.53
0.1374	0.1534	0.1300	0.223	0.175	0.43	0.53
0.1229	0.1651	0.1400	0.247	0.223	0.41	0.50
0.1096	0.1768	0.1500	0.267	0.206	0.39	0.49
0.0394	0.2697	0.2300	0.194	0.148	0.46	0.55

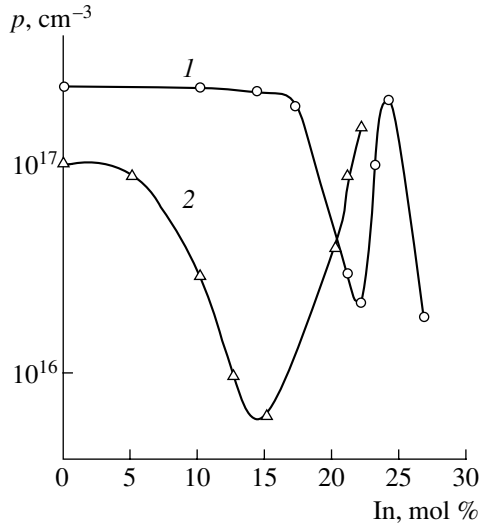

Fig. 2. Hole density p at $T = 77$ K as a function of the In content X in the GaInAsSb solid solution. Solid solutions were grown: (*1*) with the use of Pb and (*2*) without the use of Pb.

values. Previously, no epilayers more than 1 μm thick with the In content $X > 0.22$ suitable for fabricating optoelectronic devices have been obtained by LPE growth of the $Ga_{1-X}In_XAs_YSb_{1-Y}$ epilayers lattice-matched to GaSb(100) without the use of Pb. In this study, the use of Pb allowed epilayers of the $Ga_{1-X}In_XAs_YSb_{1-Y}$ solid solutions to be obtained, where $X \approx 0.27$ ($E_g \approx 0.4$ eV), see Table 1. The epilayers were 1.5–2 μm thick.

3. EXPERIMENTAL RESULTS AND DISCUSSION

The samples cut for studying galvanomagnetic effects were rectangular. On the side of the solid-solution epilayer, six In contacts were deposited and were used for measuring the electrical conductivity σ, Hall coefficient R, mobility μ, and magnetoresistance $\Delta\rho/\rho$ in a temperature range of 77–300 K. The characteristics of the samples are given in Table 2.

As can be seen from Table 2, the Hall voltage sign at $T = 77$ K for all samples (except for sample 8) is indicative of the *p*-type conduction. The dependence of the hole density at 77 K on the Sb content in the liquid phase $X^*_{Sb} = X_{Sb}/(X_{Ga} + X_{Sb})$ is shown in Fig. 1. In common with GaSb:Pb [1], a sharp decrease in the hole density with increasing X^*_{Sb} is observed. The minimum is attained at $X^*_{Sb} \approx 0.86$, which corresponds to a higher

Table 2. Characteristics of the samples investigated

Sample no.	In content (X), atomic fraction	X^*_{Sb}	$T = 300$ K			$T = 77$ K			E_{A1}, E_{A2}, E_{A3}, eV	N_{A1}, 10^{17} cm^{-3}	N_{A2}, 10^{17} cm^{-3}	N_D, 10^{16} cm^{-3}
			conduction type	n, p, 10^{17} cm^{-3}	μ, cm^2 V^{-1} s^{-1}	conduction type	n, p, 10^{17} cm^{-3}	μ, cm^2 V^{-1} s^{-1}				
1	0.120	0.777	*p*	4	500	*p*	1	1200	0.008, *A*1 0.033, *A*2	2	1.4	7
2	0.148	0.820	*p*	7	560	*p*	1.5	2200	0.008, *A*1 0.033, *A*2 0.07, *A*3	2.8	1.2	2
3	0.173	0.838	*p*	12	560	*p*	3	2300	0.01, *A*1 0.025, *A*2	4.2	3	1
4	0.210	0.862	*p*	30	80	*p*	0.46	380	0.01, *A*1 0.027, *A*2	2.3	0.5	17
5	0.223	0.858	*n*	0.3	2700	*p*	0.22	200	0.01, *A*1 0.028, *A*2	4.3	0.13	40
6	0.247	0.869	*p*	14	600	*p*	4	2700	0.008, *A*1 0.024, *A*2	4.5	0.5	5
7	0.267	0.873	*p*	5.6	530	*p*	0.18	570	0.01, *A*1 0.027, *A*2	0.48	0.2	0.6
8*	0.223	0.858	*n*	3	3900	*n*	1	4000	–	–	–	–
9*	0.247	0.869	*n*	30	2000	*p*	1.5	1400	–	–	–	–

Notes: * Denotes the Te-doped samples; $X^*_{Sb} = X_{Sb}/(X_{Sb} + X_{Ga})$; and *A*1, *A*2, and *A*3 denote the acceptor levels.

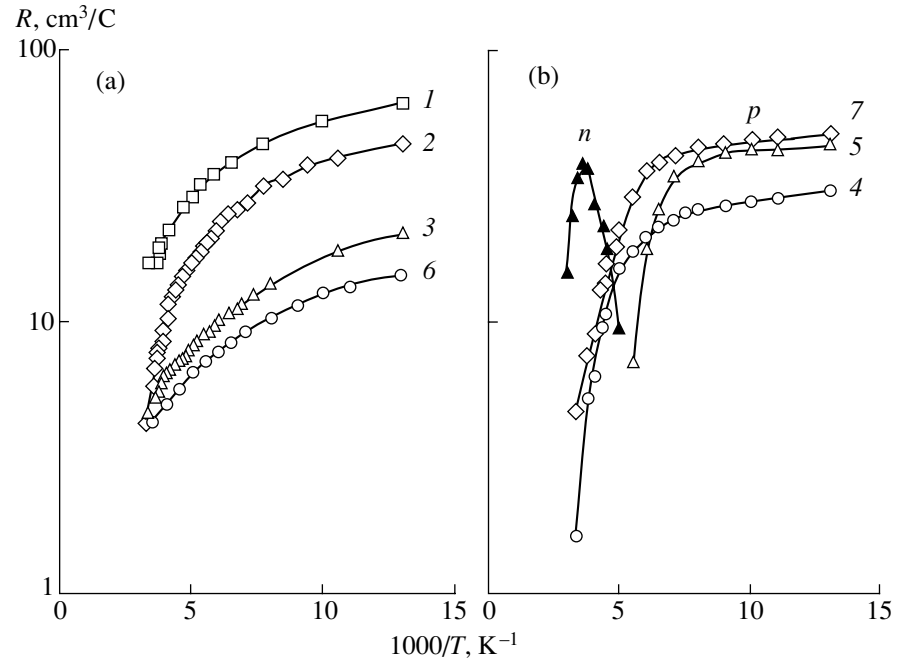

Fig. 3. Temperature dependences of the Hall coefficient R for samples with various In content X in the GaInAsSb solid solution. (a) Samples with a high mobility at $T = 77$ K and (b) samples with a low mobility at $T = 77$ K. Curve numbers correspond to sample numbers in Table 2.

Sb content in the liquid phase compared to GaSb:Pb, in which the minimum was observed at $X^*_{Sb} = 0.76$–0.8.

The dependences of the hole density on the In content in the solid solution grown in the presence of Pb (curve *1*) in comparison with solid solutions grown at the same temperatures from the same starting components without the use of Pb (curve *2*) are shown in Fig. 2. It can be seen that, if the solid solution was obtained without using Pb, the minimum of the hole density was observed at an In content of about 0.15, whereas it was impossible to obtain the solid solution for $X > 0.22$. In contrast with this, with the presence of Pb in the solution–melt, the minimum of the hole density is observed at an In content of 0.22. It is of interest that the hole density drops again at $X = 0.267$. In all cases, low mobilities correspond to low hole densities at $T = 77$ K (see Table 2).

The temperature dependences of the Hall coefficient, mobilities, and magnetic resistances for solid solutions of various compositions make it possible to investigate the energy spectrum of impurities and the mechanism of carrier scattering. The effect of Pb on the concentration and distribution of holes and structural defects for various In contents in solid solution can also be clarified.

3.1. Energy Spectrum of Impurities

The inverse-temperature dependences of the Hall coefficient for the samples listed in Table 2 are shown in Fig. 3. For the samples with a high mobility at $T = 77$ K (Fig. 3a) and with the In content $X = 0.12$–0.17 (samples 1–3), as well as for the sample with an In content of 0.247 (sample 6), shallow acceptor levels with the activation energies $E_{A1} = 0.008$–0.01 eV and deeper lying acceptor levels $E_{A2} = 0.024$–0.033 eV and $E_{A3} = 0.07$ eV are observed. The former levels are related to background impurities, which are contained in starting components of solid solutions, and the latter ones are related to the double-charged structure defect $V_{Ga}Ga_{Sb}$. For samples with a low hole density and mobility (Fig. 3b) and an In content of 0.21–0.22 (samples 4 and 5) and 0.267 (sample 7), the shallow acceptor level $E_{A1} \lesssim 0.01$ eV is also observed at $T = 77$–100 K. The deeper lying level with the activation energy $E_{A2} \approx 0.028$ eV is also observed with an increase in temperature. However, a sharp decrease in the Hall coefficient is observed for all samples at temperatures above 150 K, which points to the onset of transition to the intrinsic conductivity. For sample 7, the positive Hall voltage sign changes to a negative one at $T = 150$ K. By measuring the Hall voltage for this sample up to 400 K, we can observe that the intrinsic conductivity clearly manifests itself. However, the dependence of $RT^{3/2}$ on the inverse temperature is not exponential, and does not allow the band gap to be determined. This dependence can be explained by the pronounced compensation of impurities. For this reason, fluctuations of the potential begin to occur, and the tails of the density of states from the valence band and conduction band appear in the band gap [8].

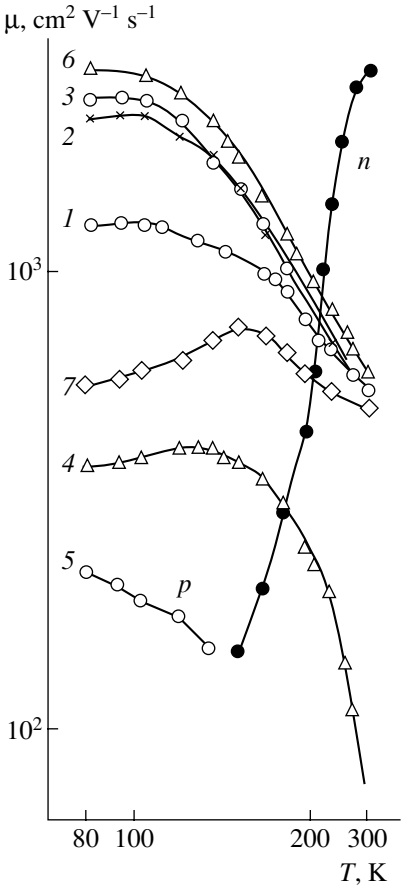

Fig. 4. Temperature dependences of mobility for samples with various In content in the solid solution. Curve numbers correspond to sample numbers in Table 2.

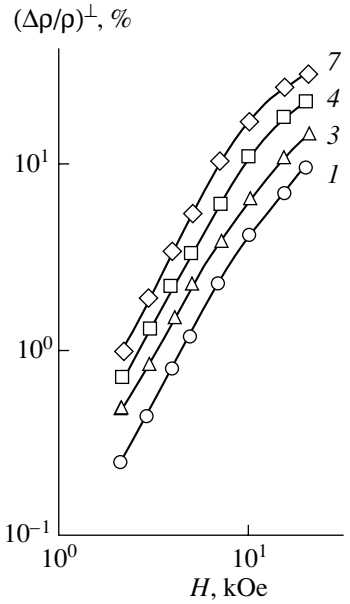

Fig. 5. Transverse magnetoresistance $(\Delta\rho/\rho)^{\perp}$ as a function of the magnetic field strength H at $T = 77$ K. Curve numbers correspond to sample numbers in Table 2.

3.2. Carrier Scattering Mechanism

Mobility μ and magnetoresistance $\Delta\rho/\rho$ are sensitive to the carrier scattering mechanism and to the type of scattering centers. The temperature dependences of mobility are shown in Fig. 4. As can be seen from Fig. 4, high mobility at 77 K is observed in the $Ga_{1-X}In_XAs_YSb_{1-Y}$ solid solutions with $X = 0.14$–0.17 and $X = 0.24$ (samples 1–3 and 6, see Table 2). At $T >$ 150 K, the mobility decreases with temperature according to the law close to $\mu \propto T^{-2}$, which is typical of lattice scattering in *p*-type III–V semiconductors [9]. At $T =$ 77–150 K, the experimental mobility μ_{exptl} is governed by scattering at impurity ions μ_I and lattice-vibration scattering μ_L

$$1/\mu_{exptl} = 1/\mu_I + 1/\mu_L. \quad (1)$$

For the samples with $X = 0.22$ and $X = 0.267$ (samples 4, 5, and 7), in which the hole density and mobility are low at $T = 77$ K, the temperature dependence of mobility at $T <$ 150–200 K points to the existence of an additional scattering mechanism apart from those involving impurity ions and lattice vibrations ($1/\mu_{exptl} = 1/\mu_I + 1/\mu_L + 1/\mu_S$). At higher temperatures, a sharp decrease in mobility is observed for these samples, whereas, in sample 5, the *p*-type conduction changes to *n*-type conduction, and the Hall mobility increases with an increase in temperature at $T >$ 150 K. In both cases, both the sharp mobility decrease and the appearance of *n*-type conduction are associated with a transition to intrinsic conductivity (appearance of electrons with a high mobility).

In order to determine the nature of the scattering centers, magnetoresistance was investigated. The transverse magnetoresistance (**I** ⊥ **H**, where **I** is the direction of a current through the sample, and **H** is the direction of the magnetic field) at $T = 77$ K is shown in Fig. 5. For all samples, the transverse magnetoresistance varies proportionally to H^2 up to 10 kOe. The coefficient $B_r^{\perp} = (\delta\rho/\rho)^{\perp}/(\mu H/c)^2$ for the samples with a high mobility (samples 1 and 3) is close to unity, which agrees with scattering by impurity ions with the participation of light and heavy holes. For the samples with a low mobility (samples 4 and 7), $B_r^{\perp} > 40$, which is well above the theoretical values calculated based on the theory of classic (Lorentzian) magnetoresistance.

For all samples, the longitudinal magnetoresistance (**I** ∥ **H**) $(\Delta\rho/\rho)^{\parallel}$ was investigated at $T = 77$ K. In this case, for the samples with a high mobility (samples 1–3 and 5), longitudinal magnetoresistance was absent. On the other hand, for all samples with a low hole mobility, longitudinal magnetoresistance was observed; however, it depended on the In content in the solid solution. It can be seen from Fig. 6 that the negative longitudinal magnetoresistance is observed for samples with an In

content of 0.21 in the solid solution (sample 4). In contrast with this, positive longitudinal magnetoresistance is observed for samples with an In content of 0.267 (sample 7).

Negative longitudinal magnetoresistance is characteristic of the quantum effect of weak localization [10]. On the other hand, so-called quantum antilocalization, or positive longitudinal magnetoresistance, is more characteristic of *p*-type Group IV and III–V semiconductors. This effect is manifested in strong spin–orbit scattering [11], which is specifically characteristic of *p*-type Group IV and III–V semiconductors. The occurrence of positive and negative magnetoresistance for the case of longitudinal magnetoresistance, in the absence of Lorentzian magnetoresistance, depends on the relationship between the frequencies of the spin–orbit scattering and phase upset for a specific sample, as in Fig. 6 at 77 K. For this interpretation, in the case of transverse magnetoresistance, large values of the coefficient $B_r^{\perp} > 40$ for samples 4 and 7 (Fig. 5) can be related to the combination of effects of quantum antilocalization (longitudinal magnetoresistance) and Lorentzian magnetoresistance.

Another explanation of the phenomena observed in the samples with low mobility also exists. Specifically, an anomalously large coefficient of the transverse magnetoresistance $B_r^{\perp}$ and appearance of the longitudinal magnetoresistance (sample 7) may be associated with clusters of impurity atoms. These clusters manifest themselves as regions distorting the paths of the current flow and bringing about the underestimation of mobility rather than as scattering centers. The effective-medium theory [12], which was developed for material with clusters of this type, yields the following formulas for mobility and magnetoresistance:

$$\mu = \mu_0(1 - 3/2)/(1 - 3/4), \quad (2)$$

$$(\Delta\rho/\rho)^{\perp} = 0.3 f(\mu_0 H/c)^2, \quad (3)$$

where μ_0 is the mobility in a homogeneous matrix, and f is the volume fraction occupied by clusters. Using the experimental data for μ and $\Delta\rho/\rho$ at $T = 77$ K and formulas (2) and (3), we determined the mobility in the matrix $\mu_0 = 4500$ cm^2 V^{-1} cm^{-1} and in the volume fraction occupied by nonuniformities $f = 0.6$.

Correlating the values of mobility μ_I at $T = 77$ K, which is determined by ion scattering and is separated out from the experimental mobility according to formula (1), with theoretical values calculated by the Brooks–Herring formula

$$\mu_I = 3.2 \times 10^{15}(m_0/m^*)^{1/2}\chi^2 T^{3/2}/N_I f(b), \quad (4)$$

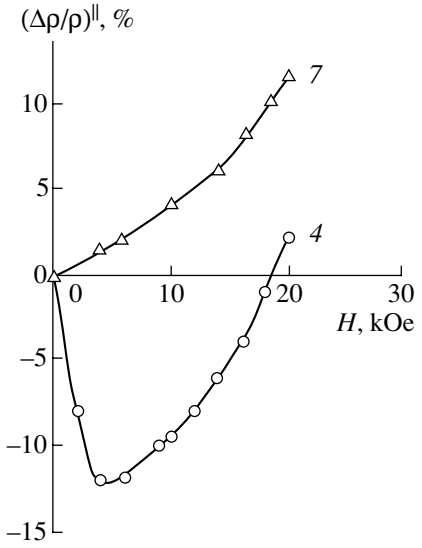

Fig. 6. Longitudinal magnetoresistance $(\Delta\rho/\rho)^{\parallel}$ as a function of the magnetic field strength H at $T = 77$ K. Curve numbers correspond to sample numbers in Table 2.

where

$$f(b) = \ln(1 + b) - b/(b + 1),$$

$$b = 1.3 \times 10^{14} T^2/p(m^*/m_0),$$

we can determine the concentration of the ionized impurity N_I (we assume that for both *p*-GaInAsSb and *p*-GaSb, the effective hole mass $m^* = 0.4m_0$, and the dielectric constant $\chi = 15.7$). For shallow impurity levels, $N_I^{(77)} = 2N_D + p^{(77)}$; thus, we can determine the acceptor concentration N_D. We determine the shallow-level acceptor concentration from the neutrality equation: $p_{\text{depl}} = N_{A1} - N_D$, where p_{depl} is the hole density corresponding to the depletion of shallow levels. We can find the concentration of the deeper lying acceptor levels N_{A2} from the concentration p at higher temperatures. The values of N_{A1}, N_{A2}, and N_D are given in Table 2.

The results obtained may be compared with the results reported previously [2, 3] for GaInAsSb solid solutions grown without using Pb. In this case, the solid solutions with the In content $X \approx 0.15$ had a low hole density and mobility and were highly compensated. In contrast with this, uncompensated material grows in the presence of Pb. For the In content $X = 0.22$, a great quantity of defects probably related to misfit dislocations was observed, whereas a highly compensated material similar to the material with an In content of 0.15, which was grown without the use of Pb, grows in the presence of Pb. Solid solutions with an In content of above 0.22 can be obtained solely in the presence of Pb in the solution–melt. In this case, solid solutions with an In content of 0.24 constituted a high-quality *p*-type uncompensated material. A great quantity of defects in

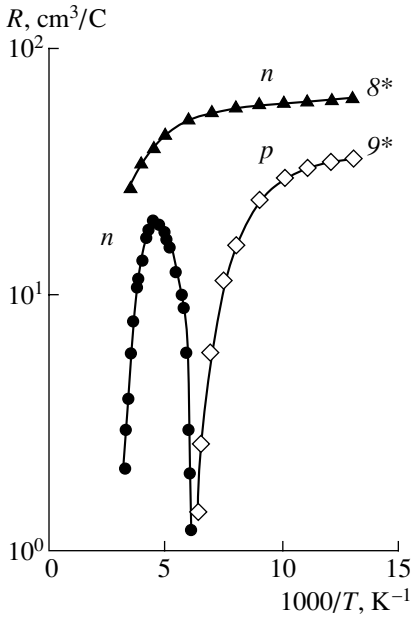

Fig. 7. Temperature dependence of the Hall coefficient for Te-doped solid solutions. Curve numbers correspond to sample numbers in Table 2.

the form of large clusters was observed in solid solutions at an In content of 0.265.

4. GaInAsSb *n*-TYPE SOLID SOLUTIONS

In order to fabricate highly efficient fast-response photodiodes for the wavelength range λ = 2.5–3 μm with low reverse currents on the basis of the $Ga_{1-X}In_XAs_YSb_{1-Y}$ solid solutions, the *n*-type epilayers with the band gap E_g = 0.4–0.5 eV are used in the device's active region. Epilayers of this type may be obtained through Te doping the solid solutions with an In content of 0.22 and 0.24.

If the starting components for growing solid solutions is not *p*-GaSb, as was described above, but *n*-GaSb:Te with the electron density $n = 5 \times 10^{17}$ cm^{-3}, the GaInSbAs solid solutions change the *p*-type conduction to *n*-type conduction. The overcompensation of the material depends on the hole density in the sample (see Table 2). With an In content in the solid solution of 0.22 (sample 5), for which the hole density is below 10^{17} cm^{-3}, complete overcompensation is observed. In this case, at T = 77 K, the material becomes *n*-type and has the electron density $n = 10^{17}$ cm^{-3} and electron mobility μ = 4000 cm^2 V^{-1} s^{-1} (see sample 8* in Table 2). A decrease in the Hall coefficient (Fig. 7, curve *8**) is observed above 200 K, which is apparently related to the onset of the transition to *p*-type conduction. With an In content in the solid solution of 0.247, for which the hole density was above 10^{17} cm^{-3} (sample 6, Table 2), with the same level of Te doping as for sample 8*, the sample is partially compensated at liquid-nitrogen temperature and preserves its *p*-type conduction (sample 9* in Table 2). However, the change of the Hall voltage sign and the transition to the intrinsic conduction occurs at T = 150 K (Fig. 7, curve *9**). The band gap E_g = 0.42 eV was determined from the slope of the $RT^{3/2}$ dependence on the inverse temperature at $T >$ 200 K, which agrees well with the value calculated (see Table 1).

5. CONCLUSIONS

In this study, the electrical properties of the $Ga_{1-X}In_XAs_YSb_{1-Y}$ solid solutions grown from the Pb-containing solution–melt on GaSb(100) substrates with an intermediate GaSb Pb-containing insulating layer were investigated for the first time. The investigations carried out allow us to make the following conclusions:

(i) The use of Pb in growing the $Ga_{1-X}In_XAs_YSb_{1-Y}$ solid solutions allowed us to obtain for the first time epilayers of these solid solutions with an In content in the solid phase X = 0.24–0.27 (E_g = 0.5–0.49 eV at T = 77 K, see Table 1) 1.5–2 μm thick, which is suitable for the development of optoelectronic devices. This was impossible without using Pb.

(ii) Undoped $Ga_{1-X}In_XAs_YSb_{1-Y}$ solid solution with the In content X = 0.22 (E_g = 0.53 eV at T = 77 K), which was obtained from the Pb-containing solution–melt, is a highly compensated material. This material is similar to a wider gap material with X = 0.15 (E_g = 0.58 eV at T = 77 K), which was obtained without using Pb.

(iii) Undoped $Ga_{1-X}In_XAs_YSb_{1-Y}$ solid solutions with the In content X = 0.247 (E_g = 0.5 eV at T = 77 K), which were obtained with the use of Pb, have low concentrations of defects and compensating impurities. They possess a high hole mobility μ = 2700 cm^2 V^{-1} s^{-1}.

(iv) Te doping of the $Ga_{1-X}In_XAs_YSb_{1-Y}$ solid solutions with the In content X = 0.22, which were obtained with the use of Pb, permits one to develop *n*-type material with a high electron mobility μ = 4000 cm^2 V^{-1} s^{-1}.

(v) The solid solutions obtained may be used to develop high-efficiency optoelectronic devices (light emitting diodes, lasers, and photodiodes) with the operating wavelength λ = 2.4–3 μm.

ACKNOWLEDGMENTS

We thank T. A. Polyanskaya, N. A. Charykov, and T. B. Popova for their help in the investigations and their participation in discussions of the results.

REFERENCES

1. A. N. Baranov, T. I. Voronina, T. S. Lagunova, *et al.*, Fiz. Tekh. Poluprovodn. (Leningrad) **23**, 780 (1989) [Sov. Phys. Semicond. **23**, 490 (1989)].
2. A. N. Baranov, A. N. Dakhno, B. E. Dzhurtanov, *et al.*, Fiz. Tekh. Poluprovodn. (Leningrad) **24**, 98 (1990) [Sov. Phys. Semicond. **24**, 59 (1990)].
3. A. N. Baranov, T. I. Voronina, A. N. Dakhno, *et al.*, Fiz. Tekh. Poluprovodn. (Leningrad) **24**, 1072 (1990) [Sov. Phys. Semicond. **24**, 676 (1990)].
4. I. A. Andreev, E. V. Kunitsyna, Yu. V. Solov'ev, *et al.*, Pis'ma Zh. Tekh. Fiz. **25** (19), 77 (1999) [Tech. Phys. Lett. **25**, 792 (1999)].
5. E. A. Kunitsyna, I. A. Andreev, N. A. Charykov, *et al.*, Appl. Surf. Sci. **142**, 371 (1999).
6. A. M. Litvak and N. A. Charykov, Zh. Khim. Fiz. **64**, 2331 (1990).
7. T. C. DeWinter, M. A. Pollack, A. K. Strivastava, and J. I. Zuskind, J. Electron. Mater. **4**, 729 (1985).
8. B. I. Shklovskiĭ and A. L. Efros, *Electronic Properties of Doped Semiconductors* (Nauka, Moscow, 1979; Springer-Verlag, New York, 1984).
9. D. Kranzer, Phys. Status Solidi A **26**, 11 (1974).
10. A. Kawabata, J. Phys. Soc. Jpn. **42** (2), 628 (1980).
11. B. L. Al'tshuler, A. G. Aronov, A. I. Larkin, and D. E. Khmel'nitskiĭ, Zh. Éksp. Teor. Fiz. **81**, 768 (1981) [Sov. Phys. JETP **54**, 411 (1981)].
12. M. H. Cohen, Phys. Rev. Lett. **30**, 698 (1973).

Translated by N. Korovin

Semiconductors, Vol. 35, No. 8, 2001, pp. 912–917. Translated from Fizika i Tekhnika Poluprovodnikov, Vol. 35, No. 8, 2001, pp. 948–953.

SEMICONDUCTOR STRUCTURES, INTERFACES, AND SURFACES

Interface States and Deep-Level Centers in Silicon-on-Insulator Structures

I. V. Antonova*, J. Stano, D. V. Nikolaev*, O. V. Naumova*, V. P. Popov*, and V. A. Skuratov****

** Institute of Semiconductor Physics, Siberian Division, Russian Academy of Sciences, pr. Akademika Lavrent'eva 13, Novosibirsk, 630090 Russia*

*** Joint Institute for Nuclear Research, ul. Joliot-Curie 6, Dubna, Moscow oblast, 141980 Russia*

Submitted January 23, 2001; accepted for publication January 31, 2001

Abstract—Deep-level centers in a split-off silicon layer and trap levels were studied by deep-level transient spectroscopy both at the Si/SiO_2 interface obtained by direct bonding and also at the Si(substrate)/⟨thermal SiO_2⟩ interface in the silicon-on-insulator structures formed by bonding the silicon wafers and delaminating one of the wafers using hydrogen implantation. It is shown that the Si/⟨thermal SiO_2⟩ interface in a silicon-on-insulator structure has a continuous spectrum of trap states, which is close to that for classical metal–insulator–semiconductor structures. The distribution of states in the upper half of the band gap for the bonded Si/SiO_2 interface is characterized by a relatively narrow band of states within the range from $E_c - 0.17$ eV to $E_c - 0.36$ eV. Furthermore, two centers with levels at $E_c - 0.39$ eV and $E_c - 0.58$ eV are observed in the split-off silicon layer; these centers are concentrated in a surface layer with the thickness of up to 0.21 μm and are supposedly related to residual postimplantation defects. © *2001 MAIK "Nauka/Interperiodica".*

INTRODUCTION

Silicon-on-insulator (SOI) structures offer several advantages over "bulk" silicon, which has stimulated interest in the properties of these structures. Among the current methods for making SOI structures, those based on the direct bonding of silicon wafers and on delaminating one of the wafers using hydrogen implantation are considered as the most promising [1–3]. The thickness of the split-off silicon layer in these structures does not exceed 0.5–0.2 μm. At this thickness, the traps at the Si/SiO_2 interface are obviously expected to profoundly affect the characteristics of devices based on the SOI structures. In addition, various metal or other contaminants may be present at the Si/SiO_2 interface and may introduce electrically active complexes with deep levels in the silicon band gap [4]. The split-off silicon layer and the Si/SiO_2 interface have been studied for the SOI structures formed by silicon implantation (the so-called "separation by implantation of oxygen," or SIMOX, technology) [5], whereas such data are lacking for the SOI structures formed by bonding. In this paper we report the results of studying the deep levels in the split-off layer and the traps at the Si/SiO_2 interface produced by direct bonding in comparison with the Si(substrate)/⟨thermal SiO_2⟩ interface in the SOI structures.

EXPERIMENTAL

In order to produce the SOI structures, we used Czochralski-grown *p*- and *n*-Si wafers 100 mm in diameter. The charge-carrier concentrations in the starting material and also in the film and substrate of SOI structures are listed in the table. The thickness of the split-off silicon layer in the structures was 0.5 μm, and the buried-insulator layer was 0.28–0.4-μm thick. In specific cases, the split-off silicon layer was additionally doped with boron by implantation of B^+ ions with an energy of 130 keV and a dose of 10^{15} cm^{-2} or with phosphorus by implanting P^+ ions with an energy of 300 keV and a dose of 10^{12} cm^{-2} with subsequent heat treatment at 900–1100°C aimed at activating the introduced impurity. As has been shown [6], *n*-type conductivity is observed in the split-off layer of the SOI structure formed using the starting *p*-Si wafer; this conductivity is designated as *n**-Si in the table. In the structures studied, the ⟨split-off silicon layer⟩/⟨buried oxide⟩ interface represents the bonding boundary, whereas the substrate/⟨buried oxide⟩ interface represents the boundary between silicon and the thermally grown oxide.

In these studies, we measured the high-frequency capacitance–voltage (*C–V*) characteristics and employed deep-level transient spectroscopy (DLTS). Charge-sensitive DLTS (Q-DLTS) was chosen from among the many varieties of DLTS methods [7]. The Q-DLTS method offers a number of advantages over classical high-frequency DLTS and extends our capabilities of studying the interfaces in the metal–insulator–semiconductor (MIS) structures [7]. The operating frequency for Q-DLTS measurements was 1 kHz. The time-window width was varied in the range of 10^{-4}–2×10^{-3} s, and the duration of a filling pulse was 10^{-5}–

2×10^{-4} s. Some measurements were performed using the conventional capacitance-related DLTS method at a frequency of 8 MHz for the same values of the time-window width and the filling-pulse duration. The bias applied to the structure in the course of measurements is henceforth designated as $U2$, and the amplitude of the filling pulse is designated by $U1$. All the measurements were performed using the mesastructures (Fig. 1). Contacts were formed by deposition of Al. The area of the mesastructures varied in the range of 0.5–1 mm^2.

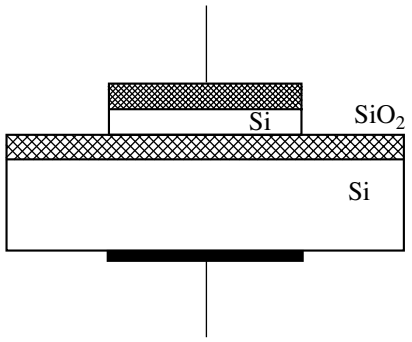

Fig. 1. Schematic representation of the mesastructures used in the measurements for the capacitance–voltage characteristics and deep-level transient spectroscopy.

RESULTS

The C–V characteristic of the n-Si/SiO_2/n-Si structures is shown in Fig. 2. It is typical of the structures with the same conductivity type in the film and substrate [8]; the value of C_{min1} is specified by the series-connected capacitances of the substrate and the buried insulator layer, whereas that of C_{min2} is specified by the series-connected capacitances of the split-off silicon layer and the buried insulator layer. The voltage range I corresponds to the situation when the depletion layer is located within the substrate, whereas the accumulation layer is within the silicon film. It is in this voltage range that recharging of both the states at the substrate/oxide interface and the deep levels in the substrate can be observed in the course of DLTS measurements. For larger reverse biases, the inversion state sets in the substrate. For range II voltages, the depletion layer is in the film, whereas the accumulation layer is located within the substrate. By choosing a voltage in this range, we can observe the recharging of both the states at the film/oxide interface and deep levels in the film. For large positive voltages, an inversion occurs in the film.

The charge-carrier concentrations in the film and the substrate (see table) were determined from the C–V characteristics for all structures; the fixed charge in the buried insulator and the densities of states at the interfaces were also determined. As follows from these measurements, the charge-carrier concentration in the substrate in the vicinity of the substrate/(buried oxide) interface is virtually the same as in the starting silicon.

In Fig. 3, we show the Q-DLTS spectra for the SOI-II and SOI-III structures; these spectra were obtained using range I voltages, in which case the substrate and the substrate/oxide interface were tested. The spectra for the SOI-I and SOI-IV structures were similar to those for the SOI-II structure. The peaks observed can be separated into two groups, for one of which the temperature position of a peak is independent of the applied bias, whereas the peaks belonging to the other group change their temperature position as the bias is varied. The peaks of the first type correspond to the bulk centers, whereas those of the second type correspond to the centers at the Si/SiO_2 interface. According to our experiments, almost all the peaks observed in Fig. 3 correspond to the continuous distribution of deep levels. This follows from processing both the spectra shown in Fig. 3 and the spectra measured for various values of the time-window width. The sole exception is peak $E1$, which is observed for SOI-II and is located at 166 K irrespective of the applied bias. The parameters of this peak are $E_c - 0.14$ eV and $\sigma = 10^{-19}$ cm^2; these parameters were determined on the assumption that the cross section σ is temperature-independent.

In order to derive the distribution of the surface-state density in the silicon band gap on the basis of the spectra obtained, we calculated the band bending in silicon at the substrate/oxide interface (Ψ_{s2}). For a grounded

Parameters of starting material and combination of wafers in the silicon-on-insulator (SOI) structures

The SOI designation	The split-off silicon layer; $n(p)$, cm^{-3}		The substrate; $n(p)$, cm^{-3}
	the starting wafer	the Si film in SOI	
SOI-I	n-Si; 1.5×10^{15}	n-Si; 5×10^{15}	n-Si; 1.5×10^{15}
SOI-II	p-Si; 1.5×10^{15}	n*-Si; 3×10^{15}	n-Si; 1.5×10^{15}
SOI-III	p-Si; $2 \times 10^{15} + B^+$	p^+-Si; 2×10^{18}	p-Si; $(1–2) \times 10^{15}$
SOI-IV	p-Si; $10^{15} + P^+$	n^+-Si; 2×10^{16}	n-Si; 3×10^{14}

Note: n* denotes the n-type conductivity that arises in the course of the SOI fabrication; B^+ or P^+ denote additional doping of the split-off silicon layer via the implantation of boron or phosphorus.

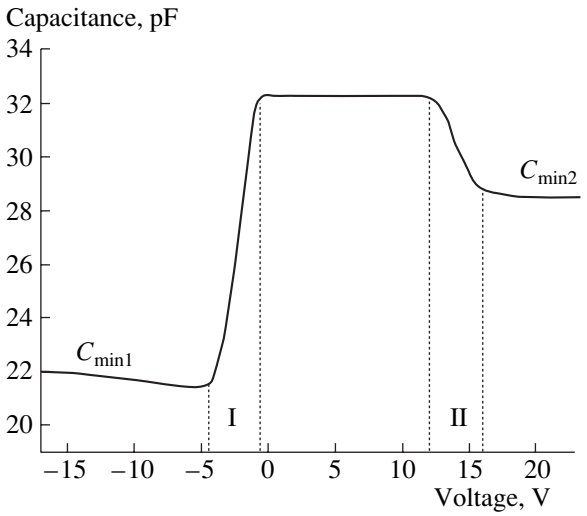

Fig. 2. A typical capacitance–voltage characteristic for an *n*-Si/SiO_2/*n*-Si silicon-on-insulator structure.

substrate, the voltage V applied to the structure may be expressed as [5]

$$V = -\Psi_{s1} + \Psi_{s2} + V_{ox} + W_{12}, \quad (1)$$

where V_{ox} is the voltage drop across the insulator; Ψ_{s1} and Ψ_{s2} are the surface potentials at the film/SiO_2 and substrate/SiO_2 interfaces, respectively; and W_{12} is the contact potential difference between the film and substrate. If the film is in the state of accumulation, the quantity Ψ_{s1} is small compared to Ψ_{s2} and may be ignored. $V_{ox} = Q/C_{ox}$, where C_{ox} is the oxide capacitance. The charge Q may be represented as

$$Q = Q_{s1} + Q_{t1} + Q_{f1} = -Q_{s2} - Q_{t2} - Q_{f2}, \quad (2)$$

where the subscripts "1" refer to the film, and the subscripts "2" correspond to the substrate; the other subscripts denote the following: "s" indicates the surface charge induced in the semiconductor, "f" corresponds to the fixed charge in the oxide, and "t" indicates the charge trapped by the interfacial centers. The data obtained from the *C–V* measurements were used in the calculations. As a result, we determined the dependence $\Psi_{s2}(V)$; the latter was used to determine the range of $\Psi_{s2}(V)$ that corresponds to the voltages $U2$ and $U2 + U1$ for each spectrum in Fig. 3. This made it possible to determine the energy range for the traps that should be recharged in the course of DLTS measurements. This method for processing the DLTS spectra was first developed for MIS structures [9, 10] and was then modified to be used for the SOI structures [5]. The obtained distribution of the density of states at the substrate/⟨thermal oxide⟩ interface is shown in Fig. 4.

The Q-DLTS spectra measured for the range II voltages, where the film and the film/oxide interface (the bonded interface) are tested, are shown in Fig. 5 for the structures SOI-I and SOI-II. The processing of the spectra shows that the peaks observed correspond to a relatively narrow range of energies in the silicon band gap (Fig. 6). The distribution of states for the more heavily doped SOI-IV structure is also shown in Fig. 6. Since we measured the spectra for the *n*-Si/SiO_2/*n*-Si structures, only the upper part of the silicon band gap was tested, i.e., from the conduction-band bottom down to $E_c - 0.74$ eV for the SOI-I and SOI-II structures and down to $E_c - 0.67$ eV for the SOI-IV structure. As was mentioned above, if *p*-Si was used for the split-off layer, then the silicon converted to the *n*-type conductivity in the course of forming the SOI structures, which made it difficult to produce structures suitable for studying the lower part of the band gap.

The "bulk" deep-level centers located in the split-off silicon layer are also observed in the SOI-I and SOI-II structures, in addition to the states related to the interface. The parameters of these deep levels are as follows: $E_c - 0.39$ eV and $\sigma = 10^{-15}$ cm^2 (the $E2$ level observed in SOI-I) and $E_c - 0.58$ eV and $\sigma = 4 \times 10^{-14}$ cm^2 (the $E3$ level observed in SOI-II). We inferred that the levels are related to centers located in the film by analyzing the spectra shown in Fig. 5 and the spectra measured for various widths of the time window. It was found that both centers are located in a layer that extends from the surface to a depth of 0.21 μm and have a concentration profile sloping down from the surface where the concentrations are 2×10^{15} and 5×10^{15} cm^{-3} for SOI-I and SOI-II, respectively. Deep-level centers were not observed in the split-off layer of the SOI-IV structure.

DISCUSSION

According to the data obtained, the distribution of states over the band gap is continuous at the substrate/⟨thermal oxide⟩ interface in the SOI structures; this distribution is similar to that observed for the states at the Si/⟨thermal SiO_2⟩ interface in conventional MIS structures (see, for example, [9, 10]). The main distinctive feature of DLTS spectra for this interface consists in the emergence of an additional peak $E1$. For the bonded Si/SiO_2 interface, the distribution of states is radically different, at least in the upper half of the band gap. However, this difference involves solely the energy range in which the levels are observed. If we superimpose the distributions shown in Figs. 4 and 6, we can see that the densities of states almost always coincide.

Such a narrow energy range in the distribution of states at the interface is not related to methodical limitations caused by relatively small thickness of the split-off silicon layer; in fact, the obtained distributions of states are virtually independent of the doping level in the film. Methodically, an increase in the doping level of the film (as in the SOI-IV structure) is equivalent to an increase in the film thickness.

The distinction between the bonded Si/SiO_2 interface and the thermally oxidized interface consists pri-

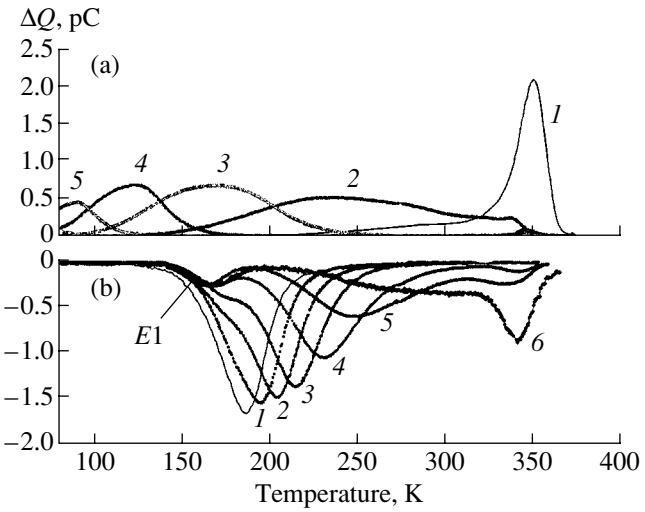

Fig. 3. The spectra of the levels obtained by charge-sensitive deep-level transient spectroscopy (Q-DLTS) for the (a) SOI-III and (b) SOI-II structures using range I bias voltages (see Fig. 2), in which case the substrate and the substrate/oxide interface are tested. The amplitude of the filling pulse $U1$ was equal to (a) –0.5 and (b) 0.5 V. The bias voltage $U2$ applied to the structure during measurements was equal to (a) (*1*) 2, (*2*) 1.5, (*3*) 1, (*4*) 0.5, and (*5*) 0 V and (b) (*1*) –1.5, (*2*) –2, (*3*) –2.5, (*4*) –3, (*5*) –3.5, and (*6*) –4 V.

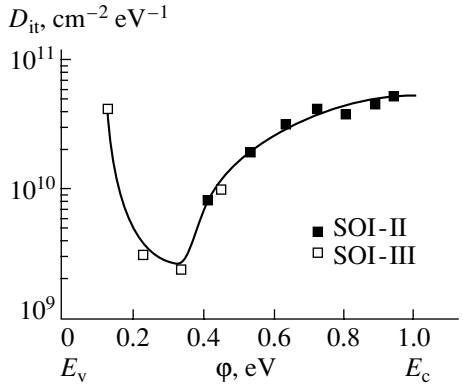

Fig. 4. The distribution of the density of states at the substrate/⟨thermal oxide⟩ interface for the SOI-II and SOI-IV structures.

marily in the different thickness of the SiO_x transition layer. In the structures under consideration, the thickness of the transition layer at the substrate/⟨buried SiO_2 layer⟩ is 3 nm, according to the ellipsometry data; in contrast, there is almost no transition layer (its thickness is 1–2 monolayers, i.e., ~0.5 nm) at the interface formed by bonding. The continuous spectrum of states at the conventional Si/SiO_2 boundary is typically related to the presence of a SiO_x layer (see, for example, [11]). Therefore, the narrowing of the energy range for the distribution of states at the Si/SiO_2 interface obtained by bonding may be chiefly caused by an anomalously thin transition layer.

Another factor that can affect the spectrum of states at the interface consists in the presence of hydrogen at the bonded interface. It is noteworthy that hydrogen has fairly high mobility in silicon and, in the course of fabricating the SOI structures, penetrates from the split-off layer both to the substrate/⟨thermal oxide⟩ interface and into the substrate [6]; as a result, hydrogen accumulates at this interface with almost the same concentration as that at the upper interface. Most probably, it is hydrogen that stimulates the formation of a complex with the energy level at E_c – 0.14 eV in the vicinity of the Si/⟨thermal SiO_2⟩ interface. Nevertheless, the conventional continuous distribution of traps in the band gap is observed at this interface. Therefore, it is likely that the narrow spectrum of states at the bonded Si/SiO_2 interface is not related to the introduction of hydrogen in the course of fabricating the SOI structures.

In addition, experiments demonstrate that, in contrast to the substrate, the centers with deep levels at E_c – 0.39 eV (in SOI-I) and E_c – 0.58 eV (in SOI-II) are observed in the film of a SOI structure. The quality of the contact between aluminum and silicon in some of the structures is important in studying the spatial distribution of deep-level centers in the split-off silicon layer. For the SOI-IV structure, the largest possible thickness of the space-charge region d_{max} is 0.20 μm; i.e., the film is partially depleted of charge carriers (the film being thicker than $2d_{max}$). The presence of a barrier at the Si/Al interface in no way affects the results obtained.

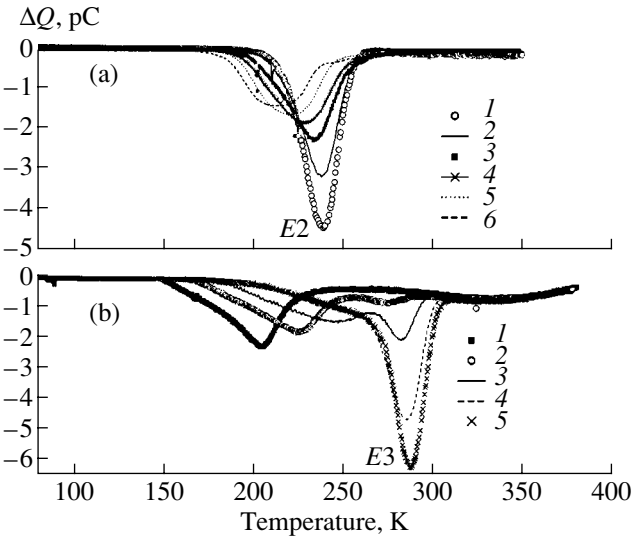

Fig. 5. The spectra obtained by charge-sensitive deep-level transient spectroscopy (Q-DLTS) and measured with range II bias voltages, in which case the film and the film/oxide interface (the bonded interface) are tested for the (a) SOI-I and (b) SOI-II structures. The parameters of the measurements were $U1$ = –2 V and τ = 1 ms. The bias voltages $U2$ applied to the structure in the course of measurements were equal to (a) (*1*) 15, (*2*) 13, (*3*) 11, (*4*) 9, (*5*) 7, and (*6*) 5 V; and (b) (*1*) 8, (*2*) 10, (*3*) 12, (*4*) 14, and (*5*) 16 V.

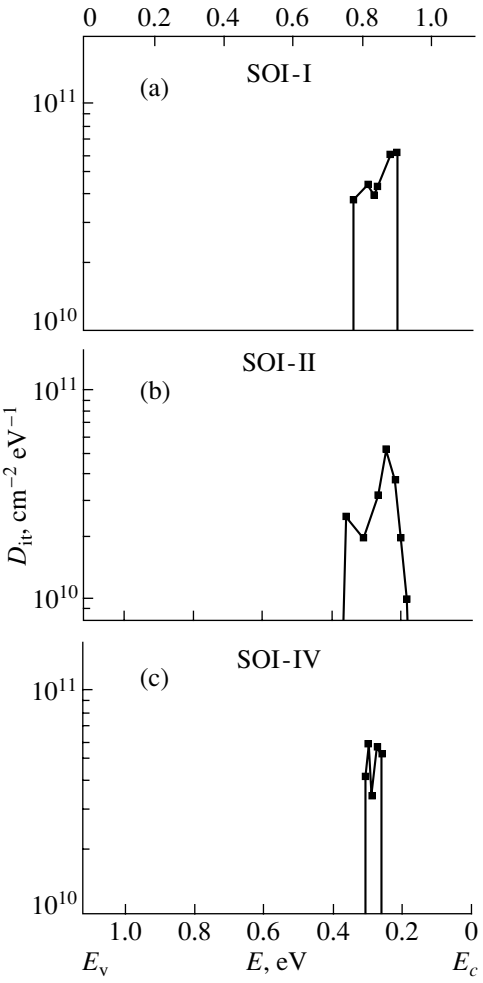

Fig. 6. The distribution of the density of states at the bonded Si/SiO_2 interface for the (a) SOI-I, (b) SOI-II, and (c) SOI-IV structures.

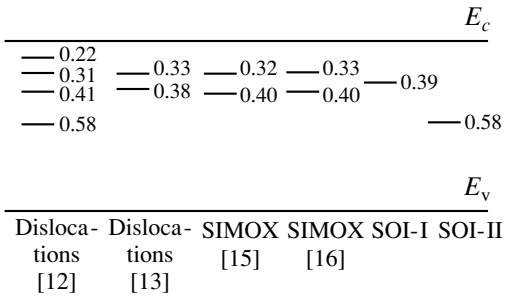

Fig. 7. The diagram of the known deep levels related to the extended defects of the dislocation type [12, 13]; the levels observed in the structures fabricated using the SIMOX technology [15, 16]; and the levels observed in this study.

For the SOI-III structure, the situation is similar owing to the high doping level of the silicon film. For the SOI-I and SOI-II structures, the value of d_{max} is equal or comparable to the thickness of the split-off layer. The presence of a contact barrier should primarily affect the thickness of the layer in which the centers $E2$ and $E3$ are observed; in fact, this layer may be somewhat thicker than 0.21–0.22 μm, which was calculated on the assumption that there is no barrier. At the same time, the above layer thickness cannot exceed 0.28 μm because the deep-level centers are no longer observed in the probed region of SOI-IV. Deposition of Al on *p*-Si typically gives rise to a barrier with a height of 0.6 eV, whereas no barrier is, as a rule, formed on the *n*-Si surface. The SOI-I and SOI-II structures are fabricated using just *n*-Si. It is then an easy matter to estimate that, for the specified charge-carrier concentrations in SOI-I and SOI-II, the barrier is not formed up to a temperature of 350 K; rather, the surface layer is somewhat enriched with charge carriers.

It is worth noting that the SOI structures studied here were not subjected to treatment consisting in thinning the split-off silicon layer by polishing or oxidation. This treatment is commonly used to remove the residual damage induced by hydrogen implantation and remained unannealed in the course of heat treatment. It is known [12, 13] that dislocations in silicon may introduce a number of deep levels into the band gap; these levels are located at $E_c - 0.22$ eV, $E_c - (0.31–0.33)$ eV, $E_c - (0.38–0.40)$ eV, and $E_c - 0.58$ eV (Fig. 7) [12, 13]. The complete set of levels is introduced by dislocations formed by plastic deformation [12], whereas the dislocation loops in ion-implanted material introduce fewer of the same or almost the same levels [14]. Thus, the centers with deep levels at $E_c - (0.32–0.33)$ eV and $E_c - (0.38–0.40)$ eV are observed in the SOI wafers obtained by the SIMOX technology [15, 16].

A comparison of the levels observed in the SOI film and reported in this paper with the levels introduced into silicon by extended defects (Fig. 7) shows that both types of levels have almost the same energy positions. In the SOI structures studied, most of the damage is located at the surface. The location of deep-level centers in a comparatively thin surface layer of the silicon film and the fact that the concentration profile of deep-level centers is a descending function of the distance from the surface provide, in our opinion, additional arguments in favor of the assumption that the levels observed in SOI-I and SOI-II are related to residual postimplantation defects. The absence of these levels in a SOI-IV structure with a more heavily doped top layer, in which case the tested region does not extend to the damaged surface layer, supports the inference that the silicon layer at a distance of ~0.3 μm from the buried oxide does not contain deep-level centers (electrically active impurities and defects).

CONCLUSION

It is shown that the Si/⟨thermal SiO_2⟩ interface in a silicon-on-insulator (SOI) structure obtained directly by the bonding of silicon wafers and by the delamination of one of the wafers using hydrogen implantation

is characterized by a continuous spectrum of states. The distinction between the spectrum of states of this interface in a SOI structure and that in a MIS structure consists in the emergence of an additional peak that corresponds to a level with an energy position of $E_c - 0.14$ eV and a cross section of $\sigma = 10^{-19}$ cm^2 and is most probably related to residual hydrogen present at the interface. The distribution of states in the upper half of the band gap for the bonded Si/SiO_2 interface is characterized by a relatively narrow band of states in the range from $E_c - 0.17$ eV to $E_c - 0.36$ eV. In addition, two types of centers are observed in the split-off silicon layer; one of these has a level at $E_c - 0.39$ eV and a cross section of $\sigma = 10^{-15}$ cm^2 (in the SOI-I structure) and the other has a level at $E_c - 0.58$ eV and cross section $\sigma = 4 \times 10^{-14}$ cm^2 (in the SOI-II structure). These centers are located in the surface layer with a thickness of up to 0.21 μm and are supposedly related to residual postimplantation defects.

ACKNOWLEDGMENTS

This study was supported by the Russian Foundation for Basic Research (project no. 01-02-16986) and was also supported in part by the International Center of Science and Technology (grant no. 563).

REFERENCES

1. M. Bruel, Electron. Lett. **31**, 1201 (1995).
2. Y. A. Li and R. W. Bower, Jpn. J. Appl. Phys. **39**, 275 (2000).
3. V. P. Popov, I. V. Antonova, V. F. Stas, L. V. Mironova, E. P. Neustroev, A. K. Gutakovskii, A. A. Franzusov, and G. N. Feofanov, in *Perspectives, Science and Technologies for Novel Silicon-on-Insulator Devices*, Ed. by P. L. F. Hemment *et al.* (Kluwer, Dordrecht, 2000), p. 47.
4. E. V. Astrova, V. A. Kozlov, A. A. Lebedev, and V. B. Voronkov, Solid State Phenom. **69/70**, 539 (1999).
5. S. Cristoloveanu and S. S. Li, *Electrical Characterization of Silicon-on-Insulator Materials and Devices* (Kluwer, Dordrecht, 1995).
6. I. V. Antonova, V. F. Stas', V. P. Popov, *et al.*, Fiz. Tekh. Poluprovodn. (St. Petersburg) **34**, 1095 (2000) [Semiconductors **34**, 1054 (2000)].
7. J. W. Farmer, C. D. Lamp, and J. M. Meese, Appl. Phys. Lett. **41**, 1063 (1982).
8. K. Nagai, T. Sekigawa, and Y. Hayashi, Solid-State Electron. **28**, 789 (1985).
9. T. Katsube, K. Kakimoto, and T. Ikoma, J. Appl. Phys. **52**, 3504 (1981).
10. K. Hofmann and M. Schulz, J. Electrochem. Soc. **132**, 2201 (1985).
11. A. A. Lebedev and W. Ecke, Fiz. Tekh. Poluprovodn. (Leningrad) **19**, 1087 (1985) [Sov. Phys. Semicond. **19**, 667 (1985)].
12. L. C. Kimerling, in *Point and Extended Defects in Semiconductors*, Ed. by G. Benedek, A. Cavallini, and W. Schroter (Plenum, New York, 1988); NATO ASI Ser., Ser. B **202** (1989).
13. N. A. Yarykin, E. B. Yakimov, S. V. Koveshnikov, and O. V. Feklisova, in *Papers Presented at Fifth International Conference on Properties and Structure of Dislocations in Semiconductors, Moscow, 1986*, p. 209.
14. I. V. Antonova, G. A. Kachurin, I. E. Tyschenko, and S. S. Shaĭmeev, Fiz. Tekh. Poluprovodn. (St. Petersburg) **30**, 2017 (1996) [Semiconductors **30**, 1051 (1996)].
15. H. S. Kang, C. G. Ahn, B. K. Kang, and Y. K. Kwon, J. Electrochem. Soc. **145**, 3581 (1998).
16. P. K. McLarty, J. W. Cole, K. F. Galloway, and D. E. Ioannou, Appl. Phys. Lett. **51**, 1078 (1987).

Translated by A. Spitsyn

Semiconductors, Vol. 35, No. 8, 2001, pp. 918–923. Translated from Fizika i Tekhnika Poluprovodnikov, Vol. 35, No. 8, 2001, pp. 954–959.

SEMICONDUCTOR STRUCTURES, INTERFACES, AND SURFACES

Simultaneous Doping of Silicon Layers with Erbium and Oxygen in the Course of Molecular-Beam Epitaxy

V. G. Shengurov[1], S. P. Svetlov[1,*], V. Yu. Chalkov[1], G. A. Maksimov[1], Z. F. Krasil'nik[2], B. A. Andreev[2], M. V. Stepikhova[2], D. V. Shengurov[2], L. Palmetshofer[3], and H. Ellmer[4]

[1] *Nizhni Novgorod Research Physicotechnical Institute, Nizhni Novgorod State University, pr. Gagarina 23/5, Nizhni Novgorod, 603600 Russia*

** e-mail: svetlov@phys.unn.runnet.ru*

[2] *Institute of Physics of Microstructures, Russian Academy of Sciences, Nizhni Novgorod, 603600 Russia*

[3] *Institute for Semiconductor and Solid State Physics, University of Linz, A-4040 Linz, Austria*

[4] *Institute of Experimental Physics, University of Linz, A-4040 Linz, Austria*

Submitted January 10, 2001; accepted for publication January 16, 2001

Abstract—Epitaxial silicon layers codoped with erbium and oxygen were grown by molecular-beam epitaxy using a silicon sublimation source. For growing the erbium-doped silicon layers, two types of impurity sources were used: (i) erbium-doped silicon plates were used as a source of fluxes of Er and Si atoms; and (ii) metallic erbium plates were used as an impurity-vapor source in combination with the silicon sublimation source. If gaseous oxygen was used for *in situ* codoping with erbium and oxygen, then concentrations ranging from 10^{18} to 10^{20} cm^{-3} were attained. When oxygen is in the growth chamber, the erbium-entrapment efficiency of a layer increases substantially, with the surface segregation of erbium also being suppressed by oxidation. © *2001 MAIK "Nauka/Interperiodica".*

1. INTRODUCTION

One of the topical problems of semiconductor optoelectronics involves designing light-emitting structures on silicon doped with rare-earth elements, in particular, with erbium [1]. In the luminescence spectrum of a center containing a triply charged erbium ion, a narrow temperature-independent line is observed at a wavelength of 1.54 μm corresponding to the lowest losses and dispersion in quartz fibers. This makes it possible to design optoelectronic devices on the basis of Si:Er and to use them in optical fiber links.

According to estimates [2], for designing light-emitting diodes on the basis of silicon–erbium structures, the concentration of this impurity must exceed 10^{18} cm^{-3}. In addition, the introduction of a large amount of erbium impurity must not cause the crystal structure of doped silicon to deteriorate.

Erbium can be introduced into the silicon matrix using various methods such as ion implantation [3], plasma enhanced chemical gas deposition [4], and molecular-beam epitaxy (MBE) [5–10].

If silicon is doped with erbium by ion implantation, high-energy (0.5–5 MeV) ions are used. This leads to the formation of defects, which are partially retained even after prolonged annealing. High doses of implanted ions and the subsequent annealing (up to 900°C) induce the formation of damaged layers with twins and lead to the precipitation of a rare-earth impurity and the formation of silicide precipitates [3, 11]. As a result of the interaction between erbium and silicon atoms, optically inactive silicide compounds of the $ErSi_2$ type are formed, which reduces the photoluminescence (PL) efficiency of these structures.

To improve the characteristics of erbium-doped silicon, it is necessary to suppress, as far as possible, the formation of precipitates and silicides. The key for overcoming this problem is to lower the temperature of the doping process and to dope the silicon with erbium and oxygen *in situ* without degrading the quality of the layers. Furthermore, codoping with oxygen is an important factor for the formation of optically active centers involving an erbium ion [1].

In MBE with coevaporation of erbium and silicon, it is possible to grow relatively thick layers eliminating the recrystallization stage compulsory for ion implantation. By increasing the erbium-source temperature from 800 to 1200°C, it was possible to obtain layers with an erbium concentration from 10^{18} to 10^{22} cm^{-3} [6]. However, the maximum PL intensity was observed in layers with an erbium concentration on the order of 10^{18} cm^{-3}. An examination of the structure of the silicon layers grown by transmission electron microscopy showed that an increase in the erbium concentration above 10^{18} cm^{-3} resulted in the formation of defects [6]. One of the reasons for this is likely to be the contamination of layers owing to thermal evaporation and gas

transport from growth-chamber assemblies (including the effusion cells) heated to a high temperature. It was probably for this reason that the background doping of epilayers in the MBE systems designed for growing erbium-doped silicon layers amounted to 8×10^{14} cm^{-3} [6].

On the other hand, the layers grown by sublimation MBE have a low background concentration of electrically active centers in silicon layers (lower than 2×10^{13} cm^{-3}) [12]. A special feature of this method distinguishing it from the traditional MBE of Si is the use of resistive heating when passing a current through the source in the form of rectangular bar cut from a Si single crystal. The use of other heated metallic components (except for the silicon-vapor source itself) in this method is virtually eliminated. To dope the layers, the silicon source doped with a given impurity is evaporated. This method was used for growing structurally perfect layers doped with a wide range of traditional impurities (B, Al, Ga, P, As, and Sb) up to high concentrations [13–15]. The purpose of this study is to investigate the possibilities of growing structurally perfect silicon epilayers doped with erbium to high concentrations (higher than 10^{18} cm^{-3}) and also of layers codoped with oxygen in the course of growth using sublimation MBE.

2. EXPERIMENTAL

The Si:Er epilayers were grown in the setup described in [16]. The ultrahigh-vacuum system for the sublimation MBE of silicon was designed and constructed at the Research Physicotechnical Institute, Nizhni Novgorod State University. The system involves a vacuum chamber with a pumping system designed following the so-called quasi-oil-free scheme: a residual-gas pressure of $\sim 5 \times 10^{-9}$ Torr was provided by an oil-free means of pumping (four GIN-0.5 titanium ion getter pumps), whereas preliminary pumping and pumping to degas the chamber and GINs were effected by an oil-vapor pump (N-5S) with a high-efficiency nitrogen trap and a backing pump (VN-2MG). The total pressure in the operation chamber was measured by a VI-14 ionization gage with an IM-27 transducer; the partial composition of residual gases was monitored by an APDM-1 unipolar mass spectrometer with an MMS-2 sensor. The gas-medium composition in the operation chamber can be set by the inlet system.

As silicon-vapor sources, we used a rectangular bar cut from a silicon single crystal with a high resistivity (KDB-15 brand; i.e., *p*-Si:B, $\rho = 15\ \Omega$ cm). The doping impurity (erbium) was evaporated either from an erbium-doped crystalline silicon or from a strip of pure metal erbium, both sources being heated resistively. We used silicon wafers cut in the (100) face as substrates. In some experiments, we used substrates covered by a thermal-oxide layer. The substrates were prepared by conventional technology including chemical and mechanical polishing and finish cleaning in toluene, hydrogen peroxide, and aqua ammonia. After placing the substrate in the growth chamber of the system and evacuating it to a pressure of $\sim 5 \times 10^{-9}$ Torr, the substrate was annealed together with the silicon- and erbium-vapor sources at maximum temperatures for 10 min.

After the substrate was annealed, its temperature was reduced to ~1000°C, then the shield was removed, and an undoped buffer layer was deposited to a thickness of ~0.1 μm. After reducing the substrate temperature to 450–700°C, the getter pumps were switched off, and the Si:Er layer was grown at a growth-chamber pressure below 2×10^{-8} Torr. In certain cases, we admitted oxygen into the growth chamber to a pressure of 3×10^{-8}–5×10^{-6} Torr in the course of depositing the erbium-doped layer. When using the substrate in the form of silicon wafers coated with thermally grown silicon oxide, we kept the substrate temperature below 750–850°C during annealing.

The crystal structure of the surface layers was studied using an ÉMR-102 electron diffractometer, and the surface relief of layers was examined by the replica technique using an electron microscope. The characteristics of defects in the bulk of layers were determined by Rutherford backscattering and by metallography using a preliminary treatment in the Schimmel etchant. The erbium concentration in the layers was determined by Rutherford backscattering, and the depth distribution of the concentration of erbium and other impurities (oxygen and carbon) within layers was investigated by secondary ion mass spectroscopy (SIMS). In the former method, the layers were irradiated with ^{4}He ions with an energy of 600 keV, and, in the latter, with oxygen or cesium ions with an energy of 1.3 keV.

3. EXPERIMENTAL RESULTS AND DISCUSSION

3.1. Growth of Layers from the Erbium-doped Silicon Source

When growing layers from the Si:Er source, the Er concentration was relatively low (~10^{17} cm^{-3}), which was associated with the limitation of its content in the source owing to the low solubility of this impurity.

In Fig. 1a, we show the erbium distribution over depth in the layer grown at a temperature of 450°C. It can be seen that the erbium-concentration distribution is nonmonotonic: as a layer begins to grow near the substrate, the concentration increases, then, decreases somewhat; after that, an increase and a decrease in the concentration again take place. Near the layer surface, its value is less than 10^{17} cm^{-3}. The erbium-concentration variation across the silicon layer observed in Fig. 1a is probably associated with the incorporation of erbium into the layer as it accumulates on the surface to a critical value after which the entrapment of impurity by deeper layers takes place. Such oscillations of doping-impurity concentration were previously observed

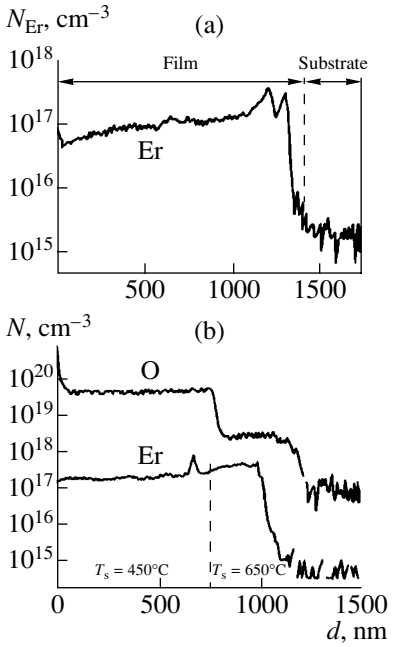

Fig. 1. Layer-by-layer SIMs analysis of the Si:Er epilayers grown at a substrate temperature T_s: (a) 450°C, without applying voltage; (b) 650 and 450°C, applying a constant voltage V = –200 V.

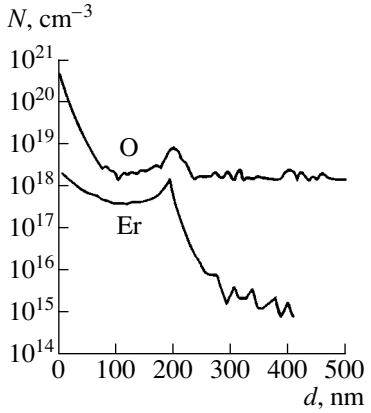

Fig. 2. Distribution of erbium and oxygen in the epilayer obtained by depositing silicon on a thermally oxidized substrate heated to 750°C (secondary-ion mass spectroscopy).

when rather large fluxes of other impurities were used (for example, Sb [17]).

In Fig. 1b, we display the SIMS data on erbium distribution over the thickness of a two-layer structure grown by applying a constant potential V = –200 V across the substrate. The first layer was grown at a substrate temperature equal to 650°C, and the second one, at 450°C. It can be seen from Fig. 1b that the erbium concentration in both cases is higher than in the previous experiment, while the increase in the oxygen concentration in the layer while varying the substrate temperature is steplike. At the instant the substrate temperature was lowered to 450°C, we observed an erbium-concentration peak in the profile; following that, the concentration was almost constant over the entire thickness of the layer.

The concentration profiles of erbium and oxygen over the thickness of the layers shown in Fig. 1b can be explained as follows. When the epilayer grows, erbium and oxygen, like the majority of other impurities, are forced back by the growth surface and are accumulated at this surface. The application of a negative constant potential to the substrate leads to the acceleration of Si^+ ions involved in the Si-atom flux towards the substrate surface. The Si^+ ions act on the erbium and oxygen adatoms enhancing their surface diffusion. This phenomenon leads to the entrapment of impurity atoms by the growing silicon layer. However, owing to the low density of the Si^+ ion flux during silicon sublimation (~10^{12} ion/(cm^2 s)), not all the impurity adatoms are subjected to the action of ions, and some of them are forced back by the growing layers. As a result, the doping efficiency of the layers remains insufficient.

3.2. Growing Layers from an Erbium-doped Silicon Source on Silicon Oxide Substrates

An increase in the oxygen and erbium concentrations in the silicon layers was also attained by the method of additional feeding with oxygen from an oxide deposited on the working side of the substrate. In Fig. 2, we display the profiles of erbium and oxygen concentrations in the epilayer, which was grown from an erbium-doped silicon source on a substrate coated with an oxide film ~0.1 μm thick and heated to 850°C. It can be seen that the erbium concentration in the layer is higher than in the previous cases (see Fig. 1a). Furthermore, its increase was observed both at the beginning of growth (i.e., near the layer–substrate interface) and near the layer surface. The erbium concentration varies synchronously with the oxygen concentration over the layer depth.

This distribution of impurities in the layer can be explained as follows. At an elevated temperature of the substrate, the effect of the silicon-atom flux on the oxide film leads to the decomposition of this film according to the reaction [18]

$$Si + SiO_2 \longrightarrow 2SiO(gas).$$

As a result, voids are formed in the oxide film. The remaining islands of oxide are covered by silicon and feed the growing silicon film with oxygen. At first, this additional feeding is intense, and then, owing to the oxygen being forced back by the growing layer towards the surface, it is reduced. Oxygen accumulates as it is forced back and is entrapped by the near-surface portion of the layer.

However, it should be noted that the layers grown by this method are characterized by a higher density of stacking faults and dislocations. The formation of an

oxide–substrate interface of a higher quality by, for example, oxidizing an atomically clean substrate surface *in situ* in the growth chamber, should be favorable to growing a higher quality silicon layer.

3.3. Growing Silicon Layers Doped from an Independent Erbium Sublimation Source

As a result of the investigations carried out, it was established that, using our metal erbium-vapor source heated resistively, it is possible to vary the erbium concentration in the layers from 5×10^{18} to $\sim 10^{21}$ cm^{-3} by varying the source temperature from 850 to 950°C. The layers grown had, as a rule, a fairly high structural quality: the minimum yield near the layer surface amounted to 3.3% according to Rutherford backscattering data. The layers with an erbium concentration of $\sim 10^{21}$ cm^{-3} were an exception: they had a mosaic structure. We note that almost the same level of erbium doping of the silicon layers was attained by traditional MBE at higher temperatures in the effusion cell [6].

The surface of layers with an erbium concentration $N_{Er} \leq 5 \times 10^{18}$ cm^{-3} was quite smooth according to investigations by the replica method in an electron microscope. However, in more heavily doped layers, a pronounced relief appears on the surface of these layers, which indicates that a fine-block structure of the layer surface with a high density of blocks is formed. The real structure of layers also varied with an increase in their doping level. For the erbium concentration $N_{Er} \geq 10^{19}$ cm^{-3}, two-dimensional defects were observed at the surface of the epilayer after brief etching in a selective etchant. These defects resembled stacking faults arising in oxidation. They had the shape of straight lines on the layer surface (Fig. 3). For the (100) substrate, the defects lie in the (111) plane, and their traces on the surface are arranged along the perpendicular ⟨110⟩ directions. Because the stacking faults in silicon are always interstitial [19], it is probable that they are produced owing to the formation of complexes of interstitials. We note that, in the silicon layers grown with the admission of oxygen into the growth chamber, these defects were not observed.

The SIMS data confirm the existence of the surface segregation of erbium in silicon layers grown without the admission of oxygen. In Fig. 4, we display the concentration profiles for the impurities (Er, O, and C) in silicon epilayers. It can be seen that, without erbium doping, the carbon concentration is virtually the same as in the substrate. The oxygen concentration in the region of the layer near the interface with the substrate is almost the same as in the substrate (except for a small peak at the interface), and it slowly increases only near the surface of the layer.

The growth of a silicon layer for the erbium-vapor source heated to 900°C is characterized by a different distribution of impurities over thickness (Fig. 4b). The carbon-concentration level remains almost the same as

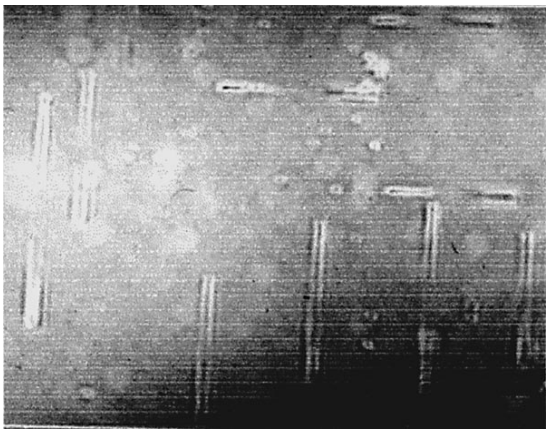

Fig. 3. Microphotography of the surface of Si:Er epilayer after etching in a selective etchant (magnification is ×500).

in the substrate. The oxygen concentration increases abruptly at the interface with the substrate and remains constant over the entire thickness of the layer. The erbium concentration increases in a steplike manner at the start of the layer growth and then decreases. This distribution of the erbium concentration is similar to its distribution shown in Fig. 1a, and, is also probably associated with the surface segregation of this impurity.

The admission of oxygen into the chamber up to a partial pressure of $\sim 5 \times 10^{-8}$ Torr during layer growth should lead to a more uniform distribution of the erbium concentration over layer thickness and to an abrupt increase in this concentration near the interface with the substrate (Fig. 4c). We note that the erbium concentration in the layer attains the same level ($\sim 10^{19}$ cm^{-3}) as in the previous case, although the impurity flux to the growth surface was lower (a source temperature of T_{Er} = 870°C). This means that the introduction of oxygen into the growth chamber is favorable to a more intense entrapment of erbium atoms by the growing layer. The introduction of a large amount of oxygen (to a partial pressure of $\sim 10^{-7}$ Torr) stimulates further increase in the erbium concentration in the layers. However, the structural quality of the layers markedly deteriorates in this case.

It should be noted that the admission of air into the growth chamber is also conducive to an increase in the erbium concentration in the layer. The profiles of distribution of erbium, oxygen, and carbon concentration over the depth (Fig. 4d) of the layer grown at a pressure of 5×10^{-6} Torr and at a source temperature of T_{Er} = 870°C support this statement. It can be seen that the erbium concentration is as high as $\sim 10^{20}$ cm^{-3} near the interface with the substrate. However, the defect density is high in such layers.

Thus, the admission of oxygen into the growth chamber leads to suppression of the Er segregation and to an increase in Er concentration in the layer. The suppression of erbium segregation by oxygen on Si(100)

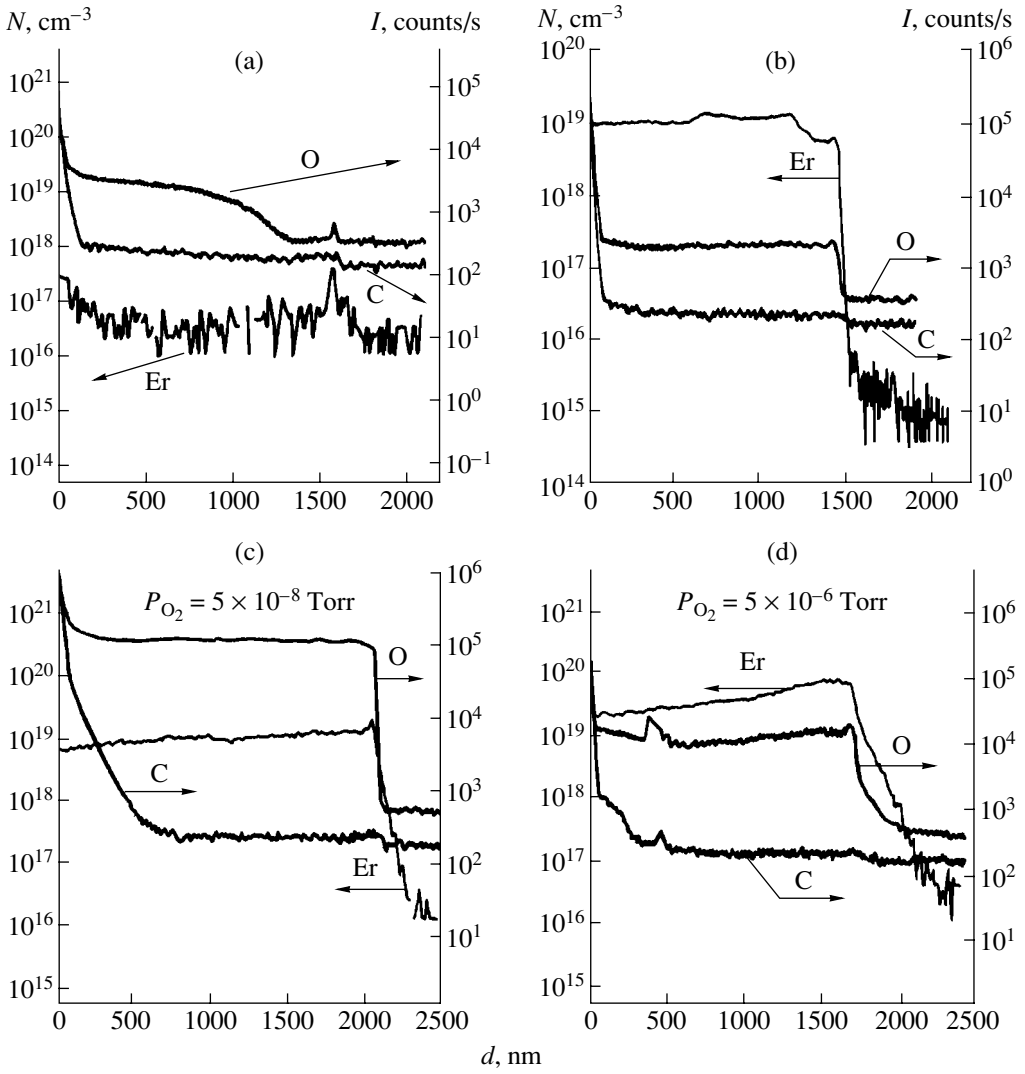

Fig. 4. Concentration profiles of Er, O, and C over depth in the Si:Er layer grown at an erbium-source temperature T_{Er} = (a) 0; (b) 900; (c) and (d) 870°C at an oxygen partial pressure of P_{O_2} = (c) 5×10^{-8} and (d) 5×10^{-6} Torr. The data were obtained by the secondary-ion mass spectroscopy.

has also been observed also in other studies devoted to growing MBE Si:Er layers [20]. In [20], the origin of this phenomenon was associated with the selective oxidation of erbium atoms. At the same time, in study [7], the more efficient incorporation of erbium into the silicon layers is associated with two causes: a possible modification of the mechanism of layer growth, for example, due to lowering the mobility of adatoms or a change in the energy barrier for shift of the steps on the layer surface, and also due to the formation of complexes when oxygen interacts with erbium, it being possible to incorporate the complexes into the growing layer.

The investigation of PL in erbium-doped and oxygen-doped silicon layers showed that the highest intensity was observed in the layers grown with the admission of oxygen into the chamber up to the lowest pressure (~3×10^{-8} Torr). When increasing the partial oxygen pressure, the PL intensity in the layers decreased [21].

4. CONCLUSION

It was shown that it is possible to dope silicon layers with erbium using sublimation MBE and to evaporate this impurity either from silicon or from an independent source by sublimation with resistive heating of a strip of this material. We considered three variants of oxygen codoping the Si:Er layers: (i) the bombardment of the growth surface with low-energy (~200 eV) Si^+ ions; (ii) additional feeding from oxide deposited on the working surface of the substrate; and (iii) the dosed admission of oxygen into the growth chamber.

The maximum erbium concentration in the silicon layers grown by evaporating from the source of erbium-doped silicon was below a value of $\sim 5 \times 10^{18}$ cm^{-3} even if a potential was applied across the substrate.

The silicon deposition on oxidized substrates heated up to 750–850°C leads to the growth of epilayers with an increased erbium concentration compared with the growth in an oxygen-free medium.

The use of an independent erbium-vapor source in the form of a resistive-heated strip from this metal for doping the silicon layers made it possible to increase the impurity concentration in the layers to 5×10^{18}–10^{21} cm^{-3} depending on the source temperature. However, even at low growth temperatures (450–650°C), erbium has a tendency toward surface segregation. Furthermore, its incorporation into the silicon crystal lattice is limited and is accompanied with the formation of extended stacking faults, whose origin is probably associated with the formation of interstitial complexes. If oxygen was let into the growth chamber during growth, then these defects were not revealed. In this case, the surface segregation of erbium is significantly suppressed, and its concentration in the layers also increases.

ACKNOWLEDGMENTS

We thank Yu.A. Karpov for putting at our disposal the erbium-doped silicon ingots from which the silicon- and erbium-vapor sources were prepared.

This study was supported in part by the Russian Foundation for Basic Research (project nos. 98-02-16619 and 99-03-32757), by the Interdisciplinary Scientific and Technical Program "Fundamental Spectroscopy" (project no. 08.02.043) and also by INTAS (project no. 99-1872) and INCAS project no. 00-2-01/ (MTsFPIN 2000 no. 00-2-01).

REFERENCES

1. N. A. Sobolev, Fiz. Tekh. Poluprovodn. (St. Petersburg) **29**, 1153 (1995) [Semiconductors **29**, 595 (1995)].
2. Y. Ho Xie, E. A. Fitzgerald, and Y. J. Mii, J. Appl. Phys. **70**, 3223 (1991).
3. A. Polman, J. Appl. Phys. **82**, 1 (1997).
4. Y. L. Rogers, P. S. Andry, W. J. Varhue, *et al.*, J. Appl. Phys. **78**, 6241 (1995).
5. H. Ennen, G. Pomrenke, A. Axmann, *et al.*, Appl. Phys. Lett. **46**, 381 (1985).
6. H. Efeoglu, J. H. Evans, T. E. Jackman, *et al.*, Semicond. Sci. Technol. **8**, 236 (1993).
7. R. Serna, M. Lohmeier, P. M. Zagviin, *et al.*, Appl. Phys. Lett. **66**, 1385 (1995).
8. K. Miyashita, Y. Shiraki, D. C. Houdhton, and S. Fukatsu, Appl. Phys. Lett. **67**, 235 (1995).
9. J. Stimmer, A. Reittinger, G. Abstreiter, *et al.*, Mater. Res. Soc. Symp. Proc. **422**, 15 (1995).
10. A. Yu. Andreev, B. A. Andreev, M. N. Drozdov, *et al.*, Fiz. Tekh. Poluprovodn. (St. Petersburg) **33** (2), 156 (1999) [Semiconductors **33**, 131 (1999)].
11. D. J. Eaglsham, J. Michel, E. A. Fizgerald, *et al.*, Appl. Phys. Lett. **58**, 2797 (1991).
12. V. V. Postnikov, M. I. Ovsyannikov, R. G. Loginova, *et al.*, Dokl. Akad. Nauk SSSR **175**, 817 (1967) [Sov. Phys. Dokl. **12**, 822 (1968)].
13. V. P. Kuznetsov, R. A. Rubtsova, A. Yu. Andreev, *et al.*, Kristallografiya **31**, 1180 (1986) [Sov. Phys. Crystallogr. **31**, 697 (1986)].
14. V. G. Shengurov, Poverkhnost **10–11**, 44 (1994).
15. V. N. Kuznetsov and V. V. Postnikov, Kristallografiya **19**, 346 (1974) [Sov. Phys. Crystallogr. **19**, 211 (1974)].
16. S. P. Svetlov, V. Yu. Chalkov, and V. G. Shengurov, Prib. Tekh. Éksp., No. 4, 141 (2000).
17. U. Koing, E. Kasper, and Y. J. Herzog, J. Cryst. Growth **52**, 151 (1981).
18. J. J. Lander and J. Morrison, J. Appl. Phys. **33**, 2098 (1962).
19. K. V. Ravi, *Imperfections and Impurities in Semiconducting Silicon* (Wiley, New York, 1981; Mir, Moscow, 1984).
20. M. Matsuoka and S. Tohno, J. Appl. Phys. **78**, 2751 (1995).
21. V. G. Shengurov, S. P. Svetlov, V. Yu. Chalkov, *et al.*, Izv. Akad. Nauk, Ser. Fiz. **64**, 353 (2000).

Translated by V. Bukhanov

Semiconductors, Vol. 35, No. 8, 2001, pp. 924–926. Translated from Fizika i Tekhnika Poluprovodnikov, Vol. 35, No. 8, 2001, pp. 960–963.

SEMICONDUCTOR STRUCTURES, INTERFACES, AND SURFACES

Pulsed Laser-Stimulated Surface Acoustic Waves in *p*-CdTe Crystals

A. Baidullaeva*, A. I. Vlasenko, É. I. Kuznetsov, A. V. Lomovtsev, P. E. Mozol', and A. B. Smirnov

Institute of Semiconductor Physics, National Academy of Sciences of Ukraine, Kiev, 03028 Ukraine

** e-mail: baidulla@class.semicond.kiev.ua*

Submitted December 13, 2000; accepted for publication January 22, 2001

Abstract—Changes in the electrical and photoelectrical properties, as well as in the dislocation structure, of crystalline *p*-CdTe under the pulsed laser irradiation were studied. A decrease in the dark current and an increase in the dislocation density in both irradiated and unirradiated parts of the crystal were observed. These changes are related to the effect of surface acoustic waves generated by the nanosecond laser pulses. © *2001 MAIK "Nauka/Interperiodica".*

INTRODUCTION

Variation of the physical properties of CdTe crystals irradiated with laser pulses of nanosecond duration [1–4] is typically attributed to intrinsic point and macroscopic defects resulted from an interaction of the laser radiation with the material. A change in the structure of defects can be due to the formation of an acoustic or shock waves and also to the electron subsystem excitation. The contribution of shock waves to the formation of defects under the laser irradiation of CdTe crystals has been previously considered [3, 4]. For a complete understanding of the mechanisms underlying the laser-induced formation of defects in semiconductors, including CdTe, a comprehensive study of the variety of processes stimulated by the laser irradiation of crystals is required.

In this paper, we report the results of studying the influence of the laser-induced surface waves on the dislocation structure and the electrical and photoelectric properties of CdTe crystals.

EXPERIMENTAL

We studied nominally undoped crystalline *p*-CdTe wafers produced by gaseous-phase synthesis of initial elements. The wafer thickness was 100 μm, and the dislocation density determined from the optical microscopy of etch pits was about 10^2 cm^{-2} [5].

The wafers were irradiated by a Q-switched ruby laser beam with a pulse width of 2×10^{-8} s and an energy density below the damage and melting threshold of the material. The laser radiation affected only half of the wafer surface area, while the other part was shielded with a metal plate or dark lacquer to prevent exposure to the radiation. Variation of the electrical properties in both parts of the wafers was studied. To do this, the contact positions on the wafer surface were adequately selected.

RESULTS

The dark currents (I_d) measured in the both parts of as-prepared wafers are nearly equal, thus indicating the electrical uniformity of wafers. After the irradiation with the ruby laser pulses with the energy density E = 0.08 J/cm^2, I_d in the irradiated part increases, while in the shielded area I_d remains practically the same. An increase in the energy density of up to E = 0.12 J/cm^2 results in a further growth of I_d in the irradiated area and initiates an increase in I_d in the shielded area of the wafer. We have attributed the increase in I_d observed in *p*-CdTe to a tellurium film formed on the crystal surface as a result of the laser irradiation [1]. To verify this conjecture, we rinsed off the tellurium film from the crystal surface with a normal solution of KOH in methanol and repeated the measurements. Irradiation of these samples with an energy density E = 0.08 J/cm^2 leads to a decrease in I_d in the exposed wafer area, whereas I_d remains nearly the same in its shielded area (Fig. 1, curves *1* and *2*, respectively). After the laser irradiation with the energy density E = 0.12 J/cm^2, both halves of the crystal show a decrease in I_d; this decrease continues for several hours after the irradiation.

Photoconductivity spectra of the shielded part of the *p*-CdTe crystal were also measured before and after irradiation. The first irradiation with the laser energy density E = 0.08 J/cm^2 causes the photosensitivity of this region to decrease. As the laser-energy fluence grows to E = 0.12 J/cm^2, photoconductivity continues to decrease. The decay of photoconductivity lasts for about one day and correlates with the relaxation time of

I_d. Along with this, the resisitivity of the wafer increases several times.

The equilibrium conductivity of the *p*-type CdTe crystal is known to drop with increasing dislocation density [6]. The observed decrease in the equilibrium conductivity of the shielded part of crystal can possibly be attributed to an increase in the dislocation density in this part as well. Therefore, we analyzed the laser-produced changes in dislocation structure in the both parts of the wafers. The dislocation density of as-prepared wafers was about 10^2 cm^{-2} (Fig. 2a). Irradiation with the energy density ranging from 0.08 to 0.16 J/cm^2 produced no noticeable damage to the crystal surface. However, selective etching revealed an increase in the dislocation density in both the irradiated and the shielded parts of the wafers. The higher the energy density or the irradiation dose, the higher the dislocation density. Thus, the irradiation with E = 0.08 J/cm^2 causes an increase in the dislocation density in the irradiated part only, whereas irradiation with an enhanced energy density (E = 0.12 J/cm^2) results in a further increase in dislocation density in the irradiated part and gives rise to dislocations in the shielded part of the wafer (Fig. 2b). We note that dislocations are predominantly accumulated at the interface between the irradiated and shielded parts of the crystal. A further growth of the dislocation density in the both parts occurs at the laser energy density of 0.16 J/cm^2 (Fig. 2c). Layer-by-layer etching indicates a decrease in the dislocation density and the recovery of its initial value at a depth of 3–5 μm. For the shielded part of the wafer, the initial value is regained at a depth of 1–3 μm.

DISCUSSION

Laser-induced changes in photoconductivity and I_d of the irradiated *p*-CdTe crystal have been attributed [1–3] to the laser-stimulated multiplication of dislocations and to draining the bulk acceptors into them. The underlying mechanism of the defect formation incorporates a number of laser-induced interrelated processes, such as the photoeffect, the formation of the elastic (acoustic and shock) waves in crystal, heating, and so on.

We now analyze the experimental results obtained for the shielded part of the wafers. In this part of crystal, the photoeffect is ruled out by the experimental conditions. The laser pulse–produced shock wave should propagate to the bulk of crystal along the normal to the surface; thus, its impact can also be excluded. Under the irradiation conditions employed, shock wave is generated deep enough under the surface to prevent its transformation into the surface shock wave. In CdTe, this depth amounts y = 39 μm at E = 0.16 J/cm^2. According to our experimental results, the typical depth of changes in the material is smaller than the depth where the shock wave is generated. The effective radius of heat conduction over the irradiated part of the wafer is estimated within ~0.35 μm, which is considerably less than the wafer length; thus, the heating also cannot

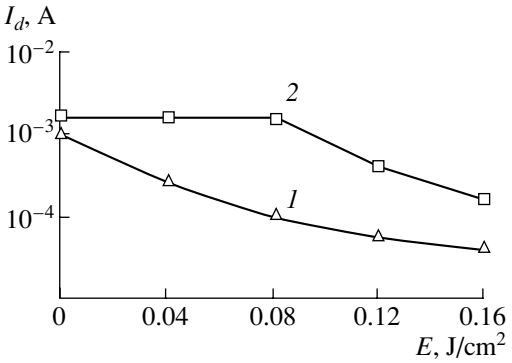

Fig. 1. Dark current I_d in (*1*) irradiated and (*2*) shielded parts of the *p*-CdTe crystal vs. the laser energy density.

be responsible for the dislocation formation in the shielded part of the crystal.

The origination of dislocations can possibly be related to the laser-induced mechanical stress, which gives rise to acoustic waves with highly diversified spectral and spatial characteristics [7, 8]. Acoustic waves can transport the absorbed laser energy over a distance that considerably exceeds the irradiation absorption depth. When transporting a sufficiently high energy density, an acoustic wave can become a carrier of the so-called long-range effect, typically stimulated by laser irradiation, thereby initiating the formation of defects in the crystal lattice outside the area exposed to laser radiation. The amplitude of the generated surface acoustic wave (SAW) is proportional to the surface stress and the pulse shape noticeably varies with distance away from the irradiated area [9]. To be specific, as the distance from irradiated increases zone, the pulse broadens and its leading edge splits into a series of pulses. These features of the SAW can be related to the manner in which the dislocation appears with the increasing laser energy density, as described in [9]. At a small energy density (and, therefore, at a low level of stress that causes an elastic wave), dislocations are observed in the irradiated region only. An increase in the energy density gives rise to dislocations first at the interface and then in the shielded part of the crystal as well (Figs. 2b, 2c).

The extinction of etch pits as a result of the layer-by-layer etching is indicative of a surface nature of the disturbance. The dislocations are observed in the vicinity of the front face of the crystal. This can result in the peeling of the surface layer.

The layer-by-layer etching of the irradiated crystal also showed that the depth up to which the crystals characteristics were affected is larger in the irradiated part of wafer than in its shielded part. This is probably due to the fact that, as the distance from the excitation source increases, the SAW propagation depth decreases as does the depth of its possible effect.

Two mechanisms for the dislocation appearance in the shielded part of the wafer are conceivable. One is

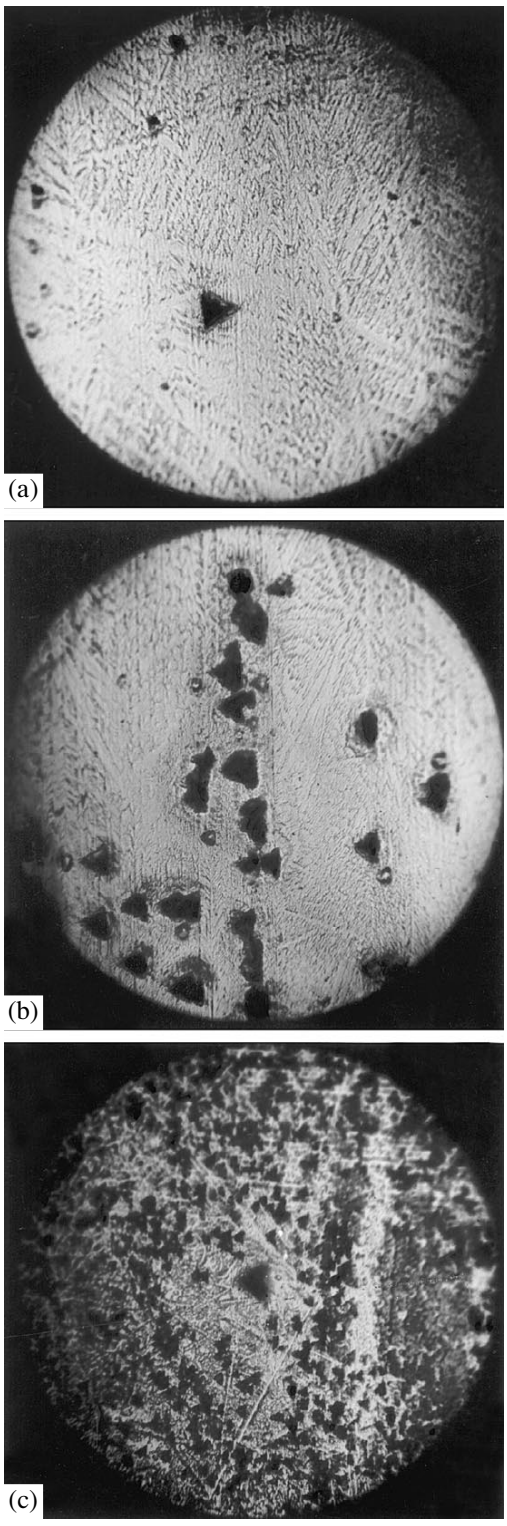

Fig. 2. Dislocation pattern in the both parts of *p*-CdTe wafer (a) before and (b, c) after the laser irradiation with E = (b) 0.12 and (c) 0.16 J/cm^2.

the direct origination of dislocations in the shielded part of crystal, and the other is the motion of dislocations from the irradiated area into the unirradiated part of the wafer; this motion is assisted by the acoustic-wave field.

CONCLUSION

Thus, we may assume that surface acoustic wave is generated as a result of the laser irradiation of CdTe crystal even though CdTe is less elastic than the conventional piezoelectrics, such as CdS or GaAs. Surface acoustic waves can change the electrical and photoelectric properties of the wafers, as well as its dislocation structure, beyond the irradiated area and thus can provide a basis for a nondestructive technique for introducing dislocations into the CdTe crystals. The controllable production of dislocation structures can be a key factor to enhancing reliability of the devices based on the II–VI semiconductor compounds.

Further experimental studies of the surface acoustic waves generated in *p*-CdTe by the ruby laser irradiation and analysis of the SAW pulse shape are required.

ACKNOWLEDGMENTS

We are grateful to B.M. Bulakh for providing us with the crystals for our experiments.

REFERENCES

1. A. Baidullaeva, A. I. Vlasenko, V. A. Gnatyuk, *et al.*, Fiz. Tekh. Poluprovodn. (St. Petersburg) **27**, 56 (1993) [Semiconductors **27**, 29 (1993)].
2. A. Baidullaeva, B. M. Bulakh, B. K. Dauletmuratov, *et al.*, Fiz. Tekh. Poluprovodn. (St. Petersburg) **26**, 801 (1992) [Sov. Phys. Semicond. **26**, 450 (1992)].
3. A. Baidullaeva, A. I. Vlasenko, Yu. V. Vlasenko, *et al.*, Fiz. Tekh. Poluprovodn. (St. Petersburg) **30**, 1438 (1996) [Semiconductors **30**, 756 (1996)].
4. A. Baidullaeva, A. I. Vlasenko, B. L. Gorkovenko, *et al.*, Fiz. Tekh. Poluprovodn. (St. Petersburg) **34**, 443 (2000) [Semiconductors **34**, 429 (2000)].
5. B. M. Bulakh and S. M. Krasikova, Izv. Akad. Nauk SSSR, Neorg. Mater. **9**, 1112 (1973).
6. B. R. Dzhumaev, G. Garyagdyev, I. Ya. Gorodetskiĭ, and N. E. Korsunskaya, in *Proceedings of the All-Union Conference on Photoelectric Phenomena in Semiconductors, Tashkent, 1989*, p. 126.
7. A. A. Karabutov, Usp. Fiz. Nauk **147**, 605 (1985) [Sov. Phys. Usp. **28**, 1042 (1985)].
8. C. K. N. Patel and A. C. Tam, Rev. Mod. Phys. **53**, 517 (1981).
9. D. Schneider, R. Hammer, and M. Jurish, Semicond. Sci. Technol. **14**, 93 (1999).

Translated by A. Sidorova-Biryukova

Semiconductors, Vol. 35, No. 8, 2001, pp. 927–931. Translated from Fizika i Tekhnika Poluprovodnikov, Vol. 35, No. 8, 2001, pp. 964–968.

SEMICONDUCTOR STRUCTURES, INTERFACES, AND SURFACES

Analysis of Inherent Potential Nonuniformities at the Extrinsic-Semiconductor Surface

V. B. Bondarenko*, M. V. Kuz'min, and V. V. Korablev***

** St. Petersburg State Technical University, ul. Politekhnicheskaya 29, St. Petersburg, 195251 Russia*

*** Ioffe Physicotechnical Institute, Russian Academy of Sciences, Politekhnicheskaya ul. 26, St. Petersburg, 194021 Russia*

Submitted October 30, 2000; accepted for publication January 25, 2001

Abstract—The concept of an inherent dimensional effect in depleted semiconductor layers (comparability of the characteristic scale of a depleted layer to an average distance between electrically active defects) is introduced. Inherent nonuniformities of an electric field and the potential at the semiconductor surface are determined for intrinsic and impurity surface states. The dependence of these nonuniformities on surface and bulk parameters is considered. © *2001 MAIK "Nauka/Interperiodica".*

The impact of charge discreteness near the solid surface on the surface electric field and potential distributions has been actively discussed [1–6]. Seemingly, the probability of significant field-strength differences in double electric layers was first reported in [1]. It is evident that this phenomenon affects the parameters of semiconductor devices, especially those of submicrometer size [3, 4]. Further analysis (see [5, 6]) has shown inevitable field nonuniformities to exist in depletion layers of semiconductor structures (even in the absence other causes). These nonuniformities are related to the inherent comparability of the depletion length (thickness of a double electric layer) to the average distance between charged impurity atoms. Thus, semiconductors surface layers are characterized by the inherent dimensional effect that controls the discrete structure of the space-charge region (SCR) in a wide doping-level range. Previous estimates and simulations have revealed a qualitative dependence of inherent field and surface potential nonuniformities on the system parameters. However, a quantitative dependence calls for a statistical analysis (similar to that of [7]) to determine the parameters of the chaotic potential in the semiconductor bulk in the approximation of a uniformly charged sphere. This study is aimed at generalizing the data of [5] and analytically determining the inherent nonuniformities of the surface electric field and potential. We emphasize that most of the relations derived below are not strict. Following [7], we use the sign of equality almost everywhere.

We begin the statistical analysis, considering a surface with delocalized inherent states ("conducting" surface). We choose a surface area with an arbitrary radius R and an adjacent SCR volume. The average number of impurity atoms residing in the formed cylinder can be calculated by multiplying the impurity concentration N_0 (for definiteness, we consider the impurity as completely and singly ionized donors) by the chosen volume $V = \pi R^2 L_0$, where $L_0 = \sqrt{\varepsilon U_0/2\pi e^2 N_0}$ is the SCR width, U_0 is the band bending near the surface, and ε is the dielectric constant of the semiconductor. It is evident that statistical parameters of this subsystem depend on its sizes, i.e., on R. Assuming that the electric field and potential within the cylinder are generally multiple to the fields of point charge and its image against the background of the total surrounding field, we determine the field nonuniformity at the semiconductor surface. In the case of delocalized surface inherent states, an element of the impurity–image system is a dipole [5].

At first, we determine the contribution of a test dipole to the total electric field at the surface area $S = \pi R^2$. To do this, we average the dipole field over probable dipole moments and over the surface. The field of the ith dipole in the surface plane contains only an axial component and, in the cylindrical frame of reference, is written as

$$\mathscr{E}_i = -\frac{ed_i}{\varepsilon(\rho^2 + d_i^2/4)^{3/2}}, \qquad (1)$$

where $\rho = \sqrt{x^2 + y^2}$ is the radial coordinate and ed_i is the dipole moment of the impurity–image system. Sequential averaging of Eq. (1) over the dipole moments and surface S yields the formula

$$\langle \mathscr{E}_i \rangle = -\frac{4e}{\varepsilon L_0 R^2}(R - \sqrt{R^2 + L_0^2} + L_0). \qquad (2)$$

An impurity distribution is uncorrelated in strongly diluted substitutional or interstitial solid solutions (i.e., in a doped semiconductor); hence, the Poisson distribu-

tion is valid for this case. As applied to the SCR, the impurity distribution density $p(N)$ is written as

$$p(N) = \frac{\langle N\rangle^N \exp(-\langle N\rangle)}{N!},$$

where N is the number of impurity atoms in the volume V. Since $N_0L_0 = N_s$ is the surface charge concentration, the average number of particles in the chosen volume or dipoles at the chosen surface area is given by

$$\langle N\rangle = N_s\pi R^2, \tag{3}$$

and the root-mean-square deviation is written as

$$\delta N = R\sqrt{\pi N_s}. \tag{4}$$

The contribution of charges inside V to the average field at the surface S is given by

$$\mathscr{E}(R) = \sum_i \langle \mathscr{E}_i\rangle, \tag{5}$$

where summation is performed over the impurity atoms whose number is defined by Eq. (3). We note that the contribution of the impurity–image dipole system of the surroundings to the surface field is, on average, a field of a flat capacitor with the plate charge density eN_s minus Eq. (5). Since the value independent (after averaging) of the summation index is under the summation sign in Eq. (5), this contribution is the product of Eqs. (2) and (3). Using Eq. (4), we can analogously write the field variance $\delta\mathscr{E}(R)$ at the chosen surface. As expected, in the limit $R \longrightarrow \infty$, the parameter $\mathscr{E}(R)$ tends to the field within a one-dimensional model

$$\lim_{R\to\infty} \mathscr{E}(R) = -\frac{4\pi eN_s}{\varepsilon}, \tag{6}$$

while $\delta\mathscr{E}(R)$ tends to zero, which is valid for the macroscopic system as a whole.

The Poisson distribution allows for the arbitrary smallness of the average number of particles in the volume V. Considering subsystems of various sizes, we arrive at a sequence of characteristic surface field nonuniformities. The choice of a specific variance most likely depends on the problem parameters and characteristic scales (e.g., electron wavelengths, charge-carrier free path, etc.). The field nonuniformity at a point should be calculated as the maximum possible in the R range from 0 to ∞. Hence, the $\delta\mathscr{E}(R)$ function maximum should be determined in the entire domain of the argument variation. Simple procedures for searching for an extremum yield $R = 0$. Uncertainties arising when calculating $\delta\mathscr{E}(R)$ are eliminated by passing to the limit $R \longrightarrow 0$. In this case, the electric field variance can be determined from the expression

$$\delta\mathscr{E} = \left|\lim_{R\to 0} \langle \mathscr{E}_i\rangle \delta N\right|, \tag{7}$$

where the notation $\delta\mathscr{E} = \delta\mathscr{E}(0)$ is introduced. An explicit form of $\delta\mathscr{E}$ follows from Eqs. (2) and (4). After substitution of these expressions into Eq. (7) and calculating the limit, we obtain

$$\delta\mathscr{E} = \frac{4e\sqrt{\pi N_s}}{\varepsilon L_0}. \tag{8}$$

Now we compare the found electric field variance to the field (6) of the surface bands' bending. To do this, it is sufficient to calculate the ratio of these values. As a result, we have

$$\delta_0 = \frac{1}{L_0\sqrt{\pi N_s}}, \tag{9}$$

where $\delta_0 = \delta\mathscr{E}/|\mathscr{E}_0|$, $\mathscr{E}_0 = \lim\limits_{R\to\infty} \mathscr{E}(R)$, and $(\pi N_s)^{-1/2}$ is the base radius of the test cylinder containing, on average, a single impurity atom.

Thus, the inherent dimensional effect in the semiconductor SCR can be estimated proceeding from Eq. (9). As a criterion for structure discreteness, the approximate equality $\delta_0 \sim 1$ can be chosen. In comparison with the ratio of the average distance between impurity atoms to the SCR length, the dependence on the impurity concentration is somewhat heavier in the found criterion. It is easily shown that the right-hand side in Eq. (9) increases as $N_0^{1/4}$ as the doping level grows. A corresponding change of N_0 by two orders of magnitude leads to approximately a threefold change in δ_0.

To calculate the potential nonuniformity at a conducting surface, we use the rule of error transfer (see, e.g., [8]). According to the potential form derived in [5] within the approximation of an unchanged density of states at the semiconductor surface with the Fermi level pinned at the surface band bottom, we have

$$U(x, y) = U_0 + kT \times \ln\frac{1 - \exp\{[\sigma(x, y) - eD\Delta E]/eDkT\}}{\exp[\sigma(x, y)/eDkT] - 1} - E_F^{(0)}, \tag{10}$$

where

$$E_F^{(0)} = kT\ln\frac{1 - \exp[(\sigma_0 - eD\Delta E)/eDkT]}{\exp(\sigma_0/eDkT) - 1}$$

is the Fermi level position with respect to the surface band bottom in the one-dimensional model of band bending, $\sigma_0 = eN_s$ is the average surface charge density, D is the density of electron states, and ΔE is the energy width of the surface band. The second term of sum (10) accounts for the functional dependence on the electric field. We separate the principal part of this term. Since the density of surface intrinsic states is as a rule high (above 10^{12} cm^{-2} eV^{-1}) and the surface band size is assumed to be greater compared to kT, the surface charge densities σ and σ_0 are much less than $eD\Delta E$. Hence, the exponential function in the denominator of

the term under logarithm can be neglected compared to unity. Equation (10) can be then rewritten as

$$U(x, y) = U_0 + kT\ln\frac{\exp(\sigma_0/eDkT) - 1}{\exp[\sigma(x, y)/eDkT] - 1}. \quad (11)$$

This expression defines the dependence of U on the random field $\mathscr{E} = -4\pi\sigma/\varepsilon$ and satisfies the condition for applicability of the rule of error transfer. In this case, the parameter δU characterizing the potential nonuniformities can be estimated as

$$\delta U \approx \left|\frac{\partial U}{\partial \mathscr{E}}(\mathscr{E}_0)\right|\delta\mathscr{E}. \quad (12)$$

The derivative of potential (11) with respect to the field at the point $\mathscr{E} = \mathscr{E}_0$ is given by

$$\frac{\partial U}{\partial \mathscr{E}}(\mathscr{E}_0) = -\frac{\varepsilon}{4\pi eD}\frac{1}{1 - \exp(-N_s/DkT)}.$$

Thus, for inherent potential nonuniformities on the conducting semiconductor surface with the Fermi level pinned at the band bottom, we obtain

$$\delta U \approx \frac{1}{DL_0}\sqrt{\frac{N_s}{\pi}}\frac{1}{1 - \exp(-N_s/DkT)}. \quad (13)$$

In the limit, when $N_s/DkT \ll 1$ under the exponent (in particular, this limit is valid at a high density of surface states and at room temperature), the potential variance taking into account Eq. (9) has the specifically clear form

$$\delta U \approx \delta_0 kT. \quad (14)$$

The quantity δ_0, defining intrinsic dimensional ratios, is on the order of unity in a wide doping-level range; however, it does not exceed unity. As a result, the surface potential nonuniformity on the average does not exceed kT at room temperature if we have intrinsic extended states with a Fermi level pinned at the surface band bottom.

If the Fermi level is pinned at midband at the surface, the potential nonuniformity can be defined in the form known as the Thomas–Fermi approximation. The charge density fluctuations should follow variations of the Fermi level position with respect to the surface band bottom, which are equivalent to the potential nonuniformity

$$\delta\sigma = eD\delta U. \quad (15)$$

It goes without saying that the potential perturbation is assumed to be small compared to the Fermi energy and that the change in the density of surface states is ignored.

Now taking into account the linear dependence of the surface charge on field, as well as Eqs. (8), (9), and (15), we can relate the quantity δU to the system parameters as

$$\delta U = \frac{N_s}{D}\delta_0. \quad (16)$$

To within the insignificant factor $\sqrt{\pi}$ on the order of unity, this result coincides with Eq. (13) when the condition $N_s/DkT \gg 1$ is met.

Expression (8) for nonuniformity of an electric field allows for the immediate determination of the inherent nonuniformity of the Schottky barrier height. As is known, the effective barrier height in the metal–semiconductor contact is related to the electric field at the interface as

$$U_{\text{eff}}(\mathscr{E}) = U_0 - \sqrt{\frac{-e^3\mathscr{E}}{\varepsilon}}. \quad (17)$$

Taking into account that the near-contact field is a random quantity with a characteristic nonuniformity amplitude $\delta\mathscr{E}$, the nonuniformity of the Schottky barrier height, similar to Eq. (12), can be written as

$$\delta U_{\text{eff}} \approx \left|\frac{\partial U_{\text{eff}}}{\partial \mathscr{E}}(\mathscr{E}_0)\right|\delta\mathscr{E}. \quad (18)$$

After simple transformations using expressions (17) and (18), we obtain

$$\delta U_{\text{eff}} \approx \frac{e^2}{\varepsilon L_0}. \quad (19)$$

Thus, the value of δU_{eff} is approximately equal to the Coulomb energy in a dielectric medium with the permittivity ε of a single-charged center at the distance L_0 from it.

The above method for calculating the nonuniformity is applicable to a "dielectric" surface with filled (localized) intrinsic and impurity states. In these cases, the surface potential nonuniformity can be determined immediately, since the method of electrostatic images yields an analytical form of the point charge potential near the surface.

The potential regularity with an unchanged and uniform surface charge can be violated due to the discrete charge of an impurity located in the SCR. According to [9], the potential of a single charged donor near the surface is given by

$$U_i = -\frac{2e^2}{(\varepsilon + 1)\sqrt{\rho^2 + z_0^2}}, \quad (20)$$

where z_0 is the impurity-charge depth. The value of z_0 varies from 0 to L_0. Averaging of Eq. (20) over possible z_0 and over a surface area of any radius R yields the

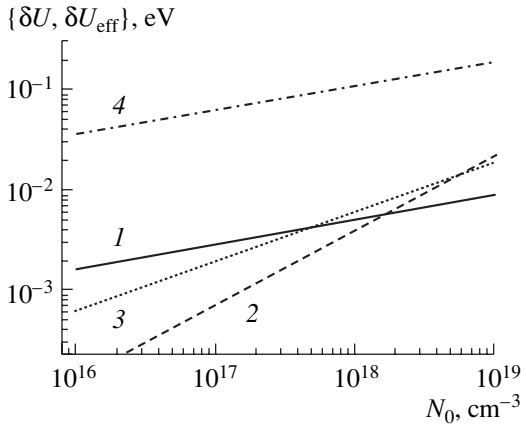

Fig. 1. Dependences of the inherent potential nonuniformity δU at the semiconductor surface ($U_0 = 0.3$ eV, $\varepsilon = 12$, $D = 10^{14}$ cm^{-2} eV^{-1}, and $T = 300$ K) and the Schottky barrier height δU_{eff} on the impurity concentration N_0, calculated by formulas (14), (16), (19), and (23) (lines *1–4*, respectively).

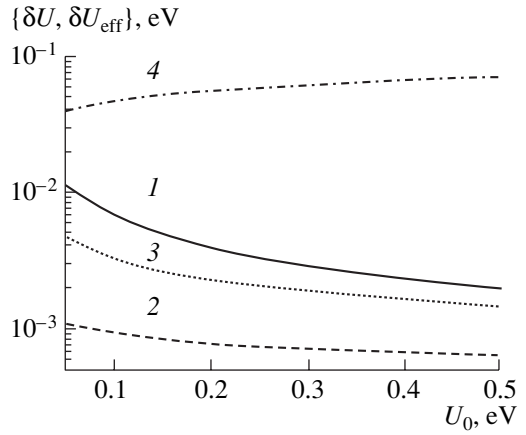

Fig. 2. Dependences of the inherent potential nonuniformity δU at the semiconductor surface ($N_0 = 10^{17}$ cm^{-3}, $\varepsilon = 12$, $D = 10^{14}$ cm^{-2} eV^{-1}, and $T = 300$ K) and the Schottky barrier height δU_{eff} on the surface potential U_0, calculated by formulas (14), (16), (19), and (23) (lines *1–4*, respectively).

average contribution $\langle U_i \rangle$ of a singe charge to the total potential. Successive integration yields

$$\langle U_i \rangle = -\frac{2e^2}{(\varepsilon + 1)L_0 R^2}$$

$$\times \left(L_0 \sqrt{R^2 + L_0^2} + R^2 \ln \frac{L_0 + \sqrt{R^2 + L_0^2}}{R} - L_0^2 \right).$$

Introducing a new variable $\xi = L_0/R$ and the function $f(\xi)$ of the form

$$f(\xi) = \xi \sqrt{\xi^2 + 1} + \ln(\xi + \sqrt{\xi^2 + 1}) - \xi^2,$$

we write the averaged potential as

$$\langle U_i \rangle = -\frac{2e^2}{(\varepsilon + 1)L_0} f(\xi). \tag{21}$$

The total contribution $\delta U(R)$ of excess charges (whose number is defined by Eq. (4)) to the potential is the product of Eqs. (21) and (4). Taking into account the adopted notation, $\delta U(R)$ is written as

$$\delta U(\xi) = \frac{2e^2 \sqrt{\pi N_s}}{\varepsilon + 1} \frac{f(\xi)}{\xi}. \tag{22}$$

The functional dependence $f(\xi)/\xi$ in Eq. (22) is monotonic and reaches its exact supremum at $\xi \longrightarrow 0$ (i.e., at $R \longrightarrow \infty$). The limit for the surface potential variance $\delta U = \lim\limits_{\xi \to 0} \delta U(\xi)$ is given by

$$\delta U = \frac{4e^2 \sqrt{\pi N_s}}{\varepsilon + 1}. \tag{23}$$

Result (23) defines the average potential nonuniformity at the surface in the case of localized intrinsic states and can be used to determine the second moment of the potential distribution over a surface with impurity discrete states. The contribution of the potential related to a subsystem of discrete charges at the surface, found by the above method, coincides with Eq. (23). If the semiconductor surface and SCR charges are distributed independently, the potential variance is given by

$$\delta U = \frac{4e^2 \sqrt{2\pi N_s}}{\varepsilon + 1}. \tag{24}$$

We note that expression (24) is consistent with the results of a numerical experiment. In particular, calculation for the system (considered in [5]) with the parameters $N_0 = 10^{17}$ cm^{-3}, $U_0 = 0.3$ eV, and $\varepsilon = 12$ by formula (24) yields $\delta U = 90$ meV.

First, we analyze the obtained results to clarify the dependences of δU and δU_{eff} [described by formulas (14), (16), (19), and (23) (or (24))] on the impurity concentration.

As is known, the doping level is the most important parameter of a semiconductor system from the practical standpoint. Hence, one should take into account possible changes in surface properties, in particular, changes in the surface potential nonuniformities when a doping level is varied. As is evident from Eqs. (14) and (23), the potential variance at conducting and insulating surfaces as N_0 increases grows according to the same law $\propto N_0^{1/4}$. The root law makes significant (specifically, in the case of impurity surface states) surface potential nonuniformities in a wide range of doping levels. When the Fermi level is pinned at the surface band center (see Eq. (16)), the dependence of the surface potential is stronger: $\delta U(N_0) \sim N_0^{3/4}$. At surface state densities about 10^{14} cm^{-2} eV^{-1}, δU reaches dozens of millielec-

tronvolts at high doping levels (above 10^{18} cm^{-3}). The growth of nonuniformities in the Schottky barrier height (see Eq. (19)) with the concentration N_0 is proportional to a square root of N_0: $\delta U_{\text{eff}}(N_0) \sim N_0^{1/2}$. The dependences of inherent potential nonuniformities at the semiconductor surface and those of the Schottky barrier height on the impurity concentration are shown in Fig. 1.

The SCR length L_0 depends on the band bending U_0 as one of the possible boundary conditions for the boundary-value problem when solving the Poisson equation. A growth of the depleted layer width predetermines an increase in the number of discrete charges in the characteristic volume L_0^3. Correspondingly, an increase in U_0 leads to statistically better averaging of the discrete distribution of impurity in the surface region, which in fact should reduce nonuniformities. Such formal reasons allow us to neglect the structure discreteness in many cases at large band bendings. We note also that, although the total relative potential nonuniformity decreases, absolute potential fluctuations qualitatively differ depending on the type surface states (see Fig. 2).

In the case of extended intrinsic states (conducting surface) δU decreases with various rates (proportional to $\sim U_0^{-3/4}$ and $\sim U_0^{-1/4}$ according to Eqs. (14) and (16), respectively) as the band bending increases, whereas the potential nonuniformity slowly grows (proportional to $\sim U_0^{-1/4}$) at the insulator surface.

REFERENCES

1. I. S. Zhuguleva and V. P. Smilga, in *Proceedings of the V Conference on Surface Forces* (Nauka, Moscow, 1974), p. 220.
2. S. G. Dmitriev and Sh. M. Kogan, Fiz. Tverd. Tela (Leningrad) **21** (1), 29 (1979) [Sov. Phys. Solid State **21**, 17 (1979)].
3. D. Arnold and K. Hess, J. Appl. Phys. **61** (11), 5178 (1987).
4. J. H. Davies and J. A. Nixon, Phys. Rev. B **39** (5), 3423 (1989).
5. V. B. Bondarenko, Yu. A. Kudinov, S. G. Ershov, and V. V. Korablev, Fiz. Tekh. Poluprovodn. (St. Petersburg) **30** (11), 2068 (1996) [Semiconductors **30**, 1078 (1996)].
6. V. B. Bondarenko, Yu. A. Kudinov, S. G. Ershov, and V. V. Korablev, Fiz. Tekh. Poluprovodn. (St. Petersburg) **32** (5), 554 (1998) [Semiconductors **32**, 495 (1998)].
7. B. I. Shklovskiĭ and A. L. Efros, *Electronic Properties of Doped Semiconductors* (Nauka, Moscow, 1979; Springer-Verlag, New York, 1984).
8. D. Hudson, *Statistics. Lectures on Elementary Statistics and Probability* (Geneva, 1964; Mir, Moscow, 1967), CERN Report.
9. L. D. Landau and E. M. Lifshitz, *Course of Theoretical Physics*, Vol. 8: *Electrodynamics of Continuous Media* (Nauka, Moscow, 1982; Pergamon, New York, 1984).

Translated by A. Kazantsev

Semiconductors, Vol. 35, No. 8, 2001, pp. 932–940. Translated from Fizika i Tekhnika Poluprovodnikov, Vol. 35, No. 8, 2001, pp. 969–978.

LOW-DIMENSIONAL SYSTEMS

Anisotropy of the Spatial Distribution of In(Ga)As Quantum Dots in In(Ga)As–GaAs Multilayer Heterostructures Studied by X-ray and Synchrotron Diffraction and Transmission Electron Microscopy

N. N. Faleev[1,*], Yu. G. Musikhin[2], A. A. Suvorova[2], A. Yu. Egorov[2], A. E. Zhukov[2], A. R. Kovsh[2], V. M. Ustinov[2], M. Tabuchi[3], and Y. Takeda[3]

[1] *Electrical Engineering Department, Texas Technical University, Lubbock, Texas, 79409, USA*
[2] *Ioffe Physicotechnical Institute, Russian Academy of Sciences, St. Petersburg, 194021 Russia*
[3] *Department of Materials Science and Engineering, Nagoya University, 464-8603, Nagoya, Japan*
** e-mail: nfaleev@ttacs.ttu.edu*

Submitted December 19, 2000; accepted for publication December 20, 2000

Abstract—High-resolution X-ray and synchrotron (crystal truncation rods) diffraction methods and transmission electron microscopy have been employed to study MBE-grown multilayer In(Ga)As–GaAs heterostructures with arrays of vertically coupled In(Ga)As quantum dots (QDs) in a GaAs matrix. Additional (vertical and lateral) spatial ordering of QDs in perfect crystalline structures, giving rise to undulations of the crystalline planes and quasi-periodic elastic strain, was shown to be essentially anisotropic with respect to crystallographic directions of the [110] type. The anisotropy of the QD formational system of can be accounted for by assuming that the spatial ordering of the QDs and the corrugation of the crystal planes are the initial stages of relaxation of the elastic strain introduced into the system by the QDs. The anisotropic relief of the crystal planes (corrugated growth surface) results from the formation of a system of spatially ordered quantum quasi-wires uniformly filled with QDs. In a multilayer heterostructure with high crystal perfection, the anisotropic relief of the crystal planes is inherited by overlying layers and its amplitude decreases gradually with increasing distance from the source of elastic strain—the superstructure containing In(Ga)As QDs in the given case. *© 2001 MAIK "Nauka/Interperiodica".*

1. INTRODUCTION

Heterostructures with quantum dots (QDs) have become the focus of various studies [1–7] because their specific electrical and optical properties offer wide prospects for the fabrication of new devices, e.g., laser diodes with unique electrical parameters [7, 8]. At the same time, QDs are novel and poorly studied structural objects. It is, therefore, of much interest to carry out investigations to understand the epitaxial growth mechanism and the processes of QD formation and to study the mechanisms of elastic strain relaxation and the generation of structural defects. Of particular interest are high-resolution X-ray and synchrotron diffraction analyses and transmission electron microscopy (TEM) studies of QDs [9–18]. These diffraction methods are complementary, as regards studying ordered nanoscale objects and, in particular, their spatial ordering, since the capabilities of TEM are limited to the volume under study [18], whereas the spatial resolution of X-ray methods is insufficient for a detailed study of objects of this size.

Previous investigations of multilayer periodical structures with InAs QDs using crystal truncation rods (CTR) and high-resolution X-ray diffraction analysis [13–16] revealed an additional long-range lateral QD ordering, giving rise to undulation of the crystal planes in the QD layers and the corresponding quasi-periodic distribution of elastic strain. It has been shown that the undulation of the planes and the degree of the QD lateral ordering intensify with an increasing total number of InAs–GaAs layer pairs in the periodic part of the structure, and that the parameter characterizing the periodicity of the lateral QD ordering corresponds to the average distance between these layers.

It is known that the formation of an array of three-dimensional (3D) quantum dots on the growing surface strongly affects the process of epitaxial growth, markedly changing the distribution of elastic strain as compared with that in planar layers. In periodic structures with QDs, this leads to additional vertical [2, 7, 17, 19] and lateral [13–16, 19] ordering of QDs and noticeable undulation of crystal planes [16]. It may be assumed that the spatial ordering of QDs and the undulation of

the crystal planes are different stages of the relaxation of elastic strains introduced into the structure by the QDs. At the beginning of this process, which may be named the adaptation stage, relaxation occurs via optimization of the spatial arrangement of QDs [20, 21], and only after that do we have plastic relaxation of elastic strain, accompanied by the formation of structural defects [22, 23]. Similar behavior is observed in planar heterostructures, where the process of relaxation of elastic strains also passes through several stages, starting with the disruption of the growth surface planarity [24, 25].

If the spatial ordering of QDs does occur via the relaxation mechanism [19–21], then the observed structural transformations must be anisotropic with respect to the crystal axes [110] and $[1\bar{1}0]$, as in planar heterostructures [25, 26]. In this case, the anisotropy of the spatial ordering of scattering centers should affect the diffraction conditions for X-ray and synchrotron radiation and be manifested in the TEM images. Therefore, investigations of the mechanisms of elastic strain relaxation and spatial ordering of scattering objects of the QD type and studies of specific features of their X-ray diffraction mapping are of considerable interest, revealing the relationship between the structure of the scattering objects and their maps.

2. EXPERIMENTAL METHODS

The samples to be studied were grown on precisely oriented (001) n^+ GaAs substrates in a Riber-32P MBE machine with a solid source of arsenic. To diminish the segregation and reevaporation of In, the substrate temperature was lowered to 480°C while growing the multilayer structures with QDs and depositing a 10-nm-thick GaAs layer over the QD array. For the rest of the structure, the growth temperature was 620°C for sample no. 1 and 600°C for sample no. 2.

In structure no. 1, the array of vertically coupled QDs was formed on a ~1.1- to 1.2-μm-thick GaAs buffer layer by depositing ten InAs QD layers separated by ~5.0-nm-thick GaAs layers. On top, the periodic InAs–GaAs structure was overgrown with a ~0.45-μm-thick GaAs layer. In structure no. 2, the array of vertically coupled QDs was formed on a ~0.5-μm-thick GaAs buffer layer, a short-period (with a period of ~4.0 nm) AlAs–GaAs superlattice (10 pairs of layers), and a 100-nm-thick GaAs layer by depositing 15 $In_{0.5}Ga_{0.5}As$ QD layers separated by ~4.0- to 4.5-nm-thick GaAs layers. On top, the periodic InGaAs–GaAs structure was overgrown with a 40-nm-thick GaAs layer, an AlAs–GaAs superlattice similar to that in structure no. 1, and a 10-nm-thick GaAs layer. The effective thickness of the InAs layers in both structures was ~0.55–0.60 nm. The total thickness of InGaAs–GaAs superlattices was ~55.0 and ~80.0 nm for structures with 10 and 15 pairs of InAs and InGaAs QD layers, respectively. These structures were selected for further study, because the vertical and lateral ordering of QDs and the corresponding undulation of crystallographic planes (the quasi-periodic distribution of elastic strain) are clearly manifested at this thickness [13, 16]. Moreover, the density of extended defects and the amount of structural distortions introduced by these defects is insignificant in this case.

In the present study, crystal truncation rods (CTR) and transmission electron microscopy (TEM) provided the principal results. The CTR measurements were carried out using a double-crystal diffractometer of a BL6A station at the photon factory in Tsukuba, Japan, using synchrotron radiation (SR) from an accumulation ring with a positron energy of 2.5 GeV (ring current 380–250 mA). The SR was monochromatized and collimated with a curved quartz mirror and a triangular Si(111) crystal bent to form a quasi-parallel beam of monochromatized radiation. Owing to the small size of the source and the high coherence of its radiation, the spatial distribution patterns of diffracted intensity could be recorded in a wide range of angles. The CTR patterns were obtained in the vicinity of the GaAs (004) reflection at a SR wavelength of 1.6 Å. Two-dimensional diffraction patterns were recorded using special imaging plates, with a subsequent optical read-out of information [27]. After that, the patterns obtained were processed further to eliminate the noncoherent background.

A Philips EM420 electron microscope operating at a 120-kV acceleration voltage was used for the TEM studies. Samples for TEM were prepared in a transverse cross-sectional configuration along two mutually perpendicular directions [110] and $[1\bar{1}0]$. It is necessary to note that the [110] and $[1\bar{1}0]$ designation of the crystallographic directions was chosen and is used henceforth arbitrarily, with the polarity of the crystallographic planes disregarded. The standard sample preparation procedure was used, including ion-milling in the final stage. The ion-milling was done in a Gatan DouMill 600 setup, with a grazing incidence of 4-keV Ar^+ ions. Bright- and dark-field images were obtained, with active diffraction vectors $g = 002$ and $g = 220$.

3. RESULTS AND DISCUSSION

3.1. X-ray Diffraction

The crystal perfection of the samples was preliminary assessed on the basis of double-crystal X-ray diffraction data. Rocking curves obtained in the vicinity of the GaAs (004) reflection show the high crystal perfection of the samples under study, and that the geometrical parameters of the layers, including In(Ga)As–GaAs periodic structures, are close to the prescribed technological parameters.

Figure 1 shows two rocking curves for sample no. 1, obtained in the $(\omega - 2\theta)$ scanning mode. Curve *1* was recorded with an open detector, and, in fact, is a super-

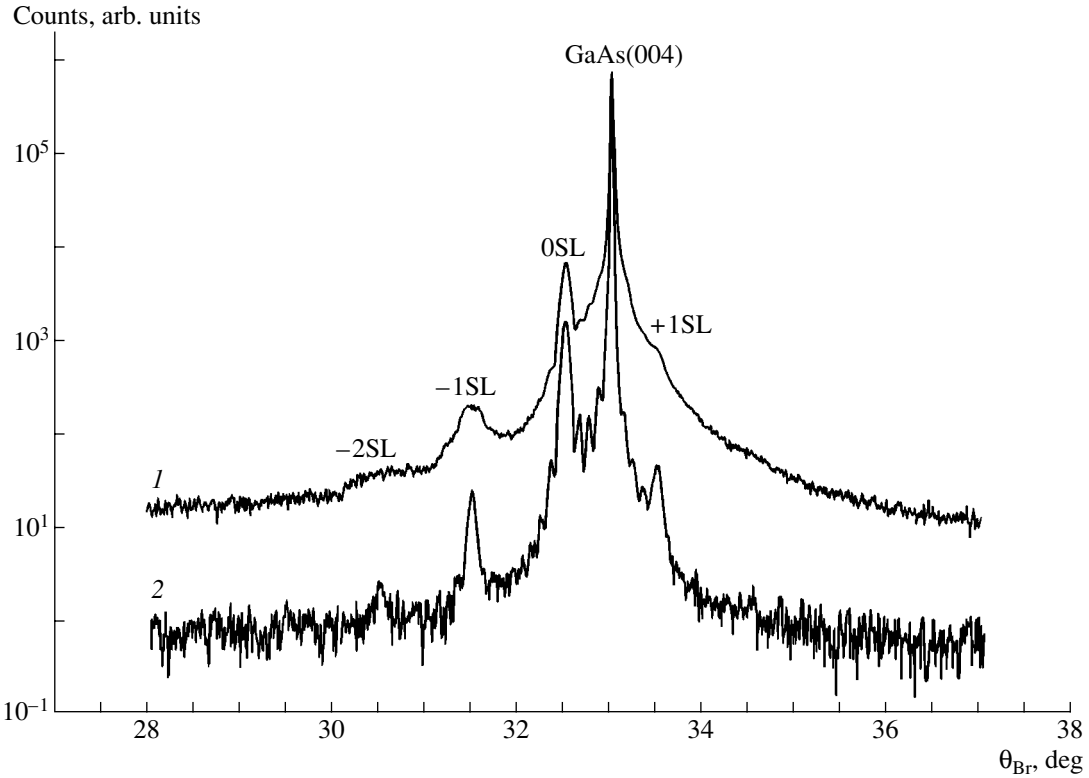

Fig. 1. (*1*) Total and (*2*) coherent double-crystal rocking curves for a structure containing ten pairs of InAs–GaAs layers. GaAs (004) reflection, Cu$K_{\alpha 1}$ emission.

position of the coherent and diffuse components of the diffracted radiation. In measuring curve *2*, a narrow slit was placed in front of the detector, which markedly reduced the contribution of the diffuse component. The resulting difference between the two curves is clearly seen (for clarity, the curves in the figure are shifted along the vertical axis). Peaks corresponding to the InAs–GaAs superstructure (–2SL, –1SL, and +1SL) are clearly pronounced, along with thickness oscillations whose period corresponds to the total thickness of the superstructure. In the rocking curve obtained with higher angular resolution, interference fringes, whose period is determined by the thickness of the top GaAs layer (~0.45 μm), are clearly seen in the vicinity of the GaAs (004) reflection. Altogether, these factors indicate a high crystal perfection of the structure, planarity of its interfaces, and a very low density of extended structural defects formed during epitaxial growth.

It is worth calling attention to some specific features of curve *1*, which contains a diffuse component of diffracted radiation. The unusual shape of the superstructure peaks –2SL and –1SL is not associated with diffuse scattering on extended defects, whose density is insignificant according to data obtained by other methods. In all probability, the shape of these peaks is related to diffuse X-ray scattering on structural imperfections caused by the undulation of crystal planes [16].

To verify this assumption, and also to confirm the occurrence of azimuthal anisotropy in the distribution of elastic strain, CTR studies were performed. Angular distribution patterns of diffracted intensity were obtained in the vicinity of the GaAs (004) reflection. The patterns were recorded at three different azimuthal positions of the samples under study, with the incident-beam direction coinciding with the $[1\bar{1}0]$, [100], or [110] crystallographic directions. Figure 2 presents the patterns obtained for sample no. 1.

A feature common to all the patterns is the presence of clear superstructure reflections, from –2SL to +2SL, whose positions are determined by the average deformation and the period of the InAs–GaAs superstructure. For the direction $[1\bar{1}0]$ (Fig. 2a), the superstructure reflections in the central part of the pattern from –1SL to +SL are elongated in the $\Delta\theta_{Br} = \theta - \theta_{Br}$ (or q_z) direction, which is typical of scatterers with a high-perfection crystal structure. Evidently, the intensity distribution in the +2SL reflection is about the same, but the low intensity of diffracted radiation gives no way of making this statement more specific. Furthermore, additional contours of diffused radiation are seen around each superstructure reflection, broadened in the lateral direction q_x, or $[1\bar{1}0]$. Their broadening increases noticeably on passing from the +1SL to –1SL

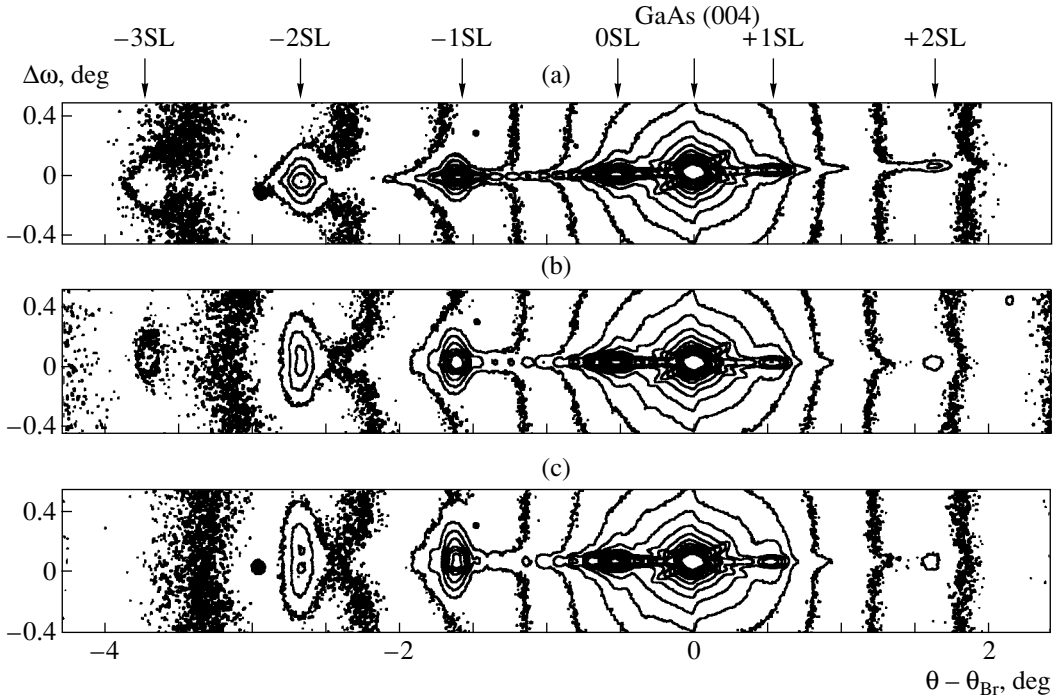

Fig. 2. CTR spatial distributions of diffracted radiation in the vicinity of the GaAs (004) reflection for structure no. 1 (ten pairs of layers); azimuthal directions (a) $[1\bar{1}0]$, (b) [100], and (c) [110]. SR wavelength 0.16 nm.

reflection. The intensity distribution around the –2SL reflection has the form of distorted ellipses elongated in the lateral direction. Additional interference fringes corresponding to thickness oscillations associated with the InAs–GaAs superstructure as a whole are clearly seen between the –1SL and +1SL superstructure reflections.

The spatial distribution patterns of diffracted radiation for the [100] and [110] directions (Figs. 2b and 2c) are markedly different. The nature of the spatial distribution of diffracted radiation remains virtually unchanged only at the zeroth superstructure reflection. Other reflections, especially –1SL and –2SL, are strongly broadened in the q_x direction and become similar to ellipses, with the peak of the –2SL superstructure reflection (Fig. 2c) becoming double-headed.

The comparison and analysis of the data obtained shows, in the first place, that the distribution of diffracted radiation with additional anisotropic lateral broadening of the superstructure diffraction peaks, observed in the patterns, is untypical of scatterers with extended structural defects (like misfit dislocations), and even more so for perfect planar structures. Evidently, the observed broadening of the diffraction peaks is due to a quasi-periodic distribution of elastic strain in the InAs–GaAs periodic structure [16], which results from the relaxation of elastic strain introduced by QDs and is anisotropic with respect to crystallographic directions of the [110] family.

The preferential direction of crystal plane undulation is [110]. The double-headed (in the q_x-direction) shape of the –2SL superstructure reflection (Fig. 2c) indicates that an additional long-range order is formed in this direction in the lateral undulation of the planes [16]. The angular distance of 400 seconds of arc between the peaks corresponds to a lateral size of 70.0 nm, coinciding with the distance between QDs in the [110] direction. Judging from the slight lateral widening of the –2SL reflection (Fig. 2a), plane undulation also exists in the perpendicular direction $[1\bar{1}0]$, but is noticeably weaker and shows no signs of any additional lateral ordering. We suppose that, for this direction, the quasi-periodic elastic deformation caused by the initial stage of elastic strain relaxation appears only in the upper part of the InAs–GaAs superstructure.

The second significant distinction observed upon altering the azimuthal direction of exposition is the change in the total angular size of the diffraction patterns and in the angular size of the pattern of thickness oscillations. The +2SL and –3SL superstructure reflections are clearly visible in the CTR pattern for the $[1\bar{1}0]$ direction (Fig. 2a). Distinct peaks of thickness oscillations with period corresponding to the total thickness of the InAs–GaAs superstructure are seen between the –1SL and +1SL superstructure reflections, i.e., in the part of the diffraction pattern in which the undulation of the crystal planes presumably produces the minimal effect on the nature of diffraction scattering.

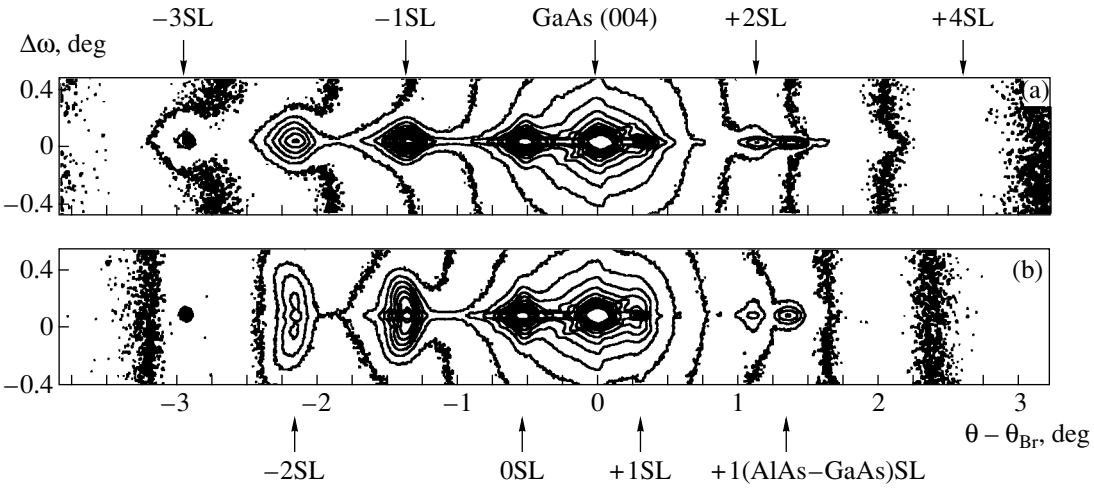

Fig. 3. CTR spatial distributions of diffracted radiation in the vicinity of the GaAs (004) reflection for structure no. 2 (15 pairs of layers); azimuthal directions (a) $[1\bar{1}0]$ and (b) [110]. SR wavelength 0.16 nm.

For the [110] direction (Fig. 2c), the total size of the diffraction pattern is much smaller: the –3SL reflection is absent, and the +2SL superstructure reflection is strongly diffuse. The thickness oscillations related to the InAs–GaAs superstructure are clearly visible between the 0SL and +1SL superstructure reflections, whereas the size of the interference pattern to the left of the 0SL peak is much smaller. A comparison of these data suggests unambiguously that the undulation of the crystal planes and the resulting quasi-periodic elastic deformation (nonplanarity of interfaces in a more general case) strongly affect the spatial resolution of X-ray diffraction. The higher the amplitude is of the quasi-periodically distributed elastic strain (nonplanarity of interfaces), the poorer the spatial resolution of the method is (Fig. 2c, [110] direction), and vice versa (Fig. 2a, $[1\bar{1}0]$ direction). This effect is manifested both at the level of the superstructure period, as a variation in the overall size of the interference pattern, and at the level of the total thickness of the periodic structure, as variation in the size of the interference pattern of total thickness oscillations. The stronger the roughness of each interface is, the more uneven the overall thickness of the superstructure becomes.

This gives reason to maintain that the spatial resolution ΔT of high-resolution X-ray diffraction analysis is generally defined not by the instrumental limitations of the method, but, in the first place, by the crystal perfection of the heterostructures under study. To avoid the loss of useful information in the experiment, the angular range $\Delta\theta_{exp}$ measured must substantially exceed the angular range $\Delta\theta_{Br} \approx L_{ext}/\Delta T_{exp}$ determined by the crystal perfection of a sample under study (here L_{ext} is the extinction thickness for an ideal crystal, and ΔT_{exp} is the spatial resolution determined by the crystal perfection of the structure, i.e., by the extent to which the interfaces are diffuse).

The results obtained for sample 2 completely confirm the data for sample no. 1. The patterns of spatial distribution of the diffracted radiation for sample 2 (Fig. 3) are more complicated owing to the presence in the structure of two additional AlAs–GaAs superlattices. However, the general character of the diffraction intensity distribution and the nature of changes caused by the lateral ordering of QDs and by the azimuthal anisotropy of crystal plane undulation remain the same. Some distinction between the spatial distribution pattern at the –2SL superstructure reflection and that for sample no. 1 is due to the greater total number of layer pairs in the InGaAs–GaAs periodic structure and the corresponding enhancement of the QD lateral ordering.

In a perfect structure, this process occurs simultaneously with the vertical ordering of QDs [16]. In this case, the more QD layers there are, the stronger their vertical and lateral ordering and crystal plane undulation [13, 16]. The critical thickness of the structure is a factor limiting the total thickness of a periodic structure with QDs. On exceeding the critical thickness, the plastic relaxation of elastic strain starts to give extended structural defects. In this case, the relaxation processes are strongly dependent on the QD size and thickness of the intermediate GaAs layers between the QDs [17].

The presence of additional AlAs–GaAs superstructures in the structure under study is responsible for an additional AlAs–GaAs superlattice reflection in the spatial distribution patterns, the +1(AlAs–GaAs)SL peak, to the right of the +2SL reflection related to the InGaAs–GaAs superlattice. It is of considerable interest that the diffracted intensity distribution around the +1(AlAs–GaAs)SL reflection varies with azimuth in the same manner as the InGaAs–GaAs superstructure spots; i.e., the diffraction peak is noticeably elongated in the lateral direction when the azimuthal direction is changed from $[1\bar{1}0]$ to [110]. This suggests that the

anisotropic undulation of crystal planes occurs not only in the InGaAs–GaAs superstructure, but also in the overlying GaAs layers (40 and 10 nm thick), and in the periodic AlAs–GaAs structure. Unfortunately, the position of the –1(AlAs–GaAs)SL superstructure reflection practically coincides with the position of the –1SL reflection related to InGaAs–GaAs, which complicates the spatial intensity distribution pattern and gives no way of ascertaining all of its features. For a detailed analysis of the crystal plane undulation in the upper part of the structure, further diffraction studies are necessary using methods with higher selectivity with respect to the penetration depth of refracted/diffracted radiation, e.g., X-ray reflectometry or grazing-incidence X-ray diffraction analysis [28, 29].

Similarly to the case of the preceding sample, the total size of the diffraction and interference patterns depends on the azimuthal direction. The estimates of the interface planarity (referring primarily to In(Ga)As–GaAs superstructures and overlying layers) obtained from the total angular size of the diffraction patterns are as follows: in structure no. 1, the average interface spread is 1.0 nm for the $[1\bar{1}0]$ direction and 1.25 nm for [110]; the respective figures for structure no. 2 are 1.1 and 1.4 nm. Depending on the azimuthal direction, this makes about 3.5–5 monolayers. The overall deviation of the InAs–GaAs superstructure from planarity is 2.5 nm for the $[1\bar{1}0]$ direction and 3.2–3.4 nm for [110] for sample no. 1; the estimates for structure no. 2 are rather approximate because of the strong broadening of the interference fringes.

Based on the data obtained, we can propose the following model of crystal plane undulation and the resulting spatial distribution of elastic strain for structure no. 2. The lower part of the structure, from the substrate upwards as far as the InGaAs–GaAs superlattice, was grown under optimal conditions, without any additional elastic strain introduced, and, therefore, this part is planar. The lower interface of the InGaAs–GaAs superstructure is correspondingly planar. The elastic strain grows with each subsequent layer containing QDs. The vertical ordering of QDs starts with the second layer, after which (the third and fourth layers) lateral ordering appears: the first adaptation stage of elastic strain relaxation begins; the undulation of crystal planes around QDs starts and intensifies, and the related quasi-periodic elastic strain grows [13, 16]. The undulation of crystal planes in the [110] direction grows faster and gradually becomes clearly pronounced, which indicates long-range ordering. The undulation of crystal planes in the $[1\bar{1}0]$ direction also exists (appearing in the upper part of the InGaAs–GaAs superstructure), but the scale of distortions is substantially smaller, and no evidence of additional lateral ordering of QDs is observed. The shape of the growth surface in the upper part of the InGaAs–GaAs superstructure becomes anisotropic, i.e., corrugated (tilelike). The ridges of this structure are oriented along the $[1\bar{1}0]$ axis.

The data obtained suggest that the relaxation of elastic strain in a perfect multilayer structure with QDs passes through several successive stages. The spatial ordering of QDs can be regarded as the initial adaptive stage of elastic strain relaxation [20, 21]. The next stage is the undulation of crystal planes, and only after that does the generation of structural defects begin. Presumably, the conditions for the generation of point defects are already created at the stage of crystal plane undulation and spatial distortion of the growth surface [24, 30]. The defects accumulate at the interfaces to form clusters and are further transformed into extended defects of the dislocation type.

In the structure studied, the relaxation distortions of the growth surface, accumulated in the superstructure with InGaAs QDs, are inherited by the overlying GaAs layer (45 nm thick) [31]. Since the accumulated elastic strain at the upper interface of the InGaAs QD layer does not exceed the critical value, it does not induce extended structural defects or additional local strain affecting the conditions of epitaxial growth. Therefore, the structure retains the conditions for subsequent defect-free overgrowth of the strained QD superlattice. Moreover, the growth of the GaAs layer in optimal conditions (this also refers to AlAs layer growth) may lead to gradual relaxation of local elastic strain in the layer. Correspondingly, the undulation of the crystal planes will also decrease. The thickness of the GaAs layer in this structure being small, the elastic strain, while gradually diminishing upwards, must continue as far as its upper boundary. The related undulation of the crystal planes is also retained, passing further into the undulation of planes in the AlAs–GaAs superstructure, with the magnitude of structural distortions and the character of their distribution being high enough for these distortions to be observed and their type and the anisotropy of their spatial distribution to be determined (Figs. 3 and 4).

In structure no. 1, where the number of QD layers is 1.5 times smaller and the upper GaAs layer is an order of magnitude thicker than that in structure no. 2, the undulation of the crystal planes “inherited” by this layer has practically no effect on the spatial ordering of diffracted radiation near the (004) GaAs reflection (Fig. 2). Apparently, under optimal epitaxial growth conditions this GaAs layer thickness is sufficient for the complete relaxation of the elastic strain generated by the underlying multilayer InAs–GaAs structure. Certainly, this is so if the elastic strain at the upper interface of the InAs–GaAs superstructure and, correspondingly, the density and size of structural defects induced by these strains do not exceed the critical level, above which they already strongly affect the epitaxial growth and structural perfection of overlying epilayers [31].

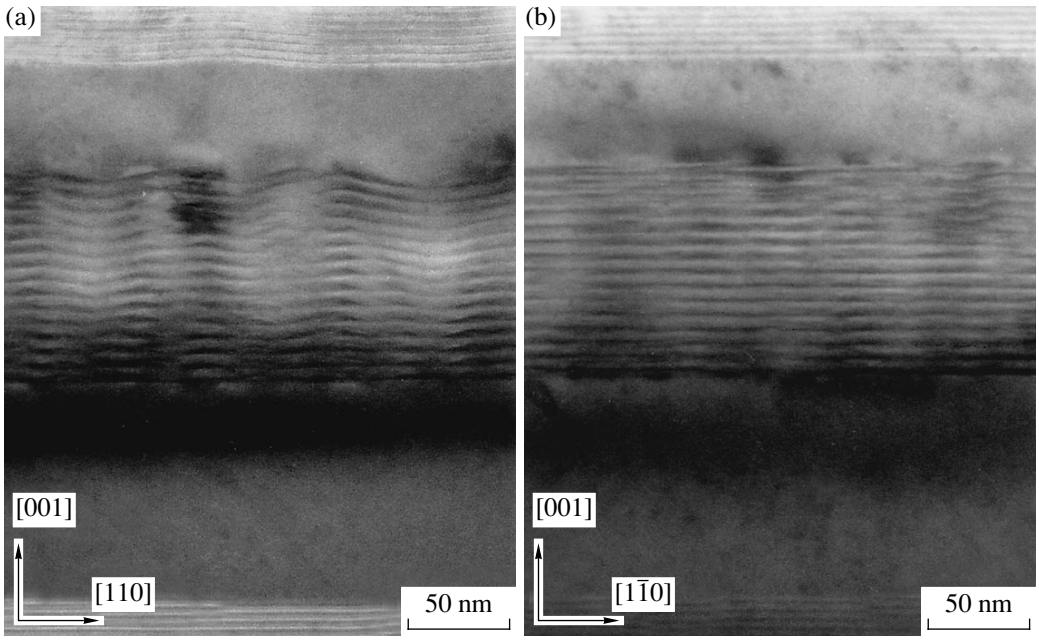

Fig. 4. Cross-sectional TEM images of structure no. 2, obtained in (200) bright-field mode for beam directions (a) [$\bar{1}$10] and (b) [110].

3.2. Electron Microscopy

Electron-microscope studies unambiguously confirm the results of X-ray diffraction analysis and CTR. Figures 4a and 4b show two cross-sectional bright-field TEM images obtained in the (200) reflection from sample no. 2, for, respectively, the azimuthal directions [$\bar{1}$10] and [110] of the incident beam. The micrograph in Fig. 4a is a usual image of a multilayer structure containing vertically coupled QDs. Specific features of the structure are clearly seen: a planar lower interface, layers of vertically coupled QDs, undulated crystal planes. An unusual contrast in the image of intermediate GaAs layers, resulting from the distortion of the growth surface planarity through the undulation of crystal planes, is clearly visible after deposition of six or seven QD layers, thus confirming the X-ray diffraction data [13]. Cross-sectional images give no way of assessing the lateral ordering of QDs, observed in the X-ray diffraction patterns. Nevertheless, the images obtained are sufficient for observing how structural distortions associated with the multilayer QD structure (undulation of crystal planes) extend upwards from the InGaAs–GaAs structure, and, somewhat diminished, are clearly manifested in the images of layer interfaces in the top AlAs–GaAs superstructure.

The micrograph obtained in the [110] direction (Fig. 4b) differs significantly from the preceding image. The feature common to both TEM images is the planar lower interface of the InGaAs–GaAs superstructure. However, the images of layers with QDs and the QDs themselves differ substantially from the image of the (1$\bar{1}$0) cross section, looking more like the electron micrograph of epilayers in structures grown with considerable deviations from planar growth conditions [25, 32]. The vertical ordering of QDs is just perceptible in some places only, and there is no clearly pronounced undulation of crystal planes. Distortions of the layer planarity are seen in the upper part of the InGaAs–GaAs periodic structure; however, these variations are irregular, which is more typical of the initial stage of elastic strain relaxation in planar structures [25]. There are no signs of QD lateral ordering, which agrees well with the CTR data (Figs. 2a and 3a). The lower interface of the top AlAs–GaAs superstructure is nearly planar (a fragment of it is seen in the upper part of Fig. 4b).

3.3. Discussion

An analysis of the TEM data confirms the conclusions based on the results of X-ray diffraction and CTR studies. The processes of spatial (vertical and lateral) ordering of QDs, giving rise to undulation of crystal planes and quasi-periodic redistribution of elastic strain, appear to be substantially anisotropic with respect to crystal axes of the [110] type. This is typical of the initial stage of elastic strain relaxation and is caused by the polarity of crystal planes of the {110} family [26, 32, 33]. The "relaxation ordering" in a multilayer periodic structure produces an additional spatial superstructure of QDs, which is gradually formed as the layers accumulate the elastic strain introduced by the QDs. Owing to the polarity of crystal planes of the {110} family, the

rate and nature of the additional spatial ordering of QDs (vertical and lateral) are substantially different for two perpendicular crystallographic directions, [110] and $[1\bar{1}0]$.

As a result, the crystal planes are corrugated in the upper part of the In(Ga)As–GaAs superstructure (starting from the sixth or seventh pair of layers) and assume a tilelike shape. The ridges and valleys of this tiling are directed along the $[1\bar{1}0]$ axis. QDs are mainly located in the ridges, forming structures of a quantum wire type (quantum quasi-wires), discretely filled with In(Ga)As QDs. The discreteness of the filling of the quantum quasi-wires is determined by the average size of the In(Ga)As QDs and the distance between them. There is no long-range ordering of QDs in the ridges. Consequently, the slight undulation of the (110) crystallographic planes, seen in the upper part of the In(Ga)As–GaAs structure (Fig. 4b), shows no signs of periodicity. Clear signs of long-range ordering are observed in the [110] direction perpendicular to the ridges (quantum wires). As a result, the ridges (quasi-wires) are spaced at nearly equal intervals (~70.0 nm).

The relief of the crystal planes is inherited by the overlying layers containing no QDs. The anisotropic undulation is preserved, with decreasing amplitude, at distances of tens of nanometers away from the InGaAs–GaAs periodic structure.

Distortions of the growth surface relief are also observed during the relaxation of elastic strain in planar heterostructures grown with a departure from the optimal 2D growth conditions [32, 33]. However, it is more difficult to create the necessary conditions for the formation of a spatially ordered structure of the growth surface for planar structures grown on precisely oriented substrates without QDs. Even in the presence of QDs, the process of formation of a corrugated growth surface is unstable and easily disrupted when extended defects appear in the structure [22].

4. CONCLUSION

Perfect multilayer structures with QDs have been studied by X-ray and synchrotron diffraction methods and transmission electron microscopy. It is shown that the spatial ordering of QDs, followed by the undulation of crystal planes and the redistribution of elastic strain is essentially anisotropic with respect to crystallographic directions of the ⟨110⟩ type, owing to the polarity of this type of crystal planes.

It is shown that anisotropic vertical and lateral ordering of QDs followed by anisotropic undulation of crystal planes are the initial stages of relaxation of the elastic strain introduced into the structure by the QDs. As a result, the crystal planes are corrugated, assuming a tilelike form.

It is shown that the crystal planes are undulated in the [110] direction, whereas the tile ridges are directed along $[1\bar{1}0]$. Beginning with a certain thickness (a certain number of layer pairs in the QD superstructure) the distance between the ridges in the [110] direction shows clear signs of long-range ordering. The ridges filled with QDs form something like quantum wires. No signs of long-range ordering are observed in the positions of the QDs along the ridges.

It is shown that the undulation of crystal planes is inherited by overlying layers. Under optimal 2D growth conditions, the amplitude of plane undulation gradually decreases away from the region of elastic strain. In the perpendicular $[1\bar{1}0]$ direction, the structural distortions are of a different type, and the undulation of the interfaces is much weaker.

ACKNOWLEDGMENTS

N.N. Faleev is grateful to V.I. Punegov for his interest in the work and participation in discussions.

This study was performed in part in the framework of the Scientific Program Monbusho Project “Venture Business Laboratory” at the State University of Nagoya, Japan, and was supported in part by the Daiko Foundation. The study was also supported by the Russian Foundation for Basic Research, INTAS, and the Ministry of Science of the Russian Federation, Program “Physics of Solid-State Nanostructures.”

REFERENCES

1. Y. Arakawa and H. Sakaki, Appl. Phys. Lett. **40**, 939 (1982).
2. L. Goldstein, F. Glas, J. Y. Marzin, *et al.*, Appl. Phys. Lett. **47**, 1099 (1985).
3. Y. Arakawa and A. Yariv, IEEE J. Quantum Electron. **QE-22**, 1887 (1986).
4. M. Asada, Y. Miyamoto, and Y. Suematsu, IEEE J. Quantum Electron. **QE-22**, 1915 (1986).
5. *Semiconductors and Semimetals*, Vol. 40: *Epitaxial Microstructures*, Ed. by A. C. Gossard (Academic, Boston, 1994).
6. *Nanostructures and Quantum Effects*, Ed. by H. Sakaki and H. Noge (Springer-Verlag, Berlin, 1994).
7. N. N. Ledentsov, V. M. Ustinov, V. A. Shchukin, *et al.*, Fiz. Tekh. Poluprovodn. (St. Petersburg) **32**, 385 (1998) [Semiconductors **32**, 343 (1998)].
8. S. V. Zaitsev, N. Yu. Gordeev, Yu. M. Sherniakov, *et al.*, in *Proceedings of the 9th International Conference on Superlattices, Microstructures and Microdevices, Liege, 1996*; A. E. Zhukov, A. Yu. Egorov, A. R. Kovsh, *et al.*, Fiz. Tekh. Poluprovodn. (St. Petersburg) **31**, 483 (1997) [Semiconductors **31**, 411 (1997)].
9. V. Holy, A. A. Darhuber, G. Bauer, *et al.*, Phys. Rev. B **52**, 8348 (1995).
10. A. A. Darhuber, E. Koppensteiner, H. Straub, *et al.*, J. Appl. Phys. **76**, 7816 (1994).
11. A. A. Darhuber, V. Holy, J. Stangl, *et al.*, Appl. Phys. Lett. **70**, 955 (1997).

12. A. A. Darhuber, P. Schittenhelm, V. Holy, *et al.*, Phys. Rev. B **55**, 15652 (1997).
13. N. Faleev, K. Pavlov, M. Tabuchi, and Y. Takeda, Jpn. J. Appl. Phys. **38**, 818 (1999).
14. N. Faleev, K. Pavlov, M. Tabuchi, and Y. Takeda, Jpn. J. Appl. Phys., Suppl. **38**, 277 (1999).
15. K. Pavlov, N. Faleev, M. Tabuchi, and Y. Takeda, Jpn. J. Appl. Phys., Suppl. **38**, 269 (1999).
16. N. N. Faleev, K. M. Pavlov, V. I. Punegov, *et al.*, Fiz. Tekh. Poluprovodn. (St. Petersburg) **33**, 1359 (1999) [Semiconductors **33**, 1229 (1999)].
17. S. Rouvimov, Z. Liliental-Weber, W. Swider, *et al.*, J. Electron. Mater. **27**, 427 (1998).
18. A. R. Kovsh, A. E. Zhukov, A. Yu. Egorov, *et al.*, J. Cryst. Growth **201/202**, 1117 (1999).
19. J. Tersoff, C. Teichert, and M. G. Lagally, Phys. Rev. Lett. **76**, 1675 (1996); C. Teichert, M. G. Lagally, L. J. Peticolas, *et al.*, Phys. Rev. B **53**, 16334 (1996).
20. I. P. Ipatova, V. G. Malyshkin, and V. A. Shchukin, J. Appl. Phys. **74**, 7198 (1993).
21. V. A. Shchukin, A. I. Borovkov, N. N. Ledentsov, and P. S. Kop'ev, Phys. Rev. B **51**, 17767 (1995).
22. E. Carlino, L. Tapfer, and H. von Kanel, Appl. Phys. Lett. **69**, 2546 (1996).
23. K. Shiramine, Y. Horisaki, D. Suzuki, *et al.*, Jpn. J. Appl. Phys. **37**, 5493 (1998).
24. V. G. Gruzdov, A. O. Kosogov, and N. N. Faleev, Pis'ma Zh. Tekh. Fiz. **20** (14), 1 (1994) [Tech. Phys. Lett. **20**, 561 (1994)].
25. A. Ponchet, A. Rocher, A. Ougazzaden, and A. Mircea, J. Appl. Phys. **75**, 7881 (1994); A. Ponchet, A. Le Corre, A. Godefroy, *et al.*, J. Cryst. Growth **153**, 71 (1995).
26. R. L. Headrick, J.-M. Baribeau, and Y. E. Strausser, Appl. Phys. Lett. **66**, 96 (1995).
27. T. Shimura and J. Harada, J. Appl. Crystallogr. **26**, 151 (1993).
28. N. Faleev, L. Grave de Peralta, H. Temkin, and V. M. Ustinov, in *Abstracts of the X-TOP 2000, Warsaw, 2000*, S4.3.
29. N. Faleev, T. Kawamura, Y. Watanabe, and V. Ustinov, in *Abstracts of the X-TOP 2000, Warsaw, 2000*, P2-HG139.
30. L. Dong, J. Schnitker, R. W. Smith, and D. J. Srolovitz, J. Appl. Phys. **83**, 217 (1998).
31. N. Faleev, R. Stabenow, M. Sinitsyn, *et al.*, Mater. Sci. Forum **166–169**, 293 (1994).
32. A. Ponchet, A. Rocher, J.-Y. Emery, *et al.*, J. Appl. Phys. **77**, 1977 (1995).
33. Z. H. Ming, Y. L. Soo, S. Huang, *et al.*, Appl. Phys. Lett. **66**, 165 (1995).

Translated by D. Mashovets

Semiconductors, Vol. 35, No. 8, 2001, pp. 941–946. Translated from Fizika i Tekhnika Poluprovodnikov, Vol. 35, No. 8, 2001, pp. 979–984.

LOW-DIMENSIONAL SYSTEMS

Optical Properties of Germanium Monolayers on Silicon

T. M. Burbaev[1,*], T. N. Zavaritskaya[1], V. A. Kurbatov[1], N. N. Mel'nik[1], V. A. Tsvetkov[1], K. S. Zhuravlev[2], V. A. Markov[2], and A. I. Nikiforov[2]

[1] *Lebedev Physical Institute, Russian Academy of Sciences, Moscow, 117924 Russia*

* *e-mail: burbaev@sci.lebedev.ru*

[2] *Institute of Semiconductor Physics, Siberian Division, Russian Academy of Sciences, Novosibirsk, 630090 Russia*

Submitted January 10, 2001; accepted for publication January 16, 2001

Abstract—Photoluminescence and Raman spectra of thin germanium layers grown on silicon at a low temperature (250°C) have been studied. In structures of this kind, in contrast to those grown at high temperatures, luminescence from quantum wells is observed at germanium layer thicknesses exceeding ~9 monolayers (ML). With the development of misfit dislocations, the luminescence lines of quantum wells are shifted to higher energies and transverse optical (TO) phonons involved in the luminescence are confined to a quasi-2D germanium layer. Introduction of an additional relaxed $Si_{0.95}Ge_{0.05}$ layer into the multilayer Ge/Si structure leads to a substantial rise in the intensity and narrowing of the luminescence line associated with quantum dots (to 24 meV), which points to their significant ordering. © *2001 MAIK "Nauka/Interperiodica".*

INTRODUCTION

Nanostructures consisting of thin germanium layers on silicon have aroused a growing interest because of the prospects for their use in various electronic and optoelectronic devices [1]. In particular, one important application is associated with the generation of direct gap luminescence in these structures for creating (by means of integrated silicon technology) devices emitting light at 1.5 μm, necessary for fiber-optic communication lines. Quasi-direct transitions are possible in nondirect semiconductors in the case of free-carrier localization. Such a localization is observed in covariant Ge/Si and SiGe/Si heterostructures, with electrons commonly localized in the silicon quantum well (QW) and holes, in the germanium QW. Another possible kind of localization is associated with self-organization on the silicon surface under the action of heteroepitaxial stresses to form an ensemble of nanoclusters—quantum dots (QDs). The difference between the crystal lattice parameters of silicon and germanium [1 monolayer (ML) of Ge is ~1.4 Å thick, and 1 ML of Si is ~1.35 Å] results in that pseudomorphic 2D growth continues in the course of heteroepitaxy to a certain critical thickness (h_c) of the germanium film: close to 4 ML, i.e., the wetting layer. With increasing thickness, the stress is relieved via self-consistent growth of dislocation-free germanium clusters on the silicon surface by the Stranski–Krastanow mechanism. First, the so-called hut clusters are formed in the form of tetrahedral pyramids; then, the larger dome clusters. With the thickness increasing further, plastic relaxation of stresses with the formation of dislocations occurs. Owing to the smallness of the clusters, they manifest effects of quantum confinement on the electronic spectrum. It has been noticed that lowering the growth temperature T_s to 200°C makes the nanoclusters smaller, their density higher, and h_c larger [2, 3]. The intensity of quasi-direct-gap luminescence from QDs must increase with a decreasing size and an improving spatial uniformity of the forming nanoclusters. One of the methods of nanocluster ordering is the successive growth of layers with germanium clusters overgrown with silicon layers (vertical self-organization). A photoluminescence spectrum of such structure was reported in [3]. It is known from the literature that the structure of the ensemble of nanoclusters changes substantially in a narrow range of germanium layer thicknesses (approximately up to 15 ML). In [4], this conclusion was confirmed by means of scanning-tunneling and atomic-force microscopies; in [2], this was done by studying the Raman scattering.

SAMPLES AND MEASUREMENT TECHNIQUE

Low-temperature photoluminescence (PL) and Raman spectra were studied at germanium layer thicknesses of up to ~15 ML. Multilayer structures with different thicknesses of Ge and Si layers were grown by molecular-beam epitaxy on *n*- and *p*-type (001)Si substrates (5–20 Ω cm). After a standard substrate cleaning procedure, a buffer layer of silicon was deposited onto the substrate at $T_s \approx 800$°C and then periodic structures consisting of Ge layers and thicker Si layers were grown at lower temperature. In the final stage, the structure was coated with a protective silicon film several hundred angstroms thick. Data on the growth modes of

the structures discussed below are presented in the table.

PL spectra were measured at $T = 2$ K with the use of an MDR-2 monochromator. A semiconductor laser with wavelength $\lambda = 0.66$ μm (quantum energy $h\nu = 1.87$ eV) served as an excitation source. The maximum radiation power was 70 mW, with the power density incident on a sample equal to 4 W/cm^2. The emission from the samples was recorded using a liquid-nitrogen–cooled germanium *p–i–n* photodiode. For some of the samples, to ensure that light is emitted by the QDs or the wetting layer (and not by the substrate), luminescence spectra were recorded from two sides of a sample. At $\lambda = 0.66$ μm photoexcited carriers are mainly formed in a layer up to several micrometers deep at the illuminated surface. In the case of illumination from the structure side, the photoexcitation region encloses the entire structure and several micrometers of the substrate and, with illumination from the substrate side, only several micrometers of the substrate, the sample thickness being 300 μm and light incident on the back side not reaching the structure. At photocarrier diffusion lengths common for silicon, we observe emission from both the structure and the substrate in the former case and mainly from the substrate in the latter.

Spectra of Raman scattering on optical phonons were measured at room temperature. The excitation was done with argon laser ($\lambda = 0.488$ μm), the emitted light was recorded with a U-1000 spectrometer.

RESULTS AND DISCUSSION

The measured PL spectra are presented in Figs. 1–5 for both the structure and the substrate. Emission from QDs appears beginning with germanium layer thicknesses ≥4 ML as a weak broad band QD at $h\nu = 0.75$–0.85 eV. With the thickness increasing to 6–8 ML, the emission intensity grows and the band narrows. With the germanium thickness increasing further (to >10–15 ML), germanium clusters form a continuous layer and stress relaxation occurs through the formation of misfit dislocations. In this case, the emission again takes the form of a broad weak band with weak dislocation-related lines observed on its background and then completely disappears. The range of the germanium thicknesses within which the emission intensity is the highest varies with the growth temperature and growth rate and depends on whether or not additional SiGe sublayers relieving the internal stress are present. At fixed growth parameters, the emission lines are shifted to longer wavelengths with increasing germanium layer thickness.

The introduction of an additional relaxed SiGe sublayer (sample 9) presumably leads to QD ordering, with the intensity of emission increasing and the emission band narrowing. The full width at half-maximum (FWHM) of the QD emission line in this sample is 24 meV. The lines of emission from QDs should be distinguished from lines associated with dislocations in silicon (D_1 line at 810 meV and D_2 at 870 meV) lying in the same energy range. The following facts testify that it is the QDs that are responsible for the emission from sample 9.

(1) The D_1 and D_2 lines commonly appear in pairs; the FWHM of dislocation lines is ~10 meV. On raising the temperature to 77 K, the intensity of dislocation-related luminescence decreases severalfold. A single luminescence line is observed in sample 9 at

Structure growth mode

Sample 8	Sample 9
Si, 235 Å, 450°C Si, 20 Å, 250°C Ge, 10 Å, 250°C } ×7 Si, 100 Å, 450°C Si, 1150 Å, 780°C Substrate: *p*-Si, 7.5 Ω cm	Si, 235 Å, 450°C Si, 20 Å, 250°C Ge, 8 Å, 250°C } ×6 Si, 100 Å, 450°C $Si_{0.95}Ge_{0.05}$, 700 Å, 450°C Annealed at 1050°C after growth Si, 1150 Å, 780°C Substrate: *p*-Si, 7.5 Ω cm

Sample 15	Sample 48	Sample 66
Si, 235 Å, 450°C Si, 20 Å, 250°C Ge, 13 Å, 250°C } ×7 Si, 100 Å, 450°C Si, 1150 Å, 780°C Substrate: *n*-Si, 4.5 Ω cm	Si, 300 Å Ge, 13 Å, 300°C Si, 700 Å Substrate: *n*-Si, 7.5 Ω cm	Si, 400 Å Si, 100 Å Ge, 12 Å } ×5 Si, 400 Å Substrate: *n*-Si, 7.5 Ω cm

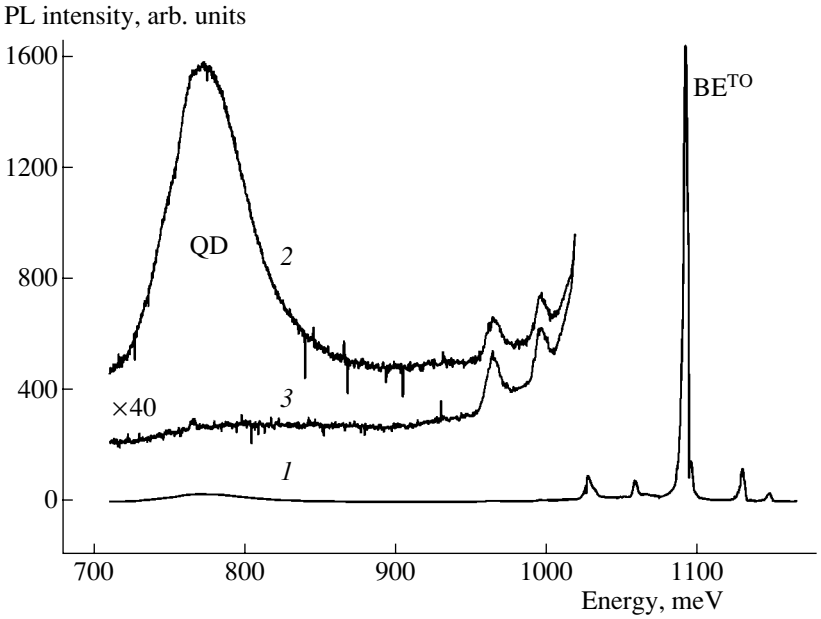

Fig. 1. (*1*) PL spectrum of sample 8 at $T = 2$ K and (*2*) part of the spectrum of the structure and (*3*) substrate at a higher amplification. QD is luminescence from QDs, BE^{TO} is the luminescence line of bound exciton with emission of a TO phonon.

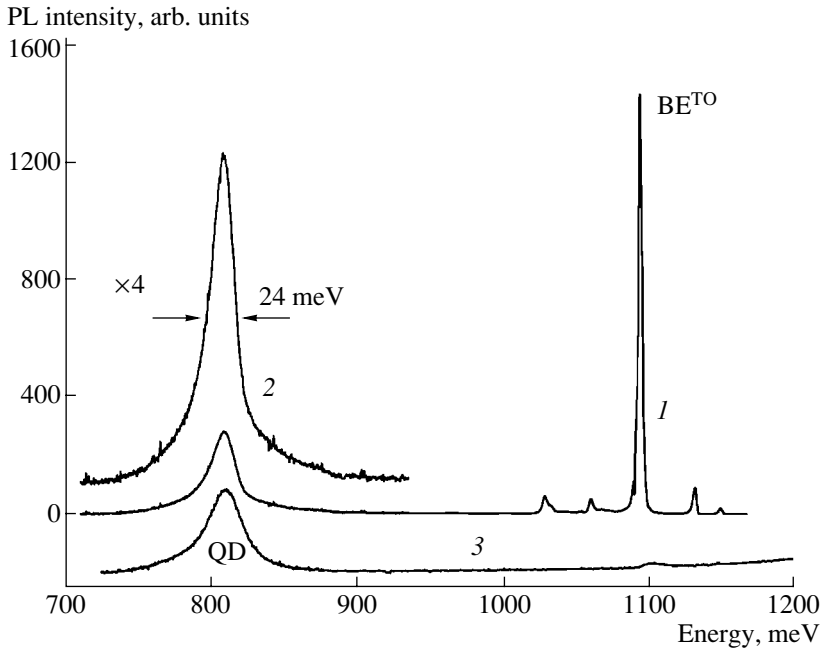

Fig. 2. PL spectrum of sample 9 with additional SiGe sublayer at $T = (1, 2)$ 2 and (*3*) 77 K.

809 meV, having nearly the same intensity at 2 and 77 K (Fig. 2).

(2) In samples with the germanium thickness of ~10 ML in which stress relaxation does occur with the formation of dislocations, their emission is very weak or not observable at all (Fig. 3, structure no. 15).

Raman spectra allow a conclusion as to the extent of relaxation of strained germanium layers on silicon. Such spectra are presented for samples 8, 9, and 15 in Fig. 6. The spectrum of sample 8 shows lines at 520 cm^{-1} (optical phonon in silicon), 420 cm^{-1} (vibrations of Si–Ge bonds), and 316 cm^{-1} (optical phonon in strained germanium). Since the frequency of an optical phonon linearly depends on the strain, then, as shown in [2], a line at 300 cm^{-1} corresponding to optical phonons in bulk germanium appears upon the relaxation of stress at dislocations. For sample 9, the line at 300 cm^{-1} is much weaker than that at 316 cm^{-1}; i.e., the

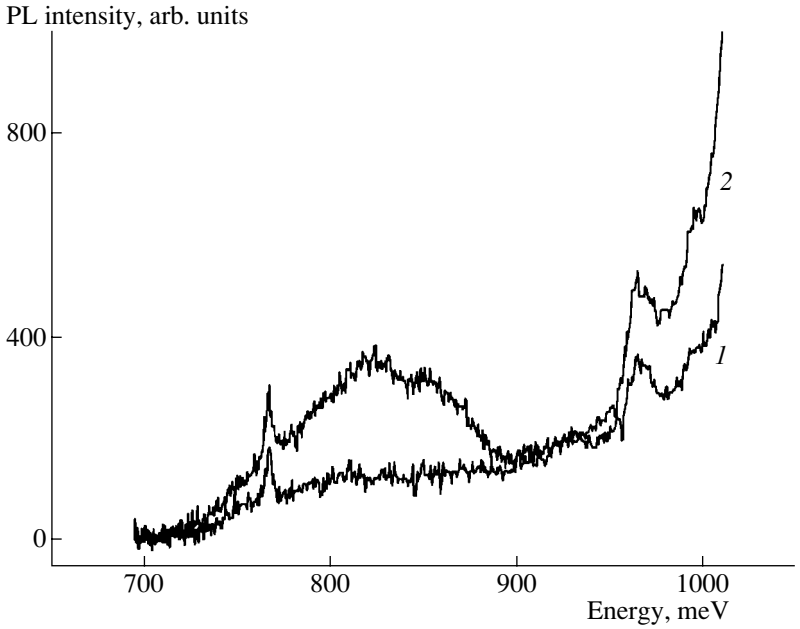

Fig. 3. PL spectra of sample 15 at T = 2 K: (*1*) structure and (*2*) substrate.

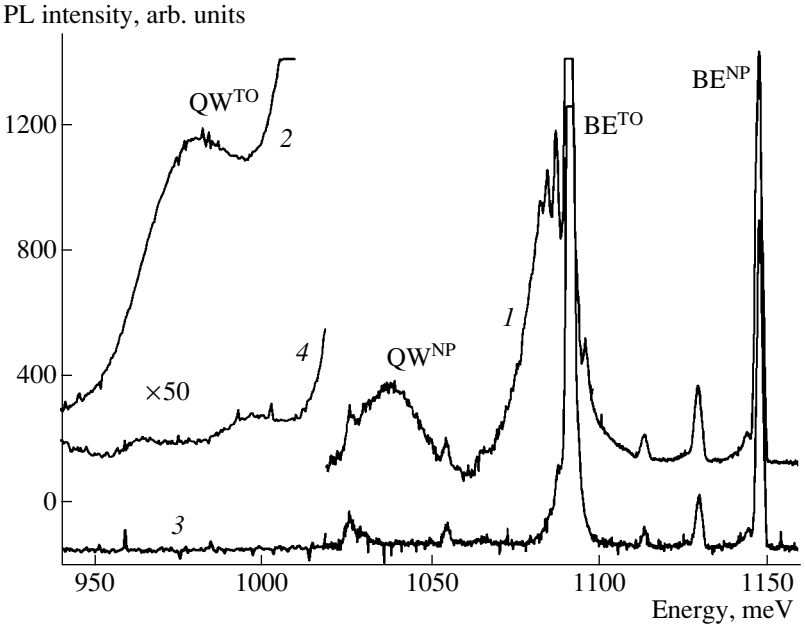

Fig. 4. (*1*, *2*) PL spectrum of the single QW in sample 48 (13 Å Ge) compared with (*3*, *4*) the emission spectrum of the substrate at T = 2 K. $QW^{NP}$and QW^{TO} are QW luminescence lines—zero-phonon and with emission of TO phonon, respectively. BE^{NP} and BE^{TO} are the corresponding lines for bound exciton.

dislocation density in this sample is relatively low. The line at 300 cm^{-1} is presumably associated with the relaxed SiGe sublayer.

It has been shown that in Si/Ge/Si structures grown at T_s = 700°C, the luminescence from a QW (i.e. strained wetting layer) and that from QDs are competing processes [5]. At small germanium thicknesses, the emission from QWs predominates. With the formation of QDs, the emission from wells becomes weaker and the emission from dots grows in intensity. Germanium layers in the samples under study were obtained at low temperatures T_s = 250–300°C. The diffusion length of adsorbed atoms is low at low temperatures; therefore, hut clusters responsible for the emission from QDs are formed simultaneously with the growth of the wetting layer, beginning with the zero thickness. For this rea-

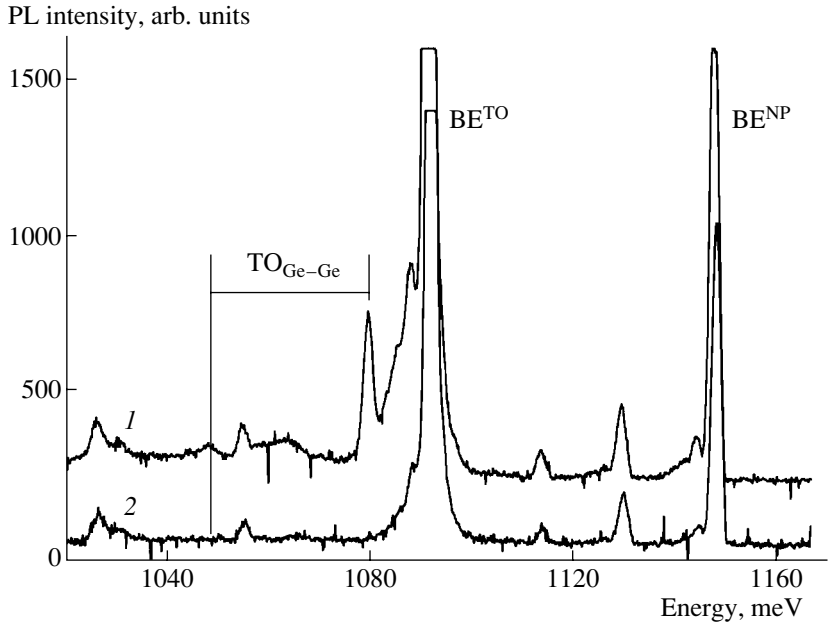

Fig. 5. PL of QW sample 66 at $T = 2$ K: (*1*) structure and (*2*) substrate. BE^{NP} and BE^{TO} are luminescence lines of bound exciton—zero-phonon and with emission of TO phonon, respectively.

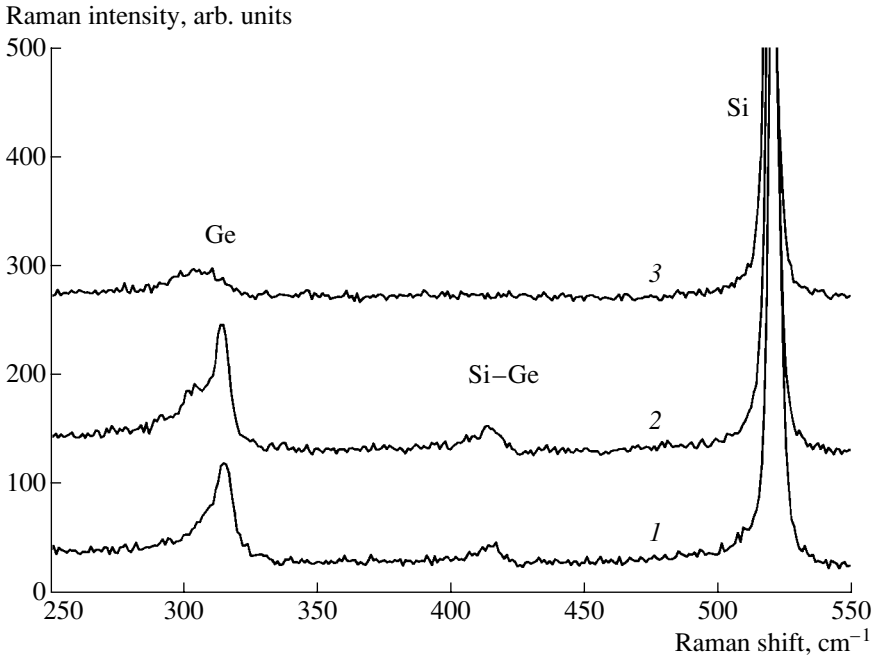

Fig. 6. Raman spectra. Samples: (*1*) 8, (*2*) 9, and (*3*) 15.

son, no emission from QWs was observed at thicknesses ≤8 ML, this emission being suppressed by that of nanoclusters. The emission from QWs was observed at thicknesses ≥9 ML, when separate clusters start to disappear, merging into a continuous layer with misfit dislocations developed. The PL spectra of samples of this kind (nos. 48 and 66) are presented in Figs 4 and 5.

A zero-phonon line QW^{NP} is observed in sample 48 at 1039 meV. Phonon replicas are observed at 982 meV—luminescence occurs with the emission of a TO phonon in silicon, $TO_{Si–Si}$ phonon (59 meV). In the spectrum of sample 66, the zero-phonon line is observed at 1080 meV, with a phonon replica (1048 meV) spaced away by approximately the energy

of TO phonon in germanium, $TO_{Ge–Ge}$ phonon. The shift of the zero-phonon line to higher energies is presumably due to a decrease in the offset of valence band edges of germanium and silicon, which is caused by the partial strain relaxation on misfit dislocations. The Raman spectrum of this sample is similar to that of sample 15, which indicates the presence of a relaxed Ge layer. The spectrum of this sample shows, in contrast to that of sample 48, a strong dislocation-related emission at 700–900 meV on sample excitation both from the side of the structure and from the opposite (substrate) side. Presumably, the strain relaxation on thin Ge is initiated by the high initial density of dislocations in the substrate.

CONCLUSION

Thus, it has been shown that a strong change in the PL spectra, resulting from competition of two kinds of emission (from QDs and QWs), is observed up to germanium thicknesses of ~15 ML in Ge/Si structures grown at low temperature (200–300°C). In contrast to structures grown at high temperatures (600–700°C), in which the luminescence from QWs predominates at thicknesses ≤4 ML, in the structures under study this kind of luminescence is observed at thicknesses ≥9 ML. With the development of misfit dislocations, the lines of luminescence from QWs are shifted to higher energies. It is noteworthy that in this case TO phonons involved in luminescence are confined to the quasi-2D layer of germanium.

It is also shown that introduction of an additional relaxed SiGe sublayer into a multilayer Ge/Si structure makes the intensity of emission from QDs much higher and the emission line narrower.

ACKNOWLEDGMENTS

We thank N.N. Sibel'din for his helpful participation in discussions of the results.

This study was supported by the Russian Foundation for Basic Research (project nos. 99-02-16675 and 00-02-17864), State programs for support of leading scientific schools of the Russian Federation (grant no. 00-15-96568), and R&D programs "Physics of Solid-State Nanostructures" (project no. 2000-2F) and "Promising Technologies and Devices of Micro- and Nanoelectronics" (project no. 1).

REFERENCES

1. P. Schittenhelm, C. Engel, F. Findeis, *et al.*, J. Vac. Sci. Technol. B **16** (3), 1575 (1998).
2. A. B. Talochkin, A. V. Efanov, V. A. Markov, and A. I. Nikiforov, Izv. Akad. Nauk, Ser. Fiz. **63**, 290 (1999).
3. O. P. Pchelyakov, Yu. B. Bolkhovityanov, L. V. Sokolov, *et al.*, Izv. Akad. Nauk, Ser. Fiz. **64**, 205 (2000).
4. Yu. G. Sadof'ev, T. M. Burbaev, V. A. Kurbatov, *et al.*, Izv. Akad. Nauk, Ser. Fiz. **64**, 273 (2000).
5. L. P. Rokhinson, D. C. Tsui, J. L. Benton, and Y.-H. Xie, Appl. Phys. Lett. **75**, 2413 (1999).

Translated by M. Tagirdzhanov

Semiconductors, Vol. 35, No. 8, 2001, pp. 947–948. Translated from Fizika i Tekhnika Poluprovodnikov, Vol. 35, No. 8, 2001, pp. 985–986.

AMORPHOUS, VITREOUS, AND POROUS SEMICONDUCTORS

The Effect of External Factors on Photoelectric Parameters of Amorphous Hydrogenated Silicon in Relation to the Initial Characteristics of the Films

N. Rakhimov, U. Babakhodzhaev, Kh. Mavlyanov, and R. Ikramov

Namangan State University, Namangan, 716019 Uzbekistan

Submitted December 6, 2000; accepted for publication December 7, 2000

Abstract—The effects of heat treatments in vacuum, implantation of Si^+ ions, and exposure to light on photoelectric parameters of *a*-Si:H films were studied. It is shown that the initial characteristics of the films play the determining role in the crystallization effect and in the manifestation of the Staebler–Wronski effect. © *2001 MAIK "Nauka/Interperiodica".*

In this paper, we report the results of studying the effects of thermal treatment (annealing) in a vacuum, implantation of Si^+ ions with an energy of 60 keV, and exposure to light (under the AM1 conditions) on photoelectric parameters of hydrogenated amorphous silicon (*a*-Si:H). The aim of this study was to demonstrate the effect of the above factors on photoconductivity of *a*-Si:H films in relation to the initial characteristics of the films.

We studied both the films of "intrinsic" *a*-Si:H for which the Fermi energy $(\varepsilon_c - \varepsilon_F)_{T=0} = 0.85$ eV (i.e., the Fermi level ε_F is located in the midgap of mobility) and the "pseudodoped" films with the Fermi energy is given by $(\varepsilon_c - \varepsilon_F)_{T=0} < 0.85$ eV. In order to determine this quantity, we measured the activation energy for the dark conductivity $\Delta E = (\varepsilon_c - \varepsilon_F)_{T=0}$, where ε_c is the energy corresponding to the conduction-band bottom. Furthermore, we studied the films with the microstructure parameter $R = 0.6$–0.7, in which case the contribution of dihydride complexes SiH_2 was quite high, in addition to the films with $R \approx 0$, i.e., the films containing only the monohydride complexes SiH. The microstructure parameter was determined by conventional methods from an analysis of the infrared (IR) absorption spectra.

We now consider the effect of annealing in a vacuum chamber with a residual pressure of 10^{-6} Torr on the properties of the films with $R \approx 0$. The films were deposited at a temperature of $T_d = 300$°C. For annealing, the films were heated gradually to $T_A = 360$°C for 30 min. After annealing at the highest temperature T_A, the activation energy ΔE for the dark electrical conductivity in pseudodoped films approached 0.85 eV; i.e., the material became "intrinsic." Correspondingly, we observed the changes in photoconductivity and a reduction in the density of defects (the Si–Si dangling bonds) according to the data obtained by the constant-photocurrent method. Thus, such a heat treatment may be considered as a method for increasing the yield of the device-quality material if the film-deposition conditions are nonoptimal.

From the standpoint of using the above material for the production of polycrystalline silicon, this material attracts particular interest in relation to applications in solar cells, thin-film field-effect transistors, and integrated circuits. In recent years, it has been shown that the structure of polycrystalline silicon obtained as a result of crystallization of *a*-Si:H is superior (the grain sizes are larger) to the structure of the material deposited using thermal decomposition of silane at $T_d = 625$°C [1]; correspondingly, electrical conductivity of the former material is higher.

In Fig. 1, we show the dependence of electrical conductivity on the duration of annealing (t_A) at $T_d = 600$°C in a vacuum chamber with residual pressure of 10^{-6} Torr for a film of intrinsic *a*-Si:H with $R \approx 0$. This dependence illustrates the dynamics of crystallization;

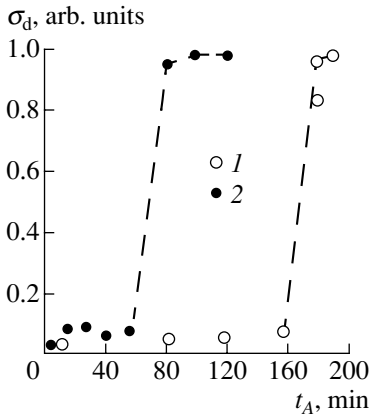

Fig. 1. Electrical conductivity of *a*-Si:H films as a function of the annealing duration for (*1*) a film with $R \approx 0$ and (*2*) a film with $R = 0.7$.

1063-7826/01/3508-0947$21.00 © 2001 MAIK "Nauka/Interperiodica"

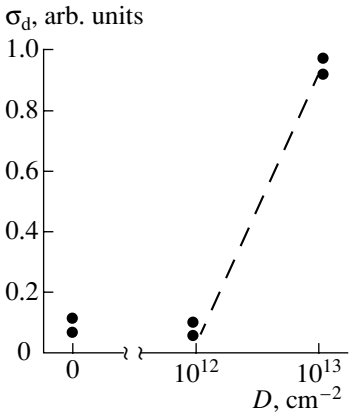

Fig. 2. Effect of implantation of Si^+ ions on electrical conductivity of an *a*-Si:H film with $R = 0.7$.

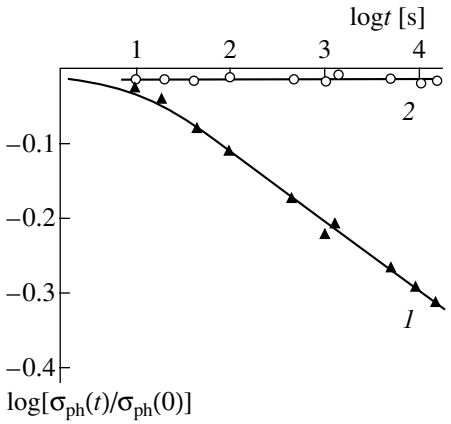

Fig. 3. The kinetics of photoconductivity decay for *a*-Si:H films exposed to natural light under the AM1 conditions in relation to the microstructure parameter *R*: curve *1* is for $R = 0.2$ and curve *2* is for $R = 0.7$. The numbers of the curves (*1*, *2*) correspond to films 1 and 2.

it can be seen that the electrical conductivity increases drastically as a result of annealing for $t_A = 160$ min. A similar dependence for another *a*-Si:H film with a microstructure factor of $R = 0.7$ is also shown in Fig. 1. It can be seen that for this film the tendency for crystallization is observed for much smaller values of t_A.

We now address the results of implantation of Si^+ ions into *a*-Si:H films that differ in microstructure. The ion energy was $E = 60$ keV, and the doses were $D = 10^{12}$ and 10^{13} cm^{-2}. After implantation (at room temperature), the films were annealed in a vacuum chamber with a residual pressure of $(3–4) \times 10^{-5}$ Torr for 1 h at a temperature of 200°C.

Prior to implantation, the films had intrinsic electrical conductivity; however, they differed in the microstructure parameter *R* ($R \approx 0$ for one type of the film, and $R = 0.7$ for the other). After implantation and annealing, the behavior of electrical conductivity for these two types of the films was found to be radically dissimilar. Electrical conductivity of the films with $R \approx 0$ was unaffected by ion implantation, whereas it increased drastically for the films with $R = 0.7$ after implantation with a dose of 10^{13} cm^{-2} (see Fig. 2). Thus, we observe a pattern that illustrates the behavior of crystallization and which is similar to that shown in Fig. 1 for the films with corresponding microstructure.

We now consider the kinetics of photoconductivity in the *a*-Si:H films that have dissimilar microstructure factors and which are exposed to natural light under the AM1 conditions. Figure 3 shows the data for two typical intrinsic-conductivity films. The deposition temperature for both films was $T_d = 350$°C, and the hydrogen content was $C_H = 5–6$ at. %; however, the films differed in the microstructure parameter *R* ($R = 0.2$ and $R = 0.7$ for films 1 and 2, respectively). The quantity γ specifies the decay rate for photoconductivity ($\sigma_{ph} \propto t^{-\gamma}$). The films were illuminated at room temperature. It can be seen that the photoconductivity of film 2 is time-independent; i.e., the Staebler–Wronski effect is not observed. It is known that the hydrogen diffusion is of paramount importance for this effect to manifest itself. Therefore, we may assume that the SiH_2 complexes have a higher stability as compared to the SiH complexes. The former complexes are typically localized at the surfaces of microvoids in the amorphous matrix of an *a*-Si:H film [2] and, in fact, form clusters. Most probably, it is these clusters that act as the centers responsible for crystallization of material as a result of both heat treatment at comparatively low temperatures and the implantation of Si^+ ions with energies in the kiloelectronvolt range.

REFERENCES

1. M. Sudhar, D. D. Cyung, W. A. Anderson, and J. Coleman, Mater. Res. Soc. Symp. Proc. **356**, 921 (1995).
2. K. Zellama, L. Chahed, P. Sládek, *et al.*, Phys. Rev. B **53** (7), 3804 (1996).

Translated by A. Spitsyn

Semiconductors, Vol. 35, No. 8, 2001, pp. 949–952. Translated from Fizika i Tekhnika Poluprovodnikov, Vol. 35, No. 8, 2001, pp. 987–990.

AMORPHOUS, VITREOUS, AND POROUS SEMICONDUCTORS

Anomalous Polarization of Raman Scattering by Transverse and Longitudinal Phonons in Porous Doped GaAs

V. N. Denisov*, B. N. Mavrin*, and V. A. Karavanskiĭ**

** Institute of Spectroscopy, Russian Academy of Sciences, Troitsk, Moscow oblast, 142190 Russia*
e-mail: mavrin@isan.troitsk.ru

*** Institute of General Physics, Russian Academy of Sciences, ul. Vavilova 38, Moscow, 117942 Russia*

Submitted December 27, 2000; accepted for publication December 27, 2000

Abstract—The Raman spectra of a porous doped GaAs(100) crystal were studied. It is established that emission in the plasma-phonon spectra of both the starting and porous crystals is highly polarized and is independent of the incident-radiation polarization. It is inferred that the contribution of the Froelich mechanism to the intensity of the plasma-phonon spectrum is predominant and that the effects of defects and multiple scattering on the scattered-light polarization in porous GaAs may be ignored. The cause for the violation of the selection rules in the spectrum of porous crystal is discussed. © *2001 MAIK "Nauka/Interperiodica".*

In doped semiconductors, the concentration of free charge carriers varies greatly near the surface due to the pinning of the Fermi level within the energy gap at the crystal surface [1]. By virtue of this circumstance, the surface layer (with a thickness of 5–30 nm) becomes depleted of charge carriers and the surface electric field $\mathbf{E}_{surf}$ is directed perpendicularly to the surface. The field $\mathbf{E}_{surf}$ may also be caused by the surface charges, which is especially probable for porous crystals obtained by anodic etching in an electrolyte. The field $\mathbf{E}_{surf}$ necessitates considering the Froelich intraband interaction responsible for the scattering of excited electrons and holes in the course the Raman process by the Coulomb field of longitudinal optical phonons (the LO phonons). Another cause of activation of the Froelich contribution to Raman scattering consists in a finite value of the wave number ($q \neq 0$) of the LO phonon involved in the Raman process [1, 2]. The magnitude of this contribution is proportional to q^2. As is known [1, 2], Froelich Raman scattering obeys the following selection rules: $\mathbf{e}_s \parallel \mathbf{e}_i$, where $\mathbf{e}_s$ and $\mathbf{e}_i$ are the polarization vectors of the scattered and incident radiation, respectively.

It is believed that the Froelich scattering mechanism is responsible for the observation of Raman scattering by LO phonons in the configurations where this scattering must be forbidden. In particular, in the III–V doped cubic semiconductors (with the symmetry group of T_d), an unscreened LO phonon has manifested itself in the Raman spectrum (for example, in InSb [3], GaAs [4], and so on) in an $\mathbf{e}_s \parallel \mathbf{e}_i$ configuration, although the involvement of this phonon is forbidden according to the selection rules.

In this paper, we show that the surface electric field $\mathbf{E}_{surf}$ in porous doped GaAs may be responsible for the violation of the selection rules not only for the Raman scattering by the LO phonons but also for the Raman scattering by the transverse optical phonons (the TO phonons). However, the cause of violation of selection rules for the Raman scattering by TO phonons is most likely not related to the Froelich mechanism of scattering; rather, it is related to a reduction in the total symmetry of the surface layer in pores in the presence of the field $\mathbf{E}_{surf}$. Furthermore, the polarization-involved measurements of the spectra show that Raman scattering by the plasma phonons in doped GaAs (in the starting substrate and in the porous crystal) is highly polarized, which is indicative of the prevalent contribution of the Froelich mechanism to the Raman scattering intensity.

We studied the Raman spectra of the Te-doped *n*-GaAs(100) substrate with electron concentration of 2×10^{18} cm^{-3}; the backscattering configuration was used. A porous crystal was obtained by the anodic etching of the substrate in an electrolyte composed of HF(49%) and C_2H_5OH (1 : 1). The Raman spectra were excited using the radiation lines at the wavelengths of λ = 488, 514.5, and 647.1 nm.

Let us first discuss the spectra of Raman scattering by the phonon-plasmon modes in the starting GaAs substrate. In the Raman spectra, we observe the bands of the phonon-plasmon modes that belong to the upper (443 cm^{-1}) and lower (266 cm^{-1}) branches according to the previous studies of concentration dependence of the phonon-plasmon modes in GaAs [5, 6]. The phonon-plasmon bands were observed more clearly when excited with a line at 647.1 nm (Fig. 1); we relate this circumstance both to the fact that this line is close to the resonance in the vicinity of the gap $E_0 + \Delta_0$ and to a larger penetration depth of the pump radiation; this

1063-7826/01/3508-0949$21.00

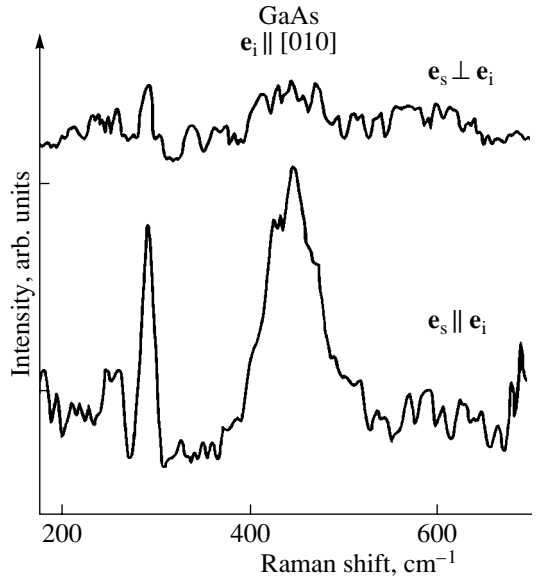

Fig. 1. The polarized Raman spectra of the substrate of a doped GaAs(100) crystal pumped with the 647.1-nm radiation.

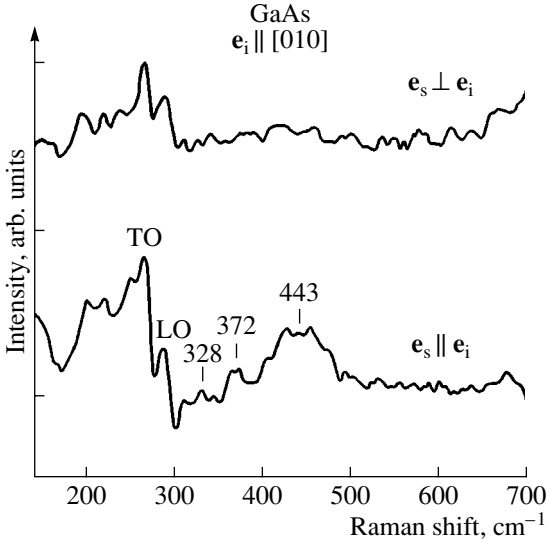

Fig. 2. The polarized Raman spectra of a porous GaAs crystal pumped with the 647.1-nm radiation.

depth exceeds the thickness of the layer depleted of charge carriers. The polarization-related properties of the Raman spectra were found to be identical for the polarization of the pump radiation $\mathbf{e}_i$ either along [011] or along [010], although these properties should differ according to the selection rules.

According to the selection rules for the Raman backscattering in the case of the GaAs(100) substrate [2], the phonon-plasmon mode should be active in the Raman process only for $\mathbf{e}_s \parallel \mathbf{e}_i$ if $\mathbf{e}_i \parallel [011]$, whereas it should be active only for $\mathbf{e}_s \perp \mathbf{e}_i$ if $\mathbf{e}_i \parallel [010]$. The observed identical polarization ($\mathbf{e}_s \parallel \mathbf{e}_i$) of the phonon-plasmon band irrespective of the direction of $\mathbf{e}_i$ may be attributed to the prevalent contribution of Froelich scattering caused by a finite value of the wave vector q for the phonon-plasmon mode (in the case under consideration, $q \sim 10^6$ cm^{-1}).

It is noteworthy that, in addition to the phonon-plasmon modes, an unscreened LO phonon (at 295 cm^{-1}) manifests itself in the Raman spectra of the substrate (Fig. 1) for $\mathbf{e}_s \parallel \mathbf{e}_i$ owing to both Froelich contributions (related both to the surface field $\mathbf{E}_{surf}$ and to $\mathbf{q} \neq 0$). According to the selection rules [2], scattering by the TO phonons is forbidden for any orientation of $\mathbf{e}_s$ and $\mathbf{e}_i$.

The Raman process in a porous GaAs crystal (Fig. 2) was accompanied with noticeable luminescence, especially when the Raman spectra were excited with the 647.1-nm line. The intensities of the bands related to the LO phonons and phonon-plasmon modes increased by a factor of 2–2.5. In addition to these bands, a broad band located at 200–260 cm^{-1} is observed; by its position and shape, this band resembles that of amorphous arsenic [7]. Furthermore, the spectra include a narrow band (at ~296 cm^{-1}) related to TO phonon and forbidden in the substrate spectrum.

Generally speaking, there may be several causes of forbidden TO phonons.

First, this effect may be caused by the misalignment of the nanocrystals' orientations in a porous crystal. However, this inference is not supported the X-ray diffraction data, according to which the porous layer maintains the macroscopic orientation of the starting substrate.

Second, the cause of this effect may be related to the formation of defects in the crystal lattice [8]. Basically, the defects may bring about a depolarization of the spectrum. In particular, the spectrum of GaAs containing the Al impurity atoms [9] is governed by the density of one-phonon states, so that a double peak with a width of 15–20 cm^{-1} arises in the vicinity of the TO-phonon frequency. At the same time, we observe a TO-phonon peak with a width of ≤3.5 cm^{-1} (Fig. 3). Moreover, according to experimental data [10], the lines are narrower in the spectrum of a porous crystal than those of the starting crystal, which is inconsistent with the assumption that defects profoundly affect the spectrum of porous crystal.

Third, the contribution of multiple scattering of both the pump and scattered radiation should be taken into consideration [8]. When assessing this contribution, it is important to bear in mind that the polarization properties of the phonon-plasmon band remain unchanged after anodic etching (Fig. 2). As in the substrate spectrum, the phonon-plasmon mode mainly manifests itself in the porous-crystal spectrum solely for $\mathbf{e}_s \parallel \mathbf{e}_i$ for any orientation of $\mathbf{e}_i$. Preservation of polarization properties is inconsistent with the assumption that the selec-

tion rules for polarization are violated in porous crystals because of multiple-scattering events [8]; this assumption was made on the basis of the fact that the TO-phonon band emerged in the forbidden configurations of scattering. We believe that the TO phonon may manifest itself for another reason, which we discuss in what follows.

The pores that have a mean diameter much smaller than the wavelength of the pump radiation and penetrate to a depth of several micrometers (the penetration depth of the pump radiation is $\lesssim 0.1$ μm in GaAs) are formed as a result of anodic etching. The pores are mainly oriented perpendicularly to the surface in the case of anodic etching of the surface that coincides with the cubic-crystal crystallographic plane perpendicular to the crystallographic axis. In this situation, there exists a component of the field $\mathbf{E}_{surf}$ that is parallel to the substrate-surface plane owing to the presence of the surface fields at the lateral surfaces of pores in addition to a component perpendicular to the above plane. A mutual orientation of the pores and the wave vector of phonons in the backscattering mode (perpendicularly to the substrate surface) hampers the manifestation of the confinement effects for TO phonons; simultaneously, the assumption that the TO spectrum becomes depolarized due to this effect [8] becomes questionable. Taking into account the major contribution of surface layers to the Raman spectrum of porous crystal, we consider the possible effect of the surface field $\mathbf{E}_{surf}$ at the lateral surfaces of pores on the selection rules.

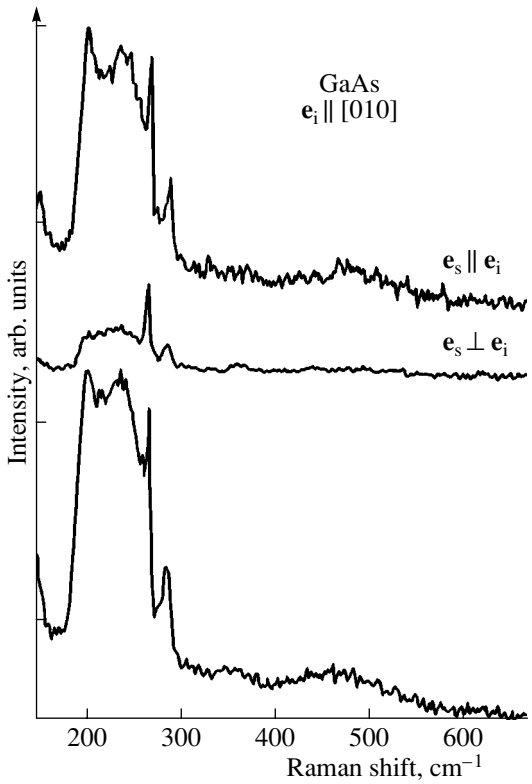

Fig. 3. The polarized Raman spectra of a porous GaAs crystal pumped with the 514.5-nm radiation. The lower spectrum was obtained without using a polarizer for the scattered light. Spectral resolution was 3.5 cm^{-1}.

For the sake of definiteness, we consider the situation where the field $\mathbf{E}_{surf}$ at the lateral surfaces is directed along [010], i.e., the direction parallel to the substrate surface. In the presence of an electric field, vibrations should be classified according to the group C_{2v}, which represents an intersection of the group T_d of the starting crystal and the group $C_{\infty v}$ of the surface electric field. Furthermore, the axis Oz in the group C_{2v} lies in the substrate plane and is oriented along [010], whereas the axis Oy (or Ox) is oriented along [100] perpendicularly to the substrate plane. Using the tables of correlations for irreducible representations of groups T_d and C_{2v} [11], we find that the Raman active triply degenerate vibration $F_2(x, y, z)$ in the group T_d becomes split into three components $A_1(z)$, $B_1(x)$, and $B_2(y)$ in the group C_{2v}. It follows from the form of the Raman tensors for the group C_{2v} that, in our experiments, the component $A_1(z)$ becomes active for $\mathbf{e}_s \parallel \mathbf{e}_i$, whereas the other components are active for $\mathbf{e}_s \perp \mathbf{e}_i$. Since under the conditions of backscattering the phonon's wave vector $\mathbf{q} \perp Oz$ and Ox (or Oy), the TO phonons are allowed in both configurations; thus, we may conclude that the surface electric field $\mathbf{E}_{surf}$ at the lateral surfaces of the pores can activate the TO phonons in the surface layers in configurations in which these phonons must be forbidden for the macroscopic symmetry T_d of porous crystal. For other directions of $\mathbf{E}_{surf}$ (parallel to the substrate surface), the analysis yields the same result. The same mechanism is probably responsible for the observation of the TO-phonon bands in the Raman spectra of isolated interface islands in superlattice structures [12].

The shift of the TO-phonon band to lower frequencies (by ≤ 1 cm^{-1}) in the spectrum of porous GaAs in reference to the frequency position of the TO-phonon band in the starting substrate indicates that there are tensile stresses in the porous crystal. If these stresses are parallel to the substrate plane, they can also make an additional large contribution to the intensity of the forbidden TO-phonon bands.

In conclusion, we note that the low-intensity bands peaking at 328 and 372 cm^{-1} can also be observed in the Raman spectrum of porous GaAs (Fig. 2). The origination of these bands is probably caused by the special features of dielectric function of a porous doped semiconductor, which were previously considered in discussing the Raman spectra of doped porous InP crystal [13].

ACKNOWLEDGMENTS

This study was supported by the Russian Foundation for Basic Research (project no. 00-02-16138) and

by the Interdisciplinary Scientific and Technological Program “Physics of Solid-State Structures” (project no. 97-1073).

REFERENCES

1. E. Burstein, in *Raman Scattering in Material Science* (Springer-Verlag, Berlin, 2000), Springer Ser. Mater. Sci. **42**, 30 (2000).
2. M. Cardona, in *Topics in Applied Physics*, Vol. 50: *Light Scattering in Solids*, Ed. by M. Cardona and G. Güntherodt (Springer-Verlag, Berlin, 1982; Mir, Moscow, 1984), Vol. II.
3. A. Pinczuk and E. Burstein, Phys. Rev. Lett. **21**, 1073 (1968).
4. H. J. Stolz and G. Abstreiter, Solid State Commun. **36**, 857 (1980).
5. A. Mooradian and A. H. McWhorter, in *Light Scattering Spectra of Solids*, Ed. by G. B. Wright (Springer-Verlag, New York, 1968), p. 297.
6. G. Abstreiter, M. Cardona, and A. Pinchuk, in *Topics in Applied Physics*, Vol. 54: *Light Scattering in Solids*, Ed. by M. Cardona and G. Güntherodt (Springer-Verlag, Berlin, 1984; Mir, Moscow, 1986), Vol. IV.
7. J. S. Lannin, Phys. Rev. B **15**, 3863 (1977).
8. I. M. Tiginyanu, G. Inner, J. Monecke, *et al.*, Semicond. Sci. Technol. **12**, 491 (1997).
9. R. Carles, A. Zwick, M. A. Renucci, and J. B. Renucci, Solid State Commun. **41**, 557 (1982).
10. N. N. Mel’nik, T. N. Zavaritskaya, M. M. Rzaev, and V. A. Karavanskiĭ, in *Proceedings of the International Conference on Raman Scattering, Moscow, 1998*, p. 398.
11. G. N. Zhizhin, B. N. Mavrin, and V. F. Shabanov, *Optical Vibration Spectra of Crystals* (Nauka, Moscow, 1984), p. 232.
12. D. Gammon, S. W. Brown, E. S. Snow, *et al.*, Science **277**, 85 (1997).
13. V. N. Denisov, B. N. Mavrin, and V. A. Karavanskii, Phys. Lett. A **259**, 62 (1999).

Translated by A. Spitsyn

Semiconductors, Vol. 35, No. 8, 2001, pp. 953–955. Translated from Fizika i Tekhnika Poluprovodnikov, Vol. 35, No. 8, 2001, pp. 991–994.

AMORPHOUS, VITREOUS, AND POROUS SEMICONDUCTORS

Effect of Temperature on Photoconductivity and Its Decay in Microcrystalline Silicon

A. G. Kazanskiĭ[1], H. Mell[2], E. I. Terukov[3], and P. A. Forsh[1]

[1] *Moscow State University, Vorob'evy gory, Moscow, 119899 Russia*

[2] *Philipps-Universität Marburg, Fachbereich Physik, D-35032 Marburg, Germany*

[3] *Ioffe Physicotechnical Institute, Russian Academy of Sciences, St. Petersburg, 194021 Russia*

Submitted January 26, 2001; accepted for publication January 31, 2001

Abstract—The effect of temperature on steady-state photoconductivity and its relaxation after illumination cut-off in lightly boron-doped microcrystalline hydrogenated silicon films has been studied. The measurements were performed in the temperature range 150–430 K with an incident photon energy of 1.4 eV. The temperature dependences of the photoresponse time and drift mobility in microcrystalline silicon have been obtained from the data on the steady-state photoconductivity and its decay. Mechanisms of carrier transport and recombination that governing these temperature dependences are discussed. © *2001 MAIK "Nauka/Interperiodica"*.

Good prospects for the application of microcrystalline hydrogenated silicon μ*c*-Si:H in thin-film electronic and optoelectronic devices are due to the absence of parameter degradation of (μ*c*-Si:H) films under illumination and also to the high carrier mobility in μ*c*-Si:H as compared with the that in amorphous hydrogenated silicon (*a*-Si:H) [1]. However, the carrier transport and nonequilibrium carrier recombination mechanisms in this material are far less known than those for *a*-Si:H [2–6]. On the one hand, this is evidently associated with low photosensitivity of undoped μ*c*-Si:H films obtained by conventional plasma-enhanced chemical vapor deposition (PECVD) [7]. This restricts the application of photoelectric methods for obtaining data on carrier transport and recombination in μ*c*-Si:H. On the other hand, data interpretation is complicated by the complexity of μ*c*-Si:H structure formed by an amorphous phase, pores, and a microcrystalline phase consisting of silicon microcrystals several nanometers to dozens of nanometers in size [1].

Introduction of relatively low concentration (10^{17}–10^{18} cm^{-3}) of boron into μ*c*-Si:H compensates for the effect of uncontrolled (in PECVD) oxygen incorporation in films [8] and essentially decreases (by 4–5 orders of magnitude) their conductivity [2, 7]. The photosensitivity of these lightly boron-doped films is high enough [2, 7] to allow measurements of their photoelectric characteristics in order to study the carrier transport and recombination in μ*c*-Si:H.

In the present work, we studied the effect of temperature (in the range of 150–430 K) on the steady-state photoconductivity and its relaxation after illumination cut-off in lightly boron-doped μ*c*-Si:H films. μ*c*-Si:H films of thickness 0.6–0.7 μm were deposited onto quartz substrates at 220°C in a standard PECVD reactor (Marburg University) via glow discharge decomposition of a silane–hydrogen mixture containing 1.5% monosilane (SiH_4). Diborane (B_2H_6) was introduced into the reactor for doping with boron. The gas volume ratio ($[B_2H_6]/[SiH_4]$) was 4×10^{-6} for sample no. 1 and 5×10^{-6} for sample no. 2. Magnesium contacts were deposited onto the film surface. The measurements were done in a vacuum of 10^{-3} Pa. Prior to measurements, the films were annealed in a vacuum for 30 min at 180°C. The photoconductivity and its relaxation were measured under illumination with radiation emitted by IR LEDs with a quantum energy of $h\nu$ = 1.4 eV and an intensity of 4×10^{16} cm^{-2} s^{-1}. The photoconductivity relaxation was recorded by a digital storage oscilloscope.

According to electron microscopic data, the films have a columnar structure, with columns 30–100 nm in diameter perpendicular to the substrate surface and containing crystals 3–30 nm in size [3]. As indicated by thermal emf measurements, the films show *p*-type conduction.

Figure 1 presents temperature dependences of the dark conductivity (σ_d) and steady-state photoconductivity ($\Delta\sigma_{ph}$) of the μ*c*-Si:H films studied. In the temperature range 220–450 K, the $\sigma_d(T)$ dependences exhibit an activated behavior with an activation energy of E_a = 0.43 (sample no. 1) and 0.27 eV (sample no. 2). Raising the doping level makes the conductivity higher and E_a lower. As seen from the figure, the $\Delta\sigma_{ph}$ value increases with temperature nearly exponentially in the range $T <$ 250 K with an activation energy of 0.13–0.14 eV. With the temperature increasing further, the rise in $\Delta\sigma_{ph}$ becomes weaker and then, in the temperature range where $\Delta\sigma_{ph} \le \sigma_d$, $\Delta\sigma_{ph}$, starts to decrease.

The temperature dependence of $\Delta\sigma_{ph}$ may be governed by variation of the lifetime and/or carrier mobil-

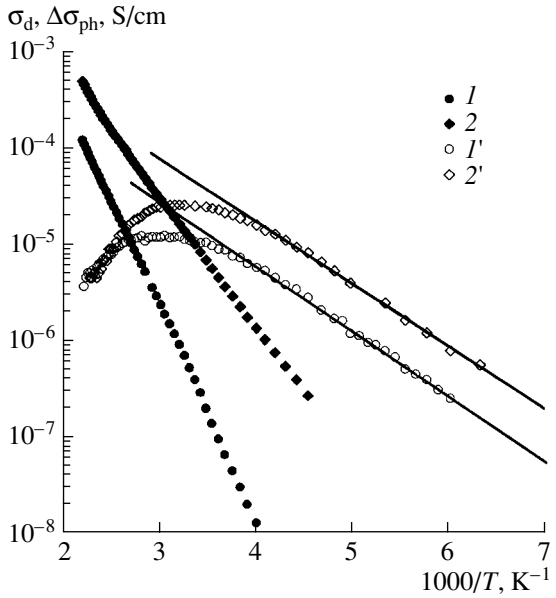

Fig. 1. Temperature dependences of (*1*, *2*) conductivity σ_d and (*1'*, *2'*) steady-state photoconductivity $\Delta\sigma_{ph}$ of μ*c*-Si:H films. The curve numbers correspond to sample numbers.

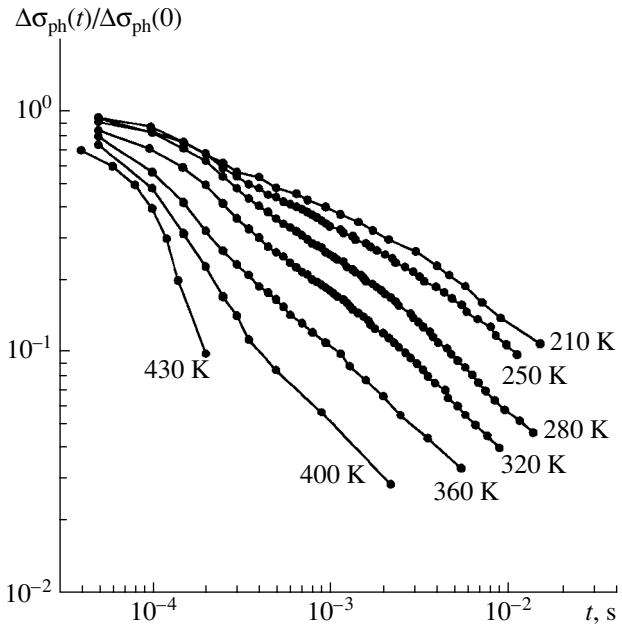

Fig. 2. Relaxation of photoconductivity in sample 1 at different temperatures (indicated at the curves).

ity with temperature. To obtain information concerning the effect of temperature on the carrier recombination in the films under study, we investigated the relaxation of photoconductivity after illumination cut-off. Figure 2 demonstrates the kinetics of the photoconductivity decay and its temperature variation for sample 1. It is seen that the photoconductivity decay cannot be described by an exponential dependence in the entire temperature range studied (150–430 K). A long-term relaxation of photoconductivity is observed. At $t > 3 \times 10^{-4}$ s, the photoconductivity decays by nearly power-law ($\Delta\sigma_{ph} \propto t^{-\beta}$). At $T > 250$ K, the relaxation time decreases with increasing temperature and the parameter β grows. In the low temperature range ($T < 200$ K), the relaxation of photoconductivity is virtually temperature-independent. Similar results were obtained for sample no. 2.

Figure 3 shows temperature dependences of the photoresponse time for the samples studied. The time of photoconductivity half-decay from the steady-state value (τ_{ph}) was chosen as a parameter characterizing the photoresponse time. (An analysis of the relaxation curves presented in Fig. 2 has shown that this value is close to the instantaneous photoresponse time $\tau_{ph}(0)$ found from the relation $\tau_{ph}(0) = \{\Delta\sigma_{ph}[\partial(\Delta\sigma_{ph})/\partial t]^{-1}\}_{t=0}$.) As seen from Fig. 3, τ_{ph} decreases with increasing temperature at high temperatures ($T > 250$ K). In the low temperature range ($T < 200$ K), τ_{ph} only slightly depends on temperature (τ_{ph} increases somewhat with increasing temperature). It should be noted that τ_{ph} grows when the doping level becomes higher. Temperature dependences of the drift mobility of nonequilibrium carriers ($\mu_{dr} = \Delta\sigma_{ph}/(eG\tau_{ph})$, where G is the generation rate) can be calculated from the measured temperature dependences of $\Delta\sigma_{ph}$ and τ_{ph}. The obtained $\mu_{dr}(T)$ dependences are presented in Fig. 3. In the temperature range 200–350 K, μ_{dr} grows exponentially with temperature with an activation energy of 0.14–0.15 eV.

Let us discuss these results. Previous studies of the absorption spectra by the constant photocurrent method [9] suggest that the carrier transport in the μ*c*-Si:H films occurs mainly via the microcrystalline phase. The nonexponential relaxation of photoconductivity indicates a significant concentration of traps for nonequilibrium carriers in μ*c*-Si:H. These traps may be localized states in the band tails appearing at microsrystallite boundaries [10]. Presumably, the prolonged photoconductivity relaxation may also be associated with the potential relief within the columns formed by microcrystals because of the possible large-scale fluctuations of potential.

The obtained $\tau_{ph}(T)$ dependences indicate that the processes of nonequilibrium carrier recombination change in the temperature range T = 200–250 K. The weak temperature dependence of τ_{ph} at $T < 200$ K points to the possible tunneling recombination in the low temperature range. In this case, the photoresponse time τ_{ph} may increase with temperature [11]. Tunnel transitions of nonequilibrium carriers may occur both between localized states in the band tails and between the band tail states and defect states [12]. In the case of potential fluctuations, carrier tunneling may also presumably occur between the fluctuation minima of the conduction and valence bands [13]. At high temperatures ($T > 250$ K), the contribution of transitions from

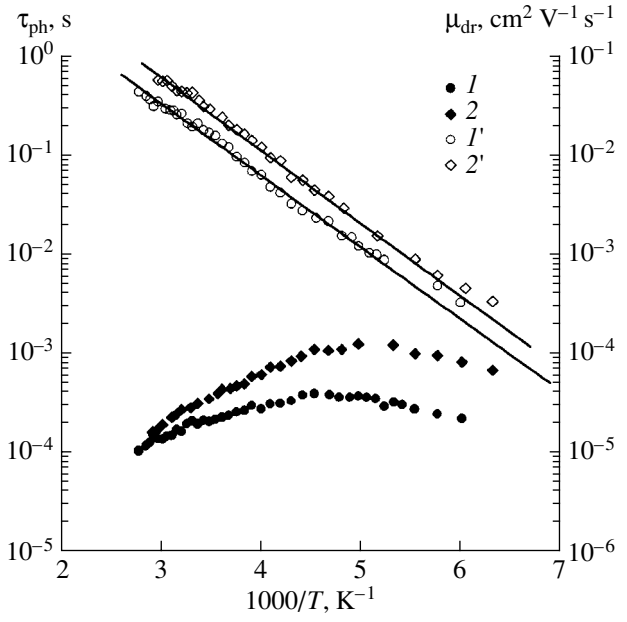

Fig. 3. Temperature dependences of (*1*, *2*) photoresponse time τ_{ph} and (*1'*, *2'*) drift mobility μ_{dr} for μc-Si:H films. The curve numbers correspond to sample numbers.

delocalized states or states lying above the percolation level (in the presence of large-scale potential fluctuations) to recombination centers may become more pronounced. In this case, the photoresponse time must decrease with increasing temperature [11]. The carrier lifetime may also decrease as temperature is elevated. The recombination centers controlling the carrier lifetime at high temperatures may be represented by the "dangling bond" defects formed at the boundaries of columns formed by microcrystals [4].

The activated character of the $\mu_{dr}(T)$ dependence at $T > 200$ K may be due to the fact that, similarly to the *a*-Si:H case, the transport of nonequilibrium carriers is controlled by their trapping into the density-of-states tails or by the activation of carriers from the fluctuation minima to the percolation level (with large-scale potential fluctuations present) [14]. The existence of potential barriers at the column boundaries may also give rise to the activation-type dependence of $\mu_{dr}(T)$. At $T <$ 200 K, the μ_{dr} temperature dependence may become weaker because of the increasing contribution to the overall carrier transport from hopping via band-tail states and from tunneling through potential barriers [14].

To conclude, our investigations have shown that the character of temperature dependences of steady-state photoconductivity and its relaxation in μc-Si:H is similar to those in *a*-Si:H. This is presumably due to the similarity of the basic features of the effective density of states distribution in these materials [15].

ACKNOWLEDGMENTS

This study was supported by INTAS (grant no. 97-1910), COPERNICUS (IC15-CT98-0819, TIMOC), and the Program "Universities of Russia."

REFERENCES

1. K. Tanaka, Mater. Res. Soc. Symp. Proc. **452**, 3 (1997).
2. M. J. Williams, C. Wang, and G. Lucovsky, Mater. Res. Soc. Symp. Proc. **219**, 389 (1991).
3. D. Ruff, H. Mell, L. Toth, *et al.*, J. Non-Cryst. Solids **227–230**, 1011 (1998).
4. D. Will, C. Lerner, W. Fuhs, and K. Lips, Mater. Res. Soc. Symp. Proc. **467**, 361 (1997).
5. J.-H. Zhou, S. D. Baranovskiĭ, Y. Yamasaki, *et al.*, Fiz. Tekh. Poluprovodn. (St. Petersburg) **32**, 905 (1998) [Semiconductors **32**, 807 (1998)].
6. J. Muller, F. Finger, R. Carius, and H. Wagner, Phys. Rev. B **60**, 11666 (1999).
7. R. Fluckiger, J. Meier, M. Goetz, and A. Shah, J. Appl. Phys. **77**, 712 (1995).
8. P. Torres, J. Meier, R. Fluckiger, *et al.*, Appl. Phys. Lett. **69**, 1373 (1996).
9. A. G. Kazanskiĭ, H. Mell, E. I. Terukov, and P. A. Forsh, Fiz. Tekh. Poluprovodn. (St. Petersburg) **34**, 373 (2000) [Semiconductors **34**, 367 (2000)].
10. J. H. Werner, in *Polycrystalline Semiconductors* (Springer-Verlag, Berlin, 1989); Springer Proc. Phys. **35**, 345 (1989).
11. T. D. Moustakas and W. Paul, Phys. Rev. B **16**, 1564 (1997).
12. P. Kanschat, K. Lips, and W. Fuhs, J. Non-Cryst. Solids **266–269**, 524 (2000).
13. K. V. Kougia and I. S. Shlimak, in *Advances in Disordered Semiconductors*, Vol. 3: *Transport, Correlation and Structural Defects*, Ed. by H. Fritzsche (World Sci., Singapore, 1990), Vol. 3, p. 213.
14. R. Carius, F. Finger, U. Backhausen, *et al.*, Mater. Res. Soc. Symp. Proc. **467**, 283 (1997).
15. F. Finger, J. Muller, C. Malten, *et al.*, J. Non-Cryst. Solids **266–269**, 511 (2000).

Translated by D. Mashovets

Semiconductors, Vol. 35, No. 8, 2001, pp. 956–961. Translated from Fizika i Tekhnika Poluprovodnikov, Vol. 35, No. 8, 2001, pp. 995–1000.

AMORPHOUS, VITREOUS, AND POROUS SEMICONDUCTORS

X-ray Spectroscopic Study of Electronic Structure of Amorphous Silicon and Silicyne

A. I. Mashin*, A. F. Khokhlov*, É. P. Domashevskaya, V. A. Terekhov**, and N. I. Mashin***

** Nizhniĭ Novgorod State University, Nizhniĭ Novgorod, 603600 Russia*

e-mail: mashin@phys.unn.runnet.ru

*** Voronezh State University, Voronezh, 394693 Russia*

Submitted November 14, 2000; accepted for publication December 27, 2000

Abstract—X-ray and ultrasoft X-ray spectroscopy have both been applied to study SiK_β and SiL_{23} emission spectra of crystalline silicon (*c*-Si), amorphous hydrogenated silicon (*a*-Si:H), and silicyne (a new allotropic linear-chain form of silicon). SiL_{23} spectra of silicyne show three peaks instead of two observed in crystalline and amorphous silicon. The third peak lies in the high-energy range at 95.7 eV, its intensity constituting ~75% of that of the main peak. An additional peak is also observed in the short-wavelength part of the SiK_β spectrum. Such a significant difference in shape between the X-ray spectra of amorphous silicon and silicyne is attributed to the existence of a pronounced π component in the chemical bonds between silicon atoms in silicyne. *© 2001 MAIK "Nauka/Interperiodica".*

INTRODUCTION

In studying the effect of annealing on the short-range order structure and properties of amorphous silicon prepared by decomposition of silane in rf glow discharge, we obtained silicon with a short-range-order structure other than tetrahedral. The new material, which we named silicyne [1, 2], was found to be amorphous. According to electron diffraction studies, it has a low coordination number (~2), a large valence angle (~180°), and an average interatomic distance (2.1 Å) smaller than that in crystalline silicon. In our opinion, this material is a silicon analog of carbine and is mainly composed of linear chains of silicon atoms with multiple bonds of the types $(–Si\equiv Si–Si\equiv Si–)_n$ and $(=Si=Si=Si=Si=)_n$. The atomic chains are bound together by van der Waals forces or bridging covalent bonds.

In turn, the atomic structure of a substance determines its electronic structure and properties. In view of the lack of a strict periodicity in amorphous substances, elucidating their electronic structure is rather complicated and has not been completely accomplished.

Two stages can be distinguished in the development of concepts concerning the electronic structure of amorphous semiconductors [3, 4]. The first of these is mainly associated with the use of qualitative models and is devoted to determining the range of the relevant problems. This stage was reflected in sufficient detail in A.I. Gubanov's monograph [5] and his later works aimed at reformulating the classical methods for electronic structure calculation, as applied to amorphous solids. The second stage of theoretical analysis of the electronic structure of noncrystalline materials, represented in N.F. Mott's monographs [6, 7], was associated with specific calculations and estimates made for real disordered systems.

Among the ideas prevailing in the theory of the electronic structure of disordered semiconductors, three concepts are commonly distinguished at present: (i) tight-binding—MO LCAO approximation [3, 8, 9]; (ii) nearly free electron approximation, relying upon the scattering theory, and the Green's function method [6, 10, 11]; and (iii) random-field approximation [12–14].

The first two concepts involve concrete numerical calculations pretending to accurately describe the electronic structure of an amorphous semiconductor. The third concept is mainly of methodological importance and allows for the assessment of the correctness of the first two.

The short-range order in amorphous silicon is the same as that in the corresponding crystal. This is only possible with the nature of chemical bonding being about the same. The valence shell of a silicon atom contains 8 states (*s* and *p*) and 4 electrons. When a crystal is formed, the shell wave functions are hybridized, becoming equivalent sp^3 orbitals. The 8 available states are split into two groups, bonding and antibonding, each with 4 states. The states of the first group are responsible for the formation of covalent chemical bonds. Since the valence shell is 4 electrons short of completion, the coordination number is 4. These same states form the basis used to construct the Bloch wave functions of the valence band. The states of the second group give rise to the conduction band. In passing to an amorphous substance, this scheme of the atomic valence state splitting remains valid [12]. Only the Bloch function considerations are to be discarded; however, as before, it would be expected that the wave func-

tions of the valence and conduction bands are mainly formed from, respectively, bonding and antibonding orbitals.

Thus, annealing leads to changes not only in the atomic structure of the substance but also in the nature of silicon bonds, accompanied by changes in the energy spectrum of valence electrons. Experimental verification of this statement requires that the energy distribution of the valence electron density be measured before and after annealing. In this study, we made an attempt to obtain the required density of states from X-ray emission spectra, since it is well known [15] that X-ray spectroscopy furnishes detailed information about the valence electron states in compounds and films.

SAMPLES AND EXPERIMENTAL PROCEDURE

Thin silicyne films were obtained by annealing films of amorphous hydrogenated silicon *a*-Si:H in a vacuum at 500°C for 30 min. The starting ~400-nm-thick *a*-Si:H was deposited by decomposition of silane in an rf glow discharge onto substrates of crystalline silicon, fused silica, and polycor. The substrate temperature in the course of deposition was 50 and 250°C.

Experimental emission SiK_β spectra were measured on a VRA-20R automated vacuum X-ray-fluorescent spectroanalyzer. X-rays were obtained using an X-ray tube with rhodium cathode. The cathode voltage was 35 kV and the current was ~20 mA. As a dispersing element, an EDDT (ethylenediamine ditartrate, $C_6H_{14}N_2O_6$) crystal in [020] orientation ($2d$ = 0.8808 nm) was used. As a detector, a flow-type proportional counter operating on a mixture of argon and methane (10%) was employed. The time of a single count was chosen so as to ensure recording of no less than 5000 pulses at each X-ray quantum energy. The signal-to-background ratio was no less than 5. The instrument ensured energy resolution no worse than 0.4 eV. All the spectra are normalized to the main peak intensity, and each curve in the figures is an average of five measurements.

SiL_{23} lines were recorded with an RSM-500 spectrometer–monochromator.

The acceleration voltage applied to the tube was 3 kV; tube current, 2 mA. As a photocathode for photon detection, a CsI film was used.

RESULTS AND DISCUSSION

Experimental SiK_β emission spectra obtained with unannealed *a*-Si:H films and those annealed at 500°C are presented in Figs. 1a and 1b.

Films of amorphous hydrogenated silicon were grown at substrate temperature of 50°C. For comparison, Fig. 1c shows a SiK_β spectrum of KDB-2000 single-crystal silicon.

As seen from Fig. 1, for all the samples the main peak of X-ray spectrum intensity lies at an energy $E \approx$ 1836 eV. Mention should also be made of the asymmetry and fine structure in virtually all of the spectra. The fine structure—designated as A_K, B_K, and C_K—is easily reproducible in repeated measurements. For crystalline silicon (Fig. 1c), the SiK_β line has two peaks—the main at 1836 eV and an additional (with intensity of ~35% relative to that of the main peak) at $E \approx$ 1832 eV [15]. The peak in the low-energy part of the SiK_β spectrum is commonly attributed [16] to the structural ordering of atoms, with its position determined by the size of the first Brillouin zone ($k = \pm\pi/a$, where a is the magnitude of the primitive vector of the crystal lattice; a is determined by the interatomic distance).

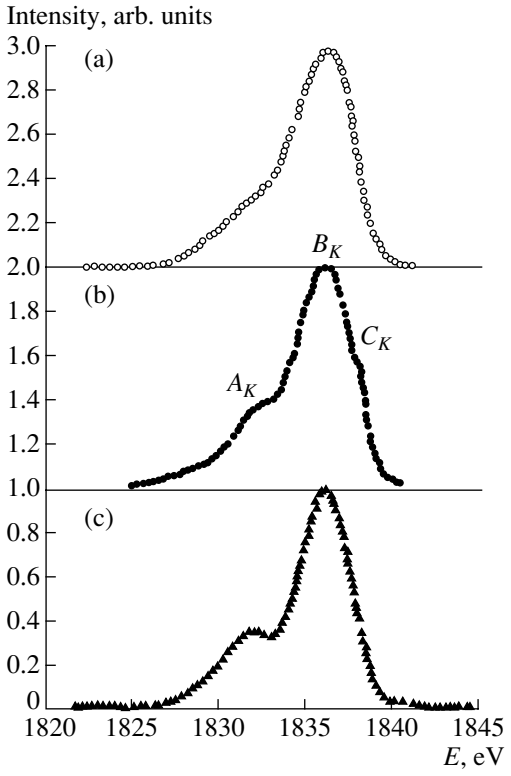

Fig. 1. SiK_β spectra (a) of unannealed and (b) annealed at 500°C amorphous hydrogenated silicon and (c) single-crystal silicon.

As would be expected, distortions of the atomic structure in amorphous silicon films lead to broadening and overlapping of peaks in the X-ray spectra (Fig. 1a), with the result that the fine structure is poorly pronounced. The fine structure may be absent in the X-ray spectra of amorphous hydrogenated silicon for other reasons. For example, some authors [3] believe that the presence of rings formed by bonds imposes boundary conditions on the wavefunctions. This leads to the quantization of the electronic spectrum and formation of density-of-states peaks in the valence band. In crystalline silicon (*c*-Si), the double-peak structure of the spectrum is due to the presence of six-membered rings not necessarily associated with the existence of a long-

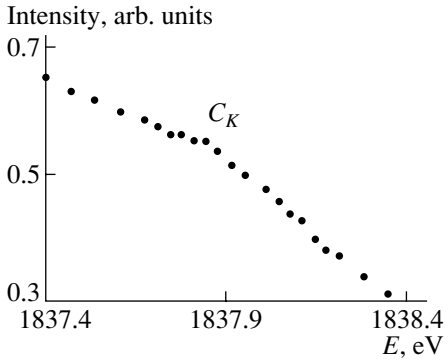

Fig. 2. Shoulder in the SiK_β spectrum of *a*-Si:H annealed at 500°C.

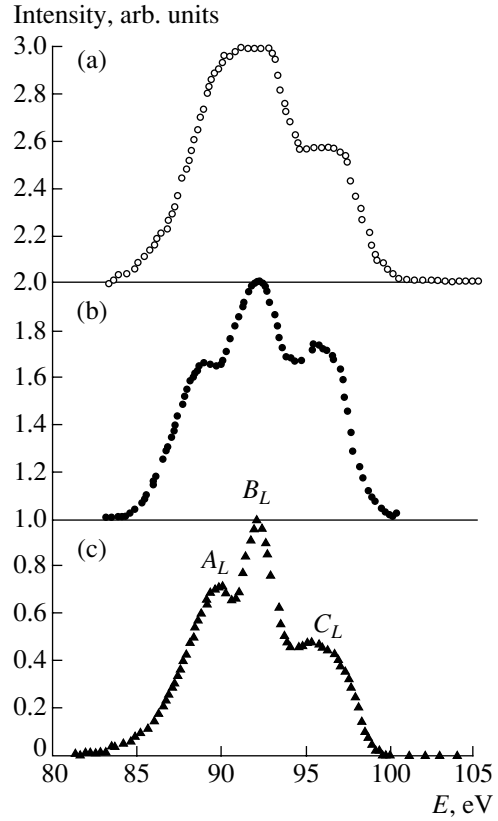

Fig. 3. SiL_{23} spectra (a) of unannealed and (b) annealed at 500°C amorphous hydrogenated silicon and (c) single-crystal silicon.

range order. If the structure contains rings of different sizes, several peaks shifted in energy must be formed, with the summation of these peaks resulting in that a smoothed and virtually structureless spectrum is observed. On the other hand, it should be kept in mind that an unannealed *a*-Si:H film under study contains up to 40 at. % hydrogen. Theoretical studies have shown [17] that at least three configurations with several hydrogen atoms—SiH_2, SiH_3, and $(SiH_2)_2$—are characterized by two density-of-states peaks in the valence band, which may yield peaks lying between peaks A_K and B_K in the X-ray spectra. In our opinion, the rearrangement of the atomic structure of amorphous silicon, manifesting itself in an increase in atomic ordering upon annealing the amorphous film at 500°C, is responsible for the appearance, in addition to the main peak B_K at ~1836 eV, of a peak A_K at ~1832 eV and shoulder C_K in the high-energy part of the spectrum at ~1838 eV. For clarity, the high-energy part of the spectrum in Fig. 1b, containing the shoulder C_K, is presented in Fig. 2. Despite the fact that the film remains amorphous upon annealing, the low-energy peak A_K is sufficiently well pronounced and its intensity (~33%) is comparable with that in crystalline silicon.

Figure 3 presents SiL_{23} spectra obtained with the same samples as the SiK_β spectra in Fig. 1, with energy measured from the 2*p* level of Si.

As seen from Fig. 3a, the distribution of valence electrons in the starting *a*-Si:H film deposited at 50°C is similar to that reported in [18]. A broad main peak B_L, corresponding to 3*s* states of Si, is observed at 90–92 eV with a shoulder characteristic of tailing of the electronic density of states.

After annealing at 500°C (Fig. 3b), the main density-of-states peak becomes more pronounced and a peak A_L appears at low energies. A similar peak can be seen in the spectrum of crystalline silicon (Fig. 3c), but its position and relative intensity are different. For example, the energy and relative intensity of peak A_L are 89.6 eV and 75% for crystalline silicon, and 89.2 eV and 70% for annealed *a*-Si:H films. In addition, annealing of *a*-Si:H results in that a peak C_L appears at 95.7 eV (with intensity of ~75%) instead of the shoulder with intensity of ~48%. No such valence electron distribution has been observed previously in silicon or solid compounds.

As in the case of X-ray emission SiK_β spectra, the existence of a fine structure of 3*s* state of Si in the form of two peaks A_L and B_L is due to partial atomic ordering. The energy spacing between two low-energy peaks of the density of *s* states in the valence band of substances composed of elements belonging to Groups IV and V of the Periodic Table was studied in [19]. It was established that for all of these materials the energy spacing ΔE between peaks A_L and B_L is related to the interatomic distance by

$$\Delta E[\text{eV}] = 8.0–2.2d[\text{Å}]. \quad (1)$$

According to Eq. (1), the increase in the energy spacing between peaks A_L and B_L by 0.4 eV, compared with crystalline silicon, is due to a decrease in the interatomic distance d by 0.2 Å. This result is in excellent agreement with the structural data obtained in the present study.

The peak C_L, untypical of Si, indicates that the type of chemical bonding between silicon atoms changes.

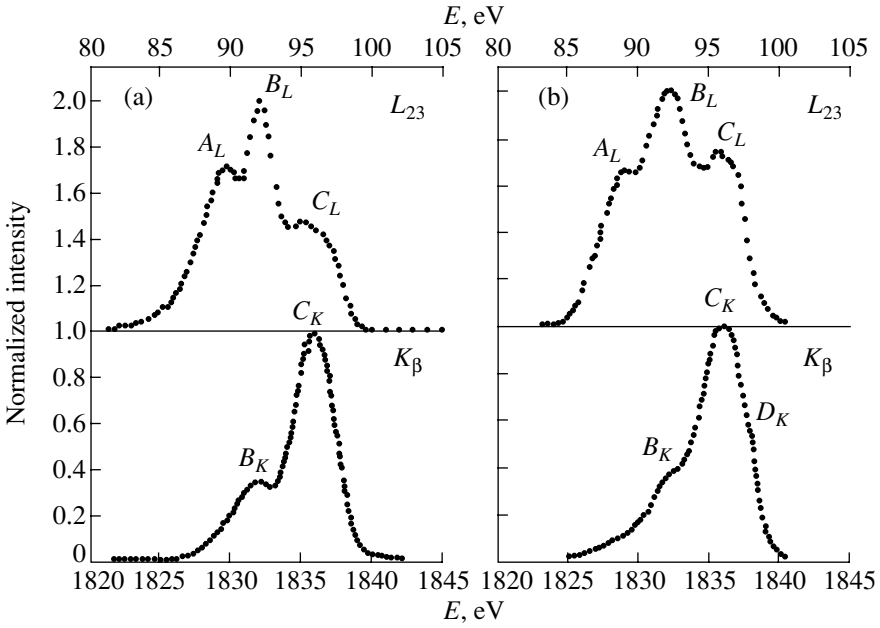

Fig. 4. SiL_{23} and SiK_β spectra (a) of KDB-2000 crystalline silicon and (b) *a*-Si:H annealed at 500°C.

It is known that X-ray emission bands of solids appear in filling of vacancies by electrons at inner levels, created by X-ray photons or high-energy electrons. SiK_β emission spectra reflect the state of 3*p* electrons ($K_{\beta 3}$ transition: $M_{II}(n = 3; l = 1; j = l - s = 1/2) \longrightarrow K(n = 1; l = 0; j = 1/2)$ and $K_{\beta 1}$ transition: $M_{III}(n = 3; l = 1; j = l - s = 3/2) \longrightarrow K(n = 1; l = 0; j = 1/2)$); Si*L* emission spectra, the state of 3*s* electrons (L_{II} transition: $M_I(n = 3; l = 1; j = 1/2) \longrightarrow L_{II}(n = 2; l = 1; j = 1/2)$ and L_{III} transition: $M_I(n = 3; l = 0; j = 1/2) \longrightarrow L_{III}(n = 2; l = 1; j = 3/2)$) and, possibly, 3*d* electrons ($L_{II\beta 1}$ transition: $M_V(n = 3; l = 2; j = 5/2) \longrightarrow L_{II}(n = 2; l = 1; j = 1/2)$, $L_{III\alpha 1}$ transition: $M_V(n = 3; l = 2; j = 5/2) \longrightarrow L_{III}(n = 2; l = 1; j = 3/2)$, and $L_{III\alpha 2}$ transition: $M_{IV}(n = 3; l = 2; j = 3/2) \longrightarrow L_{III}(n = 2; l = 1; j = 3/2)$). The distribution of the emission band intensity can be written in a single-electron approximation as follows [20–23]:

$$I(\nu) = \nu^* \sum_f |\langle \varphi_i | H' | \varphi_f \rangle|^2 \delta(E_i - E_f - h\nu). \quad (2)$$

Designating as $M_{if} = \int \varphi_i H' \varphi_f d\mathbf{r}$ the matrix element for the probability of the transition of an electron from the valence band with wave function φ_f and energy eigenvalue E_f to an inner-level vacancy with wave function φ_i and taking into account that the inner-level energy E_i is fixed and the difference $E_i - h\nu = E$ is the electron energy in the valence band, we can rewrite expression (2) as

$$I(E) = \nu^* \sum_f \delta(E - E_f) |M_{if}|^2. \quad (3)$$

In the case of a crystal, where the electron quasi-momentum **k** is a good quantum number, expression (3) is transformed to the form [20, 22]

$$I(E) = \nu^* \sum_n \int_s \{ |\langle \varphi_i | H' | \varphi_{n\mathbf{k}} \rangle|^2 / |\nabla_{\mathbf{k}} E_n(\mathbf{k})| \} ds, \quad (4)$$

where integration is done over a constant-energy surface *s* and summation, over all valence bands $E_n(\mathbf{k})$. According to [21], the expression for the density of states can be written as

$$g(E) \propto \sum_n \int_s ds / |\nabla_{\mathbf{k}} E_n(\mathbf{k})|. \quad (5)$$

A comparison of formulas (2)–(5) shows that the emission band intensity must exhibit the same features as the density of states. However, the matrix element in the formula for intensity may lead to different relative heights of features in $I(E)$ and $g(E)$ at the same energy positions. If a strongly localized core function φ_i and wave function φ_f are represented as expansions in atomic wave functions, which can be done under conditions of a dipole approximation for H', then the expression for intensity is written in the form [20]

$$I(E) \approx \nu [P_{l,l-1}(E) g_{l-1}(E) + P_{l,l+1}(E) g_{l+1}(E)], \quad (6)$$

where $P_{l,l-1}$, $P_{l,l+1}$ are the transition probabilities and g_{l-1}, g_{l+1} are the partial densities of states. According to Eq. (6), the K_β bands must reflect the distribution of *p* states, $g_p(E)$; the L_{23} bands, the distribution of *s* and *d*

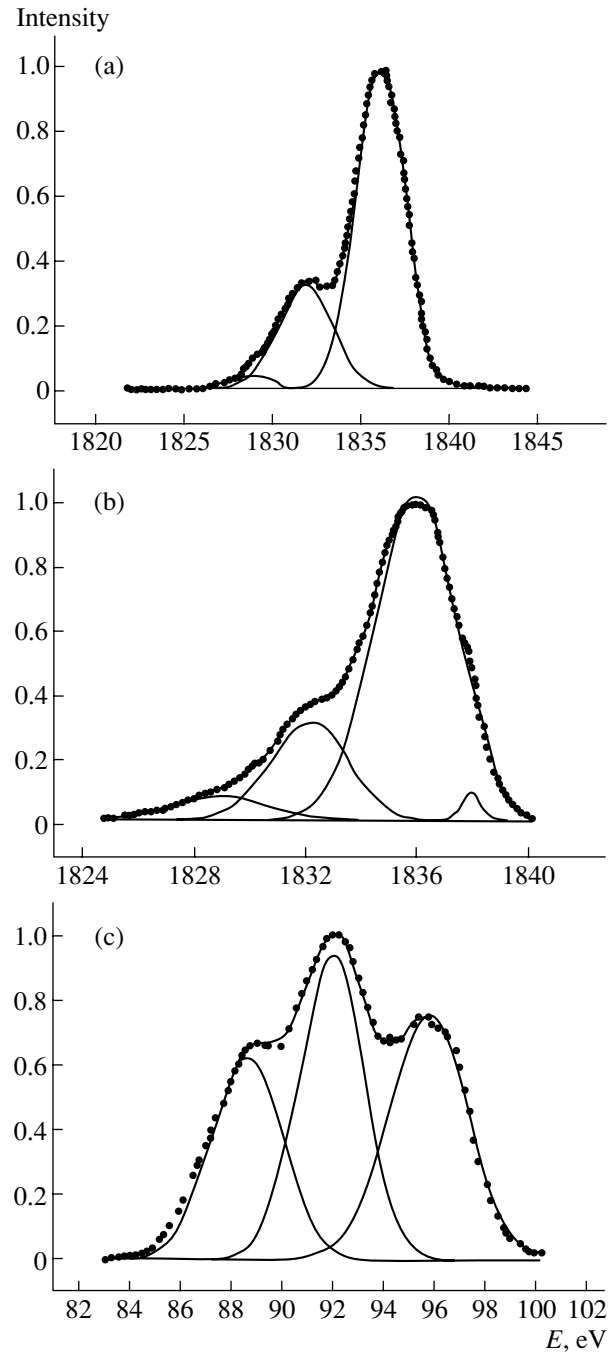

Fig. 5. SiK_β spectrum of (a) *c*-Si and (b, c) SiK_β and SiL_{23} spectra of *a*-Si:H annealed at 500°C, represented as superposition of Gaussians.

states, $g_s(E)$ and $g_d(E)$. The total density of states $g(E)$ can be represented as a sum of partial densities:

$$g(E) = g_s(E) + g_p(E) + g_d(E) + \dots . \qquad (7)$$

Due to the indeterminacy in the relative contributions from different bands, it is virtually impossible to deduce the total density of states from the experimental emission bands. However, considering the K_β and L_{23} spectra characterizing, respectively, the 3*p* and 3*s* electronic states, we can obtain a more comprehensive pattern of how the chemical bonds between silicon atoms in *a*-Si:H are transformed upon annealing.

Figures 4a and 4b show the K_β and L_{23} spectra for, respectively, *c*-Si and *a*-Si:H films annealed at 500°C. The X-ray spectra are reduced to a common energy scale.

As follows from Fig. 4a, on the common energy scale the energy positions of the B_L and B_K peaks, as well as the C_L and C_K peaks, coincide pairwise. The SiK_β spectrum contains no clearly pronounced peak corresponding to A_L. However, it can be seen that the SiK_β spectra are strongly asymmetric—the spectrum has a long tail in the low-energy region. Taking this circumstance into account, we represented the SiK_β spectra as a superposition of several Gaussians (see Fig. 5). The correctness of such an approach was reported in [24].

With this done, it can be seen (Fig. 5a) that the SiK_β spectrum for *c*-Si is a superposition of three rather than two peaks. The third peak lies in the low-energy part of the spectrum ~2.5 eV to the left of peak B_K. Thus, its position coincides rather nicely with the position of peak A_L in the SiL_{23} spectrum. The following conclusion can be made on the basis of the obtained data: molecular orbitals in the form of a superposition (in various proportions) of 3*s* and 3*p* atomic orbitals of silicon correspond to all of the three peaks in the electron density distribution in the valence band of crystalline silicon. This result seems to be quite reasonable. Indeed, silicon is tetravalent in the crystalline state. This fact can readily be accounted for by the hybridization of atomic orbitals (see, e.g. [25]). The hybridization is reduced to the formation of four identical (hybrid) molecular orbitals, designated as sp^3. All the orbitals formed belong to the σ type, with the corresponding expressions readily written on the basis of symmetry considerations:

$$\sigma_{111} = (1/2)(s + p_x + p_y + p_z),$$

$$\sigma_{\bar{1}\bar{1}1} = (1/2)(s - p_x - p_y + p_z),$$

$$\sigma_{1\bar{1}\bar{1}} = (1/2)(s + p_x - p_y - p_z),$$

$$\sigma_{\bar{1}1\bar{1}} = (1/2)(s - p_x + p_y - p_z).$$

Being equivalent, all the four hybridized orbitals appear with the same weighting coefficients. The factor 1/2 serves for normalization.

In the case of *a*-Si:H, the SiK_β and SiL_{23} spectra can also be represented as a superposition of three peaks. Their positions coincide rather well with the positions of the corresponding peaks observed in this study for *c*-Si. The only difference is that the peaks in the amorphous material are somewhat broader.

The difference between the shapes of SiK_β and SiL_{23} spectra of *a*-Si:H annealed at 500°C and those of *c*-Si and *a*-Si:H is fundamental. For example, the energy spacing between the $B_k(B_L)$ and $C_k(C_L)$ peaks increases, as already mentioned, by 0.4 eV. A peak with an intensity of ~75% appears instead of the shoulder C_L (~50%) in the SiL_{23} spectrum. Such a change in the X-ray spectra and, correspondingly, in the distribution of the electron density in the valence band of the semiconductor indicates a significant change in the character of hybridization of atomic orbitals in the formation of molecular orbitals of the σ type in the material under study. In addition, a minor peak (with an intensity of ~11%) appears in the high-energy part of the SiK_β spectrum at ~1838 eV. This peak has no counterpart in the SiL_{23} spectrum (the decomposition of the given spectrum in Gaussians (see Fig. 5c) gives only three peaks corresponding to the low-energy peaks in the SiK_β spectrum). Thus, it may be assumed that the fourth peak in the SiK_β spectrum of *a*-Si:H annealed at 500°C corresponds to a bonding molecular orbital formed only by 3*p* atomic orbitals of silicon, i.e., to a silicon π bond.

CONCLUSION

Thus, the data obtained from X-ray spectra confirm the results of our previous structural studies, indicating that the interatomic distance in amorphous silicon films decreases upon annealing at 500°C, and verify our assumptions that the nature of chemical bonding is changed in the process; i.e., there appears a substantial π component and valence atomic orbitals of Si atoms go from sp^3- to *sp*-hybridization with the formation of multiple bonds between silicon atoms.

ACKNOWLEDGMENTS

This study was financially supported by the Ministry of Education of the Russia Federation (grant no. E00-3.4-225).

REFERENCES

1. A. F. Khokhlov, A. I. Mashin, and D. A. Khokhlov, Vestn. NO Ross. Akad. Estestv. Nauk **2**, 191 (1998)
2. P. F. Schewe and B. Stein, *Physics News Update*, *The American Institute of Physics Bulletin of Physics News* (1998), No. 338, Story 3.
3. *The Physics of Hydrogenated Amorphous Silicon*, Vol. 2: *Electronic and Vibrational Properties*, Ed. by J. D. Joannopoulos and G. Lucovsky, with contributions by D. E. Carlson *et al.* (Springer-Verlag, New York, 1984; Mir, Moscow, 1988).
4. K. K. Shvarts, *Physics of Optical Recording in Dielectrics and Semiconductors* (Zinatne, Riga, 1986).
5. A. I. Gubanov, *Quantum Electron Theory of Amorphous Conductors* (Akad. Nauk SSSR, Moscow, 1963; Consultants Bureau, New York, 1965).
6. N. F. Mott, *Metal–Insulator Transitions* (Taylor & Francis, London, 1974; Nauka, Moscow, 1979).
7. N. F. Mott, Adv. Phys. **16**, 49 (1967).
8. J. D. Joannopoulos and W. Pollard, Solid State Commun. **20**, 947 (1976).
9. D. Weaire, Phys. Rev. Lett. **26**, 1541 (1971).
10. J. M. Ziman, *Models of Disorder: the Theoretical Physics of Homogeneously Disordered Systems* (Cambridge Univ. Press, Cambridge, 1979; Mir, Moscow, 1982).
11. P. Lloyd, Proc. Phys. Soc. London **90**, 207 (1967).
12. V. L. Bonch-Bruevich, I. P. Zvyagin, R. Kaiper, *et al.*, *Electron Theory of Disordered Semiconductors* (Nauka, Moscow, 1981).
13. I. M. Lifshits, S. A. Gredeskul, and L. A. Pastur, *Introduction to the Theory of Disordered Systems* (Nauka, Moscow, 1982; Wiley, New York, 1988).
14. M. I. Klinger, Solid State Commun. **45**, 949 (1983).
15. A. Simunek, M. Polcik, and G. Wiech, Phys. Rev. B **52**, 11865 (1995).
16. M. A. Blokhin, *Physics of X-rays* (Gostekhteorizdat, Moscow, 1953).
17. J. D. Joannopoulos, J. Non-Cryst. Solids **32**, 241 (1979).
18. É. P. Domashevskaya, I. Ya. Mittova, N. I. Ponomareva, *et al.*, Poverkhnost, No. 6, 138 (1985).
19. L. Ley, R. A. Pollak, S. P. Kowalczyk, *et al.*, Phys. Rev. B **8**, 641 (1973).
20. V. A. Terekhov, Author's Abstracts of Doctoral Dissertation (Voronezh, 1994).
21. V. V. Nemoshkalenko and V. G. Aleshin, *Theoretical Foundations of X-ray Emission Spectroscopy* (Naukova Dumka, Kiev, 1974).
22. A. Meisel, G. Leonhardt, and R. Szargan, *Röntgenspektren und chemische Bindung* (Geest und Portig, Leipzig, 1977; Naukova Dumka, Kiev, 1980); *X-ray Spectra and Chemical Binding* (Springer-Verlag, New York, 1989).
23. *X-ray Spectra of Molecules*, Ed. by A. V. Nikolaev (Nauka, Novosibirsk, 1977).
24. L. N. Mazalov, V. Yu. Yumatov, V. V. Murakhtanov, *et al.*, in *X-ray Spectra of Molecules*, Ed. by A. V. Nikolaev (Nauka, Novosibirsk, 1977).
25. D. M. Vasil'ev, *Physical Crystallography* (Metallurgiya, Moscow, 1981).

Translated by M. Tagirdzhanov

Semiconductors, Vol. 35, No. 8, 2001, pp. 962–969. Translated from Fizika i Tekhnika Poluprovodnikov, Vol. 35, No. 8, 2001, pp. 1001–1008.

PHYSICS OF SEMICONDUCTOR DEVICES

Threshold Characteristics of λ = 1.55 μm InGaAsP/InP Heterolasers

G. G. Zegrya, N. A. Pikhtin, G. V. Skrynnikov, S. O. Slipchenko, and I. S. Tarasov

Ioffe Physicotechnical Institute, Russian Academy of Sciences, Politekhnicheskaya ul. 26, St. Petersburg, 194021 Russia

Submitted October 2, 2000; accepted for publication October 6, 2000

Abstract—Temperature dependences of the threshold characteristics of InGaAsP/InP quantum well (QW) lasers have been studied. The main contribution to the threshold current is made by the thresholdless Auger recombination. The observed power-law temperature dependence of the threshold current is explained by the predominance of the thresholdless Auger recombination in QWs over the threshold Auger process. © *2001 MAIK "Nauka/Interperiodica".*

1. INTRODUCTION

A model describing the threshold characteristics of quantum well (QW) lasers at the lasing threshold has recently been developed [1]. This model analyzes the temperature dependence of thresholdless Auger recombination processes in QWs and the carrier emission associated with weak localization of electrons in a shallow QW. Threshold characteristics of a $\lambda \approx 1.3$ μm laser have been calculated in terms of this model [1]. However, even stronger interest is aroused by properties of long-wavelength ($\lambda = 1.55$ μm) InGaAsP/InP lasers because of their wide application in optical communication lines.

In this context, a study of how the threshold current density and its components depend on temperature, cavity length, and the number of QWs in laser structures emitting at $\lambda \approx 1.55$ μm is currently necessary. A detailed analysis of the dependence of the laser threshold characteristics on the heterostructure parameters would make it possible to optimize the structure and raise output power.

The goal of this study was to analyze experimentally the temperature and threshold characteristics of separate-confinement double heterostructure InGaAsP/InP lasers and to compare the data obtained with the results of calculations in terms of the existing theoretical model [1].

2. EXPERIMENTAL SAMPLES

Separate-confinement double heterostructures with two or ten QWs and strained active regions (Fig. 1) were chosen as objects of study. All the samples were grown on *n*-InP substrates by conventional metallo-organic chemical vapor composition [2].

Structures with different numbers of QWs had waveguide layers with dissimilar solid solution compositions. The composition of the InGaAsP solid solution of strained QWs was the same in all cases.

The QW width was chosen to be $d_a = 50$ and 70 Å for structures with two and ten QWs, respectively. The active region and waveguide layers were nominally undoped. The wide-gap *p* emitter and the 0.3-μm-thick contact layer were doped to 7×10^{17} cm^{-3} and 2×10^{18} cm^{-3}, respectively. Stripes 100 μm wide were formed by photolithography in the insulating SiO_2 layer on the fabricated laser heterostructures [3].

The structure was divided into laser diodes with cavity length varying within the range $L = 200$–2500 μm. Si/SiO_2 mirrors with reflectivity $R > 0.95$ and antireflection coating with $R < 0.04$ were deposited onto the cavity edges. The fabricated diodes were soldered with indium to a copper heat sink.

3. EXPERIMENT

A pulse duration of 2 μs was chosen for studying the laser diodes in pulsed mode. This mode is preferable, since it does not require any intricate experimental technique and allows active region heating in a laser diode to be considered negligible. We assumed that the temperature of the laser's active region is equal to that of the copper heat sink and varied in the range of 10–60°C using a Peltier element. It was measured with a copper–constantan thermocouple attached directly to the heat sink. The light–current characteristics of the lasers were recorded in the CW mode using water to cool the laser diodes.

Figures 2a and 2b present the experimentally observed temperature dependences of the threshold

1063-7826/01/3508-0962$21.00 © 2001 MAIK "Nauka/Interperiodica"

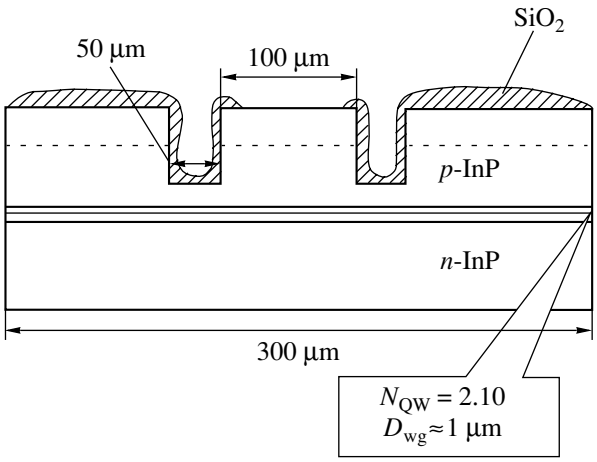

Fig. 1. Separate-confinement laser structure. $\lambda = 1.55$ μm. $N_{QW} = 2$ and 10, with, respectively, $d_a = 50$ and 70 Å; waveguide thickness $D_{wg} \approx 1$ μm.

current for lasers with two and ten QWs. For the former, the threshold current J_{th} nearly doubles when the temperature is raised from 10 to 60°C (Fig. 2a, curve *1*). If the experimental temperature dependence of the threshold current density is approximated by an exponential function [4]

$$J_{th} = J_0 \exp(-E_a/kT) \quad (1)$$

with activation energy E_a, then the E_a value is found to be much lower than kT and lower than the activation energy obtained from the expression for the bulk [7],

$$E_a = 2\frac{m_c}{m_{hh}}E_g, \quad (2)$$

where E_g is the band gap, and m_c and m_{hh} are the electron and heavy-hole effective masses. Hence, it follows that the optimal approximation for the experimental data is a power law, rather than an exponential function of temperature.

For a laser structure with ten QWs, the threshold current $J_{th}(T)$ varies by approximately a factor of 3 within the same temperature interval 10–60°C (Fig. 2b, curve *1*); i.e., the threshold current is higher for the structure with the most QWs, and its temperature dependence is steeper (in this case, the temperature dependence can also be approximated by a power-law function). As shown below, the increase in the laser threshold current and the enhancement of its temperature dependence with growing number of QWs are associated with the increase in the coefficient of intraband absorption, approximately proportional to the number of QWs [5].

Dependences of the threshold current on the inverse cavity length ($1/L$) have been studied at room temperature in a wide range of cavity lengths for two laser structures with different numbers of QWs: $N_{QW} = 2$

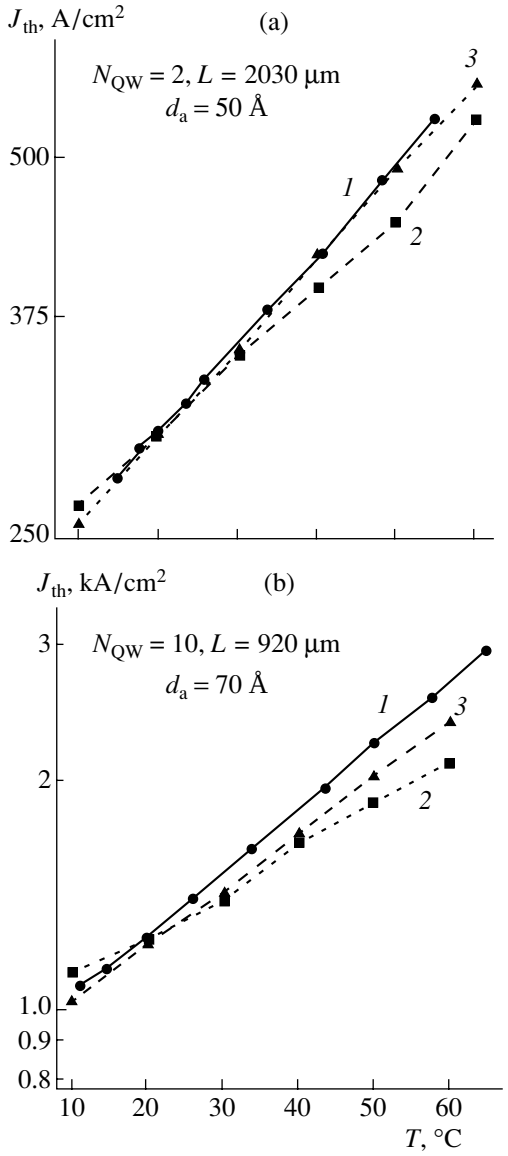

Fig. 2. Experimental (*1*) and calculated (*2*, *3*) temperature dependences of the threshold current for lasers with (a) 2 and (b) 10 QWs.

(Fig. 3a, curve *1*) and $N_{QW} = 10$ (Fig. 3b, curve *1*). As expected, the $J_{th}(1/L)$ dependences for these two structures are different owing to the increase in internal losses of laser radiation with growing number of QWs, N_{QW}.

Commonly, a characteristic temperature T_0 is used as a parameter specifying a laser structure. A rather simple approximation of the temperature dependence of the threshold current

$$J_{th}(T) = J_0 \exp(T/T_0), \quad (3)$$

yields an experimental parameter characterizing the temperature stability of a laser diode. The dependence

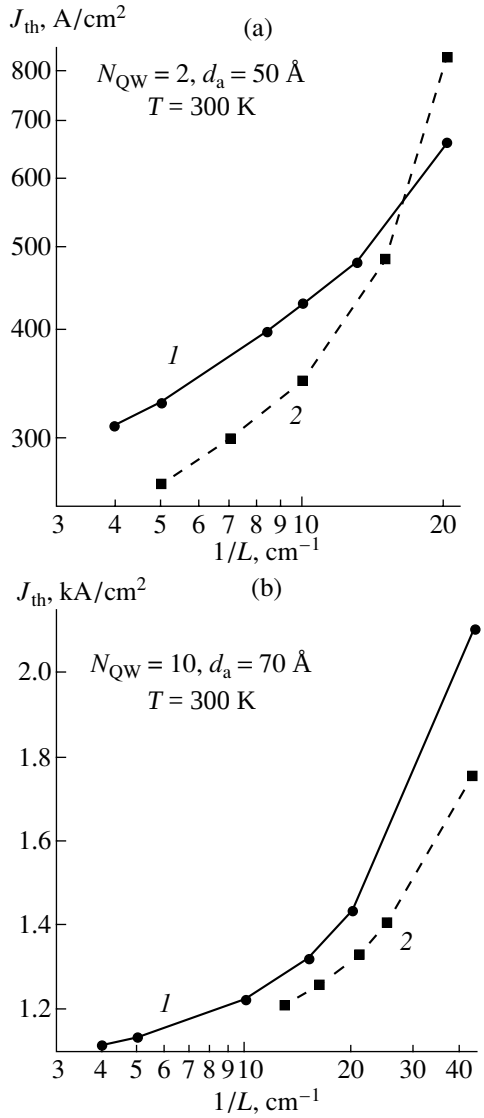

Fig. 3. Threshold current vs. inverse cavity length for lasers with (a) 2 and (b) 10 QWs. (*1*) Experiment and (*2*) calculation.

of the characteristic temperature T_0 on the cavity length L was calculated for a laser with two QWs from the experimental temperature dependences (Fig. 4, curve *1*). The characteristic temperature grows with increasing cavity length L, since the threshold current decreases with increasing L at a fixed temperature (Fig. 3). The increase in T_0 with L means, in the first place, that the threshold concentration n_{th}^{2D} decreases with increasing L.

It is noteworthy that the optical power of the long-cavity laser diodes with a 100-μm-wide mesa-stripe contact, emitting at $\lambda = 1.55$ μm, was as high as 2.5 W. As far as we know, the highest previously reported CW optical power at the $\lambda = 1.48$ μm wavelength is 5 W for a laser diode with a 200-μm-wide mesa-stripe contact [6].

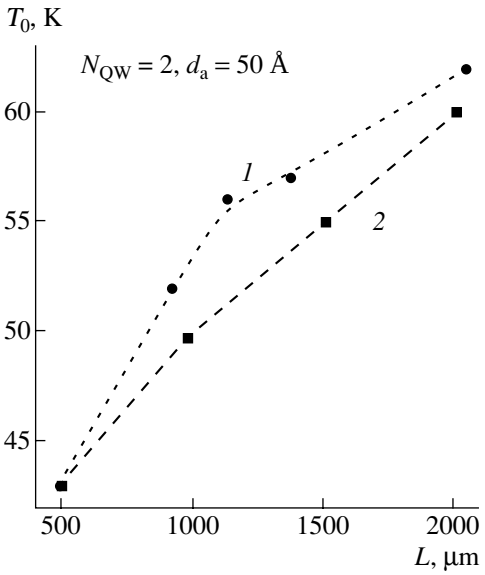

Fig. 4. Characteristic temperature T_0 vs. cavity length for a laser with 2 QWs. (*1*) Experiment and (*2*) calculation.

4. THEORETICAL MODEL

All the calculations were performed in terms of the model developed in [1]. This model takes into account the nonradiative Auger recombination, the current leakage of carriers from the active region, and the weak localization of electrons in a "shallow" QW. The Auger recombination in heterostructures differs basically from that in a homogeneous semiconductor [7]. In a QW, the Auger recombination is thresholdless and its rate is a weak (power-law) function of temperature [8, 9]. By using the thresholdless Auger recombination mechanism in the model it was possible to describe unambiguously the experimental temperature dependence of the threshold current for QW lasers.

The condition for the lasing threshold can be written as:

$$N_{QW} = \Gamma g_0^{\max} = \alpha_{int} + \alpha_{exp}, \qquad (4)$$

where Γ is the optical confinement factor for a single QW; $g_0^{\max}$, the maximum gain; α_{int}, the internal loss at the lasing threshold; and $\alpha_{exp} = (1/L)\ln(1/R)$, the mirror loss. We assume here that the effect of nonuniform carrier distribution among QWs is insignificant near the lasing threshold.

The gain per single QW can be written as [1]:

$$g_0(\hbar\omega) = I_{cv}^2 \frac{\pi}{a}\frac{\alpha}{\sqrt{\epsilon}}\frac{M}{1+M}\left(1-\frac{m_c}{m_0}\right)\frac{E_g(E_g+\Delta_0)}{E_g+(2/3)\Delta_0}\frac{1}{E_0}$$

$$\times \int_{E_0}^{\infty} \left\{ \left[\exp \frac{[M/(1+M)](E_{cv} - E_0) + \varepsilon_n - \mu_n}{T} + 1 \right]^{-1} \right.$$
$$\left. + \left[\exp \frac{[1/(1+M)](E_{cv} - E_0) + \varepsilon_p - \mu_p}{T} + 1 \right]^{-1} - 1 \right\} \quad (5)$$
$$\times \left\{ 1 + \frac{\varepsilon_n}{\varepsilon_n + [M/(1+M)](E_{cv} - E_0)} \right\} F(E_{cv}, \hbar\omega) \frac{dE_{cv}}{E_{cv}}.$$

Here, $\hbar\omega$ is the photon energy; $\alpha = e^2/\hbar c \approx 1/137$; ϵ is the dielectric constant of the cavity; m_0 is the free electron mass; $M = (m_{hh}/m_c)$; E_g, Δ_0 are, respectively, the band gap and the spin–orbit splitting in a QW; E_{cv} is the optical transition energy; $E_0 = E_g + \varepsilon_n + \varepsilon_p$, where ε_n, ε_p are the energies of size-quantization levels for electrons in the conduction band and holes in the valence band, reckoned from the respective band edges; μ_n, μ_p are the quasi-Fermi levels for electrons and holes, also reckoned from the corresponding band edges; and $F(E_{cv}, \hbar\omega)$ is the spectral broadening function having the form [10]:

$$F(E_{cv}, \hbar\omega) = \frac{1}{\pi} \frac{\hbar/\tau_{in}}{(E_{cv} - \hbar\omega)^2 + (\hbar/\tau_{in})^2}, \quad (6)$$

where τ_{in} is the intraband relaxation time. In the calculations, we assume that τ_{in} is constant and equal to 10^{-13} s. This assumption is not valid for very high concentrations at the lasing threshold, the intraband relaxation time itself being a function of temperature. Consequently, the temperature dependence of the gain becomes nonlinear and differs from that calculated using the Lorentz broadening function with τ_{in} = const (6) or the delta-function with infinite relaxation time [11].

The overlap integral of the envelopes of the electron and hole wave functions in the direction perpendicular to the QW plane, I_{cv}, are less than unity, owing to the difference between the electron and heavy-hole effective masses and to the different band offsets [9].

In a shallow QW, electrons and holes are, respectively, weakly and strongly localized. As a result, the electrons are redistributed near the active region, with the quasi-neutrality condition fulfilled in QWs and in the adjoining barrier layers and written as [1]:

$$p_{QW}^{2D} = n_{QW}^{2D} + n_b^{2D}, \quad (7)$$

n_b^{2D} is the 2D concentration of electrons in the barrier region, and n_{QW}^{2D} and p_{QW}^{2D} are the 2D electron and hole concentrations in the QW.

The threshold carrier concentration was determined by solving a self-consistent problem, with account taken of the delocalization effect [1]. It was shown that delocalization may substantially raise the threshold 2D concentration n_{th}^{2D} (Fig. 5). Figure 5 shows the temperature dependences of the threshold concentration of electrons for two cases: an infinitely deep QW, with no carriers emitted (curve *1*), and a finite QW depth, with delocalized electrons (curve *2*). It can be seen that, when the carrier emission is taken into account, the threshold concentration is substantially (nearly two times) higher.

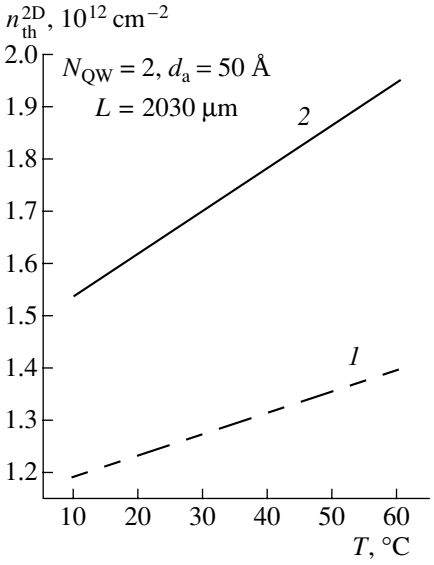

Fig. 5. Calculated temperature dependences of threshold concentration for a laser with 2 QWs: (*1*) no carrier emission from the well and (*2*) with emission taken into account.

Further, the threshold concentration and its temperature dependence are affected by at least two more factors. The first of these is the dependence of the relaxation time τ_{in} on temperature and on the nonequilibrium carrier concentration. As shown in [11], if real dependences of τ_{in} on temperature and concentration n_{th}^{2D} are taken into account, the gain $g(\hbar\omega)$ becomes a steeper function of temperature and concentration; in addition, the $g(\hbar\omega)$ value is in this case lower than at τ_{in} = const. This behavior of $g(\hbar\omega, T, n)$ leads to a higher threshold concentration n_{th}^{2D} and changes its temperature dependence. The second factor, exerting a weaker influence on the n_{th}^{2D} value, is the dependence of α_{int} on temperature and concentration. As shown in [5], the $\alpha_{int}(T)$ dependence leads to a nonlinear temperature dependence of the threshold concentration. In what follows, we restrict our consideration to a linear temperature dependence of α_{int}.

The threshold current of a laser structure can be represented as the sum of the radiative (J_R) and nonradiative (J_A) currents [1]:

$$J_{th} = J_R + J_A. \quad (8)$$

The radiative component can be written as:

$$J_R = eN_{QW}B^{2D}n_{QW}^{2D}p_{QW}^{2D}, \quad (9)$$

where B^{2D} is the 2D coefficient of radiative recombination. For the structures under study, the room-temperature value of B^{2D} is $\sim 5 \times 10^{-5}$ cm^2/s at the concentration $n_{QW}^{2D} \approx 1.5 \times 10^{12}$ cm^{-2}. For nondegenerate holes [1]

$$B^{2D} \propto \frac{1}{T}, \quad n_{QW}^{2D}, p_{QW}^{2D} \propto T. \quad (10)$$

Then, the radiative current near the lasing threshold is a linear function of temperature. If the dependence $\alpha_{int}(T)$ is taken into account, then $n_{th}^{2D} \propto T^{1+\alpha}$, where $\alpha > 0$, and, therefore, the radiative current becomes a nonlinear function of temperature: $J_R \propto T^{(1+2\alpha)}$.

The nonradiative component of the current was calculated taking into account three mechanisms of Auger recombination in QWs. In addition to the conventional threshold 2D Auger process, the thresholdless [7] and quasi-threshold [8] Auger processes were considered. As shown in [8, 9], it is the thresholdless and quasi-threshold Auger recombination processes that predominate in narrow QWs. The rate of thresholdless Auger recombination depends only slightly on temperature. Instead of the exponential dependence typical of the 3D case, the temperature dependence of the thresholdless Auger process is a power law. In this case, the Auger coefficient itself depends strongly and nonmonotonically on the QW size. It is important to note that the Auger recombination process in QWs is enhanced in comparison with that in the 3D case owing to stronger carrier localization. Consequently, the contribution of the Auger recombination to the threshold current of a QW laser is substantially larger.

In the general case, the Auger component of the current has the form:

$$J_A = eN_{QW}(C_{CHCC}^{2D}n^2p + C_{CHHS}^{2D}np^2). \quad (11)$$

Here, C_{CHCC}^{2D} is the Auger recombination coefficient for the excitation of an electron into the conduction band; C_{CHHS}^{2D} is the coefficient for the Auger recombination with excitation of a heavy hole into the spin-orbit-split band; and n and p are the 2D electron and hole concentrations, respectively. The rates of these two processes have been studied in detail in [8, 9]. The dependences of the Auger recombination coefficients on QW parameters and temperature were carefully analyzed for the three processes (thresholdless, quasi-threshold and threshold) in these studies. Both of the Auger recombination coefficients mentioned, C_{CHCC}^{2D} and C_{CHHS}^{2D}, have three components corresponding to the three mechanisms of Auger recombination; e.g.,

$$C_{CHCC}^{2D} = C_{CHCC}^{(1)} + C_{CHCC}^{(2)} + C_{CHCC}^{(3)}, \quad (12)$$

where $C_{CHCC}^{(1)}$ corresponds to thresholdless Auger recombination; $C_{CHCC}^{(2)}$, to quasi-threshold recombination; and $C_{CHCC}^{(3)}$, to the threshold process. In the limit $a \longrightarrow \infty$ (a homogeneous semiconductor), the sum of the quasi-threshold and threshold Auger coefficients, multiplied by the squared QW width, $C_{CHCC}^{(2)}a^2 + C_{CHCC}^{(3)}a^2$, tends to the bulk value of the Auger recombination coefficient, C_{CHCC}^{3D}, with the product $C_{CHCC}^{(1)}a^2$ approaching zero. For sufficiently narrow QWs, the 2D Auger recombination coefficient multiplied by a^2 exceeds the 3D value C_{CHCC}^{3D} due to the predominance of the thresholdless and quasi-threshold Auger recombination processes. For the structures under study, the sum of the 2D Auger recombination coefficients is $C^{2D} = C_{CHCC}^{2D} + C_{CHHS}^{2D} \approx 1.5 \times 10^{-16}$ cm^4/s at room temperature. The corresponding 3D Auger coefficient is $C^{2D}a^2 \approx 1 \times 10^{-28}$ cm^6/s, which is an order of magnitude higher than the average bulk value $C^{3D} \approx 10^{-29}$ cm^6/s [12]. We may conclude that Auger recombination in QWs is enhanced in comparison with the process in a homogeneous semiconductor, with this enhancement being even stronger at low temperatures. In these conditions, the 3D Auger recombination coefficient C_{CHCC}^{3D} is small because of its exponential temperature dependence [8]. It is noteworthy that the entire analysis of how the Auger recombination coefficients depend on temperature and QW parameters can be applied qualitatively to both the *CHCC* and *CHHS* Auger recombination processes.

5. DISCUSSION OF THE RESULTS

Dependences of the laser threshold current on the temperature and the cavity length were obtained in experiments with structures having different numbers and thicknesses of QWs, and also different cavity compositions. The threshold current density in the structures studied becomes higher with increasing number of QWs, being 0.26 and 1.68 kA/cm^2 for "four-cleaved" lasers with $\alpha_{ext} \approx 0$ and 2 and 10 QWs, respectively. The internal optical losses α_{int}, found from the dependence of the inverse differential efficiency on the cavity length, grow nearly in proportion to the number of QWs, being 5 and 30 cm^{-1} at room temperature for structures with two and ten QWs, respectively. This is associated with the increasing number of additional heterointerfaces in the active regions of the lasers. As shown in [5], intraband absorption of radiation in heterostructures is possible without involving a third par-

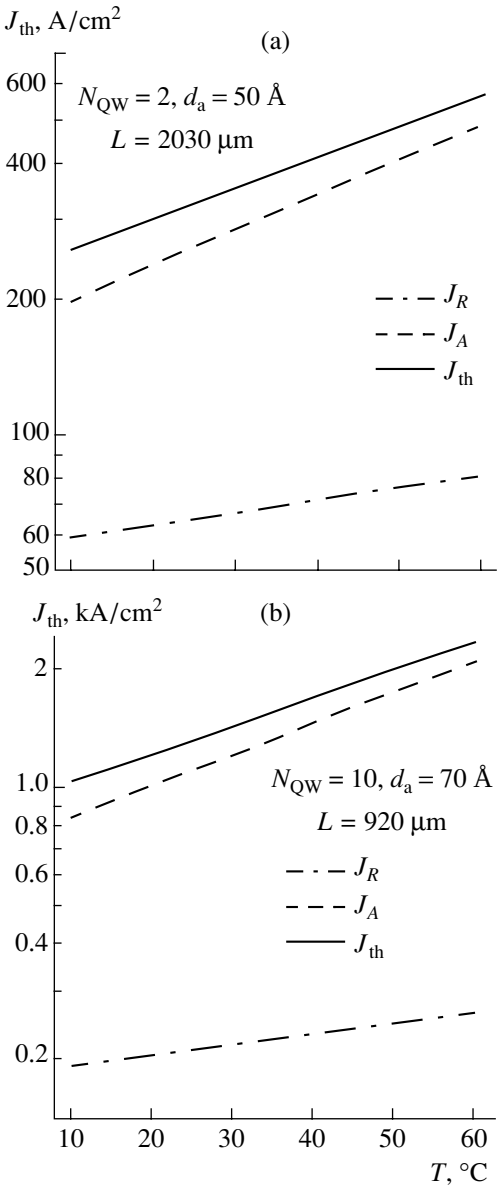

Fig. 6. Calculated temperature dependences of the threshold current components for structures with (a) 2 and (b) 10 QWs. (J_R) Radiative current, (J_A) nonradiative current, and (J_{th}) total threshold current; the same for Fig. 7.

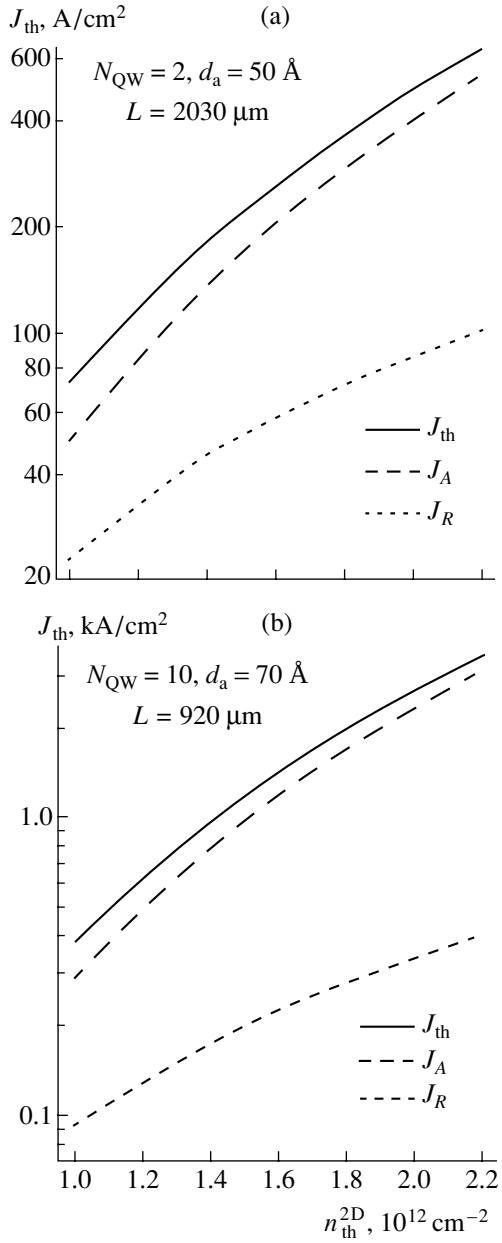

Fig. 7. Calculated dependences of the threshold current components on the threshold concentration for structures with (a) 2 and (b) 10 QWs.

ticle in addition to an electron and a photon. By absorbing a photon, an electron passes to an excited state, its momentum being scattered at heterointerfaces. Hence, the presence of a heterointerface stimulates the process of intraband absorption compared with the homogeneous case.

Room-temperature dependences of the threshold current density on the cavity length were calculated in terms of the model described (Figs. 3a and 3b, curves *2*). The structural parameters used in the calculations were as follows: E_g = 0.76 eV, m_c = 0.053m_0, and m_{hh} = 0.42m_0. The adopted QW depths for electrons (ΔE_c) and holes (ΔE_v) were 0.117 and 0.233 eV, respectively. The calculation demonstrated a good qualitative agreement between the theoretical model and the experimental data.

Temperature dependences of the threshold current were obtained for lasers with two and ten QWs by varying the crystal temperature in the range of 10–60°C by means of a Peltier element. The corresponding calculated dependences are presented in Figs. 2a and 2b (curves *2*, *3*). Qualitative and quantitative agreement

between theory and experiment is observed for lasers with different numbers of QWs, N_{QW}. Two cases were considered when calculating the threshold current: the first having constant internal losses α_{int} (curve *2*) and the second having temperature-dependent internal losses (curve *3*). In the second case, we restricted the consideration to a linear temperature dependence: $\alpha_{int} = \alpha_0(T/10°C)$, where α_0 is the room-temperature value of α_{int}. It can be seen that taking into account the temperature-dependent α_{int} somewhat improves the agreement between the experimental and calculated temperature dependences of the threshold current.

Experimental temperature dependences of the threshold current density are well approximated by power-law functions, $J_{th} \propto T^k$, with exponent $k = 1.5$. It is important that even at higher temperatures, when the principal recombination channel is the nonradiative Auger process, the temperature dependence of the threshold current still follows a power law. The absence of the exponential rise associated with the threshold Auger process typical of the 3D case indicates the predominance of the thresholdless Auger recombination in QW laser structures. The thresholdless Auger process is characterized by a power-law temperature dependence [8, 9]. To analyze the temperature dependence of the threshold current in detail, we calculated the temperature dependences of partial contributions to the threshold current (Eqs. (8), (9), (11)) for structures with two and ten QWs (Figs. 6a and 6b). As mentioned above, the radiative current at the generation threshold is a nearly linear function of temperature, $J_R \propto T^{1+2\alpha}$, and the current related to nonradiative Auger recombination is $J_A \propto T^{3/2}$. Thus, theoretical analysis shows that the Auger recombination, and specifically the thresholdless Auger recombination, makes the main contribution to the threshold current density. Evidently, to raise the quantum efficiency and, consequently, the output power of long-wavelength lasers, a laser structure should be optimized to suppress the Auger recombination [5].

The dependence of the characteristic temperature T_0 on the cavity length was found for a laser with two QWs from the experimental temperature dependences of the threshold current (Fig. 4, curve *1*). A calculated $T_0(L)$ dependence is also presented (Fig. 4, curve *2*). A good agreement between the theoretical and experimental curves is obtained. The maximum value of T_0 for the laser structure studied is 65 K.

Room-temperature dependences of separate components of the threshold current on the 2D carrier concentration were calculated for structures with two and ten QWs (Figs. 7a and 7b). The concentration was varied within the range $(0.9–2) \times 10^{12}$ cm^{-2}. The threshold current depends on concentration for two and ten QWs in the same way: $J_{th} \propto n_{th}^{2D}$.

As regards the minimum threshold current, a laser structure with two to four quantum wells is optimal; however, if higher optical emission power is necessary, and, respectively, a longer cavity is used, a structure with one (wide) QW is the optimal choice.

In analyzing the threshold characteristics of lasers with QWs we disregarded carrier and lattice heating. As shown in [13], heating affects the threshold characteristics at elevated temperatures. Heating exerts a strong influence on the light–current characteristics of a laser. This problem will be considered elsewhere. Moreover, we ignored the dependence of the intraband relaxation time τ_{in} on temperature and carrier concentration. This issue was analyzed in detail in [11].

6. CONCLUSION

The temperature dependences of the threshold characteristics of $\lambda = 1.55$ μm InGaAsP/InP QW lasers were studied. A detailed analysis of partial contributions from all the recombination processes to the threshold current was performed with account taken of the specific features of nonradiative Auger processes in QWs and weak localization of carriers.

It is established that power-law functions are the best approximation for experimental temperature dependences of the threshold current density; this indicates the domination of a thresholdless Auger recombination in laser structures with QWs. As shown in [8, 9], the thresholdless Auger process is characterized by a power-law dependence on temperature.

The good agreement between the experimental and theoretical dependences of the threshold current for lasers with different numbers of QWs on temperature and cavity length confirms that the theoretical model [1] offers an adequate description of the threshold current density for QW lasers. Another important result of the present study is the experimental confirmation of the power-law temperature dependence of the Auger recombination coefficients, first predicted in [7].

ACKNOWLEDGMENTS

We thank R.A. Suris for his helpful participation in discussions of the results.

This study was supported in part by the Russian Foundation for Basic Research (project nos. 99-02-16796, 01-07-90299, 01-07-90300, and 01-02-17851) and the Program “Physics of Solid State Nanostructures” (project nos. 99-0238, 97-0003, and 97-1035).

REFERENCES

1. I. V. Asryan, N. A. Gun’ko, A. S. Polkovnikov, *et al.*, Semicond. Sci. Technol. **15**, 1131 (2000).
2. E. G. Golikova, V. P. Duraev, S. A. Kozikov, *et al.*, Kvantovaya Élektron. (Moscow) **22**, 85 (1995).

3. E. G. Golikova, V. A. Gorbylev, N. Yu. Davidyuk, *et al.*, Pis'ma Zh. Tekh. Fiz. **26** (6), 5 (2000) [Tech. Phys. Lett. **26**, 225 (2000)].
4. E. P. O'Reilly and A. Ghiti, in *Quantum Well Lasers*, Ed. by P. S. Zory, Jr. (Academic, Boston, 1991).
5. G. G. Zegrya, *Mid-Infrared Strained Diode Lasers in Antimonide-Related Strained-Laser Heterostructures*, Ed. by M. O. Manasreh (Gordon and Breach, Amsterdam, 1997), p. 273.
6. A. Al-Muhanna, L. J. Mawst, D. Botez, *et al.*, Appl. Phys. Lett. **73**, 1182 (1998).
7. G. G. Zegrya and V. A. Kharchenko, Zh. Éksp. Teor. Fiz. **101**, 327 (1992) [Sov. Phys. JETP **74**, 173 (1992)].
8. A. S. Polkovnikov and G. G. Zegrya, Phys. Rev. B **58**, 4039 (1998).
9. G. G. Zegrya and A. S. Polkovnikov, Zh. Éksp. Teor. Fiz. **113**, 1491 (1998) [JETP **86**, 815 (1998)].
10. M. Asada, in *Quantum Well Lasers*, Ed. by P. S. Zory, Jr. (Academic, Boston, 1991); M. Asada, IEEE J. Quantum Electron. **QE-25**, 2019 (1989).
11. G. G. Zegrya, N. A. Gunko, I. A. Kostko, and G. V. Skrynnikov, in *Proceedings of the 9th International Symposium on Nanostructures: Physics and Technology, 1993*.
12. IEEE Photonics Technol. Lett. **5**, 2120 (1993).
13. L. V. Asryan, N. A. Gun'ko, A. S. Polkovnikov, *et al.*, Semicond. Sci. Technol. **14**, 1069 (1999).

Translated by D. Mashovets

Semiconductors, Vol. 35, No. 8, 2001, pp. 970–973. Translated from Fizika i Tekhnika Poluprovodnikov, Vol. 35, No. 8, 2001, pp. 1009–1012.

PHYSICS OF SEMICONDUCTOR DEVICES

An Ionization-Type Si:S-Based Semiconductor Converter of Infrared Images with Sensitivity in the Spectral Range of CO_2-Laser Radiation

V. T. Tulanov, Kh. B. Siyabekov, A. Sh. Davletova, and K. A. Ortaeva

Ulugbek State University, Universitetskaya ul. 95, Vuzgorodok, Tashkent, 700095 Uzbekistan

Submitted November 15, 2000; accepted for publication December 19, 2000

Abstract—An ionization-type semiconductor converter of infrared images that operates in the pulsed mode at a temperature of 77 K was studied. It is shown that it is possible to control the spectral range of photoconverter's photosensitivity (λ = 5–10.6 μm) by short-wavelength illumination of photodetector included in the converter. The response time of the converter is ~5×10^{-7} s. © *2001 MAIK "Nauka/Interperiodica".*

INTRODUCTION

Recently, semiconductor photographic systems [1–4] and ionization-type converters of infrared (IR) images [5–7] have been developed and improved mainly in relation to the problems of the spatial–temporal diagnostics of IR laser radiation. Considerable advances made along these lines have put the ionization systems in the forefront of the devices for the high-speed IR photography. Thus, it is now possible to extend the spectral range by shifting the long-wavelength cutoff from 0.7 to 5 μm; in addition, a photographic sensitivity of 10^6 cm^2/J, a photoresponse time of 10^{-7} s, and a threshold detected IR-radiation power of 5×10^{-4} W/cm^2 have been attained.

One of the ways of improving the photographic systems and the IR-image converters of ionization type further consists in widening the spectral range and reducing the threshold power of detected radiation.

To attain this, a special mode of doping the photoconductor material is required; this mode should ensure both the photosensitivity in the spectral region with longer wavelengths and a higher level of photoelectric gain. Such photoconductors can be fabricated on the basis of silicon doped with sulfur [8–12]. Extrinsic photoconductivity in the spectral region corresponding to CO_2-laser radiation (λ = 10.6 μm) was observed in Si:S [12]. The observed extrinsic photoconductivity can be accounted for by either the sulfur energy level at E_c – 0.08 eV [8], the level at E_c – 0.109 eV [9], or both levels (at E_c – 0.08 and E_c – 0.109 eV) simultaneously [10, 11].

In order to gain insight into the involvement of the above levels in photoconductivity in the vicinity of $\lambda \approx$ 10 μm, a number of experiments [13] were carried out in order to study the effect of the degree of compensation of the impurity-related donor levels by acceptors introduced by the γ-ray irradiation on photoconductivity in the spectral region corresponding to the CO_2-laser radiation.

Experiments have shown that, as the degree of compensation increases, the ratio of conductivities measured under illumination with a CO_2 laser and in the dark increases, which ensures the high definition (contrast) of images in the IR photographic systems using the above photodetectors. It was also shown theoretically that the energy levels of sulfur in silicon (E_c – 0.08 eV and E_c – 0.109 eV) are involved simultaneously in photoconductivity excited in the spectral region of $\lambda \approx$ 10.6 μm.

In this paper, we report the results of studying a new type of ionization-based converter of IR images; the converter operates in the pulsed mode and incorporates a Si:S photodetector.

BASICS OF OPERATION OF INFRARED CONVERTER AND EXPERIMENTAL TECHNIQUE

In general, the operation of the converter is based on controlling the discharge current in a gas-filled air gap formed by an insulator spacer *18* in projecting the IR image onto the photoconductor surface *15* (see Fig. 1). The discharge current in the system is established after a pulsed high voltage has been applied to electrodes *16* and *17*. The positive and negative (depending on the polarity of applied voltage) charges formed during the breakdown of the air gap give rise to an emission from the luminophor deposited on the inner surface of electrode *17*.

The emittance kinetics of luminophor in relation to the exposure-taking conditions is studied by photographing, visual observation, or detection with a photomultiplier. In certain cases, the image on the display can be multiply enhanced using an electron-optical image converter [14].

1063-7826/01/3508-0970$21.00

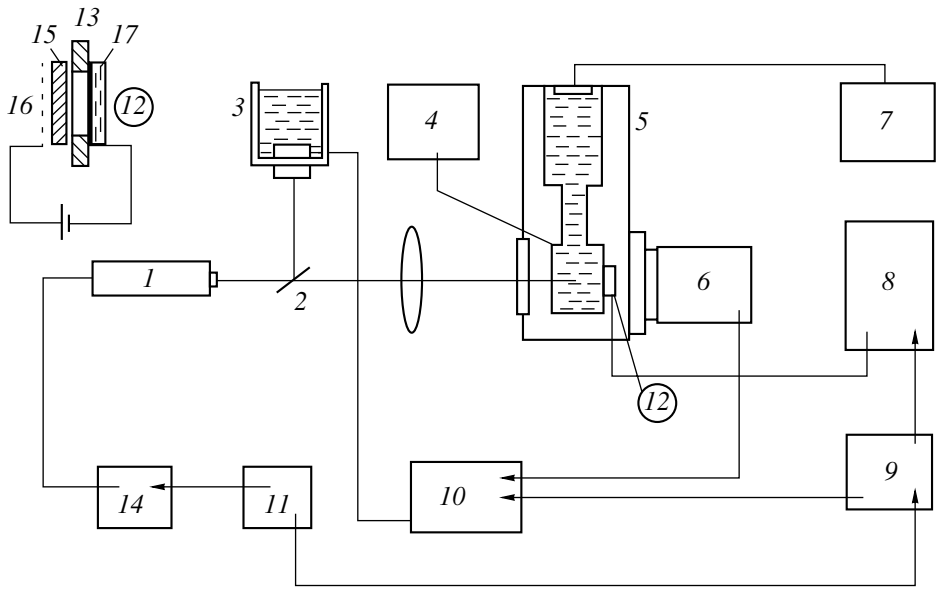

Fig. 1. Schematic representation of an ionization-type low-temperature pulsed converter of IR images. For details, see the text.

In order to accomplish photographing in the IR region of the spectrum, in particular, in the spectral region corresponding to the CO_2-laser radiation, the photographic cell *12* is installed in a cryostat *5* made in the form of a photographic device with special windows provided with IR filters.

This system is controlled with an oscillator *11*, which triggers the power supply *14* of laser *1* and simultaneously feeds a sweep signal to oscilloscope *10* via oscillator *9*.

When applying a high pulsed voltage from the source *8* (triggered by oscillator *9* via a delay line) to the system, the laser pulse passes through the IR lens *13* and forms a relief with a local variation in electrical conductivity at the photodetector. This relief controls the current density through the system and is transformed into a visible image on the display. In the course of photographing and measuring the characteristics of the photographic process, the temporal stability of the intensity of the laser beam split with mirror *2* is periodically checked with a cooled germanium photodiode *3*.

The system's temperature is measured with a copper–constantan thermocouple using a meter *4*. In order to maintain the lowest possible temperature in the course of detecting the laser beam at $\lambda = 10.6$ μm, a heat sink *7* is used.

In the course of establishing the optimal mode of photographing, the entire set of electrical measurements was performed using a storage oscilloscope *10* via a photomultiplier *6* and a photodiode *3*.

In order to measure the *D–H* characteristics (the dependence of the photolayer darkening on the illuminance power density) of the photosystem, we employed the discharge-emission photograph obtained using an airfilm-42 and a Zenit camera equipped with a Gelios objective lens and additional rings. The characteristic was measured by photographing a various number of incident pulses within the same exposure (total radiation energy at each spot was specified by the number of laser pulses).

In order to determine the resolving power of photodetectors, we analyzed the distribution of optical density of darkening at the boundary of absolute contrast. This distribution was measured using an IFO-451 microdensitometer with a slit width that ensured the linear resolution of 20 mm.

A CONVERTER WITH CONTROLLED SPECTRAL RANGE OF PHOTOSENSITIVITY

As is known, the spectral range of sensitivity for a semiconductor converter of IR images is governed by the photodetector.

Conventional photodetectors have a strictly fixed spectral range of sensitivity, which is specified by the position of local energy states in the band gap. Therefore, in order to obtain a photodetector sensitive in the medium- and long-wavelength spectral regions, one has to use various photodetectors with different positions of the levels and, correspondingly, with a different dark conductivity at a given operating temperature.

In this study, we established that it is possible to use photodetectors made of silicon doped with sulfur for operation in both the $\lambda = 1$–4 μm and $\lambda = 5$–10 μm spectral regions. Such a possibility was first theoretically demonstrated [15], experimentally implemented [12, 13], and is based on the phenomenon of induced extrinsic photoconductivity in semiconductors [16].

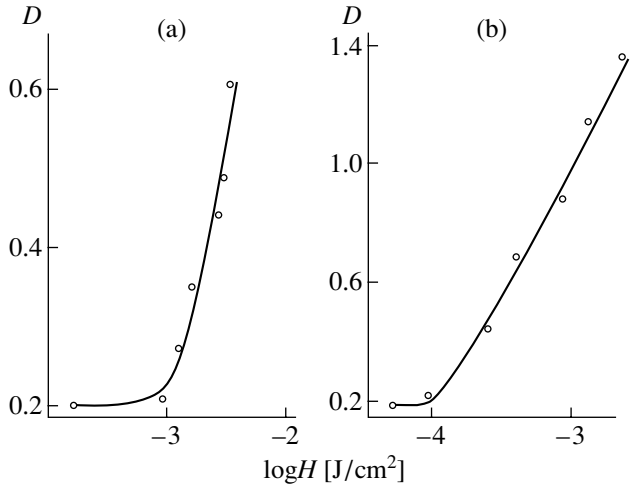

Fig. 2. The *D–H* characteristics of the laser-beam images; the characteristics were measured under (a) conventional illumination of photodetector and (b) the conditions of electron-optical enhancement.

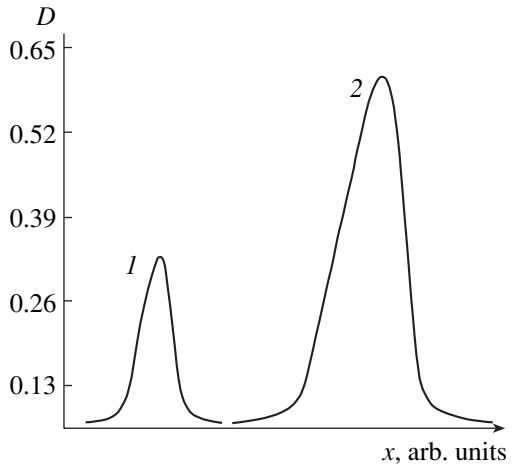

Fig. 3. A densitogram of photograph of CO_2-laser radiation along the coordinate *x* (*1*) without illumination and (*2*) under illumination through a germanium filter.

For a certain type of doping, we have a situation in which the local levels responsible for sensitivity in the medium-wavelength region of the spectrum (1–4 μm) are occupied, whereas the levels responsible for the long-wavelength sensitivity (5–10 μm) are unoccupied. In this situation, the sensitivity range of photodetector extends to 4 μm. If the entire surface of photodetector is uniformly irradiated with photons from a constant white-light source, the shallow levels become occupied and the photosensitivity in the region of up to 10 μm rises with the accompanying increase in the dark conductivity. Thus, a switch of photosensitivity from the region of $\lambda \le 4$ μm to the region of $\lambda \le 10$ μm is accomplished by a uniform constant illumination using an additional source of light.

THE RESPONSE SPEED OF THE CONVERTER

For high-speed photography, low-resistivity high-speed photodetectors are needed. As was mentioned above, such photodetectors are made of silicon doped with sulfur [12].

Calculations based on an analysis of transient processes in an ionization-type semiconductor photographic system show that, in order to attain a response time on the order of 10^{-7} s, the resistivity of semiconductor at the liquid-nitrogen temperature should be no higher than 7×10^4 Ω cm, which corresponds to the Fermi level position 0.125 eV below the conduction-band bottom. Under the conditions of our experiments, this corresponds to a current of 0.1 A for a voltage of 600 V applied to a 1-mm-thick photodetector.

If it is assumed that the shallowest energy level of sulfur is located at 0.1 eV below the conduction-band bottom, the occupancy of this level should be 2% at a temperature of 77 K.

In the experiments, we used an LGI-50 CO_2 laser that emitted pulses with a duration of 150 μs and an energy of 13 mJ. Oscillograms of the current show that the developed photodetectors make it possible to attain the transient times in the system at a level of $(3–5) \times 10^{-8}$ s. The current–power sensitivity in the spectral region in the vicinity of 10.6 μm is equal to 2.3×10^{-4} A/W.

Photographic characteristics of the system were studied using a pulsed power supply in the time range of 10^{-5} to 10^{-6} s. The sensitivity was no worse than 10^{-4} J/cm^2. The resolving power was 7 mm^{-1}.

Photographs were taken from the converter display for various exposures to the laser radiation with λ = 10.6 μm. In Fig. 2, we show the densitograms of an image (the *D–H* characteristics) of the laser beam; the characteristics were measured under (a) conventional illumination and (b) conditions of electron-optical enhancement.

Figure 3 shows the densitograms for radiation of a CO_2 laser along the coordinate *x* (*1*) without illumination and (*2*) under illumination through a germanium filter.

Thus, using the above-described ionization-type converter of IR images, one can accomplish a high-speed frame-by-frame photographing of the spatial–temporal distribution for the intensity of CO_2-laser radiation.

It should be emphasized that the aforementioned sensitometric characteristics of the photographic system under consideration are not limiting. An even higher performance can be attained by improving the specially developed technology for producing the Si:S samples and controlling the dark conductivity of these samples in combination with the electron-optical enhancement of images at the converter's display.

REFERENCES

1. L. G. Paritskiĭ and S. M. Ryvkin, Fiz. Tekh. Poluprovodn. (Leningrad) **4** (4), 764 (1970) [Sov. Phys. Semicond. **4**, 645 (1970)].
2. Yu. A. Astrov, G. B. Gorlin, L. G. Paritskiĭ, *et al.*, Available from VINITI, No. 31186-77.
3. Yu. A. Astrov, V. V. Egorov, Sh. S. Kasymov, *et al.*, Kvantovaya Élektron. (Moscow) **4**, 1681 (1977).
4. V. T. Toulanov and S. Z. Zaynabidinov, Turk. J. Phys. **21**, 1817 (1997).
5. Sh. S. Kasymov, L. G. Paritskiĭ, and S. M. Ryvkin, Fiz. Tekh. Poluprovodn. (Leningrad) **9** (4), 820 (1975) [Sov. Phys. Semicond. **9**, 543 (1975)].
6. V. T. Tulanov and A. T. Teshabaev, in *Research in Solid-State Physics* (Tashkents. Gos. Univ., Tashkent, 1981), p. 38.
7. V. T. Tulanov, Author's Abstract of Candidate's Dissertation (Fiz.-Tekh. Inst. im. S. V. Starodubtseva, Tashkent, 1998).
8. S. D. Brotherton, M. J. King, and G. J. Parker, J. Appl. Phys. **52** (7), 4649 (1981).
9. D. L. Comphausen, H. M. Jams, and R. J. Sladek, Phys. Rev. **132** (6), 1899 (1970).
10. B. Pojot, G. Grossmann, M. Astier, and C. Nand, Solid State Commun. **54** (1), 57 (1985).
11. B. Pojot and C. Naud, J. Phys. (Paris) **45**, 539 (1984).
12. Kh. B. Siyabekov and V. T. Tulanov, Fiz. Tekh. Poluprovodn. (St. Petersburg) **31**, 1425 (1997) [Semiconductors **31**, 1231 (1997)].
13. G. B. Gorlin, V. T. Tulanov, and Kh. B. Siyabekov, Zh. Tekh. Fiz. **67** (10), 142 (1997) [Tech. Phys. **42**, 1239 (1997)].
14. T. V. Burova, A. N. Lodygin, L. G. Paritskiĭ, *et al.*, Pis'ma Zh. Tekh. Fiz. **11**, 215 (1985) [Sov. Tech. Phys. Lett. **11**, 87 (1985)].
15. V. T. Tulanov and Kh. B. Siyabekov, Fiz. Tekh. Poluprovodn. (St. Petersburg) **27**, 1751 (1993) [Semiconductors **27**, 966 (1993)].
16. S. M. Ryvkin, *Photoelectric Effects in Semiconductors* (Fizmatgiz, Moscow, 1963; Consultants Bureau, New York, 1964).

Translated by A. Spitsyn

Semiconductors, Vol. 35, No. 8, 2001, pp. 974–978. Translated from Fizika i Tekhnika Poluprovodnikov, Vol. 35, No. 8, 2001, pp. 1013–1017.

PHYSICS OF SEMICONDUCTOR DEVICES

A Study of Technological Processes in the Production of High-Power High-Voltage Bipolar Transistors Incorporating an Array of Inclusions in the Collector Region

N. I. Volokobinskaya*, I. N. Komarov, T. V. Matyukhina, V. I. Reshetnikov, A. A. Rush, I. V. Falina, and A. S. Yastrebov

Bonch-Bruevich State University of Telecommunications, ul. Moĭka 61, St. Petersburg, 191186 Russia

** e-mail: volokobin@hotmail.com*

Submitted July 3, 2000; accepted for publication January 16, 2001

Abstract—Technological processes occurring in semiconductor structures during the fabrication of transistors that incorporate a new structural element in the form of an array of bulk inhomogeneities in the collector region were studied; this array inhibits the development of secondary breakdown. © *2001 MAIK "Nauka/Interperiodica".*

1. INTRODUCTION

According to theoretical analysis [1], an array of nearly spherical inclusions in the collector region can bring about a more uniform distribution of an electric field and an increase in the breakdown voltage of the common-emitter transistors.

When designing a new transistor, the electrical parameters and the geometric size of structural elements of the device were first determined from theoretical calculation and were then refined on the basis of experimental data. The geometric parameters included the diameter of inclusions, their separation, and the distance of the inclusion array from the metallurgical boundary of the collector p–n junction.

Experimental studies were performed in order to clarify and refine the details of the technological process, which included procedures for the epitaxial overgrowth of the layers and the oxidation of silicon wafers; it is known that structural defects affecting the breakdown of the collector p–n junctions are generated in the course of these procedures [2–6]. The effect of inclusion sizes on the defect density in the epilayer grown over the inclusion array had to be established.

Since the tetrahedral covalent radius of a boron atom (R_B = 0.088 nm) is smaller than that of a silicon atom (R_{Si} = 0.117 nm), the boron-doped p^+-type inclusions in the n-collector region give rise to stresses and to the generation of misfit dislocations [7, 8], which is accompanied with detrimental side effects. Dislocations and stacking faults bring about a reduction in the breakdown voltage of p–n junctions in electronic devices.

2. THE PROCESSES ACCOMPANYING THE FORMATION OF THE INCLUSION ARRAYS

Experiments have shown that the density of defects over inclusions increases noticeably as the inclusion size increases (Fig. 1). Therefore, it was necessary to limit the inclusion sizes so that the defect density does not exceed the acceptable value.

In the course of high-temperature treatment, stresses and accompanying defects are conducive to the evaporation of boron from heavily doped regions if the defect concentration is high. If the surface of the inclusions and that of the semiconductor wafer are exposed, then boron evaporates from the inclusions and is deposited on the entire surface of the semiconductor wafer; as a result, the process of self-doping with boron develops (see Fig. 2): inclusions merge into a continuous layer (*3*) in the wafer with wide (*1*) and thin (*2*) test strips of inclusions.

In order to prevent both self-doping with boron and the emergence of appreciable stresses, we implanted the impurities (needed for inclusion formation) through the SiO_2 layer using windows in the photoresist.

After the implantation of the impurities, the photoresist was removed, the oxide layer was kept intact, and high-temperature heat treatment aimed at driving in the impurities was performed. The oxide was then removed, and a silicon layer was grown epitaxially over the inclusions.

Inclusions were formed successfully when the impurities were implanted through windows 10×10 μm^2 in area.

As a result of subsequent high-temperature technological operations, the inclusions become spheroidal. The diameter of the inclusions in completed transistors of the new type was ~30 μm.

If the inclusions and the array period are small, many inclusions may then be accommodated beneath each of the emitter fingers and between these fingers. This statement can be verified by examining a photograph of the transistor surface with traces of inclusion outcrops; the transistor has a comb-shaped emitter (the brighter area) with a surrounding base (the darker area) (Fig. 3).

Small sizes of inclusions made it possible to simplify the fabrication of new transistors by eliminating the procedure for alignment of inclusions in the array with reference to the emitter fingers. Were there any need for alignment, the difficulty would consist in the fact that the silicon epilayer grows on the (111) plane at an angle to the [111] direction rather than perpendicularly to this plane; as a result, the pattern of inclusions emerging at the surface shifts along the crystallographic direction [112] by the amount δ as it is illustrated in the schematic representation (Fig. 4) of a test structure, the photograph of the angle lap of which is shown in Fig. 2.

The preliminary results made it possible to design the structure and the fabrication technology of the new transistors; the introduction of this technology does not result in a significant increase in the device cost.

3. PRODUCTION TECHNOLOGY OF TRANSISTORS WITH AN ARRAY OF INCLUSIONS

The modernized devices incorporating an array of inclusions in the collector region were fabricated using the epitaxial structures 74KÉF50/380ÉKÉS0.01;[1] the characteristics of these devices were compared with those of a conventional KT841 transistor.

The base region with a boron concentration as high as 10^{18} cm^{-3} and with a collector p–n-junction depth equal to X_{jb} = 20 μm was first formed by boron diffusion; a comblike emitter with a finger width of 246 μm, a perimeter of P_e = 77.5 mm, an area of S_e = 9.425 mm^2, and an emitter p–n junction depth equal to X_{je} = 10 μm were then formed using diffusion-based doping with phosphorus to a concentration of 10^{19} cm^{-3}. Following these technological operations, the thickness of the lightly doped collector layer beneath the active base was ~50 μm, with the collector area being equal to S_c = 18.8 mm^2.

[1] KÉF stands for P-doped n-Si; ÉKÉS, for Sb-doped n-Si; KDB (ÉKDB), for p-Si:B; the leftmost number corresponds to the thickness expressed in micrometers; and the rightmost number corresponds to the resistivity expressed in Ω cm.

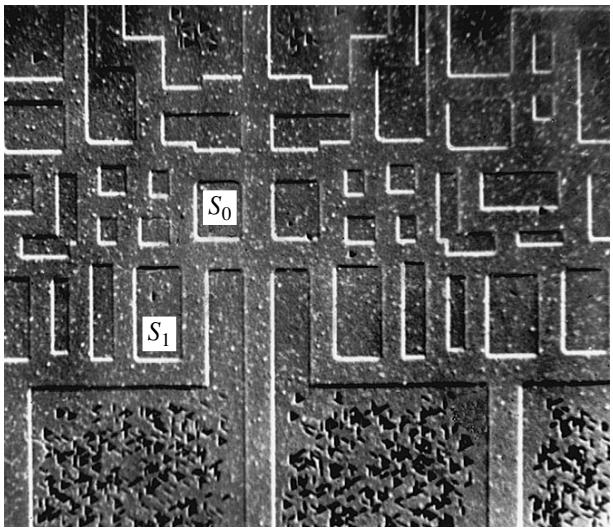

Fig. 1. A test structure with etch pits in the epilayer grown in the (111) plane over the inclusions with different areas ($S_0 < S_1 < S_2$).

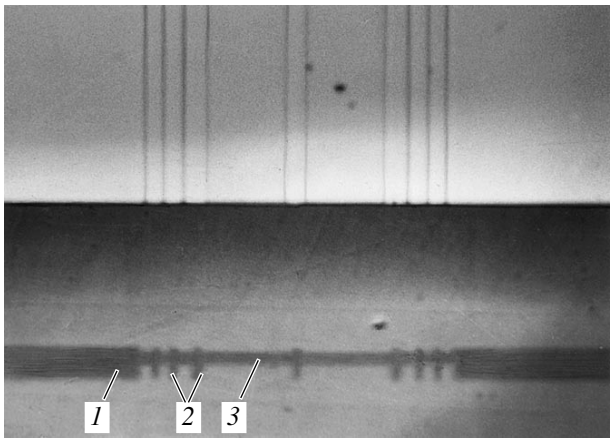

Fig. 2. A photograph of the angle lap of the test structure; the effect of merging of inclusions *1* and *2* (in the shape of strips) into continuous layer *3* as a result of self-doping with boron is illustrated.

After completing the technological operations to form the transistor structures, the wafers were cut into elements with dimensions of 5.1 × 5.1 × 0.226 mm.

In addition, we fabricated devices that differed from KT841 transistors in the depth of the collector and emitter p–n junctions and had X_{je} = 5 μm and X_{jb} = 10 μm. The new devices incorporating an array of inclusions had the same depths as the p–n junctions.

In order to prevent the surface breakdown of transistors, we formed three guard rings on silicon structures. Experiments show that this number of rings is sufficient; an increase in their number is not accompanied with an increase in the surface-breakdown voltage.

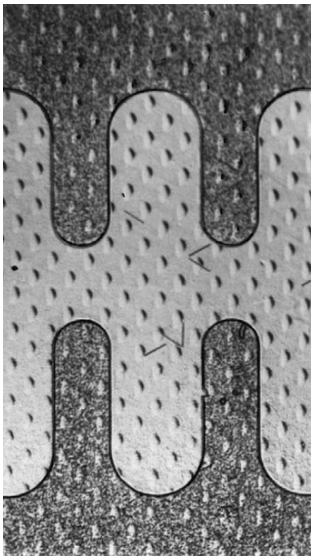

Fig. 3. The surface area of a transistor with traces of inclusions emerging at the surface.

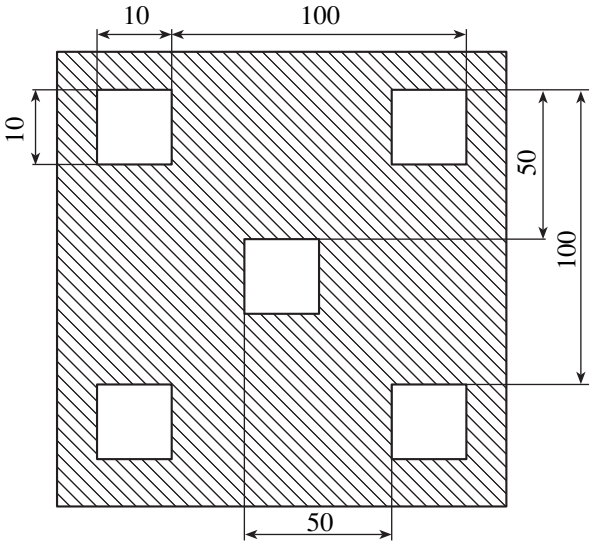

Fig. 5. A fragment of the photoresist mask for forming an array of inclusions in the collector region. The dimensions are expressed in micrometers; the windows are not shown to scale.

When fabricating the n–p–n–(p^+)–n–n^+ transistors [here, the symbol (p^+) designates spherical inclusions in the n-type collector region], the 30KÉF35/380ÉKÉS0.01, 35KÉF43/380ÉKÉS0.01, and 35KÉF53/380ÉKÉS0.01 epitaxial structures were used in three series of experiments.

The surface of the silicon wafers coincided with the (111) plane.

When fabricating the n–p–n–(p^+)–n transistors, the wafers were heated to 900°C and were coated with an oxide layer 0.17–0.20 μm thick; the photoresist layer was then deposited. Photolithography was used to form windows 10×10 μm^2 in area in the photoresist layer. The windows were arranged in a "face-centered" square lattice with a period of 100 μm; the diagonal distance between the neighboring windows was $L \approx 70$ μm (Fig. 5). An area of 1 mm^2 accommodated 200 windows.

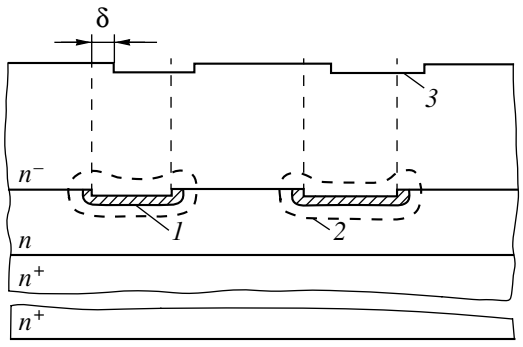

Fig. 4. Schematic representation of a test structure (in section): *1* corresponds to the boundary of a p^+ region after ion implantation, removal of oxide layer, and rinsing; *2* corresponds to the boundary of a p^+ region after epitaxial overgrowth of the n^- layer; and *3* indicates the traces of inclusions on the n^--layer surface.

We used a Vezuviĭ-5 ion accelerator to implant boron ions through the windows into the photoresist and the oxide layer; the ion energy was $E = 60$ keV, and the dose was $D = 100$ or 110 μC/cm^2. The photoresist was then removed, and boron was driven in at a temperature of 1150°C, first in an atmosphere of dry oxygen (for 120 min), then in wet oxygen (for 60 min), and finally again in dry oxygen (for 120 min). As a result, p^+-type regions were formed, with the p–n junction being located at a depth ranging from 3 to 5 μm (Fig. 6). The drive-in had to be performed under the oxide layer in order to prevent the self-doping of the entire wafer surface with boron and the resulting merger of inclusions.

The oxide layer was removed, the damaged layer with a thickness of 0.02–0.06 μm was etched off from the wafer surface, and the 47-μm-thick Si:P layer was overgrown epitaxially; the resistivity ρ of this layer was 43 or 53 Ω cm. The base with a p–n junction located at a depth of $X_{jb} = 10$ μm and the emitter with a p–n junction located at a depth of $X_{je} = 5$ μm were formed in the surface layer of the structure. Smaller thicknesses of the base and emitter regions compared to a KT841 transistor were dictated by the need to reduce the duration of the high-temperature treatment.

When fabricating the n–p–n^-–(p^+)–n–n^+ transistors with p^+-type inclusions and the n–p–n^-–n–n^+ transistors without inclusions, 30KÉF10/380ÉKÉS0.01 epitaxial structures were used; the transistors incorporated a buffer n layer and a depletion n^- layer in the collector

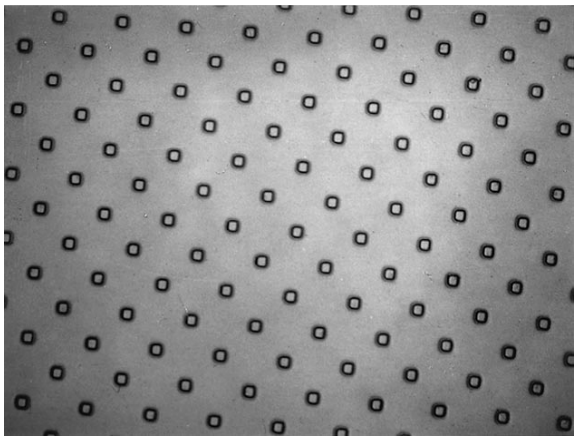

Fig. 6. The pattern of p^+-inclusions in the *n*-Si layer prior to the growth of the epilayer.

region. The KÉF-10 layer was used as an *n*-type buffer layer.

The p^+-type inclusions were formed in the surface layer of these wafers; a 70KÉF43 layer was then grown over these inclusions. Thus, the array of inclusions was located at the interface between the lightly doped and buffer layers.

The thickness and resistivity of the lightly doped and buffer layers can be calculated for a conventional transistor with a specified operating voltage and collector current [9].

As a result of high-temperature treatment, the inclusions became spherical. The diameter of the inclusions increased up to 30 μm, and their cross sections in the array plane occupied about 14.14% of the area of the collector p–n junction.

When fabricating the p–n–p^-–(n^+)–p^-–p–p^+ transistors, we used 35KDB33/16KDB10/380ÉKDB0.03 epitaxial structures.

A Vezuviĭ-8 ion accelerator was used to implant the Sb ions into the wafers through the oxide layer and the windows in the photoresist; the ion energy was E = 30 keV, and the dose was D = 30 μC/cm^2. Antimony was driven in during heat treatment for 2 h at 1200°C in an atmosphere of dry oxygen. The oxide layer was then removed, and the wafer surface was cleaned; following this procedure, an Épikvar-101M system was used to grow a surface Si:B epilayer by chloride-based technology at 1172°C.

Photographs of angle laps for the p–n–p^-–(n^+)–p^-–p–p^+ transistors are shown in Fig. 7. All the inclusions are located within the collector region in the same plane at the same distance from the metallurgical boundary of the base. Two neighboring rows of inclusions can be seen in the angle-lap plane (Fig. 7).

In order to improve the high-frequency properties and to preserve them at a level characteristic of similar transistors without inclusions, we subjected the new

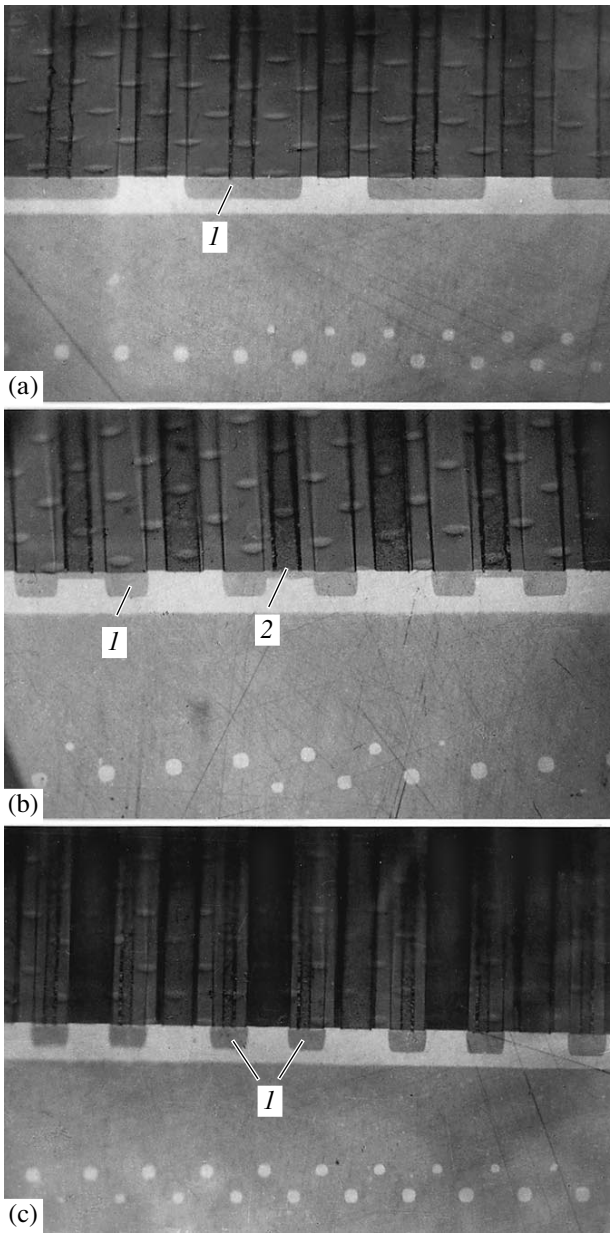

Fig. 7. Photographs of the angle laps (at an angle of 9°20′ to the surface plane) for p–n–p^-–(n^+)–p^-–p–p^+ transistors with emitters of various configurations: (*1*) emitter region, (*2*) lightly doped or undoped central region of the emitter. (a) Transistor with emitter of conventional configuration; (b) transistor with heavily doped peripheral region (*1*) and lightly doped central region (*2*) of the emitter; and (c) transistor with undoped central region of the emitter.

transistors to radiation treatment with alpha particles. In addition, we used emitters with a lightly doped central region and so-called "perforated" emitters whose central region was undoped and, consequently, was inactive. The angle laps of p–n–p^-–(n^+)–p^-–p–p^+ transistors with emitters of various configurations are represented in Fig. 7.

4. CONCLUSION

Experiments confirm the theoretical prediction that the breakdown voltage U_{ce0} can be increased to a value close to U_{cb0} by incorporating an array of inclusions in the collector region, with the value of U_{cb0} remaining almost unchanged in comparison to that in a similar transistor without inclusions [1]. Thus, it is appropriate to use the arrays of inclusion in the collector region to increase the breakdown voltage U_{ce0}.

REFERENCES

1. M. Yu. Volokobinskiĭ, I. N. Komarov, T. V. Matyukhina, *et al.*, Fiz. Tekh. Poluprovodn. (St. Petersburg) **35** (2), 245 (2001) [Semiconductors **35**, 238 (2001)].
2. L. I. Matynina, A. I. Pekarev, and Yu. D. Chistyakov, Izv. Vyssh. Uchebn. Zaved., Radiotekh. **22** (9), 3 (1978).
3. V. N. Tverskov, A. G. Kostogryz, V. M. Suvorov, *et al.*, Élektron. Tekh., Ser. 6: Mater., No. 3, 35 (1976).
4. M. G. Mil'vidskiĭ and V. B. Osvenskiĭ, *Structural Defects in Epitaxial Layers of Semiconductors* (Metallurgiya, Moscow, 1985).
5. A. Zelenov and V. Minbazin, Mikroélektronika **3** (57), 15 (1975).
6. Yu. A. Malinin, V. A. Tverikov, *et al.*, Élektron. Tekh., Ser. 6: Mater., No. 2, 55 (1975).
7. *Fundamentals of Silicon Integrated Device Technology*, Vol. 1: *Oxidation, Difusion, Epitaxy*, Ed. by R. M. Burger and R. P. Donovan (Prentice Hall, Englewood Cliffs, 1967; Mir, Moscow, 1969).
8. *Atomic Diffusion in Semiconductors*, Ed. by D. Shaw (Plenum, London, 1973; Mir, Moscow, 1975).
9. V. A. Potapchuk and M. Yu. Shneĭderman, Élektrotekh. Prom-st., Ser. Preobraz. Tekh., No. 11 (157), 4 (1983).

Translated by A. Spitsyn

Semiconductors, Vol. 35, No. 8, 2001, p. 979.

ERRATA

Erratum: "Carrier Photoexcitation from Levels in Quantum Dots to States of the Continuum in Lasing" [*Semiconductors* 35 (3), 343 (2001)]

L. V. Asryan and R. A. Suris

The right-hand side of Eq. 13 (page 345) should be multiplied by π.

1063-7826/01/3508-0979$21.00